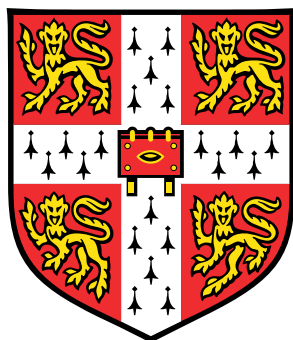# Path-integral studies of quantum statistical effects in vibrational spectroscopy

Raz Lior Benson

Sidney Sussex College

University of Cambridge

This thesis is submitted for the degree of Doctor of Philosophy

Yusuf Hamied Department of Chemistry

June 2021

Declaration

This thesis is the result of my own work and includes nothing which is the outcome of work done in collaboration except as declared in the Preface and specified in the text. I further state that no substantial part of my thesis has already been submitted, or, is being concurrently submitted for any such degree, diploma or other qualification at the University of Cambridge or any other University or similar institution except as declared in the Preface and specified in the text. It does not exceed the prescribed word limit for the relevant Degree Committee. Some of the work described in this thesis has been published in:

- R. L. Benson, G. Trenins and S. C. Althorpe, *Faraday Discuss.*, 2020, **221**, 350;

- R. L. Benson and S. C. Althorpe, *J. Chem. Phys*, 2021, **155**, 104107.

<div align="right">

Raz Lior Benson

June 2021

</div>

Path-integral studies of quantum statistical effects in vibrational spectroscopy

Raz Lior Benson

We examine the role of nuclear quantum statistical effects in the vibrational spectroscopy of molecular systems at finite temperatures.

Our starting point is Matsubara dynamics, which rigorously combines quantum Boltzmann statistics with classical real-time trajectories, by filtering out the high-frequency components of the imaginary-time Feynman paths that are responsible for quantum coherence. Using a simple model of perturbed harmonic oscillators, it is shown that most of the intensity differences between quantum and classical non-fundamental (overtone, combination, and difference) bands can be accounted for by the anharmonic coupling between the imaginary-time path centroid and the fluctuations around it. This coupling causes the amplitudes of the relevant centroid vibrations to be 'Matsubara heated' to an effective temperature that is consistent with the underlying quantum distribution. Quantum coherence thus appears to play no major role in describing such features, contrary to what has sometimes been assumed in the literature.

Practical path-integral methods for calculating vibrational spectra, such as centroid and thermostatted ring-polymer molecular dynamics, faithfully capture the harmonic behaviour of the centroid but make drastic approximations to the fluctuation dynamics. We explain how these approximations render such methods incapable of predicting non-fundamental bands with significantly more accuracy than classical mechanics. This is borne out by illustrative simulations of water in its gas, liquid, and ice phases; the linearised semiclassical initial value representation is shown to be the only established trajectory-based approach that reproduces most non-fundamental bands with qualitative accuracy, even though it suffers severe zero-point energy leakage on a sub-picosecond timescale. However, a simple quantum–classical correction formula (derived from first-order perturbation theory) is shown to bring the predictions of path-integral methods into much closer agreement with exact quantum results.

Finally, a simple model of the carbon dioxide molecule is studied numerically to establish that 'Matsubara heating' accounts for the quantum (temperature quasi-independent) behaviour of the Fermi resonance splitting, which is underestimated by path-integral methods analogously to overtone band intensities.

Acknowledgements

I owe a debt of gratitude to my supervisor, Stuart Althorpe, whose outstanding insight and unfathomable patience have enabled me to make progress in a research area I find both challenging and fascinating.

I am deeply grateful also to Michael Willatt, who taught me a great deal during the year we were both in the Althorpe Group, and whose encouraging and enthusiastic attitude helped inspire me to continue working in the field. I thank George Trenins and Eszter Pós for always being on hand to assist and advise. George in particular is acknowledged for carrying out all the QCMD simulations, as well as the condensed-phase classical MD and TRPMD simulations, that are reported in Chapter 4 and Appendix C.1; some of these results have not yet been published elsewhere. I thank Vijay Ganesh Sadhasivam for carefully reading this thesis and providing me with many useful comments and suggestions. I am grateful to all these and other members of the Althorpe Group, past and present, for interesting discussions and excellent companionship.

Thanks to Thomas Plé, Simon Huppert, Fabio Finocchi, Philippe Depondt, and Sara Bonella for sharing with us a preprint of ref. 65 prior to publication. Some of the results reported therein are complementary to those of Chapters 3–5.

My partner, Emily, has supported me better than I could have imagined—proofreading this thesis was one huge favour among many, and I cannot thank her enough. Finally, I am forever grateful to my parents, Samantha and Jonathan, and my sister, Harley, for their unending support, guidance, and generosity.

Contents

Chapter 1

Introduction

Quantum theory provides a remarkably accurate description of the atomic-scale physics of molecular systems [1, 2]. Under the Born–Oppenheimer approximation, the motion of the electrons is treated as being adiabatically separated from that of the much heavier nuclei [3], and many sophisticated computational methods have been developed to solve the electronic part of the problem with a high degree of accuracy [4, 5]. Much of the complexity that continues to drive research in this area arises because an accurate description of electronic structure is impossible if one does not account properly for fermionic exchange interaction. In contrast, nuclei often interact at distances far exceeding their average de Broglie wavelengths, so such exchange effects can be safely neglected, regardless of the true nuclear spin statistics [6].

The accurate quantum mechanical modelling of nuclei is met with its own challenges, however. Unlike electrons, which can often be regarded to a first approximation as dynamically (almost) uncorrelated, nuclei interact with one another in a highly localised manner that is mediated by the Born–Oppenheimer potential energy surface (PES). Furthermore, many molecular systems are unlikely to be thermally excited from their electronic ground states, whereas this is rarely the case for all the nuclear degrees of freedom except at extremely low temperatures. With current state-of-the-art methods, fully quantum mechanical, non-perturbative treatments of nuclear vibrational dynamics are feasible for systems with less than about twenty atoms [7–9]. These methods usually involve diagonalising the (ro)vibrational Hamiltonian (which may be approximated) in a finite basis set, to yield a finite number of energy eigenstates and eigenvalues. However, alternative approaches based on grid-based representations of the wave function are sometimes preferable, such as when the PES is highly anharmonic [10–12]. One especially popular approach—which may be considered a hybrid of basis expansion and purely grid-based techniques—is to use a discrete variable representation (DVR) of the Hamiltonian, which turns it into a matrix with a high degree of sparsity that can be exploited using well-known diagonalisation algorithms [13–15].

For larger systems, particularly those in condensed phases, computational chemists usually

resort to classical descriptions of the nuclei. Classical molecular dynamics (MD) and Monte Carlo (MC) simulations are employed routinely to study the thermodynamic, structural, and dynamical properties of a wide range of substances [6, 16], from the phase diagram of bulk water [17] to the folding of proteins [18] to radiation damage in glasses [19]. In MD, one propagates explicit classical trajectories by numerically integrating Newton's equations of motion, often attaching a thermostat of some description to encourage efficient sampling of the canonical ensemble of configurations and momenta. In contrast, MC simulations traditionally sample just the configurational part of the ensemble distribution via a series of random jumps (although the term refers in general to a much broader class of stochastic techniques) [16]. In their most primitive formulations, both MD and MC are applicable to the calculation of thermodynamic and structural (collectively *static*) properties, whereas MD can also be used to calculate dynamical properties, such as vibrational spectra and chemical reaction rate constants.

The broad success of classical approximations to nuclear motion can be attributed to several key factors. First, quantum coherence, which is a consequence of the interference between quantum probability amplitudes, usually dies away rapidly in condensed-phase systems at finite temperatures, as a result of the interactions between very large numbers of degrees of freedom [20–22]. Second, many of the nuclear degrees of freedom (especially those of translational and rotational nature) are close to the high-temperature limit, in that the spacing of their energy levels is small in comparison with k_BT (where k_B is the Boltzmann constant and T is temperature); indeed, the high-temperature ($T \rightarrow \infty$) and classical ($\hbar \rightarrow 0$) limits may be viewed as essentially equivalent [6]. Third, classical dynamics faithfully reproduces the expected quantum time dependence of linear observables for a harmonic oscillator (a corollary of Ehrenfest's theorem), and nuclear degrees of freedom that are highly quantised—typically vibrational—often carry fairly mild anharmonicities. Fourth, the empirical atomistic PESs, also known as force fields, that are often employed in MD/MC simulations are parametrised by fitting to experimental data. They therefore account implicitly for some nuclear quantum effects (NQEs) [23, 24]. That said, one must be cautious about extrapolating to conditions different from those for which the parametrisations have been performed; the theory underpinning the centroid molecular dynamics method—see below—reveals that such 'effective classical potentials' ought to vary with temperature.

In spite of these factors, NQEs can play a critical, sometimes overlooked role in determining the properties of many condensed-phase systems, especially those containing light atoms such as hydrogen [25, 26]. For example, proton delocalisation either strengthens or weakens the hydrogen bonding of DNA base pairs depending on the temperature [27], and redshifts the intramolecular stretching frequencies of liquid water and its isotopes by many tens of reciprocal centimetres [28–30]. In general, the degree of 'quantumness' in a mildly anharmonic nuclear coordinate can be crudely quantified by the dimensionless quantity $\beta\hbar|\Omega|$, where

$\beta = 1/(k_B T)$ and Ω is the frequency (under the harmonic approximation) characteristic of motion along the coordinate [26, 31]. NQEs are then most likely to be significant if $\beta\hbar|\Omega| \gg 1$. When Ω is real, corresponding to vibrational motion, the most relevant quantum mechanical phenomenon is vibrational zero-point energy, which pushes the system into more anharmonic regions of the PES than would be classically accessible at the same temperature. When Ω is imaginary, corresponding to motion over a potential barrier (such as during a chemical reaction), the most relevant phenomenon is quantum tunnelling, which increases the rates of barrier crossings beyond those predicted by classical rate theories [32]. In this work, we will focus primarily on the former scenario and its importance in vibrational spectroscopy, but it should be noted that spectral lineshapes can also be affected by condensed-phase (incoherent) tunnelling phenomena, albeit less directly. For instance, the singlet nature of the O–H stretch fundamental band in the room-temperature infrared (IR) spectrum of liquid water is thought to be attributable, in part, to tunnelling in the hydrogen bond network [33]. Water is a particularly popular target of study in general, owing to the highly quantal nature of its vibrations and hydrogen bond network, coupled with its unparalleled importance across the natural sciences [34, 35].

Even though both zero-point energy and incoherent tunnelling can be of relevance to dynamical properties, they are considered quantum *statistical* effects, because they are fully captured in the specification of quantum initial conditions. This contrasts with real-time coherence effects, which are inherently dynamical. Statistical and dynamical effects are, of course, intricately connected, and in an abstract sense may be viewed as analytic continuations of one another. This is because, under conditions of thermal equilibrium, the relevant statistics are those of the quantum canonical ensemble, encapsulated by the *Boltzmann operator* (also known as the thermal or canonical density matrix) [6, 36]. The Boltzmann operator is equivalent to the time-evolution operator, but with the time parameter t set to the imaginary value $-i\beta\hbar$. Stated differently, the thermal density matrix is equivalent to the imaginary-time propagator.

While the real-time propagator can only be resolved numerically for the smallest of systems (e.g. by solving the Schrödinger equation), a highly practical means of imaginary-time propagation—applicable to much larger systems—is provided by Feynman's celebrated path-integral formulation [37, 38]. This maps the quantum canonical ensemble onto the classical canonical ensemble of an extended system, which comprises $N \to \infty$ copies of the original system connected cyclically by temperature-dependent, harmonic springs. Each nucleus is thus represented by a 'ring polymer' of N 'beads', which may be viewed as the discretisation of a cyclic path in imaginary time. Note that the form of this so-called 'classical isomorphism' becomes considerably more complicated if one chooses not to ignore exchange effects [6, 39].

The imaginary-time path-integral formalism enables static quantum properties to be computed by sampling the phase space of the ring polymer, using relatively straightforward generalisations of classical MD/MC techniques [6, 40, 41]. The cost of such a path-integral MD/MC

(PIMD/MC) simulation is primitively about N time the cost of the corresponding classical simulation, where the number of beads per polymer N required for convergence depends heavily both on the system and on the property being calculated [25]. Already this circumvents the exponential scaling associated with explicit diagonalisation of the Hamiltonian. However, a number of elegant approaches have been developed to accelerate the convergence of PIMD in particular, including the ring-polymer contraction method [31], coloured-noise (generalised Langevin) thermostatting [42, 43], and higher-order discretisations of the imaginary-time propagator [44]. Combined with accurate *ab initio* PESs, PIMD simulation techniques have been applied to study statistical NQEs in a range of systems [25, 26] such as liquid water [45, 46], biomolecules [27, 47], and organic molecules adsorbed on surfaces [48]. In recent years, generalisations to bosonic [49] and fermionic [50] systems have also been proposed.

While PIMD is formally exact for static properties, it is not obvious how one can generalise it to dynamical properties—usually encoded in time-correlation functions (TCFs)—given the difficulties associated with real-time propagation that were mentioned above. Within the path-integral formalism, this manifests as a *sign problem*, whereby real-time paths would need to be sampled over a highly oscillatory phase factor that is unamenable to normal methods of importance sampling (although ways of substantially mitigating this have been developed for models of dissipative systems) [51]. Fortunately, for condensed-phase systems, the rapid quenching of quantum coherence means that real-time propagation at such a high level of theory is rarely necessary. A more pragmatic option is to combine quantum statistical sampling with *classical* dynamics. Two main classes of approaches have been developed to do this, which can loosely be regarded as interpolating between the high-temperature and harmonic limits in which the classical evolution of linear observables is exact.

The first class of quantum statistics–classical dynamics methods is based on Wigner's phase-space formulation of quantum mechanics [36]. The Wigner transform of the Boltzmann operator gives a quantum analogue of the classical phase-space distribution, known as the Wigner quasi-probability distribution (so called because it is not necessarily everywhere positive for anharmonic systems). Correspondingly, exact quantum real-time propagation is encoded in a quantum analogue of the classical Poisson bracket, known as the Moyal bracket (which can be obtained as the Wigner transform of a commutator) [52]. Straightforwardly replacing the Moyal bracket with the Poisson bracket, which is its $\hbar \to 0$ limit, yields an approximation to quantum time-correlation functions known usually as the linearised semiclassical initial value representation (LSC-IVR, also the classical Wigner method or linearised path integral) [53], and was developed chiefly by Miller and co-workers [20, 54–56]. It amounts to propagating classical Newtonian trajectories, but with initial conditions sampled from the Wigner distribution. Its name derives from the fact that it can also be obtained by linearising the differences between forward and backward paths in Van Vleck's semiclassical initial value

representation of the real-time propagator [54, 55]. For large systems, the sampling step has to be performed approximately, employing one of the many techniques that have been developed for this purpose [57–66], hence LSC-IVR is not strictly a method in itself but the parent approximation to a class of methods.

LSC-IVR has been applied with some success to calculate dynamical properties such as the IR [33, 67, 68] and Raman [69] spectra of liquid water, and vibrational energy relaxation rates in simple molecular liquids [70, 71]. It has the attractive property of reproducing exact quantum TCFs in the harmonic, high-temperature, and short-time limits for any pair of observables, both in and out of thermal equilibrium (assuming the Wigner distribution can be sampled exactly, which is rarely true in practice). However, it suffers the potentially serious drawback of violating detailed balance—outside of the harmonic and high-temperature limits, ensembles of classical Newtonian trajectories do not generally conserve the quantum Wigner distribution from which they were initially sampled [72]. This has been shown to manifest as severe zero-point energy 'leakage' from intramolecular to intermolecular degrees of freedom, leading to artificial lineshape broadening in the predicted IR spectrum of liquid water at room temperature [33].

The second class of methods extend PIMD to dynamical properties, by considering explicitly the classical real-time evolution of imaginary-time Feynman paths. The theory that rigorously formalises this, known as *Matsubara dynamics*, was developed only rather recently by Althorpe and co-workers [73–77]. They found the surprising result that classical trajectories arise naturally when the high-frequency 'jagged' components of the imaginary-time paths are discarded [73] or mean-field averaged [76]. This constrains the explicitly sampled phase space to that of smooth paths, in which the effective Planck constant is zero. The smooth paths are defined by their Fourier components or 'Matsubara modes', whereas the discarded 'non-Matsubara' modes are responsible for quantum coherence. Matsubara dynamics may be viewed as a refinement of LSC-IVR—it is formally exact in all the same limits, with the added benefit of satisfying detailed balance, which LSC-IVR violates because the non-Matsubara modes couple to the Matsubara modes and corrupt their trajectories. However, Matsubara dynamics is far from a practical method for condensed-phase systems, owing to a highly oscillatory phase factor in the Matsubara distribution that presents a sign problem akin to that of real-time path integrals (and plays the same role as the harmonic spring terms of PIMD/MC in accounting for momentum–position correlations) [73]. Instead, it is a theoretical framework within which practical methods can be analysed, improved, and devised.

The most well-known extensions of PIMD to dynamical properties are the centroid molecular dynamics (CMD) of Voth and co-workers [78–81], and ring-polymer molecular dynamics (RPMD) of Manolopoulos and co-workers [82, 83]. These were originally proposed heuristically but are now recognised as approximations to Matsubara dynamics [84]. CMD propagates

the centroids (centres of mass) of the imaginary-time paths along Newtonian trajectories on a temperature-dependent *potential of mean force* (PMF), which may be regarded as an effective classical potential, and is obtained by mean-field averaging the dynamics of the fluctuations about the centroids. In the Matsubara phase space, this amounts to an average over all the non-zero frequency Matsubara modes, known collectively as 'fluctuation modes' to distinguish them from the zero-frequency centroid modes. CMD circumvents the Matsubara sign problem because the Matsubara phase is independent of the centroid modes [84].

RPMD is somewhat more straightforward conceptually, as it approximates quantum TCFs directly from the classical evolution of ring-polymer beads [82, 83]. It can be derived from Matsubara dynamics starting with a non-canonical coordinate transformation that exchanges the Matsubara phase for the harmonic springs of PIMD, followed by analytic continuation to shift the new momentum coordinates onto the real axis. In itself, this is not necessarily an approximation [85], but does result in numerically unstable, complex trajectories that appear to be no easier to treat than the original sign problem [75]. The RPMD approximation is then simply to discard the imaginary parts of the equations of motion [84]. By construction, both CMD and RPMD obey detailed balance and are exact in the high-temperature limit. RPMD is also exact in the short-time limit, whereas for CMD this holds true only for a TCF of two linear observables. In the harmonic limit, RPMD is exact if at least one of the observables is linear, whereas for CMD, both observables must be linear.

CMD and RPMD have been applied successfully to calculate a range of condensed-phase dynamical properties, such as transport coefficients [34, 86–93] and reaction rate constants [94, 95]. For vibrational spectra, CMD gives very good descriptions of fundamental bands at reasonably high temperatures, such as for high-temperature compressed liquid water [29] and, to some extent, room-temperature liquid water [29, 96–98]. However, at low temperatures, the mean-field approximation can break down catastrophically, particularly if a high-frequency vibration is coupled to a low-frequency rotation or libration. This is because the imaginary-time paths (or ring polymers) can delocalise along curved valleys in the PES in a way that displaces them from their centroids, which has been shown to cause artificial redshifts and line broadening in stretch bands. This is known as the *curvature problem* [76, 99, 100]. RPMD avoids the curvature problem, but is usually unsuitable for spectrum prediction because the fictitious, high-frequency oscillations of the ring-polymer fluctuations couple to the physical vibrations of the centroid. This can lead to erroneous peaks and unphysical peak splitting, behaviour often referred to as the *spurious resonance problem* [99–101].

A simple but effective way to mitigate the spurious resonance problem was proposed by Rossi *et al.* [102]. A Langevin thermostat is attached independently to each ring-polymer fluctuation mode, which formally arises if the imaginary part of the (analytically continued) Matsubara dynamics is replaced by Langevin dynamics (rather than simply being dis-

carded) [85]. The resultant damping of the fluctuation modes prevents the appearance of artificial peaks and peak splitting in vibrational spectra. This method, known as thermostatted RPMD (TRPMD), is exact in all the same limits as RPMD, and has been applied successfully to calculate fundamental bands in the vibrational spectra of condensed-phase water [29, 98], organic molecules [103, 104], and protonated water clusters [102, 105]. Its main drawback is the artificial broadening of spectral lineshapes that stems from the interactions between the thermostats and the centroids, especially at low temperatures. It has been shown that one can reduce some of this broadening by using appropriately tuned, coloured-noise thermostats in place of the standard (white-noise) thermostats, with the stipulation that this corrupts the low-frequency part of the spectrum [104, 106].

A method that generalises CMD to avoid both the curvature and spurious resonance problems was conceived very recently by Trenins *et al.* [77, 107]. Named quasi-centroid molecular dynamics (QCMD), it is based on the premise that there is no a priori reason why the coordinates used to define the PMF should correspond to the Cartesian ring-polymer centres of mass. Instead, one introduces a curvilinear generalisation of the centroid that is defined in terms of bond lengths and bond angles, in such a way that the ring polymers are highly unlikely to delocalise around it. So far, QCMD simulations have been limited to gas- and condensed-phase water (as well as toy models), for which they give excellent predictions of fundamental bands that considerably outperform those of CMD or TRPMD at low temperatures [107]. Further work is required to generalise the method to other molecular systems, but the results for water are certainly very promising.

The most significant limitation common to path-integral methods such as [Q]CMD and [T]RPMD lies in their improper treatment of the Matsubara fluctuation dynamics, which [Q]CMD treats at the mean-field level and [T]RPMD corrupts with the ring-polymer internal springs or stochastic thermostats [77, 84, 85]. The usual justification for this is that the quantum statistics of linear observables depends explicitly only on the centroids, which are not directly affected by such approximations. However, the approximations break down for nonlinear observables, which depend explicitly also on the fluctuation modes [108]. In the context of vibrational spectroscopy, the relevant observables are the dipole moment and the polarisability for IR and Raman spectroscopy, respectively; we will focus mostly on the former. Nonlinearities in the dipole moment are known as *electrical* anharmonicity—distinct from *mechanical* anharmonicity, which is nonlinearity in the force. Small amounts of electrical anharmonicity are not usually too problematic for the calculation of (IR) fundamental bands, which are dominated by harmonic contributions, but can have much larger effects on the intensities of anharmonic features such as overtone, combination, and difference bands [109].

Even in the total absence of electrical anharmonicity, as is the case for point-charge models of dipole moment surfaces (DMSs) like q-TIP4P/F for water [33], the intensities of (symmetry-

allowed) overtone, combination, and difference bands may have non-zero contributions due to the mechanical anharmonicity of the PES. For instance, wave function–based calculations reveal that the spectrum of q-TIP4P/F ice I_h contains a pronounced bend–libration combination band [29]. Such anharmonic features are of considerable interest to the spectroscopy community [110]—they dominate the near-IR regions of most vibrational spectra, which, for aqueous systems, are typically better resolved than the mid-IR regions, and therefore act as useful sources of structural and dynamical information [111]. Furthermore, the frequency shift associated with hydrogen bonding is greater for the first overtone of the O–H stretch than for the fundamental [112], whereas the reverse is true of changes to their intensities, so detailed information about the state of hydrogen bonding is easier to deduce from the overtone band than from the fundamental band [113]. The relevance of the underlying physics also extends beyond linear spectroscopy; nonlinear spectroscopy, such as two-dimensional IR, is often performed with the explicit goal of probing anharmonic couplings by analysing overtone and combination bands [114], and the corresponding vibrational transitions play a key role in chemically relevant processes such as vibrational energy relaxation [2].

In spite of this, relatively little attention has been paid in the literature to the path-integral theoretic description of anharmonic spectral features, probably because they are assumed to be inherently linked to quantum coherence and thus inaccessible to quantum statistics–classical dynamics methods. It is known, for instance, that the 'centroid-following' methods CMD, TRPMD, and QCMD all miss the bend–libration combination band of q-TIP4P/F ice I_h [29, 107]. However, the neglect of coherence seems to be an unlikely explanation, given that LSC-IVR has been found to be successful in capturing the same feature in the IR [68] and Raman [69] spectra of liquid water, albeit with different choices of PES and DMS. In an effort to combine the detailed balance of centroid-following methods with the generality of LSC-IVR, Smith *et al.* [115] and later Willatt *et al.* [75, 116] developed the 'planetary model'—a method designed with the express aim of treating linear and nonlinear observables on a equal footing. It is based on a locally harmonic approximation to the Matsubara potential, which allows one to integrate out the Matsubara phase and capture the leading-order dynamics of the fluctuation modes by propagating trajectories for a single point on the imaginary-time path [75]. This point is termed the 'planet', which is attached to the centroid via a quasi-harmonic spring. Because the planetary model considers the fluctuation dynamics explicitly, there is no reason that it should be incapable of describing electrically anharmonic contributions to overtone and combination intensity. However, it would be somewhat surprising if it could capture the mechanically anharmonic contributions any more successfully than centroid-following methods, given the locally harmonic approximation upon which it is grounded.

After reviewing the necessary background theory in Chapter 2, in Chapter 3 of this work, we take a step back and focus on a simple model of coupled harmonic oscillators to tackle the

question of whether (and if so, how) Matsubara dynamics is capable of accurately capturing the intensities of anharmonic spectral features. For the sake of simplicity, we limit the discussion to first overtones and binary combination and difference bands, assumed in all cases to be well separated from any other band of the same symmetry, and so free from the effects of state mixing. Our analysis begins with the derivation of formal expressions for the integrated intensities of quantum, classical, and Matsubara IR absorption bands at thermal equilibrium, then we apply first-order quantum and classical perturbation theories to evaluate the intensities of anharmonic bands up to second order in the perturbation parameter (the first-order contributions can be seen to vanish because the rate of a quantum transition scales approximately with the squared magnitude of the transition dipole moment). We find that Matsubara dynamics reproduces the (second-order) quantum intensities when all the fluctuation modes are included. This confirms that the quantum mechanical intensification of first overtones and binary combination bands, and corresponding de-intensification of binary difference bands, is mainly a statistical effect. Quantum coherence plays a minor role if any, at least for our simple model. The (de-)intensification is shown to be related to the anharmonic coupling between the centroids and the fluctuation modes, which increases the amplitudes of the non-fundamental centroid vibrations to what they would be in the corresponding classical system with the oscillators prepared at their quantum effective temperatures. We refer to this phenomenon as 'Matsubara heating', and show that it can also be interpreted in terms of the corresponding heating of a point or 'bead' on the imaginary-time path. We explain that centroid-following methods like [Q]CMD and [T]RPMD do not account for the effects of Matsubara heating any better than classical MD, because they neglect or corrupt the dynamics of the fluctuation modes; the essential property of Matsubara dynamics is seen to be that the fluctuations oscillate with the *same* fundamental frequencies as the centroids. While the planetary model respects this property, it fails to account for the contributions of mechanical anharmonicity to absorption intensities, because it neglects both local anharmonicity in the dynamics of the planets and centroid–fluctuation coupling in the dynamics of the centroids. We illustrate the validity of our results in one dimension for the O–H stretch part of the q-TIP4P/F potential, and propose a very simple quantum–classical scaling factor to use as a post-processing correction to classical or path-integral anharmonic absorption intensities. The results of Chapter 3 complement those of Plé *et al.*, who used a different, but equivalent, formulation of classical perturbation theory to arrive at similar conclusions regarding the role of centroid–fluctuation coupling [65, 117].

In Chapter 4, we report the results of illustrative simulations of q-TIP4P/F water in its gas, liquid, and ice I_h phases. We assess the descriptions of IR spectra given by classical MD, TRPMD, QCMD, and LSC-IVR, where for the LSC-IVR simulations we employ the local Gaussian approximation (LGA) of Liu and Miller [60] to sample from the Wigner distribution. We argue that QCMD provides the best description of fundamental bands of any known

quantum statistics–classical dynamics method, whereas TRPMD provides a (much cheaper) damped version, and LSC-IVR is desirable if one requires a qualitatively reasonable description of anharmonic absorption intensities. We find that our post-processing scaling factor, despite its simplicity, brings the intensities in the classical and QCMD gas-phase spectra into much closer agreement with exact quantum results. The approach is further validated by application to the classical spectrum of gas-phase ammonia, where it performs just as well. Unsurprisingly, it is less applicable to the condensed-phase water spectra, which contain many overlapping bands, but it does nonetheless bring the classical absorption intensities into somewhat closer agreement with experiment when paired with the accurate MB-pol and MB-μ surfaces of Paesani and co-workers [97, 118–120].

Chapter 5 is devoted to the phenomenon of Fermi resonance, the special but important case of an overtone or combination band mixing with a fundamental band of identical symmetry and similar frequency. It is known from the perturbative analysis of Basire *et al.* that classical dynamics severely underestimates Fermi splittings in CO_2 and similar systems [121], and recent numerical work by Plé *et al.* revealed that centroid-following methods suffer the same drawback. We focus on the CO_2 model of refs. 65, 117, 121, 122 (among others), showing numerically that including the lowest six Matsubara fluctuation modes amplifies the Fermi splitting beyond the classical estimate. We then introduce a phase-free 'harmonic decorrelated' (HD) approximation to Matsubara dynamics, and a related approach to simulating classical dynamics with 'imitated Matsubara heating' (IMH), which allow us to investigate the effects of including many more fluctuation modes than would be possible by brute force. Our results suggest that Matsubara dynamics would be likely to give a Fermi splitting within a few reciprocal centimetres of the quantum result if all the fluctuation modes could be included, and that the mechanism responsible for this is Matsubara heating. For completeness, we also consider the simplest two-dimensional model to display 2 : 1 Fermi resonance, consisting of two cubically coupled harmonic oscillators. In addition to the expected Fermi splitting, we observe a secondary splitting of comparable magnitude in the classical power spectrum of the low-frequency oscillator. Both splittings increase upon including Matsubara fluctuations, but the secondary splitting disappears when an additional physical degree of freedom is introduced. Using ideas from semiclassical theory, we argue that the secondary splitting is an artefact of neglecting quantum coherence in two dimensions.

Finally, in Chapter 6, we conclude by addressing the scope and limitations of our results. We suggest areas for further work, and speculate that a physically-motivated combination of path-integral and wave function–based approaches might be the most pragmatic way to obtain reliable results for condensed-phase vibrational spectra.

Chapter 2

Background theory

2.1 Molecular systems at thermal equilibrium

Under the Born–Oppenheimer approximation and non-relativistic conditions, a molecular system in its electronic ground state and in the absence of any external forces can be characterised by the quantum nuclear Hamiltonian

$$\hat{H} = \frac{1}{2}\hat{\mathbf{p}} \cdot \mathbf{M}^{-1}\hat{\mathbf{p}} + V(\hat{\mathbf{q}}), \tag{2.1}$$

where $\hat{\mathbf{q}} \equiv (\hat{q}_1, \ldots, \hat{q}_F)^{\mathrm{T}}$ are the nuclear position operators, $\hat{\mathbf{p}} \equiv (\hat{p}_1, \ldots, \hat{p}_F)^{\mathrm{T}}$ their conjugate momentum operators, $\mathbf{M}$ is the positive-definite mass matrix, and F is the number of relevant nuclear degrees of freedom [3]. The mass matrix is diagonal if $\hat{\mathbf{q}}$ corresponds to Cartesian nuclear coordinates. The function V contains contributions from the total electronic ground state energy, as well as direct Coulombic repulsion between the nuclei, and is called the potential energy surface (PES).

When the system is isolated from its surroundings, its microscopic state is fully described by a state vector $|\psi\rangle$, normalised such that $\langle\psi|\psi\rangle = 1$ [38]. Observable properties are described by the (real) eigenvalues of Hermitian operators that act on $|\psi\rangle$; $\hat{p}_i$ and $\hat{q}_i$ defined above are examples of such operators, as are any operators constructed from them such as the Hamiltonian, $\hat{H}$. The eigenvalues $\{E_0, \ldots, E_\infty\}$ of the Hamiltonian are obtained by solving the time-independent Schrödinger equation,

$$\hat{H}|\psi_n\rangle = E_n|\psi_n\rangle, \tag{2.2}$$

and represent the total energy of the system prepared in the eigenstate $|\psi_n\rangle$ [38].

Consider some observable A that depends explicitly on momentum and/or position, but not on time. Defining the state operator $\hat{\rho} = |\psi\rangle\langle\psi|$, the expectation value of A can be written in

the Heisenberg picture as

$$\langle A(t) \rangle_{\mathrm{q}} = \mathrm{Tr}\big[\hat{\rho}\hat{A}(t)\big], \tag{2.3}$$

where $\mathrm{Tr}[\cdot]$ denotes the quantum mechanical trace and $\hat{A}(t)$ is the Hermitian operator $\hat{A} \equiv \hat{A}(0) \equiv A(\hat{\mathbf{p}}, \hat{\mathbf{q}})$ evolved for time t [36]. Its time dependence is given by the Heisenberg equation,

$$\dot{\hat{A}}(t) = \frac{\mathrm{d}\hat{A}(t)}{\mathrm{d}t} = \frac{\mathrm{i}}{\hbar}\big[\hat{H}, \hat{A}(t)\big], \tag{2.4}$$

in which $\hbar$ is the reduced Planck constant and $[\cdot, \cdot]$ denotes the commutator. The formal solution to Eq. (2.4) is

$$\hat{A}(t) = \hat{U}(-t)\hat{A}\hat{U}(t), \tag{2.5}$$

where

$$\hat{U}(t) = \mathrm{e}^{-\mathrm{i}\hat{H}t/\hbar} \tag{2.6}$$

is known as the time-evolution operator [36, 38, 123]. Alternatively, one may adopt the Schrödinger picture, in which the time dependence of observables is associated with the state vector $|\psi\rangle \equiv |\psi(0)\rangle$ (and the state operator $\hat{\rho} \equiv \hat{\rho}(0)$ by extension). Expectation values are then given by

$$\langle A(t) \rangle_{\mathrm{q}} = \mathrm{Tr}\big[\hat{\rho}(t)\hat{A}\big], \tag{2.7}$$

where

$$\hat{\rho}(t) = |\psi(t)\rangle\langle\psi(t)| \tag{2.8}$$

and $|\psi(t)\rangle = \hat{U}(t)|\psi\rangle$ formally solves the time-dependent Schrödinger equation (TDSE),

$$\mathrm{i}\hbar\,|\dot{\psi}(t)\rangle = \mathrm{i}\hbar\frac{\mathrm{d}}{\mathrm{d}t}|\psi(t)\rangle = \hat{H}|\psi(t)\rangle. \tag{2.9}$$

In what follows, we employ the Heisenberg picture unless otherwise specified.

In practice, molecular systems are not isolated from their surroundings, but interact with them in an intricate way. It is then not generally possible to specify a unique state vector but one can still define a *density operator* (or density matrix), $\hat{\rho}$, to describe a statistical ensemble of systems so that Eq. (2.3) remains valid [6, 36]. We limit our discussions to the canonical ensemble, which arises when the system is allowed to reach thermal equilibrium with its surroundings. The relevant density operator is then the *Boltzmann operator*,

$$\hat{\rho}_{\mathrm{eq}}(\beta) = \frac{\mathrm{e}^{-\beta\hat{H}}}{Z_{\mathrm{q}}(\beta)} = \frac{\hat{U}(-\mathrm{i}\beta\hbar)}{Z_{\mathrm{q}}(\beta)}, \tag{2.10}$$

where $\beta = 1/(k_{\mathrm{B}}T)$ is the inverse temperature (in units of the Boltzmann constant k_{B}, with T

the absolute temperature of the system), and

$$Z_q(\beta) = \text{Tr}\big[e^{-\beta \hat{H}}\big] \tag{2.11}$$

is the quantum partition function. As indicated in Eq. (2.10), the Boltzmann operator is equivalent (up to a proportionality constant) to the time-evolution operator with 'imaginary time' $\tau = it = \beta\hbar$. The real and imaginary-time–evolution operators clearly commute with one another, thus using the cyclic property of the trace one finds that

$$\langle A(t) \rangle_q = \langle A(0) \rangle_q \equiv \langle A \rangle_q, \tag{2.12}$$

i.e., thermal expectation values (canonical ensemble averages) are time-invariant. This very important result enables thermodynamic and structural properties of the system, collectively *static* properties, to be cast in terms of thermal expectation values with appropriate choices of $\hat{A}$ [6].

2.1.1   The classical limit

While quantum mechanics provides the most accurate description of molecular systems, at sufficiently high temperatures their behaviours become very well-approximated by classical mechanics, which may formally be considered the $\hbar \to 0$ limit of quantum mechanics [6]. In particular, for systems at thermal equilibrium, classical equations of motion apply when $k_B T$ is large compared to the spacing between the energy levels, E_n.

The classical analogue of the Hamiltonian given in Eq. (2.1) is

$$H(\mathbf{p}, \mathbf{q}) = \frac{1}{2}\mathbf{p} \cdot \mathbf{M}^{-1}\mathbf{p} + V(\mathbf{q}), \tag{2.13}$$

in which momentum and position are now represented by the variables $\mathbf{p} \equiv (p_1, \ldots, p_F)^T$ and $\mathbf{q} \equiv (q_1, \ldots, q_F)^T$. Collectively, the so-called dynamical variables $(\mathbf{p}, \mathbf{q})$ fully specify the microscopic state of the classical molecular system. They evolve in time according to Hamilton's equations of motion [6, 124],

$$\dot{\mathbf{p}} = \frac{d\mathbf{p}}{dt} = -\nabla_\mathbf{q} H(\mathbf{p}, \mathbf{q}) = -\nabla_\mathbf{q} V(\mathbf{q}) \tag{2.14a}$$

$$\dot{\mathbf{q}} = \frac{d\mathbf{q}}{dt} = \nabla_\mathbf{p} H(\mathbf{p}, \mathbf{q}) = \mathbf{M}^{-1}\mathbf{p}, \tag{2.14b}$$

in which the time dependence is implicit, and we have defined the gradient operator

$$\nabla_{\mathbf{a}} \equiv \frac{\partial}{\partial \mathbf{a}} = \begin{pmatrix} \partial/\partial a_1 \\ \vdots \\ \partial/\partial a_F \end{pmatrix}. \tag{2.15}$$

From the chain rule it follows that the observable $A \equiv A(\mathbf{p}, \mathbf{q})$ evolves in time according to

$$\dot{A} = \frac{\mathrm{d}A}{\mathrm{d}t} = -\{H, A\} = \mathcal{L}A, \tag{2.16}$$

where the Liouvillian (or Liouville operator) is defined as

$$\mathcal{L} \equiv -\{H, \cdot\} \equiv -H\left[\overleftarrow{\nabla}_{\mathbf{q}} \cdot \overrightarrow{\nabla}_{\mathbf{p}} - \overleftarrow{\nabla}_{\mathbf{p}} \cdot \overrightarrow{\nabla}_{\mathbf{q}}\right] \tag{2.17a}$$

$$= \mathbf{p} \cdot \mathbf{M}^{-1}\nabla_{\mathbf{q}} - \nabla_{\mathbf{q}}V(\mathbf{q}) \cdot \nabla_{\mathbf{p}}, \tag{2.17b}$$

and $\{\cdot, \cdot\}$ denotes a Poisson bracket [6, 16]. The overhead arrows in Eq. (2.17a) are used to indicate in which direction the gradient operators act. It is important to recognise that Eq. (2.17a) is very general, in that it still holds if $(\mathbf{p}, \mathbf{q})$ are replaced by some general set of canonical coordinates such as action-angle variables (see Section 3.1.2); in contrast, Eq. (2.17b) is specific to our choice of coordinate system, in which the mass matrix has been assumed implicitly not to depend on position. The formal solution to Eq. (2.16) is

$$A(\mathbf{p}, \mathbf{q}; t) = A(\mathrm{e}^{\mathcal{L}t}\mathbf{p}, \mathrm{e}^{\mathcal{L}t}\mathbf{q}) = \mathrm{e}^{\mathcal{L}t}A(\mathbf{p}, \mathbf{q}). \tag{2.18}$$

When the classical system is brought into thermal equilibrium with its surroundings, its statistics follow the classical analogue of the quantum canonical ensemble described above. Thermal expectation values are given by

$$\langle A(t)\rangle_{\mathrm{c}} = \int \mathrm{d}^F\mathbf{p} \int \mathrm{d}^F\mathbf{q}\, \rho_{\mathrm{eq}}(\mathbf{p}, \mathbf{q})\mathrm{e}^{\mathcal{L}t}A(\mathbf{p}, \mathbf{q}), \tag{2.19}$$

where $\int \mathrm{d}^F\mathbf{p} \equiv \int_{-\infty}^{\infty} \mathrm{d}p_1 \ldots \int_{-\infty}^{\infty} \mathrm{d}p_F$ and the canonical phase-space distribution function is given by

$$\rho_{\mathrm{eq}}(\mathbf{p}, \mathbf{q}) = \frac{\mathrm{e}^{-\beta H(\mathbf{p}, \mathbf{q})}}{(2\pi\hbar)^F Z_{\mathrm{c}}(\beta)}, \tag{2.20}$$

in which

$$Z_{\mathrm{c}}(\beta) = \frac{1}{(2\pi\hbar)^F} \int \mathrm{d}^F\mathbf{p} \int \mathrm{d}^F\mathbf{q}\, \rho_{\mathrm{eq}}(\mathbf{p}, \mathbf{q}) \tag{2.21}$$

is the classical partition function [6]. Since ρ_{eq} is a function of the Hamiltonian, we trivially have

$\mathcal{L}\rho_{eq} = 0$, while Liouville's theorem states that $(\mathbf{p}, \mathbf{q}) \to (e^{\mathcal{L}t}\mathbf{p}, e^{\mathcal{L}t}\mathbf{q})$ constitutes a canonical transformation and thus has unit Jacobian. It follows that classical thermal expectation values obey Eq. (2.12), which could of course also be deduced simply by recognising them to be the $\hbar \to 0$ limits of quantum expectation values.

2.1.2 Time-correlation functions

A time-correlation function (TCF) of observables A and B can be expressed in general as $\langle A(t_0)B(t_0 + t)\rangle_{q/c}$. Linear response theory relates equilibrium dynamical properties to *thermal* TCFs in particular, which, from Eq. (2.12), are independent of the time origin t_0, and may thus be expressed more concisely as $\langle A(0)B(t)\rangle_{q/c}$ [2, 125].

In the case of classical dynamics, there exists one unique definition of the (thermal) TCF, namely

$$c_{AB}(\beta; t) = \langle A(0)B(t)\rangle_c = \int d^F\mathbf{p} \int d^F\mathbf{q}\, \rho_{eq}(\mathbf{p}, \mathbf{q})A(\mathbf{p}, \mathbf{q})e^{\mathcal{L}t}B(\mathbf{p}, \mathbf{q}). \qquad (2.22)$$

However, properties of the classical canonical (Boltzmann) distribution give rise to certain symmetries that enable the classical TCF to be expressed in several equivalent ways [2]. Most trivially, the reality of A and B implies that the TCF is itself real, giving

$$c_{AB}(\beta; t) = c_{AB}^*(\beta; t). \qquad (2.23)$$

Furthermore, exploiting the independence of t_0 noted above, we can replace $A(\mathbf{p}, \mathbf{q})e^{\mathcal{L}t}B(\mathbf{p}, \mathbf{q})$ with $B(\mathbf{p}, \mathbf{q})e^{-\mathcal{L}t}A(\mathbf{p}, \mathbf{q})$ in the integrand of Eq. (2.22) (equivalent to setting $t_0 = -t$), which yields

$$c_{AB}(\beta; t) = c_{BA}(\beta; -t). \qquad (2.24)$$

One important consequence of Eq. (2.24) is that the time-derivative of a TCF may be expressed as

$$\frac{\partial}{\partial t}c_{AB}(\beta; t) = c_{A\dot{B}}(\beta; t) = -c_{\dot{A}B}(\beta; t). \qquad (2.25)$$

A special case of Eq. (2.25) that applies to the autocorrelation function (ACF), $c_{AA}(\beta; t)$, is

$$\frac{\partial^2}{\partial t^2}c_{AA}(\beta; t) = -c_{\dot{A}\dot{A}}(\beta; t), \qquad (2.26)$$

the usefulness of which will become apparent in Section 2.1.3.

Naively, one may promote the classical distribution function, ρ_{eq}, and variables A and B to

their corresponding quantum operators, to yield

$$
\begin{aligned}
C_{AB}(\beta; t) &= \mathrm{Tr}\!\left[\rho_{\mathrm{eq}}(\beta)\hat{A}\hat{B}(t)\right] \\
&= \frac{1}{Z_{\mathrm{q}}(\beta)}\,\mathrm{Tr}\!\left[\hat{U}(-\mathrm{i}\beta\hbar)\hat{A}\hat{U}(-t)\hat{B}\hat{U}(t)\right],
\end{aligned}
\tag{2.27}
$$

which is often known the standard (quantum) TCF. This has fewer symmetries than the classical TCF; because the commutator $[\hat{A},\hat{B}]$ is in general non-vanishing, the standard TCF is not required to be real [2, 6]. It does, however, obey the quantum *detailed balance* condition

$$
C_{AB}(\beta; t) = C^{*}_{BA}(\beta; -t),
\tag{2.28}
$$

which follows from well-known properties of the trace; the classical analogue of this result is Eq. (2.24). The time derivative of the standard TCF satisfies

$$
\frac{\partial}{\partial t}C_{AB}(\beta; t) = C_{A\dot{B}}(\beta; t) = -C^{*}_{\dot{A}B}(\beta; t),
\tag{2.29}
$$

analogous to Eq. (2.25). Crucially, however, the non-commutativity of $\hat{A}$ and $\hat{B}$ implies that the function $\mathrm{Tr}[\rho_{\mathrm{eq}}(\beta)\hat{B}(t)\hat{A}]$ is just as sensible a choice as $\mathrm{Tr}[\rho_{\mathrm{eq}}(\beta)\hat{A}\hat{B}(t)]$ for the quantum analogue of the classical TCF, and indeed also converges to it in the limit $\hbar \to 0$. In fact, these two quantities capture identical information about the dynamics of the quantum system, as it is straightforward to show that

$$
\begin{aligned}
\mathrm{Tr}\!\left[\rho_{\mathrm{eq}}(\beta)\hat{B}(t)\hat{A}\right] &= C^{*}_{AB}(\beta; t) \\
&= \mathrm{Tr}\!\left[\hat{A}\rho_{\mathrm{eq}}(\beta)\hat{B}(t)\right] \\
&= \frac{1}{Z_{\mathrm{q}}(\beta)}\,\mathrm{Tr}\!\left[\hat{A}\hat{U}(-\mathrm{i}\beta\hbar)\hat{U}(-t)\hat{B}\hat{U}(t)\right].
\end{aligned}
\tag{2.30}
$$

That is to say, there is ambiguity regarding at which end of the imaginary-time path $(0 \leqslant \tau < \beta\hbar)$ the observable A is recorded. The most general form of quantum TCF places the observation at some arbitrary point along this path, and is equivalent to analytically continuing the standard TCF into the complex plane i.e.,

$$
C_{AB}(\beta; t + \mathrm{i}\tau) = \frac{1}{Z_{\mathrm{q}}(\beta)}\,\mathrm{Tr}\!\left[\hat{U}(\mathrm{i}(\tau - \beta\hbar))\hat{A}\hat{U}(-\mathrm{i}\tau)\hat{U}(-t)\hat{B}\hat{U}(t)\right].
\tag{2.31}
$$

This recovers $C^{*}_{AB}(\beta; t)$ in the limit $\tau \to \beta\hbar$. For any choice of τ, $C_{AB}(\beta; t + \mathrm{i}\tau)$ can be related to the standard TCF by defining the (real-time) Fourier transform

$$
G_{AB}(\beta; \omega, \tau) = \frac{1}{2\pi}\int_{-\infty}^{\infty} \mathrm{d}t\, \mathrm{e}^{-\mathrm{i}\omega t} C_{AB}(\beta; t + \mathrm{i}\tau),
\tag{2.32}
$$

then making the substitution $s = t + i\tau$ to give

$$G_{AB}(\beta; \omega, \tau) = \frac{e^{-\omega\tau}}{2\pi} \int_{-\infty-i\tau}^{\infty-i\tau} ds \, e^{-i\omega s} C_{AB}(\beta; s).$$ (2.33)

Since the integrand in Eq. (2.33) is an entire function of s, the integration variable may be shifted onto the real axis to give

$$G_{AB}(\beta; \omega, \tau) = e^{-\omega\tau} G_{AB}(\beta; \omega, 0) \equiv e^{-\omega\tau} G_{AB}(\beta; \omega).$$ (2.34)

Combining Eqs. (2.28), (2.30), (2.31), and (2.33) leads to a frequency-domain expression of quantum detailed balance,

$$G_{BA}(\beta; -\omega) = e^{-\beta\hbar\omega} G_{AB}(\beta; \omega).$$ (2.35)

Note that in the classical limit, Eq. (2.35) holds without the factor of $e^{-\beta\hbar\omega}$.

The most symmetric and 'democratic' form of quantum TCF, which arises naturally in quantum linear response theory, may be obtained by averaging over the imaginary-time coordinate, τ, in what is known as a Kubo transform [2, 125]. The Kubo-transformed TCF is then defined as

$$\widetilde{C}_{AB}(\beta; t) = \frac{1}{\beta\hbar} \int_0^{\beta\hbar} d\tau \, C_{AB}(\beta; t + i\tau).$$ (2.36)

Its Fourier transform, $\widetilde{G}_{AB}(\beta; \omega)$, is related to the standard TCF via

$$G_{AB}(\beta; \omega) = \frac{\beta\hbar\omega}{1 - e^{-\beta\hbar\omega}} \widetilde{G}_{AB}(\beta; \omega),$$ (2.37)

where the prefactor

$$\frac{\beta\hbar\omega}{1 - e^{-\beta\hbar\omega}} = \left(\frac{1}{\beta\hbar} \int_0^{\beta\hbar} d\tau \, e^{-\omega\tau} \right)^{-1}$$ (2.38)

can be derived from Eq. (2.34). The Kubo-transformed TCF has all the same symmetries as the classical TCF, most importantly

$$\widetilde{C}_{AB}(\beta; t) = \widetilde{C}_{AB}^*(\beta; t)$$ (2.39)

and

$$\widetilde{C}_{AB}(\beta; t) = \widetilde{C}_{BA}(\beta; -t),$$ (2.40)

which is yet another statement of quantum detailed balance. In the frequency domain, this can

be expressed as

$$\widetilde{G}_{AB}(\beta, \omega) = \widetilde{G}_{BA}(\beta, -\omega). \tag{2.41}$$

Of all the possible equilibrium quantum TCFs, the Kubo-transformed version is often considered the 'most classical', because it has the same symmetries as the classical TCF, and can be shown to be equal to it in the harmonic limit as long as both $\hat{A}$ and $\hat{B}$ are linear functions of the position and/or momentum operators [6, 73, 74, 82]. For this reason, the frequency-dependent prefactor defined in Eq. (2.38) is known in some literature as the 'harmonic correction factor'. However, the real part of the standard TCF also satisfies the classical symmetries, and is the most natural target for some simulation methods (e.g. LSC-IVR—see Section 2.3 and references therein). It may be expressed as

$$C_{AB}^{[R]}(\beta; t) \equiv \text{Re}\left[C_{AB}(\beta; t)\right] = \frac{1}{2}\left[C_{AB}(\beta; t) + C_{AB}^*(\beta; t)\right], \tag{2.42}$$

and is therefore sometimes known as the symmetrised or 'symmetric-split' TCF. Its Fourier transform, $G_{AB}^{[R]}(\beta; \omega)$, is related to that of the standard TCF via

$$G_{AB}(\beta; \omega) = \frac{2}{1 + e^{-\beta\hbar\omega}} G_{AB}^{[R]}(\beta; \omega), \tag{2.43}$$

in which the prefactor is sometimes called the 'standard correction factor' [126, 127].

2.1.3 Vibrational spectroscopy

At ambient temperatures, the nuclear degrees of freedom for which quantum and classical descriptions differ the most are typically vibrational in nature. This is because the vibrational frequencies (and thus energy level spacings) are often large relative to $k_{\text{B}}T$. Vibrational spectroscopy is a powerful tool for probing the associated dynamics, and in this section we focus chiefly on infrared (IR) spectroscopy, where pulses of IR radiation induce transitions between vibrational energy levels. The rates of these transitions are proportional to the squared magnitudes of the transition dipole moments, $\langle\psi_{\text{initial}}|\hat{\mu}|\psi_{\text{final}}\rangle$, where $\hat{\mu} \equiv \mu(\hat{\mathbf{q}})$ is the dipole moment operator, and the function μ is called the dipole moment surface (DMS). The arguments that follow, however, can be easily modified to apply to Raman spectroscopy, for which the relevant operator is the polarisability operator [2, 6, 128].

Suppose the electric field component of an electromagnetic pulse has a field strength $\mathcal{E}$ that is constant over the frequency range of interest. Assuming the system starts out in thermal equilibrium, Fermi's Golden Rule gives the net energy absorption spectrum in terms of energy

eigenvalues and eigenstates as [6]

$$S_q(\beta; \omega) = \frac{2\pi |\mathcal{E}|^2 \omega}{Z_q(\beta)} \sum_{n=0}^{\infty} \sum_{n'=0}^{\infty} (e^{-\beta E_n} - e^{-\beta E_{n'}}) \langle \psi_n | \hat{\boldsymbol{\mu}} | \psi_{n'} \rangle \cdot \langle \psi_{n'} | \hat{\boldsymbol{\mu}} | \psi_n \rangle \delta(E_{n'} - E_n + \hbar\omega). \quad (2.44)$$

The theoretical quantity $S_q(\beta; \omega)$ is directly proportional to the absorbance multiplied by the frequency-dependent refractive index; in practice, the latter can be obtained from the former using the Kramers–Kronig relations (and its frequency dependence is often fairly weak), thus $S_q(\beta; \omega)$ is a reasonable proxy for the IR spectrum [6]. In deriving Eq. (2.44), one must account explicitly for detailed balance, which is to recognise that the magnitude of the absorption observed at frequency $\omega = (E_{n'} - E_n)/\hbar$ includes both positive contributions from the transition $|n\rangle \rightarrow |n'\rangle$ and negative contributions from $|n'\rangle \rightarrow |n\rangle$. The net absorption is necessarily non-negative at thermal equilibrium, where there is no population inversion.

By using the relationship

$$(e^{-\beta E_n} - e^{-\beta E_{n'}}) \delta(E_{n'} - E_n + \hbar\omega) = e^{-\beta E_n} (1 - e^{-\beta \hbar\omega}) \delta(E_{n'} - E_n + \hbar\omega), \quad (2.45)$$

the Fourier-space representation of the Dirac delta function

$$\delta(E_{n'} - E_n + \hbar\omega) = \frac{1}{2\pi\hbar} \int_{-\infty}^{\infty} dt \, e^{i\omega t} e^{i(E_{n'} - E_n)t/\hbar}, \quad (2.46)$$

and the eigenvalue relation $\hat{U}(t)|\psi_n\rangle = e^{-iE_n t/\hbar}|\psi_n\rangle$, Eq. (2.44) can be re-expressed as [6]

$$
\begin{aligned}
S_q(\beta; \omega) = 2\pi |\mathcal{E}|^2 \beta \omega^2 \frac{1 - e^{-\beta\hbar\omega}}{\beta\hbar\omega} \\
\times \frac{1}{2\pi} \int_{-\infty}^{\infty} dt \, \frac{e^{i\omega t}}{Z_q(\beta)} \sum_{n=0}^{\infty} \sum_{n'=0}^{\infty} \langle \psi_n | \hat{U}(-i\beta\hbar) \hat{\boldsymbol{\mu}} | \psi_{n'} \rangle \cdot \langle \psi_{n'} | \hat{U}(-t) \hat{\boldsymbol{\mu}} \hat{U}(t) | \psi_n \rangle.
\end{aligned}
\quad (2.47)
$$

Since resolution of the identity in the energy basis gives $\hat{1} = \sum_{n'=0}^{\infty} |\psi_{n'}\rangle \langle \psi_{n'}|$, it is clear that the term on the second line of Eq. (2.47) is just the Fourier transform of the standard dipole moment autocorrelation function (ACF) i.e., Eq. (2.27) with $\hat{A} = \hat{B} = \hat{\boldsymbol{\mu}}$. Thus

$$S_q(\beta; \omega) = 2\pi |\mathcal{E}|^2 \beta \omega^2 \frac{1 - e^{-\beta\hbar\omega}}{\beta\hbar\omega} G_{\mu\mu}(\beta; \omega), \quad (2.48)$$

where $G_{\mu\mu}$ is shorthand for $G_{\mu\cdot\mu}$. Alternatively, we can use Eq. (2.37) to write the spectrum in terms of the Kubo-transformed ACF as

$$S_q(\beta; \omega) = 2\pi |\mathcal{E}|^2 \beta \omega^2 \widetilde{G}_{\mu\mu}(\beta; \omega), \quad (2.49)$$

or Eq. (2.43) to write it in terms of the symmetrised ACF as

$$S_{\mathrm{q}}(\beta; \omega) = 2\pi|\mathcal{E}|^2 \beta \omega^2 \frac{\tanh(\beta\hbar\omega/2)}{\beta\hbar\omega/2} G_{\mu\mu}^{[\mathrm{R}]}(\beta; \omega). \tag{2.50}$$

Using quantum analogues of Eq. (2.26), each of Eqs. (2.48–2.50) may be recast in terms of dipole-*derivative* ACFs as

$$S_{\mathrm{q}}(\beta; \omega) = 2\pi|\mathcal{E}|^2 \beta \frac{1 - \mathrm{e}^{-\beta\hbar\omega}}{\beta\hbar\omega} G_{\dot{\mu}\dot{\mu}}(\beta; \omega) \tag{2.51a}$$

$$= 2\pi|\mathcal{E}|^2 \beta \frac{\tanh(\beta\hbar\omega/2)}{\beta\hbar\omega/2} G_{\dot{\mu}\dot{\mu}}^{[\mathrm{R}]}(\beta; \omega) \tag{2.51b}$$

$$= 2\pi|\mathcal{E}|^2 \beta \widetilde{G}_{\dot{\mu}\dot{\mu}}(\beta; \omega), \tag{2.51c}$$

where e.g. $G_{\dot{\mu}\dot{\mu}} \equiv G_{\dot{\mu}\cdot\dot{\mu}}$. Expressed in words, Eq. (2.51c) says that the energy absorption spectrum is directly proportional to the Fourier transform of the Kubo-transformed dipole-derivative ACF, which makes the latter a particularly attractive target quantity for molecular simulations.

In the classical limit, the standard, symmetrised, and Kubo-transformed ACFs become equivalent. The energy absorption spectrum is then given by

$$S_{\mathrm{c}}(\beta; \omega) = 2\pi|\mathcal{E}|^2 \beta \omega^2 g_{\mu\mu}(\beta; \omega) \tag{2.52a}$$

$$= 2\pi|\mathcal{E}|^2 \beta g_{\dot{\mu}\dot{\mu}}(\beta; \omega), \tag{2.52b}$$

where $g_{\mu\mu}(\beta; \omega)$ is the Fourier transform of the classical dipole moment ACF, $c_{\mu\mu}(\beta; t)$ (given by Eq. (2.22) with $A = B = \boldsymbol{\mu}$), and similarly for $g_{\dot{\mu}\dot{\mu}}(\beta; \omega)$. In practice, however, the classical ACF is often employed as the starting point for IR spectrum prediction even far from the classical limit [129–131], owing to the intractability of the nuclear Schrödinger equation for large molecular systems. It is therefore pertinent to ask which of the quantum ACFs described above—standard, Kubo-transformed, or symmetrised—is best approximated by the classical result. Comparing Eq. (2.49) with Eq. (2.52a) suggests the Kubo-transformed ACF to be the best candidate, and this is supported by the general result noted in Section 2.1.2 that the classical and Kubo-transformed TCFs of linear observables are equal in the harmonic limit.

Of particular interest to us are the ways in which the accurate, quantum descriptions of IR (and Raman) spectra differ from their classical counterparts. This comes under the general banner of *nuclear quantum effects* (NQEs) [25], named so because (under the Born–Oppenheimer approximation) the electronic degrees of freedom are treated implicitly as quantum mechanical, even if the nuclei are not. For a system with only a small number of interacting vibrations, such as gas-phase water, the quantisation of vibrational and rotational energy can have a drastic, qualitative effect on the appearance of its spectra. For instance, vibrational excitations can

occur simultaneously with rotational transitions, giving rise to detailed rotational fine structure in vibrational absorption bands—with sufficiently high resolution, each observed rovibrational transition manifests as a single, sharp line [128].[a] In the time domain, this corresponds to long-time recurrences in TCFs, otherwise known as coherence. Such coherence is preserved in the classical limit only for harmonic vibrations [22]; otherwise, vibrational absorption bands adopt broad lineshapes. 'Quantum coherence' in this context thus refers to the long-time recurrences present in the dynamics of *anharmonic* degrees of freedom.

In condensed-phase systems, the number of interacting degrees of freedom is increased dramatically. Molecular translations and rotations become frustrated (i.e., rotations become librations) and couple more strongly with the (intramolecular) vibrations. In this regime, quantum coherence effects are usually assumed to be negligible, with any long-time recurrences in TCFs becoming unobservable on the time scale of vibrational spectroscopy [20–22]. However, other NQEs may still be at play, including zero-point energy and (incoherent) quantum tunnelling—both connected directly to quantum uncertainty, or delocalisation. In contrast to coherence, which is inherently dynamical, zero-point energy and tunnelling are considered quantum *statistical* effects, as they are captured entirely by the initial phase-space distribution. The concept of quantum phase-space distributions is formalised in Sections 2.2 and 2.3. Zero-point energy is of particular relevance to vibrational spectroscopy, as it can cause frequency shifts of up to many tens of reciprocal centimetres [28–30, 104, 105].

Even in the condensed phase, certain spectral features exhibit drastic NQEs. Namely, the intensities of overtones and combination bands are significantly underestimated by classical mechanics, as are the magnitudes of Fermi resonance splittings. These effects will be explored in detail in subsequent chapters. What they have in common is that they are inherently anharmonic, meaning they are not observed at all when the PES is quadratic (mechanically harmonic) and the DMS is linear (electrically harmonic). Whether they are purely statistical effects, or if quantum coherence plays some role, has been a matter of some disagreement [69, 102].

---

[a]In practice, homogeneous broadening effects cause spectral lines to have approximately Lorentzian profiles with small, but finite, widths, even at infinite resolution [2]. However, this is beyond the scope of our discussion.

2.2 Path-integral molecular dynamics

2.2.1 Phase-space path integrals

Consider the Trotter decomposition of the time-evolution operator in one dimension ($F = 1$),

$$\hat{U}(t) = e^{-i\hat{H}t/\hbar} = \lim_{N\to\infty} \left(e^{-i\hat{V}t_N/\hbar}e^{-i\hat{T}t_N/\hbar}\right)^N, \tag{2.53}$$

where $\hat{T} = \hat{p}^2/2m$ and $\hat{V} \equiv V(\hat{q})$ are the kinetic and potential operators, respectively, and $t_N = t/N$. Inserting N copies of the resolution of the identity in the momentum basis,

$$\hat{1} = \frac{1}{2\pi\hbar} \int_{-\infty}^{\infty} dp\, |p\rangle\langle p|\,, \tag{2.54}$$

and also in the position basis

$$\hat{1} = \int_{-\infty}^{\infty} dq\, |q\rangle\langle q|\,, \tag{2.55}$$

gives

$$\hat{U}(t) = \lim_{N\to\infty} \frac{1}{(2\pi\hbar)^N} \iint dp_1 dq_0 \dots \iint dp_N dq_{N-1} \prod_{l=1}^{N} |q_{l-1}\rangle\langle q_{l-1}|e^{-i\hat{V}t_N/\hbar}|p_l\rangle\langle p_l|e^{-i\hat{T}t_N/\hbar}, \tag{2.56}$$

where we have dropped the integration limits for brevity. Then, using

$$e^{-i\hat{T}t_N/\hbar}|p\rangle = \exp\left(-\frac{it_N p^2}{2m\hbar}\right)|p\rangle \tag{2.57a}$$

$$e^{-i\hat{V}t_N/\hbar}|q\rangle = \exp\left(-\frac{it_N V(q)}{\hbar}\right)|q\rangle \tag{2.57b}$$

and $\langle p|q\rangle = e^{-ipq/\hbar}$, Eq. (2.56) simplifies to [38]

$$\hat{U}(t) = \lim_{N\to\infty} \frac{1}{(2\pi\hbar)^N} \iint dp_1 dq_0 \dots \iint dp_N dq_{N-1} e^{-ip_N q_N/\hbar} |p_N\rangle\langle q_0|$$
$$\times \exp\left(\frac{it_N}{\hbar} \sum_{l=1}^{N} \left[\frac{p_l(q_l - q_{l-1})}{t_N} - H(p_l, q_{l-1})\right]\right). \tag{2.58}$$

Note q_N is not yet an integration variable in Eq. (2.58); the factor of $e^{-ip_N q_N/\hbar}$ on the first line is included to eliminate $e^{+ip_N q_N/\hbar}$ on the second line. Thus, using $\langle q_0|q\rangle = \delta(q_0 - q)$, we can

write a general matrix element of the time-evolution operator in the position basis as

$$
\begin{aligned}
\langle q|\hat{U}(t)|q_0\rangle = \lim_{N\to\infty} \frac{1}{(2\pi\hbar)^N} &\int \mathrm{d}^N\mathbf{p} \int \mathrm{d}^N\mathbf{q}\, \delta(q-q_N) \\
&\times \exp\left(\frac{\mathrm{i}t_N}{\hbar}\sum_{l=1}^{N}\left[\frac{p_l(q_l-q_{l-1})}{t_N}-H(p_l,q_{l-1})\right]\right),
\end{aligned}
\tag{2.59}
$$

also known as the propagator or kernel [38], where $\mathbf{p} \equiv (p_1,\ldots,p_N)^{\mathrm{T}}$ and likewise for $\mathbf{q}$ (note that these differ from the definitions of $\mathbf{p}$ and $\mathbf{q}$ used in Section 2.1, where multiple molecular degrees of freedom were involved). More generally, for a function of the position operator $\hat{A} \equiv A(\hat{q})$, we can use $\langle q_N|A(\hat{q})|p_N\rangle = A(q_N)\mathrm{e}^{\mathrm{i}p_N q_N/\hbar}$ to write

$$
\begin{aligned}
\langle q|\hat{A}\hat{U}(t)|q_0\rangle = \lim_{N\to\infty} \frac{1}{(2\pi\hbar)^N} &\int \mathrm{d}^N\mathbf{p} \int \mathrm{d}^N\mathbf{q}\, \delta(q-q_N) \\
&\times \exp\left(\frac{\mathrm{i}t_N}{\hbar}\sum_{l=1}^{N}\left[\frac{p_l(q_l-q_{l-1})}{t_N}-H(p_l,q_{l-1})\right]\right)A(q_N).
\end{aligned}
\tag{2.60}
$$

To obtain the quantum partition function, we simply set $t = -\mathrm{i}\beta\hbar$ and $q = q_0$ in Eq. (2.59), then integrate over q_0 to yield

$$
Z_{\mathrm{q}}(\beta) = \mathrm{Tr}\left[\hat{U}(-\mathrm{i}\beta\hbar)\right] = \int \mathrm{d}q_0\, \langle q_0|\hat{U}(-\mathrm{i}\beta\hbar)|q_0\rangle
\tag{2.61}
$$

$$
= \lim_{N\to\infty} \frac{1}{(2\pi\hbar)^N} \int \mathrm{d}^N\mathbf{p} \int \mathrm{d}^N\mathbf{q}\, \mathrm{e}^{-\beta_N[H_N(\mathbf{p},\mathbf{q})+\mathrm{i}\theta_N(\mathbf{p},\mathbf{q})]},
\tag{2.62}
$$

in which $\beta_N = \beta/N$ and it is understood that $(p_l,q_l) \equiv (p_{l+N},q_{l+N})$. We have defined a Hamiltonian for the cyclic imaginary-time path[b]

$$
H_N(\mathbf{p},\mathbf{q}) = \sum_{l=1}^{N} H(p_l,q_l),
\tag{2.63}
$$

and a phase

$$
\theta_N(\mathbf{p},\mathbf{q}) = -\sum_{l=1}^{N} \frac{p_l(q_l-q_{l-1})}{\beta_N\hbar} = -\mathbf{p}\cdot\mathcal{W}\mathbf{q},
\tag{2.64}
$$

in which $\mathcal{W}$ is a matrix with elements $\mathcal{W}_{l,l'} = (\delta_{l,l'}-\delta_{l,l'+1})/\beta_N\hbar$, and it is understood that Kronecker deltas are defined modulo N i.e., $\delta_{l,l'} = 1$ if $l \equiv l'$ mod N; 0 otherwise. Thermal

---

[b]The replacement $H(p_l,q_{l-1}) \to H(p_l,q_l)$ is justified because the Hamiltonian does not mix momentum with position.

expectation values are given analogously by

$$
\begin{aligned}
\langle A \rangle_{\mathrm{q}} &= \frac{1}{Z_{\mathrm{q}}(\beta)} \, \mathrm{Tr}\big[\hat{A}\hat{U}(-\mathrm{i}\beta\hbar)\big] \\
&= \lim_{N\to\infty} \frac{1}{(2\pi\hbar)^N Z_{\mathrm{q}}(\beta)} \int \mathrm{d}^N\mathbf{p} \int \mathrm{d}^N\mathbf{q} \, \mathrm{e}^{-\beta_N [H_N(\mathbf{p},\mathbf{q})+\mathrm{i}\theta_N(\mathbf{p},\mathbf{q})]} A_N(\mathbf{q}),
\end{aligned}
\tag{2.65}
$$

where we have defined the path-integral estimator $A_N(\mathbf{q})$ analogously to $H_N(\mathbf{p},\mathbf{q})$.

Defining the imaginary time variable $\tau = l\beta_N\hbar$, such that the phase space $(\mathbf{p},\mathbf{q})$ is represented by the periodic functions $(p(\tau), q(\tau)) = (p(\tau+\beta\hbar), q(\tau+\beta\hbar)) \equiv (p_l, q_l)$, gives rise to an elegant 'continuum' notation for the imaginary-time phase-space path integrals of Eqs. (2.61) and (2.65). The expectation value is written as

$$
\begin{aligned}
\langle A \rangle_{\mathrm{q}} = \frac{1}{Z_{\mathrm{q}}(\beta)} \oiint \mathcal{D}p\mathcal{D}q \, \exp\!\left(-\frac{1}{\hbar}\int_0^{\beta\hbar} \mathrm{d}\tau \left[H\big(p(\tau),q(\tau)\big) - \mathrm{i}p(\tau)\frac{\partial q(\tau)}{\partial\tau} \right]\right) \\
\times \frac{1}{\beta\hbar}\int_0^{\beta\hbar} \mathrm{d}\tau \, A\big(q(\tau)\big),
\end{aligned}
\tag{2.66}
$$

where $\oiint \mathcal{D}p\mathcal{D}q \equiv \lim_{N\to\infty}(2\pi\hbar)^{-N} \int \mathrm{d}^N\mathbf{p} \int \mathrm{d}^N\mathbf{q}$ denotes integration over all possible cyclic paths. An analogous expression may be written for the partition function. However, Eq. (2.66) is not as rigorous as Eq. (2.65); since the functions $(p(\tau), q(\tau))$ are not generally smooth, it is not generally legitimate to interpret the summand in Eq. (2.64) as a finite-difference derivative [38]. This idea will be built upon in the discussion of Matsubara dynamics in Section 2.4.

2.2.2 Ring-polymer formulation

Eq. (2.65) is of limited utility for practical calculations of expectation values, as $A_N(\mathbf{q})$ has to be sampled over a highly oscillatory phase factor, which is not usually amenable to importance sampling. However, making the substitution $\mathbf{p} = (\mathcal{M}/m)^{-1/2}\overline{\mathbf{p}} + \mathrm{i}m\mathcal{W}\mathbf{q}$ then analytically continuing $\overline{\mathbf{p}}$ onto the real axis yields the phase-free expression

$$
\langle A \rangle_{\mathrm{q}} = \lim_{N\to\infty} \frac{1}{(2\pi\hbar)^N Z_{\mathrm{q}}(\beta)\sqrt{\det(\mathcal{M}/m)}} \int \mathrm{d}^N\overline{\mathbf{p}} \int \mathrm{d}^N\mathbf{q} \, \mathrm{e}^{-\beta_N R_N(\overline{\mathbf{p}},\mathbf{q})} A_N(\mathbf{q}),
\tag{2.67}
$$

where we have defined a new Hamiltonian

$$
R_N(\overline{\mathbf{p}},\mathbf{q}) = \frac{1}{2}\overline{\mathbf{p}}\cdot\mathcal{M}^{-1}\overline{\mathbf{p}} + \frac{1}{2}\mathbf{q}\cdot\mathcal{K}\mathbf{q} + V_N(\mathbf{q}).
\tag{2.68}
$$

Here $\mathcal{K} = m\mathcal{W}^{\mathrm{T}}\mathcal{W}$ is a force constant matrix with elements

$$\mathcal{K}_{l,l'} = \frac{m}{(\beta_N \hbar)^2}\left(2\delta_{l,l'} - \delta_{l,l'-1} - \delta_{l,l'+1}\right), \tag{2.69}$$

and $V_N(\mathbf{q})$ is defined analogously to $H_N(\mathbf{p}, \mathbf{q})$ and $A_N(\mathbf{q})$. The matrix $\mathcal{M}$, known as the Parrinello–Rahman mass matrix [41], is required to be symmetric and positive-definite but the values of its elements are otherwise arbitrary. With A dependent only on position, $\bar{\mathbf{p}}$ can be integrated out analytically from Eq. (2.67) to yield the simplified expression

$$\langle A \rangle_{\mathrm{q}} = \lim_{N \to \infty} \frac{1}{Z_{\mathrm{q}}(\beta)}\left(\frac{m}{2\pi\beta_N \hbar^2}\right)^{N/2} \int \mathrm{d}^N\mathbf{q}\, \exp\left(-\beta_N\left[\frac{1}{2}\mathbf{q} \cdot \mathcal{K}\mathbf{q} + V_N(\mathbf{q})\right]\right) A_N(\mathbf{q}). \tag{2.70}$$

Comparing Eqs. (2.70) and (2.67) (and analogous expressions for $Z_{\mathrm{q}}(\beta)$) with Eqs. (2.19) and (2.21) reveals a formal equivalence in the $N \to \infty$ limit between the Boltzmann statistics of a quantum system at temperature T, and that of a classical 'ring polymer' at temperature NT, in which N replicas of the system ('beads') are cyclically connected by harmonic springs [6, 39]. The variables $\bar{\mathbf{p}}$ represent the 'momenta' of the ring-polymer beads, even though $\mathbf{p}$ bears a stronger physical relationship to the momentum of the original quantum system.

In path-integral molecular dynamics (PIMD) simulations, quantum thermal expectation values are obtained by sampling the configuration spaces of ring polymers along thermostatted classical trajectories [6, 41, 132]. The number of beads, N, is treated as a convergence parameter, with $N = 1$ being equivalent to classical MD, whereas exact quantum statistics is achieved with $N \gg \beta\hbar\Omega_{\mathrm{max}}$, where Ω_{max} is the largest physical frequency (usually vibrational) characteristic of the system under study [25]. The values of the elements of the Parrinello–Rahman mass matrix, $\mathcal{M}$, may be tuned so as to maximise the efficiency of importance sampling. Using PIMD, numerically exact static thermal averages can be calculated as a matter of routine, even with expensive *ab initio* PESs [45–47, 133].

2.3   Linearised semiclassical initial value representation

2.3.1   Wigner phase-space formulation

Section 2.2 outlined one way to cast quantum Boltzmann statistics in terms of a phase-space probability distribution. Another approach employs the Wigner transforms of quantum operators. By inserting resolutions of the identity in the position basis, it is straightforward to show that the quantum expectation value of A can be written generally as [36]

$$\langle A(t) \rangle_{\mathrm{q}} = \mathrm{Tr}\left[\hat{\rho}\hat{A}(t)\right] = \int \mathrm{d}^F\mathbf{q} \int \mathrm{d}^F\mathbf{\Delta}\, \langle \mathbf{q} + \mathbf{\Delta}/2|\hat{\rho}|\mathbf{q} - \mathbf{\Delta}/2\rangle\langle \mathbf{q} - \mathbf{\Delta}/2|\hat{A}(t)|\mathbf{q} + \mathbf{\Delta}/2\rangle \tag{2.71}$$

(where we have returned to the multidimensional scenario, so $\mathbf{p} \equiv (p_1, \ldots, p_F)^{\mathrm{T}}$ and likewise for $\mathbf{q}$ and $\boldsymbol{\Delta}$). Further inserting the identity

$$1 = \int \mathrm{d}^F \boldsymbol{\Delta}' \prod_{i=1}^{F} \delta(\Delta + \Delta') = \frac{1}{(2\pi\hbar)^F} \int \mathrm{d}^F \mathbf{p} \int \mathrm{d}^F \boldsymbol{\Delta} \, \mathrm{e}^{\mathrm{i}\mathbf{p}\cdot(\boldsymbol{\Delta}+\boldsymbol{\Delta}')/\hbar} \tag{2.72}$$

yields

$$\langle A(t) \rangle_{\mathrm{q}} = \frac{1}{(2\pi\hbar)^F} \int \mathrm{d}^F \mathbf{p} \int \mathrm{d}^F \mathbf{q} \, [\hat{\rho}]_{\mathrm{W}}(\mathbf{p}, \mathbf{q}) \, [\hat{A}(t)]_{\mathrm{W}}(\mathbf{p}, \mathbf{q}), \tag{2.73}$$

where the Wigner transform of an operator $\hat{O}$ is defined as [36]

$$[\hat{O}]_{\mathrm{W}}(\mathbf{p}, \mathbf{q}) = \int \mathrm{d}^F \boldsymbol{\Delta} \, \mathrm{e}^{\mathrm{i}\mathbf{p}\cdot\boldsymbol{\Delta}/\hbar} \, \langle \mathbf{q} + \boldsymbol{\Delta}/2 | \hat{O} | \mathbf{q} - \boldsymbol{\Delta}/2 \rangle. \tag{2.74}$$

By similar argument, the standard quantum TCF may be written as [63, 134]

$$C_{AB}(\beta; t) = \frac{1}{(2\pi\hbar)^F Z_{\mathrm{q}}(\beta)} \int \mathrm{d}^F \mathbf{p} \int \mathrm{d}^F \mathbf{q} \, [\hat{U}(-\mathrm{i}\beta\hbar)\hat{A}]_{\mathrm{W}}(\mathbf{p}, \mathbf{q}) \, [\hat{B}(t)]_{\mathrm{W}}(\mathbf{p}, \mathbf{q}), \tag{2.75}$$

and the partition function as

$$Z_{\mathrm{q}}(\beta) = \frac{1}{(2\pi\hbar)^F} \int \mathrm{d}^F \mathbf{p} \int \mathrm{d}^F \mathbf{q} \, [\hat{U}(-\mathrm{i}\beta\hbar)]_{\mathrm{W}}(\mathbf{p}, \mathbf{q}). \tag{2.76}$$

The Kubo-transformed TCF may be obtained by replacing $\hat{U}(-\mathrm{i}\beta\hbar)\hat{A}$ in Eq. (2.75) with $(\beta\hbar)^{-1} \int_0^{\beta\hbar} \mathrm{d}\tau \, \hat{U}(-\mathrm{i}(\beta\hbar - \tau))\hat{A}\hat{U}(-\mathrm{i}\tau)$. The Wigner transform of the density operator, $(2\pi\hbar)^{-F} Z_{\mathrm{q}}^{-1}(\beta)[\hat{U}(-\mathrm{i}\beta\hbar)]_{\mathrm{W}}(\mathbf{p}, \mathbf{q})$, appearing in Eq. (2.76) is known as the Wigner quasi-probability distribution function.

If the observable A depends only on position, then the zero-time Wigner transform $[\hat{A}]_{\mathrm{W}}(\mathbf{q}) \equiv [A(\hat{\mathbf{q}})]_{\mathrm{W}}(\mathbf{q})$ can shown to be equivalent to the classical variable, $A(\mathbf{q})$. An analogous result holds for functions of only momentum, and since the Hamiltonian does not mix momentum with position, it follows that its Wigner transform is similarly equivalent to the corresponding classical variable i.e., $[\hat{H}]_{\mathrm{W}}(\mathbf{p}, \mathbf{q}) = H(\mathbf{p}, \mathbf{q})$. The time dependence of a Wigner transform can then be shown to follow the equation of motion

$$\frac{\mathrm{d}}{\mathrm{d}t} [\hat{A}(t)]_{\mathrm{W}} = \left[\frac{\mathrm{i}}{\hbar} [\hat{H}, \hat{A}(t)] \right]_{\mathrm{W}} = -\{\{H, [\hat{A}(t)]_{\mathrm{W}}\}\} = \mathcal{L}_{\mathrm{W}} [\hat{A}(t)]_{\mathrm{W}}, \tag{2.77}$$

in which $\{\{\cdot, \cdot\}\}$ denotes the Moyal bracket (the quantum phase-space analogue of the Poisson

bracket) [52], and the quantum (Wigner) phase-space Liouvillian is given by

$$\mathcal{L}_W \equiv -\{\{H, \cdot\}\} \equiv -\frac{2}{\hbar} H \sin\left(\frac{\hbar}{2}\left[\overleftarrow{\nabla}_\mathbf{q} \cdot \overrightarrow{\nabla}_\mathbf{p} - \overleftarrow{\nabla}_\mathbf{p} \cdot \overrightarrow{\nabla}_\mathbf{q}\right]\right) \tag{2.78}$$

$$= \mathbf{p} \cdot \mathbf{M}^{-1}\nabla_\mathbf{q} - \frac{2}{\hbar}V \sin\left(\frac{\hbar}{2}\overleftarrow{\nabla}_\mathbf{q} \cdot \overrightarrow{\nabla}_\mathbf{p}\right). \tag{2.79}$$

The formal solution to Eq. (2.77) is

$$\left[\hat{A}(t)\right]_W(\mathbf{p}, \mathbf{q}) = e^{\mathcal{L}_W t}\left[\hat{A}\right]_W(\mathbf{p}, \mathbf{q}). \tag{2.80}$$

2.3.2 Linearisation of the dynamics

Evaluating Eq. (2.80) exactly amounts to solving an infinite series of partial differential equations, and is certainly no easier than solving the TDSE by conventional means. For Eq. (2.75) to be useful for large (e.g. condensed-phase) molecular systems, drastic approximations are necessary. When quantum coherence can be neglected, the most obvious approximation is to truncate the Taylor expansion of Eq. (2.79) at $O(\hbar^0)$, giving the much simpler classical Liouvillian, $\mathcal{L}$ [53]. This is known as the linearised semiclassical initial value representation (LSC-IVR) or classical Wigner method [20, 54–56], with TCFs approximated by

$$C_{AB}(\beta; t) \approx \frac{1}{(2\pi\hbar)^F Z_q(\beta)} \int d^F\mathbf{p} \int d^F\mathbf{q} \left[\hat{U}(-i\beta\hbar)\hat{A}\right]_W(\mathbf{p}, \mathbf{q}) \, e^{\mathcal{L}t}\left[\hat{B}\right]_W(\mathbf{p}, \mathbf{q}), \tag{2.81}$$

or equivalently for the Kubo-transformed version. Since $e^{\mathcal{L}t}\left[\hat{B}\right]_W(\mathbf{p}, \mathbf{q}) = \left[\hat{B}\right]_W(e^{\mathcal{L}t}\mathbf{p}, e^{\mathcal{L}t}\mathbf{q})$, the time evolution in Eq. (2.81) is captured by normal Newtonian trajectories, which are usually straightforward to evaluate numerically. In the case that B depends only on position, this simplifies further to $e^{\mathcal{L}t}\left[\hat{B}\right]_W(\mathbf{q}) = B(e^{\mathcal{L}t}\mathbf{q})$ (likewise for momentum).

Provided with an efficient means for sampling over $[\hat{U}(-i\beta\hbar)\hat{A}]_W(\mathbf{p}, \mathbf{q})$ (see e.g. Appendix A.3 and refs. 57–66), LSC-IVR is a practical method that combines accurate, quantum Boltzmann statistics with classical real-time propagation. It is thus an attractive and, historically, popular choice for approximating the quantum TCFs of condensed-phase systems. It has been applied with some success to calculate a range of dynamical properties, including the IR [33, 67, 68] and Raman [69] spectra of liquid water. However, it suffers the significant drawback of violating detailed balance; that is, the classical trajectories do not conserve the quantum Wigner distribution. In condensed-phase molecular systems like liquid water, this manifests as zero-point energy 'leakage', whereby energy flows unphysically from high-frequency intramolecular modes to low-frequency intermolecular modes. This can lead to artificially fast decay in TCFs, and a corresponding erroneous lineshape broadening in vibrational spectra [33].

2.4 Matsubara dynamics and its approximations

Using the phase-space path-integral representation of the imaginary-time–evolution operator, and resolving the trace in a basis of position eigenstates $|q_N\rangle$, the analytically continued TCF defined in Eq. (2.31) may be expressed formally as

$$C_{AB}(\beta; t + \mathrm{i}l'\beta_N\hbar) = \lim_{N\to\infty} \frac{1}{(2\pi\hbar)^N Z_{\mathrm{q}}(\beta)} \int \mathrm{d}^N\mathbf{p} \int \mathrm{d}^N\mathbf{q} \int \mathrm{d}q_0 \, A(q_{l'}) \, \langle q_0|\hat{U}(-t)\hat{B}\hat{U}(t)|q_N\rangle$$
$$\times \exp\left(-\beta_N \sum_{l=1}^{N}\left[H(p_l, q_{l-1}) - \frac{\mathrm{i}p_l(q_l - q_{l-1})}{\beta_N\hbar}\right]\right),$$

(2.82)

where $l' \in \{0, \ldots, N\}$, and we have assumed that A depends only on position. Assuming the same for B, then using $\langle q_0|q_N\rangle = \delta(q_0 - q_N)$, the TCF simplifies at time $t = 0$ to

$$C_{AB}(\beta; \mathrm{i}l'\beta_N\hbar) = \lim_{N\to\infty} \frac{1}{(2\pi\hbar)^N Z_{\mathrm{q}}(\beta)} \int \mathrm{d}^N\mathbf{p} \int \mathrm{d}^N\mathbf{q} \, \mathrm{e}^{-\beta_N[H_N(\mathbf{p},\mathbf{q})+\mathrm{i}\theta_N(\mathbf{p},\mathbf{q})]} A(q_{l'})B(q_N).$$

(2.83)

In systems for which quantum coherence can safely be neglected, one would expect the real-time evolution to be captured accurately by some flavour of classical trajectories. This requires a momentum coordinate conjugate to every position coordinate, and can only be achieved in Eq. (2.82) if q_0 remains collapsed onto q_N at finite times. Physically, one can regard this as resulting from the vanishing separation between forward and backward real-time paths (since it is this separation that enables the paths to interfere, leading to coherence) [73]. Thus we seek some classical Liouvillian, $\widetilde{\mathcal{L}} = -\{\widetilde{H}, \cdot\}$, such that

$$\lim_{N\to\infty} \frac{1}{(2\pi\hbar)^N Z_{\mathrm{q}}(\beta)} \int \mathrm{d}^N\mathbf{p} \int \mathrm{d}^N\mathbf{q} \, \mathrm{e}^{-\beta_N[H_N(\mathbf{p},\mathbf{q})+\mathrm{i}\theta_N(\mathbf{p},\mathbf{q})]} A(q_{l'})\mathrm{e}^{\widetilde{\mathcal{L}}t}B(q_N)$$

(2.84)

gives the best possible approximation to $C_{AB}(\beta; t + \mathrm{i}l'\beta_N\hbar)$ at finite times.

The most obvious choice would be to set $\widetilde{H}(\mathbf{p}, \mathbf{q}) = H_N(\mathbf{p}, \mathbf{q})$ i.e., have the Hamiltonian $H_N(\mathbf{p}, \mathbf{q})$ generate the classical trajectories. Since $H_N(\mathbf{p}, \mathbf{q})$ is a simple linear combination of 'bead' Hamiltonians $H(p_l, q_l)$, such dynamics would amount to propagating N replicas of the system independently from one another. The problem with this approach is that it fails in general to conserve the phase $\theta_N(\mathbf{p}, \mathbf{q})$ i.e., $\mathcal{L}_N\theta_N(\mathbf{p}, \mathbf{q}) \neq 0$, which causes detailed balance to be violated. Thermal expectation values calculated in this way would depend erroneously on time, except in the harmonic limit. Some deeper insight can be gained from the schematic

'continuum' representation of Eq. (2.84),

$$\frac{1}{Z_q(\beta)} \oiint \mathcal{D}p\mathcal{D}q \exp\left(\frac{1}{\hbar}\int_0^{\beta\hbar} d\tau\left[H(p(\tau),q(\tau)) - \mathrm{i}p(\tau)\frac{\partial q(\tau)}{\partial \tau}\right]\right) A(q(\tau))\mathrm{e}^{\widetilde{\mathcal{L}}t}B(q(\beta\hbar)),$$

(2.85)

from which we can see that the phase $\theta_N(\mathbf{p}, \mathbf{q})$ resembles a generalised momentum variable that is canonically conjugate to imaginary time. In other words, the phase would be the conserved quantity corresponding (by Noether's theorem [124]) to imaginary-time translation invariance, *if* said invariance were to constitute a differentiable symmetry. The paths $(p(\tau), q(\tau))$ are not generally smooth, so $\partial q(\tau)/\partial \tau$ is not usually a well-defined quantity. But if we could constrain the 'jagged' components of paths and propagate only the smooth components, the phase would be conserved and detailed balance observed.

To accomplish this, we consider the discrete Fourier decomposition

$$\mathbf{q} = \sqrt{N}\mathbf{T}\mathbf{Q} \iff \mathbf{Q} = \frac{1}{\sqrt{N}}\mathbf{T}^{\mathrm{T}}\mathbf{q},$$

(2.86)

where (taking N to be odd) $\mathbf{T}$ is a matrix with elements

$$T_{l,k} = \begin{cases} \sqrt{1/N} & k = 0 \\ \sqrt{2/N}\sin(2\pi lk/N) & k \in \{1, \ldots, \overline{N}\} \\ \sqrt{2/N}\cos(2\pi lk/N) & k \in \{1, \ldots, \overline{N}\}, \end{cases}$$

(2.87)

and $\overline{N} = (N-1)/2$. Note that $\mathbf{Q} \equiv (Q_{-\overline{N}}, \ldots, Q_{\overline{N}})^{\mathrm{T}}$ are proportional to the normal mode coordinates of a free ring polymer, and a set of momentum coordinates $\mathbf{P}$ are defined analogously [31]. In the limit $N \to \infty$, this Fourier decomposition provides a natural way to separate smooth and jagged components of the imaginary-time path. We define some odd, positive integer $M \ll N$, such that a linear combination of only the lowest M Fourier components (known as 'Matsubara modes') is a smooth function of τ [73]. The smoothed path is then given by the truncated Fourier series

$$\tilde{q}(\tau) = Q_0 + \sqrt{2}\sum_{k=1}^{\overline{M}}\left[\sin(\omega_k\tau)Q_k + \cos(\omega_k\tau)Q_{-k}\right],$$

(2.88)

and similarly for $\tilde{p}(\tau)$, where $\overline{M} = (M-1)/2$ and

$$\omega_k = \frac{2\pi k}{\beta\hbar}$$

(2.89)

are known as *Matsubara frequencies*. The phase partitions neatly into

$$\theta_N(\mathbf{p}, \mathbf{q}) = N\widetilde{\theta}_M(\mathbf{P}, \mathbf{Q}) + \frac{N}{\beta_N \hbar} \sum_{\overline{M} < |k| \leqslant \overline{N}} P_k \big[\big(\cos(2\pi k/N) - 1\big) Q_k + \sin(2\pi k/N) Q_{-k} \big], \quad (2.90)$$

where the 'Matsubara phase' is given by

$$\widetilde{\theta}_M(\mathbf{P}, \mathbf{Q}) = -\frac{1}{\beta\hbar} \int_0^{\beta\hbar} \mathrm{d}\tau \, \tilde{p}(\tau) \frac{\partial \tilde{q}(\tau)}{\partial \tau} = \sum_{k=-\overline{M}}^{\overline{M}} \omega_k P_k Q_{-k}. \quad (2.91)$$

We now choose to set $\widetilde{H} = N\widetilde{H}_M$, where the 'Matsubara Hamiltonian' is

$$\widetilde{H}_M(\mathbf{P}, \mathbf{Q}) = \frac{1}{\beta\hbar} \int_0^{\beta\hbar} \mathrm{d}\tau \, H\big(\tilde{p}(\tau), \tilde{q}(\tau)\big) = \sum_{k=-\overline{M}}^{\overline{M}} \frac{P_k^2}{2m} + \widetilde{U}_M(\mathbf{Q}), \quad (2.92)$$

with the 'Matsubara potential' defined analogously as

$$\widetilde{U}_M(\mathbf{Q}) = \frac{1}{\beta\hbar} \int_0^{\beta\hbar} \mathrm{d}\tau \, V\big(\tilde{q}(\tau)\big). \quad (2.93)$$

The corresponding 'Matsubara Liouvillian',

$$\widetilde{\mathcal{L}}_M = -\{\widetilde{H}_M, \, \cdot \, \} = \sum_{k=-\overline{M}}^{\overline{M}} \left[\frac{P_k}{m} \frac{\partial}{\partial Q_k} - \frac{\partial \widetilde{U}_M(\mathbf{Q})}{\partial Q_k} \frac{\partial}{\partial P_k} \right], \quad (2.94)$$

conserves the Matsubara phase $\widetilde{\theta}_M(\mathbf{P}, \mathbf{Q})$ (and, trivially, the remainder $\theta_N(\mathbf{p}, \mathbf{q}) - N\widetilde{\theta}_M(\mathbf{P}, \mathbf{Q})$ as this depends only on non-Matsubara modes). It does not necessarily conserve the original Hamiltonian $H_N(\mathbf{p}, \mathbf{q})$, which mixes Matsubara modes with non-Matsubara modes in the potential. However, provided we choose M such that the largest Matsubara frequency greatly exceeds the largest relevant physical frequency (i.e., $\omega_{\overline{M}} \gg \Omega_{\text{max}}$), one can show that the non-Matsubara part of the distribution integrates out analytically at $t = 0$ [135, 136]. That is,

$$C_{AB}(\beta; \mathrm{i}\tau) = \lim_{M \to \infty} C_{AB}^{[M]}(\beta; 0; \mathrm{i}\tau), \quad (2.95)$$

where

$$C_{AB}^{[M]}(\beta; 0; \mathrm{i}\tau) = \frac{\alpha_M}{2\pi\hbar\widetilde{Z}_M(\beta)} \int \mathrm{d}^M\mathbf{P} \int \mathrm{d}^M\mathbf{Q} \, \mathrm{e}^{-\beta[\widetilde{H}_M(\mathbf{P},\mathbf{Q}) + \mathrm{i}\widetilde{\theta}_M(\mathbf{P},\mathbf{Q})]} A\big(\tilde{q}(\tau)\big) B\big(\tilde{q}(\beta\hbar)\big) \quad (2.96a)$$

$$\widetilde{Z}_M(\beta) = \frac{\alpha_M}{2\pi\hbar} \int \mathrm{d}^M\mathbf{P} \int \mathrm{d}^M\mathbf{Q} \, \mathrm{e}^{-\beta[\widetilde{H}_M(\mathbf{P},\mathbf{Q}) + \mathrm{i}\widetilde{\theta}_M(\mathbf{P},\mathbf{Q})]}, \quad (2.96b)$$

in which $\alpha_M = \hbar^{1-M}\overline{M}!^2$ is the system-independent contribution to the partition function from the non-Matsubara modes that have been integrated out [73]. It is understood that $\int \mathrm{d}^M\mathbf{Q}$ is shorthand for $\int_{-\infty}^{\infty} \mathrm{d}Q_{-\overline{M}} \ldots \int_{-\infty}^{\infty} \mathrm{d}Q_{\overline{M}}$, and similar for $\mathbf{P}$. It follows that the 'Matsubara TCF'

$$\widetilde{C}_{AB}^{[M]}(\beta;t) = \frac{\alpha_M}{2\pi\hbar\widetilde{Z}_M(\beta)} \int \mathrm{d}^M\mathbf{P} \int \mathrm{d}^M\mathbf{Q}\, e^{-\beta[\widetilde{H}_M(\mathbf{P},\mathbf{Q})+\mathrm{i}\widetilde{\theta}_M(\mathbf{P},\mathbf{Q})]} \widetilde{A}_M(\mathbf{Q}) e^{\widetilde{\mathcal{L}}_M t}\widetilde{B}_M(\mathbf{Q}), \quad (2.97)$$

where $\widetilde{A}_M$ and $\widetilde{B}_M$ are defined analogously to $\widetilde{U}_M$, converges at $t = 0$ to the exact Kubo-transformed TCF in the limit $M \to \infty$, and also obeys the detailed balance condition

$$\widetilde{C}_{AB}^{[M]}(\beta;t) = \widetilde{C}_{BA}^{[M]}(\beta;-t). \tag{2.98}$$

The approach we have outlined, known as Matsubara dynamics [73], thus combines *exact* quantum Boltzmann statistics (i.e., exact imaginary-time evolution) with *classical* real-time evolution that conserves the quantum distribution.

Although the presentation of Matsubara dynamics here has been heuristic, Althorpe and co-workers derived it rigorously by expressing the exact Kubo-transformed TCF in terms of generalised Wigner transforms defined for the extended phase space $(\mathbf{p}, \mathbf{q})$. Classical trajectories were shown to arise upon discarding the jagged components of the generalised Wigner phase-space Liouvillian, because the space restricted to smooth paths has an effective Planck constant of zero [73–75]. More recently, Trenins and Althorpe showed that Matsubara dynamics can be formulated alternatively as a mean-field approximation to exact quantum dynamics. Rather than assuming the jagged components of the Liouvillian can be discarded a priori, the whole Liouvillian is replaced by its mean-field average over the $N - M$ non-Matsubara modes [76]. This yields a TCF identical to Eq. (2.97), but with $\widetilde{U}_M(\mathbf{Q})$ replaced by the free energy $\widetilde{\mathcal{F}}_M(\mathbf{Q})$, where

$$e^{-\beta\widetilde{\mathcal{F}}_M(\mathbf{Q})} = \lim_{N\to\infty} \left(\frac{m}{2\pi\beta\hbar^2}\right)^{(N-M)/2} \exp\left(\frac{\beta}{2}\sum_{k=-\overline{M}}^{\overline{M}} m\omega_k^2 Q_k^2\right)$$

$$\times N^{N/2} \int \mathrm{d}^N\mathbf{q}\, \exp\left(-\beta_N\left[\frac{1}{2}\mathbf{q}\cdot\mathcal{K}\mathbf{q} + V_N(\mathbf{q})\right]\right) \prod_{k=-\overline{M}}^{\overline{M}} \delta\left(Q_k - \frac{1}{\sqrt{N}}\sum_{l=1}^{N} T_{l,k}q_l\right). \tag{2.99}$$

It is expected that the two formulations of Matsubara dynamics would yield identical results in the limit $M \to \infty$ (or, more strictly, when $\omega_{\overline{M}} \gg \Omega_{\max}$). However, let us define a new odd integer $M' = 2\overline{M}' + 1$, satisfying $M < M' \ll N$. Provided $\omega_{\overline{M}'} \gg \Omega_{\max}$, the components of

the imaginary-time path with $|k| > \overline{M}'$ can be integrated out analytically in Eq. (2.99), giving

$$
\begin{aligned}
\mathrm{e}^{-\beta\widetilde{\mathcal{F}}_M(\mathbf{Q})} = \lim_{M'\to\infty} & \left(\frac{m}{2\pi\beta\hbar^2}\right)^{(M'-M)/2} \\
& \times \int \mathrm{d}^{M'-M}\mathbf{Q}_{|k|>\overline{M}} \exp\left(-\beta\left[\frac{1}{2}\sum_{\overline{M}<|k|\leqslant\overline{M}'}m\omega_k^2 Q_k^2 + \widetilde{U}_{M'}(\mathbf{Q})\right]\right),
\end{aligned}
\tag{2.100}
$$

where we have introduced the shorthand

$$
\int \mathrm{d}^{M'-M}\mathbf{Q}_{|k|>\overline{M}} \equiv \int_{-\infty}^{\infty}\int_{-\infty}^{\infty}\mathrm{d}Q_{\overline{M}+1}\mathrm{d}Q_{-\overline{M}-1}\cdots\int_{-\infty}^{\infty}\int_{-\infty}^{\infty}\mathrm{d}Q_{\overline{M}'}\mathrm{d}Q_{-\overline{M}'}.
\tag{2.101}
$$

The right-hand side of Eq. (2.100) conveniently involves only Matsubara mode ($|k| \leqslant \overline{M}'$) coordinates, so for small values of M, mean-field Matsubara dynamics can be viewed as approximating the $M \to \infty$ limit of the original Matsubara dynamics (and could indeed be derived by mean-field averaging over the original Matsubara Liouvillian). This is a superior approximation to that which arises from simply choosing a small value of M in Eq. (2.97), since it preserves the exact short-time limit of the TCF for linear observables. However, the original 'truncated' form is easier to implement numerically, and easier to study mathematically, since the truncated potential $\widetilde{U}_M(\mathbf{Q})$ can more often be written in closed form than the mean-field potential (or free energy) $\widetilde{\mathcal{F}}_M(\mathbf{Q})$. For this reason, except where otherwise specified, the term 'Matsubara dynamics' used throughout the remainder of this work refers to the truncated formulation.

Numerical tests on toy models have indicated that both formulations of Matsubara dynamics provide good approximations to quantum Kubo-transformed TCFs, assuming that quantum coherence can be ignored [73, 75–77]. Of particular relevance here are the mean-field Matsubara simulations carried out on a two-dimensional model of an O–H molecule in ref. 76 (see also ref. 77), which show that near-perfect agreement with exact quantum dynamics (up to quantum coherence) can be achieved at realistic temperatures with $M < 7$; the exact number of modes required for convergence decreases with temperature. However, Matsubara dynamics is not a practical method for systems with more than a few degrees of freedom. This is because the phase factor $\mathrm{e}^{-\mathrm{i}\beta\widetilde{\theta}_M(\mathbf{P},\mathbf{Q})}$ in the Matsubara distribution is highly oscillatory—the near-cancellation of positive and negative contributions make it unamenable to importance sampling. In many-body theory this is known as a *sign problem*.

In spite of the sign problem, Matsubara dynamics provides a powerful theoretical framework for combining quantum statistics (i.e., imaginary-time propagation) with classical real-time propagation. It is useful for analysing established path-integral dynamics methods such as [thermostatted] ring-polymer molecular dynamics ([T]RPMD), centroid molecular dynamics (CMD), and the planetary model [75, 116], and was recently used to devise the quasi-centroid

molecular dynamics (QCMD) method for calculating accurate vibrational spectra of aqueous systems [107]. In what follows we present each of these methods within the unified Matsubara dynamics framework. We point out here that an exciting, recent generalisation of Matsubara dynamics to multi-time correlation functions has enabled the formulation of corresponding multi-time generalisations of [T]RPMD and CMD, which are applicable to calculating nonlinear vibrational spectra [137–139], but this is outside the scope of the present work.

2.4.1 [Thermostatted] ring-polymer molecular dynamics

Following ref. 84, let us consider the effect of the substitution $P_k = \overline{P}_k - im\omega_k Q_{-k}$ on the Matsubara TCF. This is equivalent (under the assumption $|k| \ll \overline{M}$) to the substitution $\mathbf{p} = (\mathcal{M}/m)^{-1/2}\overline{\mathbf{p}} + im'\mathcal{W}\mathbf{q}$ used in Section 2.2.2, with $\mathcal{M} = m\mathbf{I}$. One obtains

$$
\widetilde{C}_{AB}^{[M]}(\beta;t) = \frac{\alpha_M}{2\pi\hbar\widetilde{Z}_M(\beta)} \int \mathrm{d}^M\mathbf{Q} \prod_{k=-\overline{M}}^{\overline{M}} \left[\int_{-\infty-im\omega_k Q_{-k}}^{\infty-im\omega_k Q_{-k}} \mathrm{d}P_k \right] \mathrm{e}^{-\beta\widetilde{R}_M(\overline{\mathbf{P}},\mathbf{Q})}
$$
$$
\times \widetilde{A}_M(\mathbf{Q})\mathrm{e}^{(\widetilde{\mathcal{L}}_M^{[\mathrm{RP}]}+i\widetilde{\mathcal{L}}_M^{[\mathrm{I}]})t}\widetilde{B}_M(\mathbf{Q}), \tag{2.102}
$$

where

$$
\widetilde{R}_M(\overline{\mathbf{P}},\mathbf{Q}) = \frac{1}{2}\sum_{k=-\overline{M}}^{\overline{M}}\left[\frac{\overline{P}_k^2}{m} + m\omega_k^2 Q_k^2\right] + \widetilde{U}_M(\mathbf{Q}), \tag{2.103}
$$

$$
\widetilde{\mathcal{L}}_M^{[\mathrm{RP}]} = -\{\widetilde{R}_M, \cdot\} = \sum_{k=-\overline{M}}^{\overline{M}}\left[\frac{\overline{P}_k}{m}\frac{\partial}{\partial Q_k} - \left(m\omega_k^2 Q_k + \frac{\partial\widetilde{U}_M(\mathbf{Q})}{\partial Q_k}\right)\frac{\partial}{\partial\overline{P}_k}\right], \tag{2.104}
$$

and

$$
\widetilde{\mathcal{L}}_M^{[\mathrm{I}]} = \sum_{k=-\overline{M}}^{\overline{M}}\omega_k\left(\overline{P}_{-k}\frac{\partial}{\partial\overline{P}_k} - Q_{-k}\frac{\partial}{\partial Q_k}\right). \tag{2.105}
$$

At time $t = 0$, and at $t > 0$ for a wide range of potentials, $\overline{\mathbf{P}}$ can be safely analytically continued onto the real axis in Eq. (2.102) to yield the same expression but with the momentum integration limits shifted onto the real axis [85]. The Matsubara phase thus appears to be eliminated by this transformation. However, this is not enough to turn Matsubara dynamics into a practical method, because a large fraction of the complex trajectories generated by $\widetilde{\mathcal{L}}_M^{[\mathrm{RP}]}+i\widetilde{\mathcal{L}}_M^{[\mathrm{I}]}$ can lead to the real part of $\sum_{k=-\overline{M}}^{\overline{M}}\overline{P}_k^2/(2m)$ becoming negative, causing numerical instability as the system is able to sample regions of the potential that are normally thermally inaccessible [75].[c]

Ring-polymer molecular dynamics (RPMD) [82, 83] is the approximation that arises from

---

[c]Work is underway by Althorpe and co-workers to determine whether these trajectories can be stabilised in specific cases by the addition of a suitable stochastic thermostat, without significantly compromising the information accessible about the dynamics of the physical system.

discarding the imaginary part of the Liouvillian, $\widetilde{\mathcal{L}}_M^{[\mathrm{I}]}$ [84]. In practical terms, it amounts to a straightforward extension of PIMD; the classical (microcanonical) ring-polymer trajectories are interpreted literally as a means to probe the real-time evolution of the quantum system. Explicitly, Kubo-transformed TCFs are approximated by

$$\widetilde{C}_{AB}(\beta;t) \approx \lim_{M\to\infty} \frac{\alpha_M}{2\pi\hbar\widetilde{Z}_M(\beta)} \int \mathrm{d}^M\overline{\mathbf{P}} \int \mathrm{d}^M\mathbf{Q}\ \mathrm{e}^{-\beta\widetilde{R}_M(\overline{\mathbf{P}},\mathbf{Q})} \widetilde{A}_M(\mathbf{Q})\mathrm{e}^{\widetilde{\mathcal{L}}_M^{[\mathrm{RP}]}t}\widetilde{B}_M(\mathbf{Q}) \quad (2.106a)$$

$$= \lim_{N\to\infty} \frac{1}{(2\pi\hbar)^N Z_{\mathrm{q}}(\beta)} \int \mathrm{d}^N\overline{\mathbf{p}} \int \mathrm{d}^N\mathbf{q}\ \mathrm{e}^{-\beta_N R_N(\overline{\mathbf{p}},\mathbf{q})} A_N(\mathbf{q})\mathrm{e}^{\mathcal{L}_N^{[\mathrm{RP}]}t}B_N(\mathbf{q}), \quad (2.106b)$$

where $\mathcal{L}_N^{[\mathrm{RP}]} = -\{R_N,\ \cdot\ \}$ and it is understood that $\boldsymbol{M} = m\mathbf{I}$. The equivalence of Eqs. (2.106a) and (2.106b) follows because the non-Matsubara spring terms in Eq. (2.106b) integrate out and cancel with equivalent terms in the partition function. Eq. (2.106b) is more practical to implement numerically and is known to converge more favourably at $t = 0$ [136]. However, in what follows we will frame our discussions mostly in terms of Eq. (2.106a), given its more direct connection with Matsubara dynamics.

TCFs calculated using RPMD satisfy detailed balance, and reproduce exact Kubo-transformed TCFs in the classical, high-temperature and short-time limits. In the case that A and/or B are linear in position, RPMD is also exact in the harmonic limit, but it fails even for harmonic systems when both observables are nonlinear [82]. This is because, when $A \equiv A(q)$ is linear, the corresponding estimator $A_M(\mathbf{Q})$ depends only on the centroid (centre-of-mass) coordinate Q_0, whereas the estimators for nonlinear observables depend also on the non-centroid, or 'fluctuation', coordinates $Q_{k\neq0}$. For a harmonic oscillator with frequency Ω, the frequency of oscillation of each fluctuation mode in RPMD is $\sqrt{\Omega^2 + \omega_k^2}$, whereas in Matsubara dynamics it is Ω. Nonlinear estimators in the former therefore introduce unphysical oscillations into the TCF.

While RPMD can be used to successfully predict some properties, such as diffusion coefficients and reaction rate constants [89, 90, 140], for vibrational spectroscopy the unphysical vibrations of the fluctuation modes can be a significant source of error. This is true even if the DMS is linear, because the anharmonicity in the potential couples the centroid to the fluctuations, which can lead to erroneous, temperature-dependent peaks in the spectrum. Furthermore, at specific temperatures, the low-frequency fluctuations can come into resonance with the centroid, leading to artificial peak splitting and intensity borrowing. This is sometimes known as the *spurious resonance problem* of RPMD [99–101].

In thermostatted RPMD (TRPMD), the spurious resonance problem is mitigated by attaching a Langevin thermostat to each fluctuation mode [102]. Formally, instead of simply

discarding $i\widetilde{\mathcal{L}}_M^{[\mathrm{I}]}$, one replaces it with the sum of Fokker–Planck operators

$$\mathcal{A}_M = \sum_{k=-\overline{M}}^{\overline{M}} \gamma_k \left(\frac{m}{\beta} \frac{\partial^2}{\partial \overline{P}_k^2} - \overline{P}_k \frac{\partial}{\partial \overline{P}_k} \right), \tag{2.107}$$

which generate friction and a random force on each fluctuation mode [85]. The friction coefficients are usually chosen as $\gamma_k = |\omega_k|$, which yields optimal damping [102].[d] TRPMD is exact in the same limits as RPMD, and usually gives better predictions of vibrational spectra because the damping of the fluctuation modes washes out spurious peaks and prevents significant intensity borrowing from the centroid vibrations, thus reducing or eliminating the spurious resonance problem. However, it has the disadvantage that the damping causes considerable artificial lineshape broadening, which becomes more severe as the temperature is lowered [102].

2.4.2 [Quasi-]centroid molecular dynamics

As noted above, for observables that are linear functions of position, the path-integral estimators depend only on the centroid coordinate. One therefore does not need to keep track of the detailed, real-time dynamics of the fluctuation modes. Since the Matsubara phase is independent of the centroid, one way to eliminate the sign problem (while preserving detailed balance) is to approximate the effect of the fluctuations at the mean-field level. The centroid then evolves on an effective classical potential. This is the basis of the centroid molecular dynamics (CMD) method due to Voth and co-workers [78–81], which we now understand to be a special case of mean-field Matsubara dynamics in which M is set to unity [76]. In other words, it is the lowest in a hierarchy of mean-field approximations to exact quantum dynamics, but has the important advantage of being phase-free.

Written explicitly, CMD approximates the Kubo-transformed TCF by

$$\widetilde{C}_{AB}(\beta; t) \approx \frac{1}{2\pi\hbar Z_{\mathrm{q}}(\beta)} \int \mathrm{d}P_0 \int \mathrm{d}Q_0 \exp\left(-\beta \left[\frac{P_0^2}{2m} + \mathcal{F}(Q_0) \right] \right) A(Q_0) e^{\mathcal{L}^{[\mathrm{C}]} t} B(Q_0), \tag{2.108}$$

where $\mathcal{F}(Q_0) \equiv \widetilde{\mathcal{F}}_1(\mathbf{Q})$, and the Liouvillian is

$$\mathcal{L}^{[\mathrm{C}]} = \frac{P_0}{m} \frac{\partial}{\partial Q_0} - \frac{\partial \mathcal{F}(Q_0)}{\partial Q_0} \frac{\partial}{\partial P_0}. \tag{2.109}$$

---

[d]In practice, since TRPMD is usually implemented by simulating the full N-bead ring-polymer rather than just its Matsubara modes, the friction coefficients are set to the natural frequencies of the ring-polymer, $\gamma_k = 2\sin(\beta_N \hbar |\omega_k|/2)/\beta_N \hbar$. It is easy to show that this gives $|\omega_k|$ in the limit $N \to \infty$.

The CMD force is thus given by

$$-\frac{\partial \mathcal{F}(Q_0)}{\partial Q_0} = -\lim_{M \to \infty} \frac{\int d^{M-1}\mathbf{Q}_{|k|>0} \exp\left(-\beta\left[\frac{1}{2}\sum_{0<|k|\leqslant \overline{M}} m\omega_k^2 Q_k^2 + \widetilde{U}_M(\mathbf{Q})\right]\right) \frac{\partial \widetilde{U}_M(\mathbf{Q})}{\partial Q_0}}{\int d^{M-1}\mathbf{Q}_{|k|>0} \exp\left(-\beta\left[\frac{1}{2}\sum_{0<|k|\leqslant \overline{M}} m\omega_k^2 Q_k^2 + \widetilde{U}_M(\mathbf{Q})\right]\right)}$$

(2.110)

$$= -\lim_{N \to \infty} \frac{\int d^N\mathbf{q} \exp\left(-\beta_N\left[\frac{1}{2}\mathbf{q}\cdot\mathcal{K}\mathbf{q} + V_N(\mathbf{q})\right]\right)\delta\left(Q_0 - N^{-1}\sum_{l=1}^N q_l\right)\frac{1}{N}\sum_{l=1}^N V'(q_l)}{\int d^N\mathbf{q} \exp\left(-\beta_N\left[\frac{1}{2}\mathbf{q}\cdot\mathcal{K}\mathbf{q} + V_N(\mathbf{q})\right]\right)\delta\left(Q_0 - N^{-1}\sum_{l=1}^N q_l\right)},$$

(2.111)

where the equivalence of Eqs. (2.110) and (2.111) results from cancellation of the non-Matsubara spring terms in the latter. Physically, these expressions represent the centroid-constrained thermal average over the force acting on the centroid, hence $\mathcal{F}(Q_0)$ is often called the centroid *potential of mean force* (PMF) [81]. In practice, neither expression is usually implemented explicitly, which would require centroid-constrained importance sampling (i.e., centroid-constrained PIMD/MC) to be carried out at every time step of the simulation. Instead, CMD is implemented in a way that is algorithmically identical to TRPMD other than in the choice of Parrinello–Rahman mass matrix, $\mathcal{M}$. Whereas for TRPMD one sets $\mathcal{M} = m\mathbf{I}$, for CMD one sets $\mathcal{M}$ to be diagonal only in the eigenbasis of $\mathcal{K}$, with elements scaled to yield a natural frequency of $\Gamma/\beta_N\hbar$ for each ring-polymer fluctuation mode [88, 101, 141]. In the limit $\Gamma \to \infty$, the fluctuations become adiabatically separated from the (much slower) centroid motion; in practice Γ is treated as a convergence parameter. This is known as the [partially] adiabatic implementation of CMD, or [P]A-CMD.

As a special case of (mean-field) Matsubara dynamics, CMD satisfies detailed balance and is exact in the classical and high-temperature limits. In the short-time and harmonic limits, it is exact in the special case that *both A and B* are linear, but remains inherently approximate for nonlinear observables because the fluctuation modes are absent from the CMD phase space; implicitly in Eq. (2.108) we have made the approximation $A_M(\mathbf{Q}) \approx A(Q_0)$, and likewise for *B*.

In the context of vibrational spectroscopy, CMD works well provided the temperature is high enough for the ring-polymer distribution around the centroid to remain compact. In this regime, it gives more accurate spectra than TRPMD, since the centroid motion is uncorrupted by the thermostat (but it is more expensive, since a smaller time step is required to cope with the high-frequency oscillations of the fluctuation modes). It also works surprisingly well for one-dimensional systems at extremely low temperatures—this anomalous behaviour was first explained by Ramírez *et al.* [142–144] and is discussed further in Section 3.4.4. However,

for low-temperature molecular (multidimensional) systems, the mean-field approximation can break down, in particular when a high-frequency vibration is coupled to a low-frequency rotation or libration. Consider, for instance, an O–H bond in a water molecule: if the centroids of O and H are constrained to the short-range repulsive region of the bond potential, their associated ring polymers might be able to minimise their potential energies by spreading out into crescents that curve around the centroids. The result is an unphysical 'flattening' of the centroid PMF, and a corresponding reduction in vibrational frequency, leading to artificial redshifts and lineshape broadening in the stretch fundamental region of the IR spectrum. This in known as the *curvature problem* [99, 100]. It is now understood that the onset of the curvature problem is related to the formation of artificial instantons in centroid-constrained trajectories, which is found to occur in gas-phase water below about 250 K [76, 77].

The curvature problem may be viewed as an artefact of using Cartesian coordinates to define the centroid in multidimensional systems. When the ring-polymer bead distribution is localised to a curved valley in the PES, its mode will be offset from the Cartesian centroid. In quasi-centroid molecular dynamics (QCMD), one transforms to a curvilinear coordinate system designed such that upon constraining the (now curvilinear) centroids, the bead distribution remains compact. To obtain mean-field dynamics that is real and phase-free, Trenins showed that the definition of the curvilinear centroid must be invariant with respect to both translation and reversal in imaginary time [77].

QCMD is most easily motivated for a two-dimensional system with Cartesian coordinates $(x, y) = (r \cos(\theta), r \sin(\theta))$. In terms of corresponding ring-polymer (rather than Matsubara) coordinates, the Cartesian centroids are given by

$$X_0 = \frac{1}{N} \sum_{l=1}^{N} x_l \tag{2.112a}$$

$$Y_0 = \frac{1}{N} \sum_{l=1}^{N} y_l, \tag{2.112b}$$

where $(x_l, y_l) = (r_l \cos(\theta_l), r_l \sin(\theta_l))$. We can then define the polar centroid coordinates (R, Θ) as the averages of the corresponding polar bead coordinates,

$$R = \frac{1}{N} \sum_{l=1}^{N} r_l \tag{2.113a}$$

$$\Theta = \frac{1}{N} \sum_{l=1}^{N} \theta_l. \tag{2.113b}$$

Classical trajectories are obtained by mean-field averaging the quantum (or Matsubara) Liouvillian about (R, Θ). The 'quasi-centroid' coordinates (X_{QC}, Y_{QC}), used to estimate observables

such as the dipole moment, are defined as

$$X_{QC} = R \cos(\Theta) \tag{2.114a}$$

$$Y_{QC} = R \sin(\Theta), \tag{2.114b}$$

and will satisfy $(X_{QC}, Y_{QC}) \simeq (X_0, Y_0)$ provided the ring-polymer bead distribution remains compact.

The reader is referred to ref. 77 for a much more detailed exposition of QCMD, including its practical implementation and generalisation to gas- and condensed-phase water. The key point is that it is exact in all the same limits as CMD, while avoiding the significant drawback of the curvature problem at low temperatures. The quasi-centroid PMF does not suffer the same artificial 'flattening' as the centroid PMF, because the coordinate system is explicitly chosen to respect the curvature of the PES. Accordingly, as discussed further in Chapter 4, QCMD provides the best approximation of any known path-integral method to the fundamental bands in the IR spectra of condensed-phase water. Further work will be required to generalise this promising method to more complex molecular systems.

2.4.3   The planetary model

Viewed as approximations to Matsubara dynamics, the main drawback that [T]RPMD and [Q]CMD have in common is of corrupting, or completely neglecting, the dynamics of the Matsubara fluctuations. This makes them largely inapplicable to calculating TCFs of nonlinear observables, such as *ab initio* dipole moments in the context of IR spectroscopy. In general this seems to be a necessary evil for constructing practical methods to probe the dynamics of the centroid, due to the sign problem that otherwise arises from the large Matsubara phase factor. It is interesting, however, that for harmonic systems the fluctuations can be integrated out analytically. The centroid–fluctuation coupling is an inherently anharmonic phenomenon, but provided the effect of this coupling is small, one should expect to be able to devise a phase-free, quasi-harmonic approximation to the fluctuation dynamics to complement 'centroid-following' methods like [T]RPMD and [Q]CMD.

This is the premise of the planetary model [75, 116], which is a generalisation of the Feynman–Kleinert quasi-classical Wigner 'method 1' due to Smith *et al.* [115]. One starts with a locally harmonic approximation to the Matsubara potential,

$$\widetilde{U}_M(\mathbf{Q}) \approx L(Q_0) + \frac{1}{2} m \Omega^2(Q_0) \sum_{0 < |k| \leqslant \overline{M}} Q_k^2, \tag{2.115}$$

where the functional forms of $L(Q_0)$ and $\Omega(Q_0)$ are yet to be specified. The corresponding

approximation to the Matsubara Liouvillian is

$$\widetilde{\mathcal{L}}_M \approx \underbrace{\frac{P_0}{m}\frac{\partial}{\partial Q_0} - \left[L'(Q_0) + m\Omega(Q_0)\Omega'(Q_0)\sum_{0<|k|\leqslant \overline{M}}Q_k^2\right]\frac{\partial}{\partial P_0}}_{\text{centroid}}$$

$$+ \underbrace{\sum_{0<|k|\leqslant \overline{M}}\left[\frac{P_k}{m}\frac{\partial}{\partial Q_k} - m\Omega^2(Q_0)Q_k\frac{\partial}{\partial P_k}\right]}_{\text{fluctuations}},$$

(2.116)

where a prime indicates differentiation with respect to Q_0, and we have used braces to highlight the variables upon which the various contributions to the Liouvillian operate. The next approximation is to replace the centroid term with its mean-field average over the fluctuation modes (using the locally harmonic Matsubara distribution consistent with Eq. (2.115)), giving

$$\widetilde{\mathcal{L}}_M \approx \underbrace{\frac{P_0}{m}\frac{\partial}{\partial Q_0} - W'(Q_0)\frac{\partial}{\partial P_0}}_{\text{centroid}} + \underbrace{\sum_{0<|k|\leqslant \overline{M}}\left[\frac{P_k}{m}\frac{\partial}{\partial Q_k} - m\Omega^2(Q_0)Q_k\frac{\partial}{\partial P_k}\right]}_{\text{fluctuations}},$$

(2.117)

where

$$W(Q_0) = L(Q_0) + \frac{1}{\beta}\ln\left(\frac{\sinh\left(\beta\hbar\Omega(Q_0)/2\right)}{\beta\hbar\Omega(Q_0)/2}\right).$$

(2.118)

This approximation is fairly drastic, eliminating any influence of the dynamics of the fluctuations on those of the centroid. However, it is practically useful, as it enables the formulation of a phase-free approximation to Matsubara dynamics in which one is permitted to choose whatever forms of $L(Q_0)$ and $\Omega(Q_0)$ are the most convenient for simulating centroid trajectories.

The locally harmonic form of Eq. (2.115), combined with the independence of $W(Q_0)$ on the fluctuations, allows us to integrate out all but a single pair of fluctuation variables from the Matsubara TCF at finite times. In particular, we can probe the *standard* quantum TCF by focusing not on an arbitrary Matsubara mode (P_k, Q_k), but a linear combination of modes $(\tilde{p}_\delta, \tilde{q}_\delta)$ representing the displacement of a single point on the imaginary-time path from the centroid i.e.,

$$\tilde{p}_\delta = \tilde{p}(\tau) - P_0 \tag{2.119a}$$

$$\tilde{q}_\delta = \tilde{q}(\tau) - Q_0 \tag{2.119b}$$

for arbitrary $0 \leqslant \tau < \beta\hbar$. We refer to the pseudo-particle represented by $(P_0 + \tilde{p}_\delta, Q_0 + \tilde{q}_\delta)$ as

the 'planet'. Integrating out all other fluctuation variables leads to [75]

$$
\begin{aligned}
C_{AB}^{[M]}(\beta; t; 0) \approx {} & \frac{1}{2\pi\hbar Z_{\mathrm{q}}(\beta)} \int \mathrm{d}P_0 \int \mathrm{d}Q_0 \exp\!\left(-\beta\left[\frac{P_0^2}{2m} + W(Q_0)\right]\right) \\
& \times \frac{1}{2\pi m\Omega(Q_0)a^2(Q_0)} \int \mathrm{d}\tilde{p}_\delta \int \mathrm{d}\tilde{q}_\delta \exp\!\left(-\beta\left[\frac{\tilde{p}_\delta^2}{2m^2\Omega^2(Q_0)a^2(Q_0)} + \frac{\tilde{q}_\delta^2}{2a^2(Q_0)}\right]\right) \\
& \times f_A^{[\mathrm{P}]}(Q_0 + \tilde{q}_\delta, \tilde{p}_\delta)\, \mathrm{e}^{\mathcal{L}^{[\mathrm{P}]}t} B(Q_0 + \tilde{q}_\delta),
\end{aligned}
\tag{2.120}
$$

where

$$
a^2(Q_0) = \frac{(\beta\hbar\Omega(Q_0)/2)\coth(\beta\hbar\Omega(Q_0)/2) - 1}{\beta m\Omega^2(Q_0)}
\tag{2.121}
$$

is the average radius of gyration of the imaginary-time path,

$$
\begin{aligned}
f_A^{[\mathrm{P}]}(Q_0 + \tilde{q}_\delta, \tilde{p}_\delta) = {} & \frac{m\Omega(Q_0)a(Q_0)}{\sqrt{2\pi}\hbar} \exp\!\left(\frac{\tilde{p}_\delta^2}{2m^2\Omega^2(Q_0)a^2(Q_0)}\right) \\
& \times \int \mathrm{d}\Delta\, \mathrm{e}^{\mathrm{i}\tilde{p}_\delta\Delta/\hbar} \exp\!\left(-\frac{m^2\Omega^2(Q_0)a^2(Q_0)\Delta^2}{2\hbar^2}\right) A(q + \Delta/2)
\end{aligned}
\tag{2.122}
$$

is the static estimator for observable A, and the Liouvillian is

$$
\mathcal{L}^{[\mathrm{P}]} = \underbrace{\frac{P_0}{m}\frac{\partial}{\partial Q_0} - W'(Q_0)\frac{\partial}{\partial P_0}}_{\text{centroid}} + \underbrace{\frac{\tilde{p}_\delta}{m}\frac{\partial}{\partial \tilde{q}_\delta} - m\Omega^2(Q_0)\tilde{q}_\delta\frac{\partial}{\partial \tilde{p}_\delta}}_{\text{fluctuation}}.
\tag{2.123}
$$

However, since $(\tilde{p}_\delta, \tilde{q}_\delta)$ are sampled from a distribution dependent on the position, Q_0, of the centroid, the dynamics of (2.123) violates detailed balance (and, in effect, conservation of energy). Detailed balance is recovered by modifying the Liouvillian to

$$
\begin{aligned}
\mathcal{L}^{[\mathrm{P}]} = {} & \underbrace{\frac{P_0}{m}\frac{\partial}{\partial Q_0} - W'(Q_0)\frac{\partial}{\partial P_0}}_{\text{centroid}} \\
& + \underbrace{\frac{\tilde{p}_\delta}{m}\frac{\partial}{\partial \tilde{q}_\delta} - m\Omega^2(Q_0)\tilde{q}_\delta\frac{\partial}{\partial \tilde{p}_\delta} + \frac{P_0}{m}\left[\frac{\mathrm{d}\ln(\Omega^2(Q_0)a^2(Q_0))}{\mathrm{d}Q_0}\frac{\tilde{p}_\delta}{2}\frac{\partial}{\partial \tilde{p}_\delta} + \frac{\mathrm{d}\ln(a^2(Q_0))}{\mathrm{d}Q_0}\frac{\tilde{q}_\delta}{2}\frac{\partial}{\partial \tilde{q}_\delta}\right]}_{\text{fluctuation}},
\end{aligned}
\tag{2.124}
$$

which defines the dynamics of the planetary model [75].

All that remains is to specify the functional forms of $L(Q_0)$ and $\Omega(Q_0)$, though in practice it is more sensible to choose convenient forms of $W(Q_0)$ and $\Omega(Q_0)$, then let $L(Q_0)$ be

defined implicitly. In the original formulation, Poulsen and co-workers derived them using Feynman–Kleinert variational theory [145], yielding $W(Q_0)$ as an approximation to the centroid PMF. An obvious refinement would be to use the exact PMF, such that the centroids undergo CMD. However, Willatt *et al.* pointed out that it is more efficient (and more accurate at low temperatures) to propagate the centroids using TRPMD [75, 116]. In this formulation, $W(Q_0)$ is not a well-defined quantity, but that presents no issue for detailed balance, given that the centroid and fluctuation distributions are still independently conserved. The same authors chose $\Omega(Q_0)$ to be the 'path-integral frequency', defined by the centroid-constrained thermal average

$$
\begin{aligned}
&m\Omega^2(Q_0) \\
&= \lim_{N\to\infty} \frac{\int \mathrm{d}^N\mathbf{q}\,\exp\!\left(-\beta_N\left[\frac{1}{2}\mathbf{q}\cdot\boldsymbol{\mathcal{K}}\mathbf{q}+V_N(\mathbf{q})\right]\right)\delta\!\left(Q_0-N^{-1}\sum_{l=1}^N q_l\right)N^{-1}\sum_{l=1}^N V''(q_l)}{\int \mathrm{d}^N\mathbf{q}\,\exp\!\left(-\beta_N\left[\frac{1}{2}\mathbf{q}\cdot\boldsymbol{\mathcal{K}}\mathbf{q}+V_N(\mathbf{q})\right]\right)\delta\!\left(Q_0-N^{-1}\sum_{l=1}^N q_l\right)},
\end{aligned}
$$

(2.125)

which can be calculated via centroid-constrained PIMD/MC.

For further details of the planetary model, including its multidimensional generalisation and implementation, the reader is referred to ref. 75. Unlike [T]RPMD and [Q]CMD, it is exact in the harmonic limit *even for nonlinear observables*. For anharmonic systems, it is exact in the classical and high-temperature limits, but only approximately correct in the short-time limit on account of the locally harmonic distribution of fluctuation variables $(\tilde{p}_\delta, \tilde{q}_\delta)$. The method has been shown to give reasonably good descriptions of the fundamental bands in the IR spectra of gas- and condensed-phase water, with lineshapes improved substantially upon those that can be obtained from TRPMD centroid trajectories alone. One significant limitation is in the descriptions of rotational and librational motions, which are poorly captured by the locally harmonic approximation of Eq. (2.115) [75, 116].

Chapter 3

Anharmonic absorption intensities

As mentioned in Section 2.1.3, nuclear quantum effects (NQEs) on vibrational spectra range from exceedingly subtle to very dramatic. Condensed-phase spectra do not typically exhibit the same marked real-time quantum dynamical effects as gas-phase spectra, due to the quenching of quantum coherence by the coupling between large numbers of intramolecular and inter-molecular degrees of freedom [22]. However, quantum statistical effects can be significant, and motivate the development of methods such as [T]RPMD and [Q]CMD for approximating the real-time propagation of imaginary-time Feynman paths.

A great deal of attention has been given in the literature to understanding the role of quantum statistical effects on the appearances of fundamental bands, and the accuracies of path-integral methods in describing them, particularly in condensed-phase water [28–30, 33, 34, 96–98, 107, 116, 146, 147]. For instance, zero-point energy in the intramolecular vibrations of liquid water causes the stretch and bend fundamental bands to redshift relative to classical predictions; combined with accurate many-body potential energy and dipole moment surfaces, CMD has been shown to be capable of reproducing this effect over a range of temperatures [30]. Path-integral descriptions of the fundamental band regions of some more complex molecular systems have also been studied, mainly using TRPMD [102–105, 148].

On the other hand, relatively little attention has been given to path-integral descriptions of inherently anharmonic spectral features. Among the most interesting of these are Fermi resonances, a detailed discussion of which will be reserved for Chapter 5. Here we focus instead on the intensities of overtone, combination, and difference bands when they are well separated in frequency from other bands of the same symmetry (i.e., they are non-resonant). We restrict the discussion for simplicity to linear (one-dimensional) IR spectroscopy, but note that much of the interest in describing anharmonic features arises from their relevance to nonlinear spectroscopies, such as two-dimensional IR [114]. Limited earlier studies have suggested that centroid-following methods are incapable of accurately capturing these features, significantly underestimating the intensities of combination bands in particular [102, 107].

It is tempting to blame this on the neglect of quantum coherence, but this explanation is unconvincing given that LSC-IVR (which also neglects coherence) does not appear to suffer the same drawback [68, 69]. When electrical anharmonicity is significant (i.e., the dipole moment is highly nonlinear), we know that part of the problem is the mapping of nonlinear operators to functions on the Matsubara phase space that depend explicitly on the fluctuation modes—we expect the planetary model to correct for this [75]. Otherwise, the question remains of which approximations made by centroid-following path-integral methods are responsible for the discrepancies, and how to correct for them.

Given the connection of these methods to Matsubara dynamics (see Section 2.4), developing a unified understanding of absorption intensities under the Matsubara framework would be a sensible starting point. We begin in Section 3.1 by formalising the quantum, classical, and Matsubara descriptions of absorption bands for a simplified—yet fairly general—model of molecular vibrations, providing general expressions for the integrated intensities. In Section 3.2, we use first-order perturbation theories to evaluate these expressions for the specific class of absorptions in which the vibrational quantum numbers change by a total magnitude of two, namely *first overtone*, *binary combination*, and *binary difference* bands. We find that Matsubara dynamics, in the $M \to \infty$ limit, reproduces the quantum integrated intensities exactly up to second order in the perturbation parameter. In Section 3.3, we explain how this results from the coupling of the centroid to the fluctuation modes, which 'Matsubara heat' the amplitudes of the relevant centroid vibrations to what they would be in a classical system with each oscillator prepared at its quantum effective temperature. In Section 3.4, we discuss the implications of our results for the accuracies of path-integral methods, using a one-dimensional model of an O–H bond for illustrative purposes. We also propose a simple, post-processing correction procedure to bring the results of classical or path-integral calculations into closer agreement with exact quantum mechanics.

3.1 Formal expressions for integrated absorption intensities

3.1.1 Quantum spectra

Consider again the molecular system with the Hamiltonian of Eq. (2.1). Since we are primarily interested in vibrational dynamics with minimal rovibrational coupling, it is convenient to focus only on (F) vibrational degrees of freedom. We assume that the system only accesses the basin of a single potential energy minimum, and choose $\hat{\mathbf{p}}$ and $\hat{\mathbf{q}}$ to be the corresponding mass-weighted normal mode momentum and position operators, respectively. The Hamiltonian then simplifies to

$$\hat{H} = \hat{H}^{(0)} + \varepsilon \hat{V}^{(1)}, \tag{3.1}$$

where

$$\hat{H}^{(0)} = \frac{1}{2} \sum_{i=1}^{F} \left(\hat{p}_i^2 + \Omega_i^2 \hat{q}_i^2 \right) \tag{3.2a}$$

$$\varepsilon \hat{V}^{(1)} \equiv \varepsilon V^{(1)}(\hat{\mathbf{q}}) = V(\hat{\mathbf{q}}) - \frac{1}{2} \sum_{i=1}^{F} \Omega_i^2 \hat{q}_i^2, \tag{3.2b}$$

in which

$$\Omega_i = \sqrt{\left. \frac{\partial^2 V(\mathbf{q})}{\partial q_i^2} \right|_{\mathbf{q}=\mathbf{0}}}, \tag{3.3}$$

and the leading-order terms in $V^{(1)}$ are at least cubic. For future convenience, we have factored out a real, dimensionless constant ε from the anharmonic part of the potential. If ε is small, it is useful to regard the system as resulting from a weak, time-independent perturbation $\varepsilon \hat{V}^{(1)}$ to a set of uncoupled harmonic oscillators. We make the further, significant assumption that the eigenvalue spectrum of $\hat{H}^{(0)}$ contains no degeneracies, meaning the harmonic frequencies $\mathbf{\Omega} \equiv (\Omega_1, \ldots, \Omega_F)^{\mathrm{T}}$ are not rationally related.

In Chapter 2, energy eigenstates were indexed by the single quantum number $n \in \{0, \ldots, \infty\}$, but here it will prove more convenient to use the full set of vibrational quantum numbers $\mathbf{n} \equiv (n_1, \ldots, n_F)^{\mathrm{T}}$. More precisely, as $\varepsilon \to 0$, the wave functions are assumed to vary smoothly from $|\psi_{\mathbf{n}}\rangle$ to $|\psi_{\mathbf{n}}^{(0)}\rangle$, where

$$|\psi_{\mathbf{n}}^{(0)}\rangle \equiv |\mathbf{n}\rangle \equiv |n_1, \ldots, n_F\rangle \equiv |n_1\rangle \otimes \cdots \otimes |n_F\rangle, \tag{3.4}$$

$$\hat{H}^{(0)} |\mathbf{n}\rangle = E_{\mathbf{n}}^{(0)} |\mathbf{n}\rangle, \tag{3.5}$$

and

$$E_{\mathbf{n}}^{(0)} = \hbar \mathbf{n} \cdot \mathbf{\Omega} + \frac{\hbar}{2} \sum_{i=1}^{F} \Omega_i. \tag{3.6}$$

In the equilibrium IR spectrum, a stimulated transition from $|\psi_{\mathbf{n}}\rangle$ to $|\psi_{\mathbf{n}'}\rangle$ gives rise to net absorption and a corresponding peak centred at frequency

$$\omega_{\mathbf{n} \to \mathbf{n}'} = \frac{1}{\hbar} \left(E_{\mathbf{n}'} - E_{\mathbf{n}} \right) = \Delta\mathbf{n} \cdot \mathbf{\Omega} + O(\varepsilon). \tag{3.7}$$

In the harmonic ($\varepsilon \to 0$) limit, this absorption frequency clearly depends only on the change in quantum numbers, $\Delta\mathbf{n} = \mathbf{n}' - \mathbf{n}$, thus peaks corresponding to the same $\Delta\mathbf{n}$ will be superposed. When ε is finite but still small, it is convenient to consider the envelope of peaks of equal $\Delta\mathbf{n}$ as a single entity, often known as an '(absorption) band system'. Because we will mostly be unconcerned with the fine structure of such features, in what follows we refer to them simply

as 'bands',[a] and label them either by $\Delta\mathbf{n}$ or (more conventionally) $\Delta n_1 \nu_1 + \cdots + \Delta n_F \nu_F$. Here $\nu_i \simeq \Omega_i/2\pi$ represents the fundamental (ordinary) frequency of oscillator i.

In general, the dipole moment of the system is a three-dimensional vector $\boldsymbol{\mu} \equiv (\mu_x, \mu_y, \mu_z)^{\mathrm{T}}$, which depends on all the normal mode coordinates $\mathbf{q}$ as well as the spatial orientation of the molecule. However, since we are assuming negligible rovibrational coupling, we can simplify the algebra by considering just one arbitrary (scalar) component of $\boldsymbol{\mu}$ in the body-fixed frame. We denote this component $\mu \equiv \mu(\mathbf{q})$, with corresponding quantum operator $\hat{\mu} \equiv \mu(\hat{\mathbf{q}})$. Applying Eq. (2.44), the net energy absorption spectrum is then given by

$$S_{\mathrm{q}}(\beta; \omega) = \frac{2\pi |\mathcal{E}|^2}{\hbar Z_{\mathrm{q}}(\beta)} \sum_{\mathbf{n}} \sum_{\mathbf{n}'} \left(\mathrm{e}^{-\beta E_{\mathbf{n}}} - \mathrm{e}^{-\beta E_{\mathbf{n}'}} \right) \left(E_{\mathbf{n}'} - E_{\mathbf{n}} \right) \left| \langle \psi_{\mathbf{n}} | \hat{\mu} | \psi_{\mathbf{n}'} \rangle \right|^2 \delta \left(E_{\mathbf{n}'} - E_{\mathbf{n}} + \hbar \omega \right), \quad (3.8)$$

where $\sum_{\mathbf{n}}$ is shorthand for $\sum_{n_1=0}^{\infty} \cdots \sum_{n_F=0}^{\infty}$. It follows that the integrated intensity of the $\Delta\mathbf{n}$ band must be given by

$$\begin{aligned}
\mathcal{I}_{\Delta\mathbf{n}}^{[\mathrm{q}]}(\beta) &\equiv \mathcal{I}_{\Delta n_1 \nu_1 + \cdots + \Delta n_F \nu_F}^{[\mathrm{q}]}(\beta) \\
&= \frac{2\pi |\mathcal{E}|^2}{\hbar^2 Z_{\mathrm{q}}(\beta)} \sum_{\mathbf{n} \in \mathrm{orig}(\Delta\mathbf{n})} \left(\mathrm{e}^{-\beta E_{\mathbf{n}}} - \mathrm{e}^{-\beta E_{\mathbf{n}+\Delta\mathbf{n}}} \right) \left(E_{\mathbf{n}+\Delta\mathbf{n}} - E_{\mathbf{n}} \right) \left| \langle \psi_{\mathbf{n}} | \hat{\mu} | \psi_{\mathbf{n}+\Delta\mathbf{n}} \rangle \right|^2,
\end{aligned} \quad (3.9)$$

where

$$\mathrm{orig}(\Delta\mathbf{n}) = \left\{ \mathbf{n} \mid \forall i \in \{1, \ldots, F\}, n_i + \Delta n_i \geqslant 0 \right\} \quad (3.10)$$

specifies the set of states $|\psi_{\mathbf{n}}\rangle$ for which $|\psi_{\mathbf{n}+\Delta\mathbf{n}}\rangle$ exists. Typically only the lowest-energy states in $\mathrm{orig}(\Delta\mathbf{n})$ contribute appreciably to $\mathcal{I}_{\Delta\mathbf{n}}^{[\mathrm{q}]}(\beta)$.

3.1.2 Classical spectra

As indicated in Section 2.1.3, the classical energy absorption spectrum is given by

$$S_{\mathrm{c}}(\beta; \omega) = \lim_{\hbar \to 0} S_{\mathrm{q}}(\beta; \omega) = |\mathcal{E}|^2 \beta \omega^2 \int_{-\infty}^{\infty} \mathrm{d}t \, \mathrm{e}^{-\mathrm{i}\omega t} c_{\mu\mu}(\beta; t), \quad (3.11)$$

where $c_{\mu\mu}(\beta; t)$ is the classical dipole moment ACF. Eq. (3.11) is useful because the ACF can be computed directly via classical MD simulations, but it does not provide any obvious means by which to partition the spectrum into well-defined bands (as was straightforward in the energy basis of the quantum system). To proceed, we assume that the Hamilton–Jacobi equation is completely separable in $(\mathbf{p}, \mathbf{q})$, such that there exists some set of canonical action-angle

---

[a]However, we will use the term 'band system' in Chapter 4 to refer to a collection of overlapping bands, such as the ν_1/ν_3 band system of gas-phase water.

variables $(\mathbf{J}, \boldsymbol{\phi})$ with actions $\mathbf{J} \equiv (J_1, \ldots, J_F)^{\mathrm{T}}$ defined by

$$J_i = \frac{1}{2\pi} \oint \mathrm{d}q_i p_i, \tag{3.12}$$

where $\oint \mathrm{d}q_i$ implies a line integral over a complete period of the orbit in the (p_i, q_i) plane [124]. The Hamiltonian is independent of the conjugate angles, $\boldsymbol{\phi} \equiv (\phi_1, \ldots, \phi_F)^{\mathrm{T}}$, so may be written as

$$H(\mathbf{p}, \mathbf{q}) = E(\mathbf{J}). \tag{3.13}$$

The classical Liouvillian is thus given by

$$\mathcal{L} = \boldsymbol{\gamma}(\mathbf{J}) \cdot \frac{\partial}{\partial \boldsymbol{\phi}}, \tag{3.14}$$

where

$$\boldsymbol{\gamma}(\mathbf{J}) = \frac{\partial E}{\partial \mathbf{J}}, \tag{3.15}$$

which implies that the angles vary linearly in time according to

$$\mathrm{e}^{\mathcal{L}t} \boldsymbol{\phi} = \boldsymbol{\phi} + \boldsymbol{\gamma}(\mathbf{J})t. \tag{3.16}$$

In general, each of the position variables q_i is implicitly a periodic function of all $\phi_1, \ldots, \phi_F$, with a period of 2π, so may be represented by the Fourier series

$$\mathbf{q} = \sum_{\mathbf{n}} \mathbf{q_n}(\mathbf{J}) \mathrm{e}^{\mathrm{i}\mathbf{n} \cdot \boldsymbol{\phi}} \tag{3.17}$$

and likewise for $\mathbf{p}$. Hence $\boldsymbol{\gamma}(\mathbf{J})$ can be interpreted as the vector of (action-dependent) frequencies that characterise the dynamics. Note that in order for $\mathbf{q}$ to be real, we require $\mathbf{q_n} = \mathbf{q}^*_{-\mathbf{n}}$. The dipole moment, being a function of position, has a similar Fourier series representation,

$$\mu\left(\sum_{\mathbf{n}} \mathbf{q_n}(\mathbf{J}) \mathrm{e}^{\mathrm{i}\mathbf{n} \cdot \boldsymbol{\phi}}\right) = \sum_{\mathbf{n}} \mu_{\mathbf{n}}(\mathbf{J}) \mathrm{e}^{\mathrm{i}\mathbf{n} \cdot \boldsymbol{\phi}}, \tag{3.18}$$

with $\mu_{\mathbf{n}}(\mathbf{J}) = \mu^*_{-\mathbf{n}}(\mathbf{J})$. Using Liouville's theorem (that the Jacobian for a canonical transformation is unity) and Eq. (3.18), the classical dipole moment ACF may be expressed as

$$c_{\mu\mu}(\beta; t) = \frac{1}{\hbar^F Z_{\mathrm{c}}(\beta)} \sum_{\mathbf{n}} \int \mathrm{d}^F \mathbf{J}\, \mathrm{e}^{-\beta E(\mathbf{J})} |\mu_{\mathbf{n}}(\mathbf{J})|^2 \mathrm{e}^{\mathrm{i}\mathbf{n} \cdot \boldsymbol{\gamma}(\mathbf{J})t}, \tag{3.19}$$

and the partition function as

$$Z_{\mathrm{c}}(\beta) = \frac{1}{\hbar^F} \int \mathrm{d}^F \mathbf{J}\, \mathrm{e}^{-\beta E(\mathbf{J})}, \tag{3.20}$$

from which it follows that the classical energy absorption spectrum is given by

$$S_{\mathrm{c}}(\beta;\omega) = \frac{2\pi\beta|\mathcal{E}|^2}{\hbar^F Z_{\mathrm{c}}(\beta)} \sum_{\mathbf{n}} \int \mathrm{d}^F \mathbf{J}\, e^{-\beta E(\mathbf{J})} |\mu_{\mathbf{n}}(\mathbf{J})|^2 [\mathbf{n} \cdot \boldsymbol{\gamma}(\mathbf{J})]^2 \delta(\omega - \mathbf{n} \cdot \boldsymbol{\gamma}(\mathbf{J})). \tag{3.21}$$

Note that the action variables can take only non-negative values, thus $\int \mathrm{d}^F \mathbf{J}$ is shorthand for $\int_0^\infty \mathrm{d}J_1 \ldots \int_0^\infty \mathrm{d}J_F$.

We now note that the action-angle variables $(\mathbf{J}^{(0)}, \boldsymbol{\phi}^{(0)})$ for the unperturbed Hamiltonian, $H^{(0)}(\mathbf{p}, \mathbf{q})$, satisfy the relations

$$p_i = \sqrt{2\Omega_i J_i^{(0)}} \cos\!\left(\phi_i^{(0)}\right) \tag{3.22a}$$

$$q_i = \sqrt{\frac{2J_i^{(0)}}{\Omega_i}} \sin\!\left(\phi_i^{(0)}\right), \tag{3.22b}$$

with

$$H^{(0)}(\mathbf{p}, \mathbf{q}) = E^{(0)}\!\left(\mathbf{J}^{(0)}\right) = \boldsymbol{\Omega} \cdot \mathbf{J}^{(0)}. \tag{3.23}$$

It follows that

$$\boldsymbol{\gamma}(\mathbf{J}) = \boldsymbol{\Omega} + \mathcal{O}(\varepsilon), \tag{3.24}$$

so for small ε, one can partition Eq. (3.21) into bands labelled by the vector of integers $\mathbf{n}$; to emphasise the connection with the quantum mechanical bands defined in Section 3.1.1, we will relabel $\mathbf{n}$ as $\Delta\mathbf{n}$. The classical integrated intensity of a band centred at frequency $\omega_{\Delta\mathbf{n}} \simeq \Delta\mathbf{n} \cdot \boldsymbol{\Omega}$ is thus given by

$$\mathcal{I}_{\Delta\mathbf{n}}^{[\mathrm{c}]}(\beta) = \frac{2\pi\beta|\mathcal{E}|^2}{\hbar^F Z_{\mathrm{c}}(\beta)} \int \mathrm{d}^F \mathbf{J}\, e^{-\beta E(\mathbf{J})} |\mu_{\Delta\mathbf{n}}(\mathbf{J})|^2 [\Delta\mathbf{n} \cdot \boldsymbol{\gamma}(\mathbf{J})]^2. \tag{3.25}$$

3.1.3 Matsubara spectra

We now seek to generalise Eq. (3.25) to Matsubara dynamics. For the time being, we limit the discussion for simplicity to one physical degree of vibrational freedom ($F = 1$). The Matsubara Hamiltonian is then

$$\widetilde{H}_M(\mathbf{P}, \mathbf{Q}) = \widetilde{H}_M^{(0)}(\mathbf{P}, \mathbf{Q}) + \varepsilon \widetilde{U}_M^{(1)}(\mathbf{P}, \mathbf{Q}), \tag{3.26}$$

where

$$\widetilde{H}_M^{(0)}(\mathbf{P}, \mathbf{Q}) = \frac{1}{2} \sum_{k=-\overline{M}}^{\overline{M}} \left(P_k^2 + \Omega^2 Q_k^2\right) \tag{3.27}$$

and

$$\widetilde{U}_M^{(1)}(\mathbf{P}, \mathbf{Q}) = \frac{1}{\beta\hbar} \int_0^{\beta\hbar} \mathrm{d}\tau\, V^{(1)}\!\left(q(\tau)\right). \tag{3.28}$$

Let us assume, similar to the classical system in Section 3.1.2, that there exists a canonical transformation from $(\mathbf{P}, \mathbf{Q})$ to action-angle variables $(\mathcal{J}, \boldsymbol{\varphi})$, such that

$$\mathcal{J}_k = \frac{1}{2\pi} \oint \mathrm{d}Q_k P_k, \tag{3.29}$$

$$\widetilde{H}_M(\mathbf{P}, \mathbf{Q}) = \widetilde{E}_M(\mathcal{J}), \tag{3.30}$$

$$\widetilde{\mathcal{L}}_M = \widetilde{\boldsymbol{\gamma}}_M(\mathcal{J}) \cdot \frac{\partial}{\partial \boldsymbol{\varphi}}, \tag{3.31}$$

$$\widetilde{\theta}_M(\mathbf{P}, \mathbf{Q}) = \widetilde{\Theta}_M(\mathcal{J}, \boldsymbol{\varphi}), \tag{3.32}$$

$$\mathbf{Q} = \sum_{\tilde{\mathbf{n}}} \mathbf{Q}_{\tilde{\mathbf{n}}}(\mathcal{J}) \mathrm{e}^{\mathrm{i}\tilde{\mathbf{n}}\cdot\boldsymbol{\varphi}}, \tag{3.33}$$

and

$$\tilde{\mu}_M\left(\sum_{\tilde{\mathbf{n}}} \mathbf{Q}_{\tilde{\mathbf{n}}}(\mathcal{J}) \mathrm{e}^{\mathrm{i}\tilde{\mathbf{n}}\cdot\boldsymbol{\varphi}}\right) = \sum_{\tilde{\mathbf{n}}} \tilde{\mu}_{M,\tilde{\mathbf{n}}}(\mathcal{J}) \mathrm{e}^{\mathrm{i}\tilde{\mathbf{n}}\cdot\boldsymbol{\varphi}}, \tag{3.34}$$

where

$$\widetilde{\boldsymbol{\gamma}}_M(\mathcal{J}) = \frac{\partial \widetilde{E}_M(\mathbf{J})}{\partial \mathcal{J}}. \tag{3.35}$$

The indices $\tilde{\mathbf{n}} \equiv (\tilde{n}_{-\overline{M}}, \ldots, \tilde{n}_{\overline{M}})^{\mathrm{T}}$ take non-negative integer values. The Matsubara dipole moment ACF is then given by

$$\widetilde{C}_{\mu\mu}^{[M]}(\beta; t) = \frac{\alpha_M}{2\pi\hbar\widetilde{Z}_M(\beta)} \sum_{\tilde{\mathbf{n}},\tilde{\mathbf{n}}'} \int \mathrm{d}^M\mathcal{J} \int \mathrm{d}^M\boldsymbol{\varphi} \, \mathrm{e}^{-\beta[\widetilde{E}_M(\mathcal{J})+\mathrm{i}\widetilde{\Theta}_M(\mathcal{J},\boldsymbol{\varphi})]}$$
$$\times \tilde{\mu}_{M,\tilde{\mathbf{n}}'}^*(\mathcal{J})\tilde{\mu}_{M,\tilde{\mathbf{n}}}(\mathcal{J})\mathrm{e}^{\mathrm{i}(\tilde{\mathbf{n}}-\tilde{\mathbf{n}}')\cdot\boldsymbol{\varphi}}\mathrm{e}^{\mathrm{i}\tilde{\mathbf{n}}\cdot\widetilde{\boldsymbol{\gamma}}_M(\mathcal{J})t}, \tag{3.36}$$

with

$$\widetilde{Z}_M(\beta) = \frac{\alpha_M}{2\pi\hbar} \sum_{\tilde{\mathbf{n}},\tilde{\mathbf{n}}'} \int \mathrm{d}^M\mathcal{J} \int \mathrm{d}^M\boldsymbol{\varphi} \, \mathrm{e}^{-\beta[\widetilde{E}_M(\mathcal{J})+\mathrm{i}\widetilde{\Theta}_M(\mathcal{J},\boldsymbol{\varphi})]}, \tag{3.37}$$

from which it follows that the energy absorption spectrum is given by

$$S_M(\beta; \omega) = \frac{\alpha_M\beta|\mathcal{E}|^2}{\hbar\widetilde{Z}_M(\beta)} \sum_{\tilde{\mathbf{n}},\tilde{\mathbf{n}}'} \int \mathrm{d}^M\mathcal{J} \int \mathrm{d}^M\boldsymbol{\varphi} \, \mathrm{e}^{-\beta[\widetilde{E}_M(\mathcal{J})+\mathrm{i}\widetilde{\Theta}_M(\mathcal{J},\boldsymbol{\varphi})]}$$
$$\times \tilde{\mu}_{M,\tilde{\mathbf{n}}'}^*(\mathcal{J})\tilde{\mu}_{M,\tilde{\mathbf{n}}}(\mathcal{J})\mathrm{e}^{\mathrm{i}(\tilde{\mathbf{n}}-\tilde{\mathbf{n}}')\cdot\boldsymbol{\varphi}}\left[\tilde{\mathbf{n}} \cdot \widetilde{\boldsymbol{\gamma}}_M(\mathcal{J})\right]^2\delta\left(\omega - \tilde{\mathbf{n}} \cdot \widetilde{\boldsymbol{\gamma}}_M(\mathcal{J})\right). \tag{3.38}$$

Analogous to the classical system, the action-angle variables $(\mathcal{J}^{(0)}, \boldsymbol{\varphi}^{(0)})$ for the unperturbed Matsubara Hamiltonian, $\widetilde{H}_M^{(0)}(\mathbf{P}, \mathbf{Q})$, satisfy

$$P_k = \sqrt{2\Omega\mathcal{J}^{(0)}} \cos\left(\varphi_k^{(0)}\right) \tag{3.39a}$$

$$Q_k = \sqrt{\frac{2\mathcal{J}_k^{(0)}}{\Omega}} \sin\!\left(\varphi_k^{(0)}\right), \tag{3.39b}$$

with

$$\widetilde{H}_M^{(0)}(\mathbf{P}, \mathbf{Q}) = \widetilde{E}^{(0)}\!\left(\mathcal{J}^{(0)}\right) = \Omega \sum_{k=-\overline{M}}^{\overline{M}} \mathcal{J}_k^{(0)}. \tag{3.40}$$

It follows that

$$\widetilde{\boldsymbol{\gamma}}_M(\mathcal{J}) = (\Omega, \ldots, \Omega)^{\mathrm{T}} + \mathcal{O}(\varepsilon), \tag{3.41}$$

so for small ε, one can partition Eq. (3.38) into bands by recognising that the only terms contributing to the Δn band must satisfy $\tilde{\mathbf{n}} \in \mathrm{tot}_M(\Delta n)$, where

$$\mathrm{tot}_M(\Delta n) = \left\{ \tilde{\mathbf{n}} \;\middle|\; \sum_{k=-\overline{M}}^{\overline{M}} \tilde{n}_k = \Delta n \right\}. \tag{3.42}$$

The integrated absorption intensity is therefore given by

$$\begin{aligned}
\mathcal{I}_{\Delta n}^{[M]}(\beta) = \frac{\alpha_M \beta |\mathcal{E}|^2}{\hbar \widetilde{Z}_M(\beta)} \sum_{\tilde{\mathbf{n}} \in \mathrm{tot}_M(\Delta n)} \sum_{\tilde{\mathbf{n}}'} \int \mathrm{d}^M \mathcal{J} \int \mathrm{d}^M \boldsymbol{\varphi} \; \mathrm{e}^{-\beta[\widetilde{E}_M(\mathcal{J}) + \mathrm{i}\widetilde{\Theta}_M(\mathcal{J}, \boldsymbol{\varphi})]} \\
\times \tilde{\mu}_{M,\tilde{\mathbf{n}}'}^*(\mathcal{J}) \tilde{\mu}_{M,\tilde{\mathbf{n}}}(\mathcal{J}) \mathrm{e}^{\mathrm{i}(\tilde{\mathbf{n}} - \tilde{\mathbf{n}}') \cdot \boldsymbol{\varphi}} \big[\tilde{\mathbf{n}} \cdot \widetilde{\boldsymbol{\gamma}}_M(\mathcal{J})\big]^2.
\end{aligned} \tag{3.43}$$

Because of the dependence of the Matsubara phase on $\boldsymbol{\varphi}$, Eq. (3.43) has a form considerably more complicated than its classical counterpart, Eq. (3.25). We can simplify it slightly knowing that the phase is a constant of the motion, which implies that all finite-frequency Fourier components of the Matsubara distribution must vanish. The only non-vanishing terms in Eq. (3.43) must therefore satisfy $\tilde{\mathbf{n}} - \tilde{\mathbf{n}}' \in \mathrm{tot}_M(0) \implies \tilde{\mathbf{n}}' \in \mathrm{tot}_M(\Delta n)$, giving

$$\begin{aligned}
\mathcal{I}_{\Delta n}^{[M]}(\beta) = \frac{\alpha_M \beta |\mathcal{E}|^2}{\hbar \widetilde{Z}_M(\beta)} \sum_{\tilde{\mathbf{n}}, \tilde{\mathbf{n}}' \in \mathrm{tot}_M(\Delta n)} \int \mathrm{d}^M \mathcal{J} \int \mathrm{d}^M \boldsymbol{\varphi} \; \mathrm{e}^{-\beta[\widetilde{E}_M(\mathcal{J}) + \mathrm{i}\widetilde{\Theta}_M(\mathcal{J}, \boldsymbol{\varphi})]} \\
\times \tilde{\mu}_{M,\tilde{\mathbf{n}}'}^*(\mathcal{J}) \tilde{\mu}_{M,\tilde{\mathbf{n}}}(\mathcal{J}) \mathrm{e}^{\mathrm{i}(\tilde{\mathbf{n}} - \tilde{\mathbf{n}}') \cdot \boldsymbol{\varphi}} \big[\tilde{\mathbf{n}} \cdot \widetilde{\boldsymbol{\gamma}}_M(\mathcal{J})\big]^2.
\end{aligned} \tag{3.44}$$

Setting $M = 1$ in Eq. (3.44) recovers the classical result i.e., $\mathcal{I}_{\Delta n}^{[1]}(\beta) \equiv \mathcal{I}_{\Delta n}^{[\mathrm{c}]}(\beta)$.

3.2 Perturbative evaluation of integrated absorption intensities

3.2.1 Choice of potential energy and dipole moment surfaces

Our primary objective is to assess the ability of classical and path integral–based approaches to capture non-fundamental bands in vibrational spectra; using the terminology of Section 3.1.1, these are defined by the condition $\|\Delta\mathbf{n}\|_1 > 1$, where $\|\ldots\|_1$ denotes the ℓ^1 or 'taxicab' norm.[b] For simplicity, we limit our discussion to $\|\Delta\mathbf{n}\|_1 = 2$ bands, which are usually expected to be the most intense (aside from fundamental bands). They include:

- first overtone bands, where a single oscillator is doubly excited;

- binary combination bands, where two different oscillators are singly excited;

- binary difference bands, where one oscillator is singly excited and another is singly de-excited.

Of these, difference bands tend to be the least intense, since they necessarily involve only transitions from excited states (i.e., they are always 'hot bands').

In Section 3.1, we specified that our PES is weakly anharmonic, which allowed us to meaningfully partition the absorption spectrum into distinct bands indexed by the change in quantum numbers, $\Delta\mathbf{n}$. We can also split the DMS into linear and nonlinear components according to

$$\mu(\mathbf{q}) = \mu^{(0)}(\mathbf{q}) + \varepsilon\mu^{(1)}(\mathbf{q}), \tag{3.45}$$

where

$$\mu^{(0)}(\mathbf{q}) = \mu_0 + \boldsymbol{\xi} \cdot \mathbf{q}, \tag{3.46}$$

in which μ_0 is the permanent dipole contribution (which has no effect on the IR spectrum), $\boldsymbol{\xi} \equiv (\xi_1, \ldots, \xi_F)^{\mathrm{T}}$ has dimensions of charge, and $\mu^{(1)}$ is a function in which the leading-order terms are at least quadratic. This nonlinearity in the DMS is sometimes called *electrical anharmonicity*. Making the assumption that this is small, we have factored out the constant ε, just as we did in Eq. (3.1) to emphasise the smallness of the *mechanical* anharmonicity in the PES. While fundamental bands are observable in the absence of any type of anharmonicity (i.e., in the limit $\varepsilon \to 0$), the leading-order contributions to $\|\Delta\mathbf{n}\|_1 = 2$ bands are from cubic terms in the PES and/or quadratic terms in the DMS. We will restrict out discussions to such

---

[b]In contrast, $|\ldots|$ is used in this work to denote (of a vector) the ℓ^2 or Euclidean norm, which may also be written as $\|\ldots\|_2$.

contributions, assuming the perturbations

$$V^{(1)}(\mathbf{q}) = \frac{1}{6} \sum_{i=1}^{F} \sum_{j=1}^{F} \sum_{k=1}^{F} \eta_{ijk} q_i q_j q_k \tag{3.47}$$

and

$$\mu^{(1)}(\mathbf{q}) = \frac{1}{2} \sum_{i=1}^{F} \sum_{j=1}^{F} \kappa_{ij} q_i q_j, \tag{3.48}$$

where constants η_{ijk} and κ_{ij} are the elements of symmetric tensors.

3.2.2 Quantum spectra

Following standard non-degenerate Rayleigh–Schrödinger perturbation theory (PT), the eigenvalues and eigenkets of $\hat{H}$ are expanded as power series in ε,

$$E_{\mathbf{n}} = \sum_{\alpha=0}^{\infty} \varepsilon^{\alpha} E_{\mathbf{n}}^{(\alpha)} \tag{3.49a}$$

$$|\psi_{\mathbf{n}}\rangle = \sum_{\alpha=0}^{\infty} \varepsilon^{\alpha} |\psi_{\mathbf{n}}^{(\alpha)}\rangle, \tag{3.49b}$$

where we recall that $E_{\mathbf{n}}^{(0)}$ and $|\psi_{\mathbf{n}}^{(0)}\rangle \equiv |\mathbf{n}\rangle$ are the energy eigenvalues and eigenkets for the harmonic reference system (see Eq. (3.4–3.6)), and we impose the orthonormality condition $\langle \psi_{\mathbf{n}}^{(\alpha)} | \psi_{\mathbf{n}}^{(\alpha')} \rangle = \delta_{\alpha\alpha'}$ without loss of generality [123]. We will only be concerned here with the first-order corrections, given by

$$E_{\mathbf{n}}^{(1)} = \langle \mathbf{n} | \hat{V}^{(1)} | \mathbf{n} \rangle \tag{3.50}$$

and

$$|\psi_{\mathbf{n}}^{(1)}\rangle = \sum_{\mathbf{n}' \neq \mathbf{n}} \frac{|\mathbf{n}'\rangle \langle \mathbf{n}' | \hat{V}^{(1)} | \mathbf{n} \rangle}{\hbar(\mathbf{n} - \mathbf{n}') \cdot \mathbf{\Omega}}. \tag{3.51}$$

Assuming the PES and DMS specified in Section 3.2.1, we show in Appendix B.1 that, for a $\|\Delta \mathbf{n}\|_1 = 2$ band, Eq. (3.9) for the integrated intensity reduces to

$$\mathcal{I}_{v_i \pm v_j}^{[\mathrm{q}]} = \varepsilon^2 I_{v_i \pm v_j}^{[\mathrm{q}]} + O(\varepsilon^3), \tag{3.52}$$

where

$$I_{v_i \pm v_j}^{[\mathrm{q}]}(\beta) = C_{ij}(\boldsymbol{\eta}, \boldsymbol{\xi}, \boldsymbol{\kappa}, \mathbf{\Omega}) \tilde{I}^{[\mathrm{q}]}(\beta; \Omega_i, \pm \Omega_j), \tag{3.53}$$

in which

$$\tilde{I}^{[\text{q}]}(\beta; \Omega_i, \Omega_j) = \frac{\pi|\mathcal{E}|^2 \hbar (\Omega_i + \Omega_j)}{2\Omega_i \Omega_j} \left[\coth\left(\frac{\beta \hbar \Omega_i}{2}\right) + \coth\left(\frac{\beta \hbar \Omega_j}{2}\right) \right] \tag{3.54}$$

and

$$C_{ij}(\boldsymbol{\eta}, \boldsymbol{\xi}, \boldsymbol{\kappa}, \boldsymbol{\Omega}) = \frac{2 - \delta_{ij}}{4} \left[\kappa_{ij} + \sum_{k=1}^{F} \frac{\eta_{ijk}\xi_k}{(\Omega_i \pm \Omega_j)^2 - \Omega_k^2} \right]^2. \tag{3.55}$$

Eq. (3.53) applies to overtone ($2\nu_i$), combination ($\nu_i + \nu_j$), and difference ($\nu_i - \nu_j$) bands, and is equivalent to the result obtained in 1976 by Yao and Overend using Van Vleck canonical transformations (the quantum analogue of classical canonical PT; see Section 3.2.3) [149]. The special case of a mechanically harmonic system was treated earlier by Breeze *et al.* [109]. Interestingly, the scaling of the intensity with respect to temperature is governed entirely by the functional form of $\tilde{I}^{[\text{q}]}(\beta; \Omega_i, \Omega_j)$; it is independent of whether the anharmonicity is mechanical, electrical, or both.

3.2.3 Classical spectra

The classical expression for the second-order intensity can be easily obtained by taking the $\hbar \to 0$ limit of Eq. (3.54),

$$\tilde{I}^{[\text{c}]}(\beta; \Omega_i, \Omega_j) = \lim_{\hbar \to 0} \tilde{I}^{[\text{q}]}(\beta; \Omega_i, \Omega_j) = \frac{\pi|\mathcal{E}|^2 (\Omega_i + \Omega_j)^2}{\beta \Omega_i^2 \Omega_j^2}. \tag{3.56}$$

However, it will be instructive to derive this result directly from the classical equations of motion, using classical canonical PT (CPT) as summarised in Appendix A.2.

It is evident that the Fourier components of the dipole moment for $\|\Delta\mathbf{n}\|_1 > 1$ must satisfy $|\mu_{\Delta\mathbf{n}}(\mathbf{J})|^2 = O(\varepsilon^2)$. Thus, for non-fundamental bands, Eq. (3.25) simplifies to

$$I_{\Delta\mathbf{n}}^{[\text{c}]}(\beta) = \varepsilon^2 I_{\Delta\mathbf{n}}^{[\text{c}]}(\beta) + O(\varepsilon^3), \tag{3.57}$$

where

$$I_{\Delta\mathbf{n}}^{[\text{c}]}(\beta) = \frac{2\pi|\mathcal{E}|^2 \beta (\Delta\mathbf{n} \cdot \boldsymbol{\Omega})^2}{\hbar^F Z_{\text{c}}^{(0)}(\beta)} \int d^F\mathbf{J} \, e^{-\beta\boldsymbol{\Omega}\cdot\mathbf{J}} \lim_{\varepsilon \to 0} \frac{1}{\varepsilon^2} |\mu_{\Delta\mathbf{n}}(\mathbf{J})|^2, \tag{3.58}$$

and

$$Z_{\text{c}}^{(0)}(\beta) = \prod_{i=1}^{F} \frac{1}{\beta \hbar \Omega_i} \tag{3.59}$$

is the zeroth-order classical partition function. Because the distribution in Eq. (3.58) is factorisable into independent contributions from each oscillator, the expression is easily generalised to a multiple-temperature scenario, in which each oscillator (J_i, ϕ_i) is prepared at its own temperature $T_i = 1/(k_B \beta_i)$. The relevance of such a setup will become clear in Section 3.3. The zeroth-order partition function becomes

$$Z_c^{(0)}(\mathbf{B}) = \prod_{i=1}^{F} \frac{1}{\beta_i \hbar \Omega_i} \tag{3.60}$$

and in the integrand of Eq. (3.58) we make the replacement

$$e^{-\beta \mathbf{\Omega} \cdot \mathbf{J}} \rightarrow e^{-\mathbf{B} \mathbf{\Omega} \cdot \mathbf{J}}, \tag{3.61}$$

where $\mathbf{B} = \text{diag}(\beta_1, \ldots, \beta_F)$. To take care of the frequency-dependent prefactor, we recognise its origin as being the classical limit of the $\omega(1 - e^{-\beta \hbar \omega})$ prefactor that appears in Eq. (2.48) to account for detailed balance. Hence the replacement that we need to make is

$$\beta(\Delta \mathbf{n} \cdot \mathbf{\Omega})^2 \rightarrow \lim_{\hbar \to 0} \frac{1}{\hbar} \Delta \mathbf{n} \cdot \mathbf{\Omega} \left(1 - e^{-\hbar \Delta \mathbf{n} \cdot \mathbf{B} \mathbf{\Omega}}\right) = (\Delta \mathbf{n} \cdot \mathbf{\Omega})(\Delta \mathbf{n} \cdot \mathbf{B} \mathbf{\Omega}). \tag{3.62}$$

The second-order, multiple-temperature classical intensity is therefore given by

$$I_{\Delta \mathbf{n}}^{[c]}(\mathbf{B}) = \frac{2\pi |\mathcal{E}|^2 (\Delta \mathbf{n} \cdot \mathbf{\Omega})(\Delta \mathbf{n} \cdot \mathbf{B} \mathbf{\Omega})}{\hbar^F Z_c^{(0)}(\mathbf{B})} \int d^F \mathbf{J} \, e^{-\mathbf{B} \mathbf{\Omega} \cdot \mathbf{J}} \lim_{\varepsilon \to 0} \frac{1}{\varepsilon^2} |\mu_{\Delta \mathbf{n}}(\mathbf{J})|^2. \tag{3.63}$$

In Appendix B.2, we show that classical CPT gives the position coordinate of oscillator i expanded to first order as

$$
\begin{aligned}
q_i = &\sqrt{\frac{2J_i}{\Omega_i}} \sin(\phi_i) \\
&- \frac{\varepsilon}{2} \sum_{j=1}^{F} \sum_{k=1}^{F} \eta_{ijk} \sqrt{\frac{J_j J_k}{\Omega_j \Omega_k}} \left[\frac{\cos(\phi_j + \phi_k)}{(\Omega_j + \Omega_k)^2 - \Omega_i^2} - \frac{\cos(\phi_j - \phi_k)}{(\Omega_j - \Omega_k)^2 - \Omega_i^2} \right] + O(\varepsilon^2).
\end{aligned}
\tag{3.64}
$$

Substituting Eq. (3.64) into the dipole moment (given by Eq. (3.45) with Eqs. (3.46) and (3.48)), then substituting the resultant expression into Eq. (3.63), yields

$$I_{\nu_i \pm \nu_j}^{[c]}(\mathbf{B}) = \frac{2\pi |\mathcal{E}|^2 (\Omega_i \pm \Omega_j)(\beta_i \Omega_i \pm \beta_j \Omega_j)}{\hbar^F \Omega_i \Omega_j Z_c^{(0)}(\mathbf{B})} \frac{2 - \delta_{ij}}{4} C_{ij}(\boldsymbol{\eta}, \boldsymbol{\xi}, \boldsymbol{\kappa}, \boldsymbol{\Omega}) \int d^F \mathbf{J} \, e^{-\mathbf{B} \mathbf{\Omega} \cdot \mathbf{J}} J_i J_j \tag{3.65}$$

$$= C_{ij}(\boldsymbol{\eta}, \boldsymbol{\xi}, \boldsymbol{\kappa}, \boldsymbol{\Omega}) \tilde{I}^{[c]}(\mathbf{B}; \Omega_i, \pm \Omega_j) \tag{3.66}$$

for a general $\|\Delta\mathbf{n}\|_1 = 2$ band, where

$$\tilde{I}^{[\mathrm{c}]}(\mathbf{B};\Omega_i,\Omega_j) = \frac{\pi|\mathcal{E}|^2(\Omega_i+\Omega_j)(\beta_i\Omega_i+\beta_j\Omega_j)}{\beta_i\beta_j\Omega_i^2\Omega_j^2}. \tag{3.67}$$

This reduces to Eq. (3.56) in the single-temperature case, $\mathbf{B} = \beta\mathbf{I}$, which was derived independently by Plé *et al.* using an alternative formulation of classical PT based on a Dyson series expansion of the classical propagator, $\mathrm{e}^{\mathcal{L}t}$ [65].

3.2.4   Matsubara spectra

Here we introduce 'Matsubara CPT', which is just the special case of classical CPT applied to the Matsubara Hamiltonian. Let

$$\widetilde{Y}_M\big(\mathbf{J},\boldsymbol{\varphi}^{(0)}\big) = \sum_{\alpha=0}^{\infty} \varepsilon^\alpha \widetilde{Y}_M^{(\alpha)}\big(\mathbf{J},\boldsymbol{\varphi}^{(0)}\big) \tag{3.68}$$

be the Matsubara analogue of $Y(\mathbf{J},\boldsymbol{\phi}^{(0)})$ defined in Appendix A.2, with

$$\widetilde{Y}_M^{(\alpha)}\big(\mathbf{J},\boldsymbol{\varphi}^{(0)}\big) = \sum_{\tilde{\mathbf{n}}} \widetilde{Y}_{M,\tilde{\mathbf{n}}}^{(\alpha)}(\mathcal{J})\mathrm{e}^{\mathrm{i}\tilde{\mathbf{n}}\cdot\boldsymbol{\varphi}^{(0)}}, \tag{3.69}$$

and likewise let

$$\overline{\widetilde{U}}_M^{(1)}\big(\mathcal{J}^{(0)},\boldsymbol{\varphi}^{(0)}\big) = \sum_{\tilde{\mathbf{n}}} \overline{\widetilde{U}}_{M,\tilde{\mathbf{n}}}^{(1)}\big(\mathcal{J}^{(0)}\big)\mathrm{e}^{\mathrm{i}\tilde{\mathbf{n}}\cdot\boldsymbol{\varphi}^{(0)}} \tag{3.70}$$

be the Matsubara analogue of $\overline{V}^{(1)}(\mathbf{J}^{(0)},\boldsymbol{\phi}^{(0)})$. The formulation of Matsubara CPT could potentially be complicated by the fact that

$$\frac{\partial\widetilde{E}_M^{(0)}\big(\mathcal{J}^{(0)}\big)}{\partial\mathcal{J}_k^{(0)}} = \Omega \tag{3.71}$$

is the same for all $k \in \{-\overline{M},\dots,\overline{M}\}$, meaning the reference system is degenerate. The arguments outlined in Appendix A.2 can thus formally break down, with the first-order Fourier coefficients of the generating function,

$$\widetilde{Y}_{M,\tilde{\mathbf{n}}}^{(1)}(\mathcal{J}) = \frac{\mathrm{i}}{\Omega}\left(\sum_{k=-\overline{M}}^{\overline{M}} \tilde{n}_k\right)^{-1}\overline{\widetilde{U}}_{M,\tilde{\mathbf{n}}}^{(1)}(\mathcal{J}), \tag{3.72}$$

becoming undefined when $\tilde{\mathbf{n}} \in \text{tot}_M(0)$. However, for cubic perturbations to the potential, we will find that

$$\forall \tilde{\mathbf{n}} \in \text{tot}_M(0), \overline{\widetilde{U}}^{(1)}_{M,\tilde{\mathbf{n}}}(\mathbf{J}) = 0, \tag{3.73}$$

implying that the resonances are only manifested at second order in ε. In the present work, we are concerned only with first-order corrections to the dynamical variables, so it is justified to proceed as if the system were non-resonant. The corresponding zero-frequency components of the generating function will be undetermined in principle, but each of them produces only a constant phase shift and can thus be set to zero without loss of generality i.e.,

$$\forall \tilde{\mathbf{n}} \in \text{tot}_M(0), \widetilde{Y}^{(1)}_{M,\tilde{\mathbf{n}}}(\mathbf{J}) = 0. \tag{3.74}$$

Another important result, shown in Appendix B.3.1, is that the first-order perturbation to the Matsubara phase vanishes. That is,

$$\widetilde{\Theta}_M(\mathcal{J}, \boldsymbol{\varphi}) = \widetilde{\Theta}^{(0)}_M(\mathcal{J}, \boldsymbol{\varphi}) + O(\varepsilon^2), \tag{3.75}$$

where

$$\widetilde{\Theta}^{(0)}_M\big(\mathcal{J}^{(0)}, \boldsymbol{\varphi}^{(0)}\big) = \overline{\theta}_M(\mathbf{P}, \mathbf{Q}) = -2 \sum_{k=1}^{\overline{M}} \omega_k \sqrt{\mathcal{J}^{(0)}_k \mathcal{J}^{(0)}_{-k}} \sin\big(\varphi^{(0)}_k - \varphi^{(0)}_{-k}\big). \tag{3.76}$$

In the case of a cubic perturbation to the potential, we also have $\widetilde{E}_M(\mathcal{J}) = \widetilde{E}^{(0)}_M(\mathcal{J}) + O(\varepsilon^2)$, hence Eq. (3.43) can be expanded to second order as

$$I^{[M]}_{\Delta n}(\beta) = \varepsilon^2 I^{[M]}_{\Delta n}(\beta) + O(\varepsilon^3), \tag{3.77}$$

where

$$I^{[M]}_{\Delta n}(\beta) = \frac{\alpha_M \beta |\mathcal{E}|^2 (\Delta n \Omega)^2}{\hbar \widetilde{Z}^{(0)}_M(\beta)} \sum_{\tilde{\mathbf{n}}', \tilde{\mathbf{n}} \in \text{tot}_M(\Delta n)} \int d^M \mathcal{J} \int d^M \boldsymbol{\varphi}$$
$$\times e^{i(\tilde{\mathbf{n}} - \tilde{\mathbf{n}}') \cdot \boldsymbol{\varphi}} e^{-\beta[\widetilde{E}^{(0)}_M(\mathcal{J}) + i\widetilde{\Theta}^{(0)}_M(\mathcal{J}, \boldsymbol{\varphi})]} \lim_{\varepsilon \to 0} \frac{1}{\varepsilon^2} \tilde{\mu}^*_{M,\tilde{\mathbf{n}}'}(\mathcal{J}) \tilde{\mu}_{M,\tilde{\mathbf{n}}}(\mathcal{J}) \tag{3.78}$$

and

$$\widetilde{Z}^{(0)}_M(\beta) = \frac{\alpha_M}{\beta \hbar \Omega} \prod_{k=1}^{\overline{M}} \frac{4\pi^2}{\beta^2 (\Omega^2 + \omega_k^2)}. \tag{3.79}$$

If the perturbation is specifically given by

$$V^{(1)}(q) = \frac{\eta}{6} q^3, \tag{3.80}$$

which is the $F = 1$ case of Eq. (3.47), then the corresponding perturbation to the Matsubara potential is

$$\widetilde{U}_M^{(1)}(\mathbf{P}, \mathbf{Q}) = \frac{\eta}{6}Q_0^3 + \frac{\eta}{2}Q_0 \sum_{0 < |k| \leqslant \overline{M}} Q_k^2 + \dots, \tag{3.81}$$

where '...' has been used to denote a sum of centroid-independent terms (see Appendix B.3.2 for the full expression). Expressed in terms of 'old' action-angle variables, Eq. (3.81) becomes

$$\overline{\widetilde{U}}_M^{(1)}\left(\mathcal{J}^{(0)}, \boldsymbol{\varphi}^{(0)}\right) = \widetilde{U}_M^{(1)}(\mathbf{P}, \mathbf{Q})$$

$$= \eta\sqrt{\frac{2\left(\mathcal{J}_0^{(0)}\right)^3}{9\Omega^3}} \sin^3\left(\varphi_0^{(0)}\right) + \eta\sqrt{\frac{2\mathcal{J}_0^{(0)}}{\Omega^3}} \sin\left(\varphi_0^{(0)}\right) \sum_{0 < |k| \leqslant \overline{M}} \mathcal{J}_k^{(0)} \sin^2\left(\varphi_k^{(0)}\right) + \dots, \tag{3.82}$$

Following the standard CPT procedure of Appendix A.2, we find

$$\mathcal{J}_0^{(0)} = \mathcal{J}_0 - \varepsilon\eta\sqrt{\frac{\mathcal{J}_0}{72\Omega^5}} \sum_{k=-\overline{M}}^{\overline{M}} \mathcal{J}_k \left[6\sin(\varphi_0) - \sin(\varphi_0 + 2\varphi_k) + 3\sin(\varphi_0 - 2\varphi_k)\right] + O(\varepsilon^2) \tag{3.83a}$$

$$\varphi_0^{(0)} = \varphi_0 - \frac{\varepsilon\eta}{\sqrt{288\Omega^5\mathcal{J}_0}} \sum_{k=-\overline{M}}^{\overline{M}} \mathcal{J}_k \left[6\cos(\varphi_0) - \cos(\varphi_0 + 2\varphi_k) + 3\cos(\varphi_0 - 2\varphi_k)\right] + O(\varepsilon^2), \tag{3.83b}$$

which gives

$$Q_0 = \sqrt{\frac{2\mathcal{J}_0}{\Omega}} \sin(\varphi_0) - \frac{\varepsilon\eta}{6\Omega^3} \sum_{k=-\overline{M}}^{\overline{M}} \mathcal{J}_k \left[\cos(2\varphi_k) + 3\right] + O(\varepsilon^2). \tag{3.84}$$

This shows that all the Matsubara modes $Q_{-\overline{M}}, \dots, Q_{\overline{M}}$ make equal contributions to the overtone component of Q_0. This symmetric dependence could perhaps have been anticipated from the form of the perturbative force on the centroid,

$$-\frac{\partial\widetilde{U}_M^{(1)}(\mathbf{Q})}{\partial Q_0} = -\frac{\eta}{2} \sum_{k=-\overline{M}}^{\overline{M}} Q_k^2. \tag{3.85}$$

The intensity of the first overtone ($\Delta n = 2$) band is obtained by substituting Eq. (3.84) into the dipole moment estimator

$$\tilde{\mu}_M(\mathbf{Q}) = \mu_0 + \xi Q_0 + \frac{\varepsilon\kappa}{2} \sum_{k=-\overline{M}}^{\overline{M}} Q_k^2, \tag{3.86}$$

then substituting the resultant expression into Eq. (3.78), leading to

$$I_{2\nu}^{[M]}(\beta) = \frac{\alpha_M \beta |\mathcal{E}|^2}{4\hbar\Omega^4 \widetilde{Z}_M^{(0)}(\beta)} \left(\frac{\eta\xi}{3} + \kappa\Omega^2\right)^2$$
$$\times \sum_{k=-\overline{M}}^{\overline{M}} \sum_{k'=-\overline{M}}^{\overline{M}} \int d^M \mathcal{J} \int d^M \boldsymbol{\varphi} \, e^{-\beta[\widetilde{E}_M^{(0)}(\mathcal{J})+i\widetilde{\Theta}_M^{(0)}(\mathcal{J},\boldsymbol{\varphi})]} e^{2i(\varphi_k - \varphi_{k'})} J_k J_{k'}. \tag{3.87}$$

To make progress towards evaluating this integral, by analogy with Eq. (3.39) we define

$$\Pi_k = \sqrt{2\Omega\mathcal{J}_k} \cos(\varphi_k), \tag{3.88a}$$

$$X_k = \sqrt{\frac{2\mathcal{J}_k}{\Omega}} \sin(\varphi_k), \tag{3.88b}$$

which satisfy $(\Pi_k, X_k) = (P_k, Q_k) + O(\varepsilon)$. The overtone intensity is then given by

$$I_{2\nu}^{[M]}(\beta) = \frac{\alpha_M \eta^2 \xi^2 \beta |\mathcal{E}|^2}{16\hbar\Omega^5 \widetilde{Z}_M^{(0)}(\beta)} \left(\frac{\eta\xi}{3} + \kappa\Omega^2\right)^2$$
$$\times \sum_{k=-\overline{M}}^{\overline{M}} \sum_{k'=-\overline{M}}^{\overline{M}} \int d^M \boldsymbol{\Pi} \int d^M \mathbf{X} \, e^{-\beta[\widetilde{H}_M^{(0)}(\boldsymbol{\Pi},\mathbf{X})+i\widetilde{\theta}_M(\boldsymbol{\Pi},\mathbf{X})]} \left(\Pi_k + i\Omega X_k\right)^2 \left(\Pi_{k'} - i\Omega X_{k'}\right)^2. \tag{3.89}$$

This is straightforward to evaluate by analytically continuing each $\overline{\Pi}_k = \Pi_k + i\omega_k X_{-k}$ onto the real axis, giving

$$I_{2\nu}^{[M]}(\beta) = \frac{\pi|\mathcal{E}|}{\beta\Omega^6} \left(\frac{\eta\xi}{3} + \kappa\Omega^2\right)^2 \sum_{k=-\overline{M}}^{\overline{M}} \frac{\Omega^2}{\Omega^2 + \omega_k^2}. \tag{3.90}$$

In Appendix B.3.2, we show that the mean-field Matsubara potential, $\widetilde{\mathcal{F}}_M(\mathbf{Q})$, is equivalent to the truncated Matsubara potential, $\widetilde{U}_M(\mathbf{Q})$, up to $O(\varepsilon)$ for a one-dimensional oscillator with only cubic anharmonicity. It follows that the arguments presented above leading to Eq. (3.90) are equally applicable to both formalisms. In Appendix B.3.3, we show how one can generalise Eq. (3.90) to the system of F coupled oscillators defined in Section 3.2.1, leading to the expression

$$I_{\nu_i \pm \nu_j}^{[M]}(\beta) = I_{\nu_i \pm \nu_j}^{[c]}(\mathbf{B}^{[M]}) \tag{3.91}$$

for a general $\|\Delta\mathbf{n}\|_1 = 2$ band, where we have defined

$$\frac{1}{\beta_i^{[M]}} = \frac{1}{\beta} \sum_{k=-\overline{M}}^{\overline{M}} \frac{\Omega_i^2}{\Omega_i^2 + \omega_k^2} \tag{3.92}$$

and $\mathbf{B}^{[M]} = \mathrm{diag}(\beta_1^{[M]}, \ldots, \beta_F^{[M]})$.

3.3　The physical interpretation: 'Matsubara heating'

Eq. (3.91) can be interpreted as follows: the Matsubara intensity of a $\|\Delta\mathbf{n}\|_1 = 2$ band at temperature $T = 1/(k_B\beta)$ is equal (to leading order) to the corresponding classical intensity with the oscillators prepared at the Matsubara *effective* temperatures $T_i^{[M]} = 1/(k_B\beta_i^{[M]})$. In the limit $M \to \infty$, these tend to the quantum effective temperatures $T_i^{[\infty]} = 1/(k_B\beta_i^{[\infty]})$, where

$$\frac{1}{\beta_i^{[\infty]}} = \lim_{M \to \infty} \frac{1}{\beta_i^{[M]}} = \frac{\hbar\Omega_i}{2} \coth\left(\frac{\beta\hbar\Omega_i}{2}\right). \tag{3.93}$$

Matsubara dynamics thus converges to the exact quantum intensity,

$$\lim_{M \to \infty} I_{\nu_i \pm \nu_j}^{[M]}(\beta) = I_{\nu_i \pm \nu_j}^{[c]}(\mathbf{B}^{[\infty]}) = I_{\nu_i \pm \nu_j}^{[q]}(\beta), \tag{3.94}$$

as also shown by Plé *et al.* using the Dyson series approach to classical PT [65]. In what follows, we rationalise this 'Matsubara heating' behaviour, by inspecting more closely the effect of perturbing a single Matsubara oscillator as described in Section 3.2.4.

3.3.1　Matsubara mode picture

Consider again Eq. (3.84), which gives the centroid coordinate Q_0 in terms of the perturbed action-angle variables $(\mathcal{J}, \boldsymbol{\varphi})$. To zeroth order, every $\cos(2\varphi_k)$ term oscillates at the overtone frequency 2Ω. The total, thermally averaged amplitude of the centroid overtone vibrations is therefore proportional to

$$\left\langle \varepsilon \sum_{k=-\overline{M}}^{\overline{M}} \mathcal{J}_k \right\rangle_M = \left\langle \frac{\varepsilon}{2\Omega} \sum_{k=-\overline{M}}^{\overline{M}} \left(\Pi_k^2 + \Omega^2 X_k^2\right) \right\rangle_M = \frac{\varepsilon}{\beta^{[M]}\Omega} + O(\varepsilon^2), \tag{3.95}$$

where $\langle \ldots \rangle_M$ denotes an average over the Matsubara distribution. When $M = 1$, the right-hand side of Eq. (3.95) reduces to $\varepsilon/(\beta\Omega) + O(\varepsilon^2)$. Hence we can say that the amplitudes of the centroid overtone vibrations are 'Matsubara heated' to what they would be for a classical oscillator at temperature $T^{[M]}$, owing to the cubic coupling of the centroid to the fluctuation modes. We stress that this phenomenon is possible because, to zeroth order, all $M-1$ fluctuation modes oscillate in concert with the centroid at the fundamental frequency, Ω. It follows that the force on the centroid, given by Eq. (3.85), contains (at zeroth order) only Fourier components with frequencies $\pm 2\Omega$ and amplitudes that grow monotonically with M.

In the case of electrical anharmonicity, it is not the overtone vibrations of the centroid

variable Q_0 that are relevant, but the fundamental vibrations of *all* the Matsubara modes. They contribute with equal weight to the quadratic component of the DMS, giving rise to overtone oscillations of the form

$$\frac{\varepsilon\kappa}{2} \sum_{k=-\overline{M}}^{\overline{M}} Q_k^2 = \frac{\varepsilon\kappa}{\Omega} \sum_{k=-\overline{M}}^{\overline{M}} \mathcal{J}_k \sin^2(\varphi_k) + O(\varepsilon^2). \tag{3.96}$$

The total, thermally averaged amplitude of these oscillations is clearly proportional to $1/\beta^{[M]}$, analogous to the mechanically anharmonic contribution discussed above. The Matsubara heating interpretation is therefore still applicable. This is unsurprising in retrospect; both the mechanical and electrical contributions to the overtone arise from q^2 nonlinearity, only one is in the force and the other is in the dipole moment.

3.3.2 Matsubara 'bead' picture

To give more weight to the validity of the Matsubara heating interpretation, we introduce the concept of a Matsubara 'bead'. We define, for $F = 1$,

$$\pi_l = \sqrt{M} \sum_{k=-\overline{M}}^{\overline{M}} \widetilde{T}_{l,k} \Pi_k \tag{3.97a}$$

$$\chi_l = \sqrt{M} \sum_{k=-\overline{M}}^{\overline{M}} \widetilde{T}_{l,k} \mathrm{X}_k, \tag{3.97b}$$

where $\widetilde{\mathbf{T}}$ is defined like $\mathbf{T}$ of Eq. (2.87) but with $N = M$. These 'bead-like' variables satisfy $(\pi_l, \chi_l) = (\tilde{p}_l, \tilde{q}_l) + O(\varepsilon)$, where $\tilde{q}_l = \tilde{q}(\tau = l\beta\hbar/M)$ and likewise for $\tilde{p}_l$. Hence, evaluating absorption intensities in the bead picture is analogous to working in the imaginary-time domain, rather than the corresponding (Matsubara) frequency domain symbolised by the mode picture.

To see why defining these bead-like variables is a useful starting point for understanding Matsubara heating, consider the Matsubara distribution expressed in terms of $(\pi, \chi) = (\tilde{\mathbf{p}}, \tilde{\mathbf{q}})$ in the harmonic limit. Let

$$\mathbf{\Gamma} = \begin{pmatrix} \pi \\ \chi \end{pmatrix} \tag{3.98}$$

and

$$\mathbf{\Sigma} = \begin{pmatrix} \Omega^2\lambda & \mathrm{i}\zeta \\ \mathrm{i}\zeta^{\mathrm{T}} & \lambda \end{pmatrix}, \tag{3.99}$$

where

$$\lambda_{l,l'} = \frac{1}{M\beta} \sum_{k=-\overline{M}}^{\overline{M}} \frac{\widetilde{T}_{l,k}\widetilde{T}_{l',k}}{\Omega^2 + \omega_k^2} = \frac{1}{\beta} \sum_{k=-\overline{M}}^{\overline{M}} \frac{1}{\Omega^2 + \omega_k^2} \cos\left(\frac{2\pi k(l-l')}{M}\right) \tag{3.100a}$$

$$\zeta_{l,l'} = -\frac{1}{M\beta} \sum_{k=-\overline{M}}^{\overline{M}} \frac{\omega_k \widetilde{T}_{l,-k}\widetilde{T}_{l',k}}{\Omega^2 + \omega_k^2} = \frac{1}{\beta} \sum_{k=-\overline{M}}^{\overline{M}} \frac{\omega_k}{\Omega^2 + \omega_k^2} \sin\left(\frac{2\pi k(l-l')}{M}\right). \tag{3.100b}$$

The harmonic Matsubara phase-space distribution function is then

$$\frac{\exp\left(-\beta\left[\widetilde{H}_M^{(0)}\left(\frac{\widetilde{\mathbf{T}}^{\mathsf{T}}\boldsymbol{\pi}}{\sqrt{N}}, \frac{\widetilde{\mathbf{T}}^{\mathsf{T}}\boldsymbol{\chi}}{\sqrt{N}}\right) + i\widetilde{\theta}_M\left(\frac{\widetilde{\mathbf{T}}^{\mathsf{T}}\boldsymbol{\pi}}{\sqrt{N}}, \frac{\widetilde{\mathbf{T}}^{\mathsf{T}}\boldsymbol{\chi}}{\sqrt{N}}\right)\right]\right)}{2\pi\hbar\alpha_M^{-1}\widetilde{Z}_M^{(0)}(\beta)} = \frac{\exp\left(-\frac{1}{2}\boldsymbol{\Gamma}\cdot\boldsymbol{\Sigma}^{-1}\boldsymbol{\Gamma}\right)}{\sqrt{\det(2\pi\boldsymbol{\Sigma})}}. \tag{3.101}$$

Using $\forall l \in \{1, \ldots, M\}, \Omega^2\lambda_{l,l} = 1/\beta^{[M]}$, the normalised, marginal distribution of (π_l, χ_l) is thus given by

$$\frac{1}{\sqrt{\det(2\pi\boldsymbol{\Sigma})}} \int d^{2M}\boldsymbol{\Gamma}' \exp\left(-\frac{1}{2}\boldsymbol{\Gamma}'\cdot\boldsymbol{\Sigma}^{-1}\boldsymbol{\Gamma}'\right)\delta(\pi_l - \pi_l')\delta(\chi_l - \chi_l')$$
$$= \frac{\beta\Omega}{2\pi} \exp\left(-\frac{\beta^{[M]}}{2}(\pi^2 + \Omega^2\chi^2)\right), \tag{3.102}$$

which is just the classical canonical distribution function at the effective temperature $T^{[M]}$. The beads therefore follow effective classical Boltzmann statistics that are consistent with Matsubara heating.

To evaluate $\|\Delta\mathbf{n}\|_1 = 2$ intensities directly from the perturbed dynamics of $\tilde{\mathbf{q}}$ would be cumbersome, because the Matsubara potential couples each bead with every other bead. Thus, for example, $\tilde{q}_0$ has first-order contributions from each (π_l, χ_l), $l \neq 0$. However, we can recast Eq. (3.89) (which was derived from the perturbed dynamics of Q_0) as an integral over bead-like variables, so as to probe the ensemble of $O(\varepsilon)$ bead-like trajectories implicitly. Substituting Eq. (3.97) into Eq. (3.89), and exploiting the cyclic permutational symmetry of the Matsubara distribution (i.e., invariance under the relabelling $l \to l + 1$) to eliminate one of the sums over bead indices, yields

$$I_{2\nu}^{[M]} = \frac{\pi|\mathcal{E}|^2\beta}{8M\Omega^6}\left(\frac{\eta^2\xi^2}{9} + \frac{\eta\xi\kappa\Omega^2}{3} + \kappa^2\Omega^4\right)$$
$$\times \sum_{l=1}^{M} \frac{1}{\sqrt{\det(2\pi\boldsymbol{\Sigma})}} \int d^{2M}\boldsymbol{\Gamma} \exp\left(-\frac{1}{2}\boldsymbol{\Gamma}\cdot\boldsymbol{\Sigma}^{-1}\boldsymbol{\Gamma}\right)(\pi_0 - i\Omega\chi_0)^2(\pi_l + i\Omega\chi_l)^2. \tag{3.103}$$

Within each summand of Eq. (3.103), for $l' \notin \{0, l\}$, the only dependence on $(\pi_{l'}, \chi_{l'})$ lies in the distribution function. We can therefore immediately integrate these variables out to yield the marginal distribution of $\boldsymbol{\Gamma}_l \equiv (\pi_0, \pi_l, \chi_0, \chi_l)^{\mathrm{T}}$, giving

$$
I_{2\nu}^{[M]} = \frac{\pi |\mathcal{E}|^2 \beta}{8M\Omega^6} \left(\frac{\eta^2 \xi^2}{9} + \frac{\eta \xi \kappa \Omega^2}{3} + \kappa^2 \Omega^4 \right)
$$
$$
\times \sum_{l=1}^{M} \frac{1}{\sqrt{\det(2\pi\Sigma_l)}} \int \mathrm{d}^4 \boldsymbol{\Gamma}_l \exp\left(-\frac{1}{2} \boldsymbol{\Gamma}_l \cdot \Sigma_l^{-1} \boldsymbol{\Gamma}_l \right) (\pi_0 - \mathrm{i}\Omega\chi_0)^2 (\pi_l + \mathrm{i}\Omega\chi_l)^2,
$$

(3.104)

where

$$
\Sigma_l = \begin{pmatrix} \Omega^2 \lambda_{0,0} & \Omega^2 \lambda_{0,l} & 0 & \mathrm{i}\zeta_{0,l} \\ \Omega^2 \lambda_{0,l} & \Omega^2 \lambda_{l,l} & -\mathrm{i}\zeta_{0,l} & 0 \\ 0 & -\mathrm{i}\zeta_{0,l} & \lambda_{0,0} & \lambda_{0,l} \\ \mathrm{i}\zeta_{0,l} & 0 & \lambda_{0,l} & \lambda_{l,l} \end{pmatrix}.
$$

(3.105)

Integrating out (π_l, χ_l), and simplifying using

$$
\Omega^2 \lambda_{0,0} = \Omega^2 \lambda_{l,l} = \frac{\beta\Omega^2}{M} \sum_{l=1}^{M} (\Omega\lambda_{0,l} + \zeta_{0,l})^2 = \frac{1}{\beta^{[M]}},
$$

(3.106)

gives

$$
I_{2\nu}^{[M]}(\beta) = \frac{|\mathcal{E}|^2 (\beta^{[M]})^2}{16\Omega^5} \left(\frac{\eta^2 \xi^2}{9} + \frac{\eta \xi \kappa \Omega^2}{3} + \kappa^2 \Omega^4 \right)
$$
$$
\times \int \mathrm{d}\pi_0 \int \mathrm{d}\chi_0 \ \exp\left\{ -\frac{\beta^{[M]}}{2} (\pi_0^2 + \Omega^2 \chi_0^2) \right\} (\pi_0^2 + \Omega^2 \chi_0^2)^2.
$$

(3.107)

Defining the 'action-like' and 'angle-like' variables $(\widetilde{J}_0, \widetilde{\phi}_0)$ by

$$
\pi_0 = \sqrt{2\Omega\widetilde{J}_0} \cos(\widetilde{\phi}_0)
$$

(3.108a)

$$
\chi_i = \sqrt{\frac{2\widetilde{J}_0}{\Omega}} \sin(\widetilde{\phi}_0)
$$

(3.108b)

(which are rigorously action-angle variables for the zeroth bead in the harmonic limit), the integral becomes

$$
I_{2\nu}^{[M]}(\beta) = \frac{\pi |\mathcal{E}|^2 (\beta^{[M]})^2}{2\Omega^3} \left(\frac{\eta^2 \xi^2}{9} + \frac{\eta \xi \kappa \Omega^2}{3} + \kappa^2 \Omega^4 \right) \int \mathrm{d}\widetilde{J}_0 \ \mathrm{e}^{-\beta^{[M]}\Omega\widetilde{J}_0} \widetilde{J}_0^2.
$$

(3.109)

Comparing Eq. (3.109) with the one-dimensional case of Eq. (3.65) reveals an isomorphism between the classical and Matsubara overtone intensities evaluated at temperatures of $T^{[M]}$ and T, respectively. The Matsubara heating of $\|\Delta \mathbf{n}\|_1 = 2$ bands can be attributed to the elevated effective temperatures of the Matsubara beads, which is consistent with the effects of quantum mechanical zero-point energy in the $M \to \infty$ limit.

3.3.3   The peculiar case of difference bands

The Matsubara heating of difference bands is, at a glance, counter-intuitive, as it results in a *lowering* of the intensity in the $M \to \infty$ limit. Physically, this is a consequence of quantum detailed balance; when $\beta \hbar \Omega_{\max} \gg 1$, the quantum effective temperatures become inversely proportional to frequency, since

$$\lim_{\beta \to \infty} \frac{1}{\beta_i^{[\infty]}} = \frac{\hbar \Omega_i}{2}. \tag{3.110}$$

The numerator in

$$\tilde{I}^{[q]}(\mathbf{B}; \Omega_i, -\Omega_j) = \frac{\pi |\mathcal{E}|^2 (\Omega_i - \Omega_j)\left(\beta_i^{[\infty]}\Omega_i - \beta_j^{[\infty]}\Omega_j\right)}{\beta_i^{[\infty]}\beta_j^{[\infty]}\Omega_i^2 \Omega_j^2} \tag{3.111}$$

therefore becomes vanishingly small. Of course, this is consistent with the quantum statistical effects expected based on the Schrödinger picture: since difference bands arise from transitions in which one quantum number is lowered, the initial state is always vibrationally excited and therefore has a vanishingly small population.

In Fig. 3.1, we illustrate how the Matsubara intensities of $\|\Delta \mathbf{n}\|_1 = 2$ bands vary with respect to M for two coupled oscillators with frequencies $\Omega_1 = 1$ a.u. and $\Omega_2 = \sqrt{2}$ a.u. We plot the ratio of the Matsubara intensity to the classical intensity, given by

$$\frac{I_{\nu_i \pm \nu_j}^{[M]}(\beta)}{I_{\nu_i \pm \nu_j}^{[c]}(\beta)} = \frac{\beta\left(\beta_i^{[M]}\Omega_i \pm \beta_j^{[M]}\Omega_j\right)}{\beta_i^{[M]}\beta_j^{[M]}(\Omega_i \pm \Omega_j)}, \tag{3.112}$$

against M at three different temperatures. It is interesting to note that, while the overtone and combination band intensities always increase monotonically with M, the difference band intensity decreases monotonically at high temperatures, but peaks at $M > 1$ at lower temperatures (specifically, one can show, when $\beta \hbar \sqrt{\Omega_1 \Omega_2} > 2\pi$). This makes it computationally challenging to illustrate the fluctuation-induced lessening of difference band intensity in simulations, even for toy models such as the one presented in Fig. 3.1, because the severity of the Matsubara sign problem increases dramatically both with temperature and with the number of modes (i.e., it is worsened both by *actual* heating and by *Matsubara* heating).
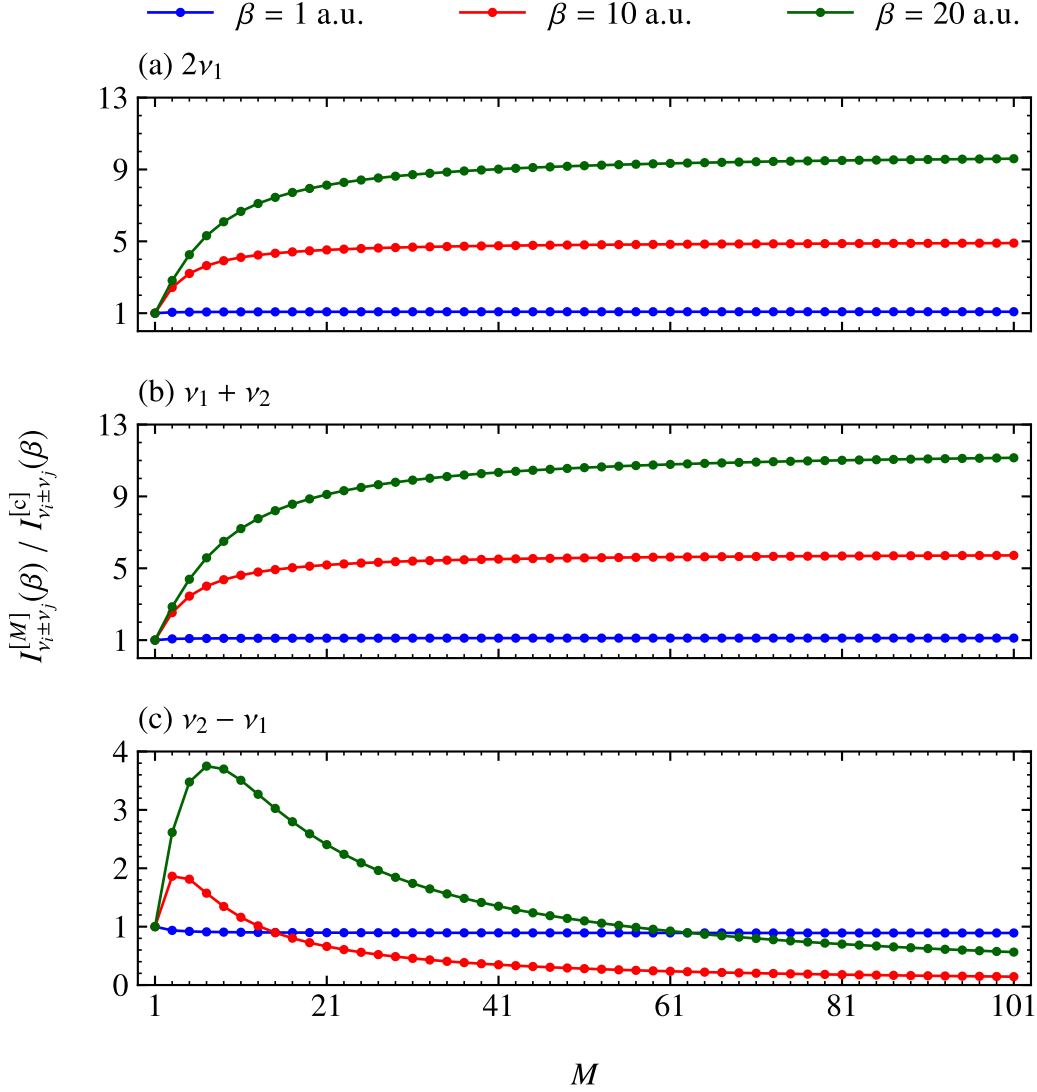
Figure 3.1: Ratio of Matsubara to classical $\|\Delta \mathbf{n}\|_1 = 2$ intensities for a two-dimensional system with $\Omega_1 = 1$ a.u. and $\Omega_2 = \sqrt{2}$ a.u..

3.4 Numerical illustration and discussion

3.4.1 One-dimensional model of O–H

In this section, to illustrate the effects of Matsubara heating, we study a simple one-dimensional model of an O–H bond at 300 K. We employ the q-TIP4P/F interatomic potential of ref. 33, which is given by

$$V_{\text{OH}}(q) = D_0 \left[\alpha^2 q^2 - \alpha^3 q^3 + \frac{7}{12} \alpha^4 q^4 \right], \tag{3.113}$$

where q represents the (unweighted) displacement from equilibrium bond length, $D_0 = 0.185001$ a.u., and $\alpha = 1.21023$ a.u. Eq. (3.113) is just a fourth-order Taylor series approximation to a Morse potential with the same parameters. The (reduced) mass is set to $m = 1741.05$ a.u, and the dipole moment is taken to be linear, such that the quantum IR spectrum is proportional to the Fourier transform of the Kubo-transformed velocity ACF as per Eq. (2.51c).

We stress from the outset that these one-dimensional calculations should not be interpreted as tests of the overall performances of Matsubara dynamics or any of its approximations. Such imaginary-time path-integral dynamics approaches have been developed specifically for the purposes of simulating condensed-phase systems, which will be explored in Chapter 4. In a one-dimensional anharmonic oscillator, real-time quantum coherence has a very large effect on the dynamics, which we would certainly not expect Matsubara dynamics to be capable of capturing (and in fact, increasing the number of fluctuation modes *reduces* the amount of coherence captured by the dynamics—an artefact upon which we will expand in Section 3.4.4). Within the context of integrated $\|\Delta\mathbf{n}\|_1 = 2$ absorption intensities, however, it is a valid system to use for illustrating the effects of Matsubara heating (or neglect thereof) outlined in Sections 3.3, because coherence does not play a role up to $O(\varepsilon^2)$. To aid visual comparisons, all the spectra shown in this chapter have been convolved with the Gaussian filter

$$\tilde{f}_G(\omega) = \frac{w}{\sqrt{2\pi}} e^{-w^2\omega^2/2}, \tag{3.114}$$

with $w = 0.25$ ps, which one may regard as crudely imitating the effects of decoherence that would be expected to occur in the condensed phase. In practice, the convolution was achieved in the time domain, by damping the Kubo-transformed dipole-derivative ACFs (or approximations thereof) with the Gaussian window function

$$f_G(t) = \exp\left(-\frac{t^2}{2w^2}\right). \tag{3.115}$$

Further computational details are given in Appendix D.1.

We also point out that Matsubara dynamics is known to suffer long convergence 'tails' with respect to M at low temperatures, as found similarly in the calculation of some static properties [135]. Since the severity of the sign problem grows with the size of the fluctuations, we will thus be unable to reach the number of modes (likely hundreds) required to converge the Matsubara dynamics spectra. The slow convergence of anharmonic absorption intensities is already evident from Fig. 3.1, which is relevant to both the truncated and mean-field formulations of the theory. Truncated Matsubara dynamics exhibits similarly slow convergence for peak positions, but mean-field averaging almost entirely alleviates this, by capturing the effects of zero-point energy on the fundamental oscillation frequencies [77].
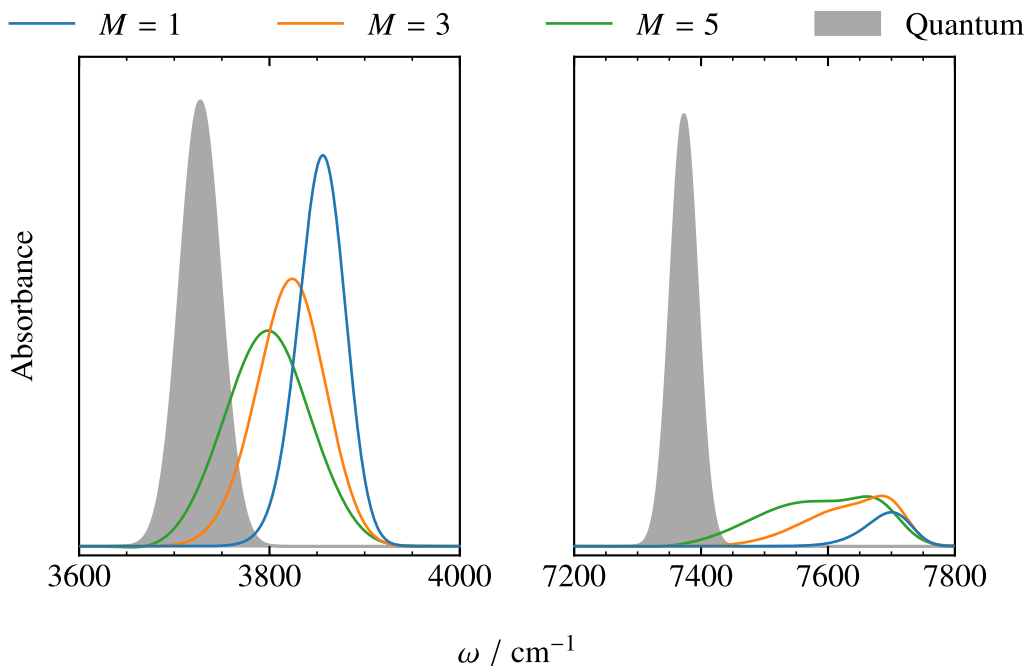
Figure 3.2: IR absorption spectra calculated for the one-dimensional q-TIP4P/F oscillator at 300 K. The predictions of truncated Matsubara dynamics are compared against the exact quantum spectrum. The absorbances in the two panels are scaled as 1 : 50 (left-to-right).

In Fig. 3.2, we compare the IR spectra calculated with (truncated) Matsubara dynamics to the exact quantum result, which was obtained using the discrete variable representation (DVR) of Colbert and Miller [14]. Examining first the fundamental band near 3800 cm^{-1}, we find that increasing the number of Matsubara modes from $M = 1$ (equivalent to classical dynamics) to $M = 5$ causes the peak to redshift slightly, bringing it closer to the exact quantum result. This is to be expected, given that the dominant anharmonicity is cubic, and quantum zero-point energy enables more sampling of the shallow, outer wall of the potential than is allowed by the classical distribution (which is also the origin of Matsubara heating, although the $O(\varepsilon^2)$ redshift is beyond the scope of the first-order perturbative analysis of Section 3.2). However, the integrated intensity is hardly affected, with all the Matsubara predictions within ~2% of the quantum result. This is because the fundamental band has a leading zeroth-order contribution from the linear (i.e., harmonic) part of the centroid force, which is independent of M, so any difference in the intensity must be $O(\varepsilon)$. It is consistent with Matsubara heating, since the fundamental band intensity for a harmonic oscillator is independent of temperature. In spite of this, the overall lineshape of the fundamental band slightly broadens as M increases, which might seem paradoxical given the relative sharpness of the quantum peak; this effect is discussed further in Section 3.4.4.

Turning to the overtone band near 7500 cm^{-1}, the Matsubara peak position, while more

strongly blueshifted, follows the same overall trend with increasing M. In contrast, the integrated intensity shows qualitatively different behaviour to that of the fundamental band, with the classical prediction only about one tenth of the quantum result. The intensity increases with the number of Matsubara modes, reaching about half the quantum intensity at $M = 5$. This is the behaviour expected from the perturbative analysis of Section 3.2; the cubic coupling of the fluctuations to the centroid increases the amplitude of the overtone vibrations of the latter, in accordance with Matsubara heating (the quartic part of the potential plays no significant role in this context). For $M > 5$, the Matsubara sign problem becomes too severe to converge the spectra numerically, but we expect that near-quantitative agreement with the exact overtone intensity would be achieved, hypothetically, in the $M \rightarrow \infty$ limit.

One peculiarity of the Matsubara results presented in Fig. 3.2 is the bifurcation of the $M = 3$ and $M = 5$ overtone bands, not observed in the quantum spectrum. To understand why this is the case, in Fig. 3.3(a) we compare the power spectrum of the centroid mode, (P_0, Q_0), to that of the fluctuation modes, $(P_{\pm 1}, Q_{\pm 1})$, for the case $M = 3$ (obtained by taking the Fourier transforms of the relevant velocity ACFs, so the centroid power spectrum is proportional to the $M = 3$ IR spectrum plotted in Fig. 3.2). We find that the fluctuation modes oscillate, on average, with a fundamental frequency about 20 cm^{-1} higher than the centroid mode—an effect not captured by the first-order perturbative analysis of Section 3.2. The $Q_{\pm 1}^2$ driving terms will thus cause centroid overtone vibrations at a slightly higher frequency than the Q_0^2 terms, consistent with a bifurcated overtone band.

This artefact turns out to be avoided if we account for the higher-frequency fluctuation modes at the mean-field level; Fig. 3.3(b) shows that the frequency discrepancy between centroid and fluctuation $M = 3$ power spectra frequencies is removed almost entirely when recalculated using mean-field Matsubara dynamics (so the $M = 1$ dynamics is now equivalent to CMD). The mean-field Matsubara IR spectra are plotted in Fig. 3.4 where we find, reassuringly, that the overtone band is no longer bifurcated. As expected, the integrated intensities are again consistent with Matsubara heating, and the mean-field averaging considerably improves the positions of both peaks.

As more concrete evidence of the validity of the results of Section 3.2, in Table 3.1 we give the integrated intensities of the Matsubara fundamental and overtone bands as percentages of the exact quantum intensities. In the final column, we compare these to the expected results for the overtone based on first-order PT, using

$$\frac{I_{2\nu}^{[M]}(\beta)}{I_{2\nu}^{[q]}(\beta)} = \frac{\beta^{[\infty]}}{\beta^{[M]}} = \frac{\tanh(\beta\hbar\Omega/2)}{\beta\hbar\Omega/2} \sum_{k=-\overline{M}}^{\overline{M}} \frac{\Omega^2}{\Omega^2 + \omega_k^2}, \tag{3.116}$$

with $\Omega = \sqrt{2D_0\alpha^2/m} = 0.0176426$ a.u. We find that the mean-field Matsubara spectra follow
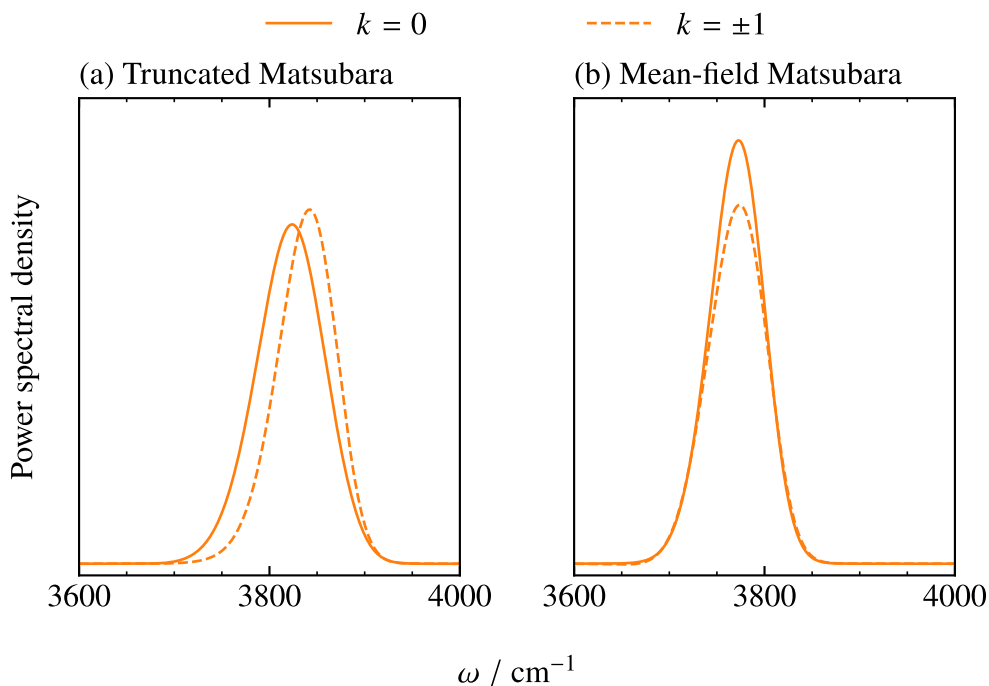
Figure 3.3: Comparison of power spectra for truncated and mean-field $M = 3$ Matsubara dynamics of the one-dimensional q-TIP4P/F oscillator at 300 K.

the expected trend fairly closely, while truncated Matsubara dynamics deviates from it by 15–20%.

3.4.2 Limitations of path-integral methods

As discussed in Section 2.4, path-integral methods such as [Q]CMD, [T]RPMD, and the planetary model avoid the sign problem of Matsubara dynamics by making drastic approximations to the time evolution of the fluctuation modes. The perturbative analysis of Section 3.2 enables us to assess the impact of these approximations on the ability of path-integral methods to capture $\|\Delta\mathbf{n}\|_1 = 2$ band intensities faithfully. While we continue focus on a one-dimensional oscillator for now, in Chapter 4, we will extend our investigations to more realistic gas- and condensed-phase systems. Computational details of the calculations reported in this section are given in Appendix D.1.

CMD is equivalent to mean-field Matsubara dynamics with $M = 1$, which, as indicated in Section 3.2.4 and proved in Appendix B.3.2, gives first-order perturbative results identical to classical dynamics (i.e., truncated Matsubara dynamics with $M = 1$). Indeed, the results of Figs. 3.4 and Table 3.1 demonstrate numerically that CMD drastically underestimates the first overtone intensity for the q-TIP4P/F O–H oscillator. In general, Matsubara heating of the centroid $\|\Delta\mathbf{n}\|_1 = 2$ vibrations will clearly be impossible when the centroid–fluctuation coupling is accounted for only at the mean-field level. The electrically anharmonic contributions are
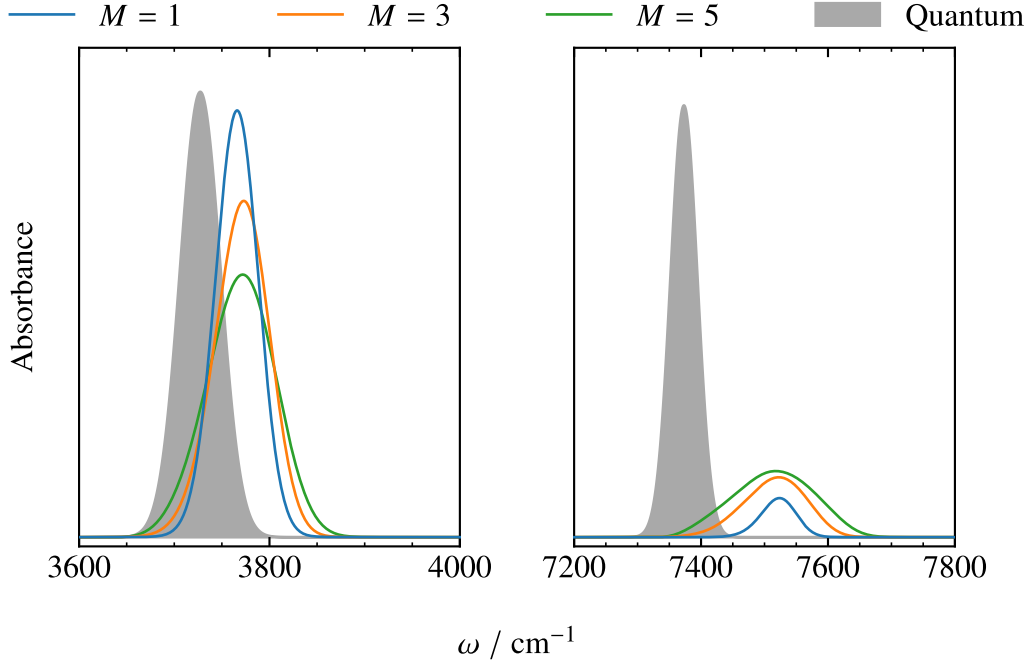
Figure 3.4: As in Fig. 3.2, but using the mean-field version of Matsubara dynamics.

likewise neglected, since the proper path-integral estimator for a nonlinear quantum operator depends explicitly on the fluctuation modes. Similar arguments apply to QCMD, so both methods are expected to treat $\|\Delta \mathbf{n}\|_1 = 2$ band intensities at a level comparable to classical MD. Of course, they are generally expected to improve the peak positions, except at low temperatures where CMD is plagued by the curvature problem for certain vibrations [76, 99, 100].

The RPMD and TRPMD spectra for the q-TIP4P/F oscillator are compared with the classical and quantum results in Fig. 3.5. In RPMD, an effect of discarding the imaginary part of the Liouvillian is to shift the oscillation frequencies of the fluctuation modes away from those of the centroid. As noted in Section 2.4, for a harmonic oscillator with frequency Ω, the frequency of oscillation of mode $(\overline{P}_k, Q_k)$ shifts from Ω to $\sqrt{\Omega^2 + \omega_k^2}$. In the perturbing force on the centroid given by Eq. (3.85), the $Q_{k \neq 0}^2$ driving terms will therefore oscillate at the wrong frequencies to be able to contribute to the overtone band at $\omega \simeq 2\Omega$. Instead, they give rise to $\overline{M}$ spurious peaks centred at $\omega \simeq 2\sqrt{\Omega^2 + \omega_k^2}$, $|k| \in \{1, \dots, \overline{M}\}$, two of which are captured in Fig. 3.5. Electrical anharmonicity (specifically, quadratic terms in the DMS) would contribute intensity at the same frequencies. Sometimes, particularly in multidimensional systems, the spurious peaks may happen to occur near genuine overtone or combination frequencies, and thus could be mistaken for physical overtone or combination bands; in Appendix C.3, we discuss an example of this occurring for the SPC/F model of liquid water of ref. 150. In TRPMD, the internal vibrations of the ring polymer are damped off by the presence of a Langevin thermostat attached to each fluctuation mode, which mitigates the problem of spurious peaks in the spectrum, but

Table 3.1: Integrated intensities of the Matsubara fundamental (ν) and first overtone (2ν) bands, as percentages of those given by exact quantum mechanics, for the one-dimensional q-TIP4P/F oscillator at 300 K. For the overtone, we compare our numerical results with the predictions of first-order PT.

M	ν band		2ν band		
	Trunc	MF	Trunc	MF	PT
1	102%	102%	13%	12%	11%
3	101%	102%	36%	32%	30%
5	101%	100%	52%	48%	45%
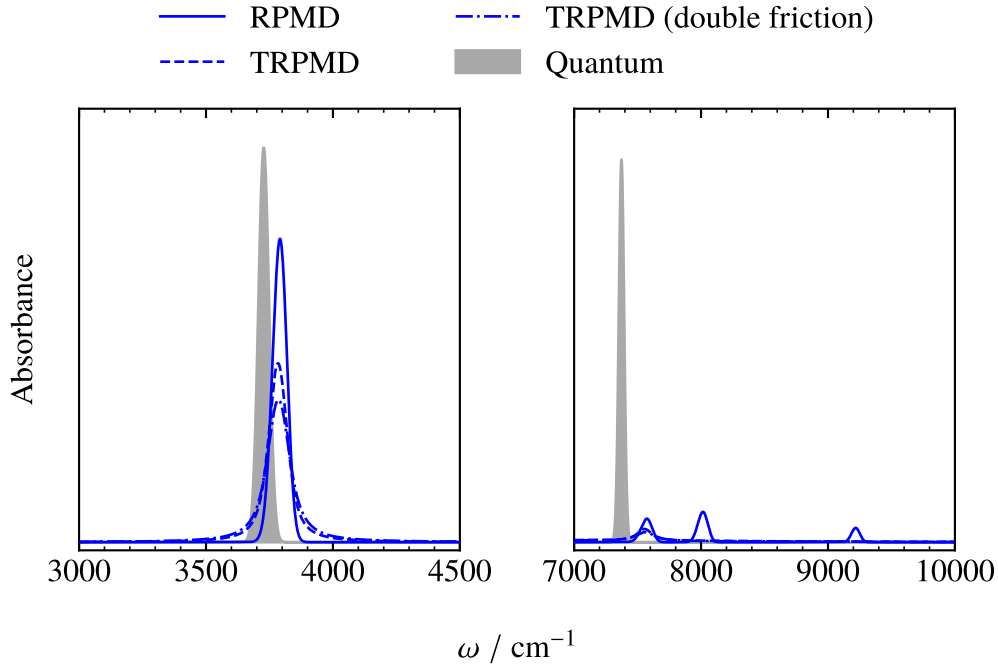
Figure 3.5: IR absorption spectra calculated for the one-dimensional q-TIP4P/F oscillator at 300 K. The predictions of RPMD and TRPMD are compared against the exact quantum spectrum. Also included is the spectrum given by TRPMD with the friction coefficients doubled to $\gamma_k = 2|\omega_k|$. The absorbances in the two panels are scaled as 1 : 50 (left-to-right).

does nothing otherwise to improve the description of quantum $\|\Delta\mathbf{n}\|_1 = 2$ bands.

For a one-dimensional harmonic oscillator, Hele pointed out in ref. 85 that the time-evolved phase-space density

$$e^{\mathcal{A}_M t} Q_0 = e^{-\gamma_k t/2} \left[Q_k \cos(\omega_k' t) + \left(\frac{P_k}{m\omega_k'} + \frac{\gamma_k Q_k}{2\omega_k'} \right) \sin(\omega_k' t) \right] \qquad (3.117)$$

oscillates with the correct physical frequency, Ω, if one sets $\gamma_k = 2|\omega_k|$, rather than the more

conventional $\gamma_k = |\omega_k|$. Here $\mathcal{A}_M$ is the sum of Fokker–Planck operators, defined as in Eq. (2.107), and

$$\omega_k' = \sqrt{\Omega^2 + \omega_k^2 - \gamma_k^2/4}. \tag{3.118}$$

One may expect, naively, that setting $\gamma_k = 2|\omega_k|$ should therefore yield the correct overtone intensity, but in Fig. 3.5 we find that the only significant effect of increasing the friction is to intensify the artificial damping of the spectrum.[c] This is because the phase-space density of Eq. (3.117) does not represent a deterministic trajectory, but a probability distribution of thermostatted trajectories.

Unlike other path-integral methods, the planetary model was proposed with the explicit aim of calculating TCFs of nonlinear observables. As shown in ref. 75 and discussed in Section 2.4.3, it can be derived as a locally harmonic approximation to Matsubara dynamics, whereby the Matsubara potential is expanded to second order about the centroid, and the force exerted by the fluctuations on the centroid is treated at the CMD or TRPMD level. In the (mechanically) harmonic limit, this force vanishes anyway, so the planetary model is exact. It can therefore faithfully capture $\|\Delta \mathbf{n}\|_1 = 2$ bands, and indeed all other absorption bands, if they are caused purely by nonlinearity in the DMS. However, in the case of a cubic perturbation to the potential, it is precisely the anharmonic centroid–fluctuation coupling that enables Matsubara heating of the $\|\Delta \mathbf{n}\|_1 = 2$ bands. For a linear DMS, we therefore would not expect the planetary model to perform any better than classical dynamics at capturing the correct $\|\Delta \mathbf{n}\|_1 = 2$ intensities, and this is borne out for the q-TIP4P/F oscillator in Fig. 3.6. Following Willatt *et al.* [75, 116], we have used TRPMD to propagate the centroids in our planetary model simulations.

We also include in Fig. 3.6 the spectrum given by LSC-IVR, which is found to reproduce the quantum overtone intensity far more closely than any of the centroid-following methods discussed above. This is consistent with the results of refs. 65, 117, in which Plé *et al.* showed that LSC-IVR captures $\|\Delta \mathbf{n}\|_1 = 2$ intensities exactly up to second order in ε. Heuristically, we can go some way towards understanding this as follows: LSC-IVR approximates the dynamics of a single Matsubara bead by removing the constraint of imaginary-time smoothness, such that each $(\tilde{p}_l, \tilde{q}_l)$ is propagated along independent, Newtonian trajectories. For an oscillator with purely cubic anharmonicity, the force on the Matsubara centroid (Eq. (3.85)) is equivalent to that which would result if the beads were uncoupled by the Hamiltonian i.e., if the Hamiltonian were

$$\frac{1}{M} \sum_{l=1}^{M} H(\tilde{p}_l, \tilde{q}_l).$$

Within the scope of first-order PT, it thus makes no difference to the dynamics of the centroid

---

[c]Because TRPMD was implemented by simulating the full N-bead ring-polymer, rather than just its Matsubara modes, in practice the friction coefficients were set to $\gamma_k = 4 \sin(\beta_N \hbar |\omega_k|/2)/\beta_N \hbar$.
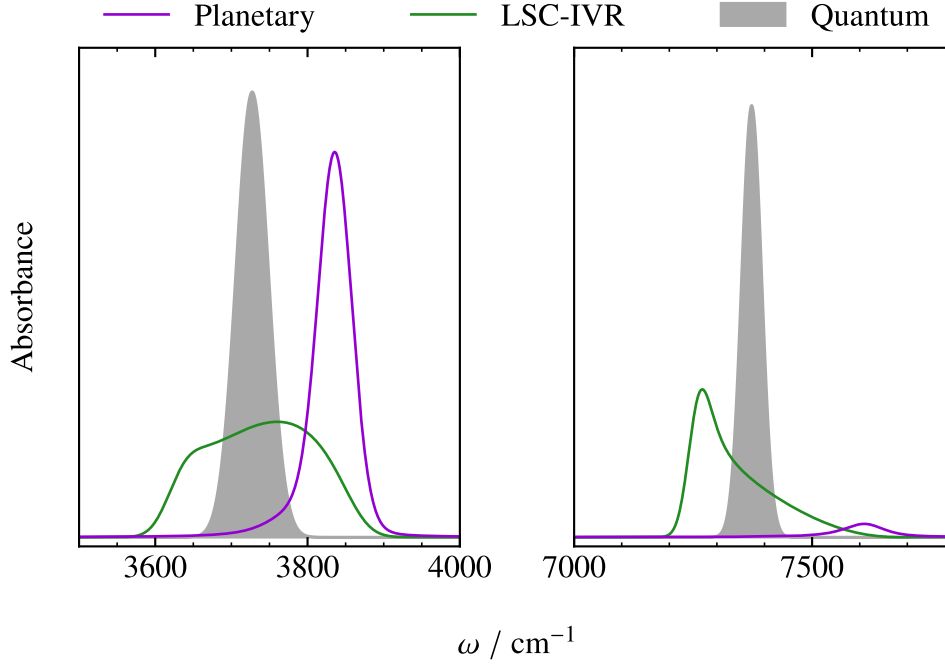
Figure 3.6: IR absorption spectra calculated for the one-dimensional q-TIP4P/F oscillator at 300 K. The predictions of the planetary model and LSC-IVR are compared against the exact quantum spectrum. The absorbances in the two panels are scaled as 1 : 50 (left-to-right).

whether or not the imaginary-time paths are constrained to be smooth. Of course, LSC-IVR does not explicitly consider the dynamics of the centroid, so for the more rigorous derivation the reader is referred to refs. 65, 117. It is also important to note the drawbacks of this method that arise from the violation of detailed balance; for our one-dimensional q-TIP4P/F oscillator, this manifests as artificial broadening of the spectral lineshapes, and small regions of negative absorbance. In condensed-phase systems, it can lead to severe zero-point energy 'leakage' on the timescale of a typical simulation, discussed further in Chapter 4.

3.4.3   A simple post-processing correction procedure

The results presented thus far in Section 3.4 suggest a class of very simple scaling factors one could apply to $\|\Delta \mathbf{n}\|_1 = 2$ bands in classical or path-integral spectra to bring their intensities into better agreement with exact quantum mechanics. Namely, to leading order in ε, the quantum integrated intensity is related to the classical one by the factor

$$\frac{I^{[\mathrm{q}]}_{\nu_i \pm \nu_j}(\beta)}{I^{[\mathrm{c}]}_{\nu_i \pm \nu_j}(\beta)} = \frac{\beta\big(\beta_i^{[\infty]}\Omega_i \pm \beta_j^{[\infty]}\Omega_j\big)}{\beta_i^{[\infty]}\beta_j^{[\infty]}(\Omega_i \pm \Omega_j)} = \frac{\beta\hbar\Omega_i\Omega_j}{2(\Omega_i \pm \Omega_j)}\left[\coth\left(\frac{\beta\hbar\Omega_j}{2}\right) \pm \coth\left(\frac{\beta\hbar\Omega_i}{2}\right)\right]. \tag{3.119}$$

It is interesting that we could have obtained this without doing any classical PT explicitly, and certainly without knowledge of Matsubara dynamics; all that is required is to divide the quantum PT result of Section 3.2.2 by its $\hbar \to 0$ limit. Nonetheless, even though the quantum result has been known since 1976 [149], nobody to our knowledge has yet proposed employing Eq. (3.119) as a means of post-processing correction.

In a broader sense, the idea of scaling classical spectra during post-processing is, of course, not new. Indeed the 'standard' and 'harmonic' correction factors mentioned in Section 2.1.2 have often been applied to obtain inexpensive (but crude) approximations to quantum spectra from classical data. Another well-known approach involves the 'Schofield' correction factor, $e^{\beta\hbar\omega/2}$. Each of these have been studied in some depth and are suited to correlation spectra involving different types of observables [82, 126, 127, 151, 152]. However, despite having similar functional forms, they are unrelated to the scaling factors of Eq. (3.119). The standard, harmonic, and Schofield correction factors are functions of the continuous variable ω and are designed to recover the correct harmonic behaviour when multiplied by the *entire* classical spectrum. They have been largely superseded by path-integral methods. In contrast, our scaling factors depend on the system-dependent, harmonic frequencies Ω_i, and are designed to be applied to *specific* bands to account for the anharmonic effects that path-integral methods fail to capture.

The theoretical analysis of Section 3.2, and the numerical results of Fig. 3.4 and Table 3.1, justify using Eq. (3.119) to correct the spectra given by CMD or QCMD. This is because these methods are expected to yield intensities similar to those of classical MD (within the limits of their respective applicabilities). Application to TRPMD spectra might be justified in principle, but in practice, the unphysical lineshape broadening can cause bands that should be well separated to overlap too significantly for one to isolate the contributions in need of 'correcting'. Application to planetary model spectra could only be justified in the case of a linear DMS, otherwise the electrically anharmonic contributions to the intensity (which the planetary model treats accurately) would be double-counted.

For the overtone band of a one-dimensional system, Eq. (3.119) reduces to

$$\frac{I_{2\nu}^{[q]}(\beta)}{I_{2\nu}^{[c]}(\beta)} = \frac{\beta\hbar\Omega}{2} \coth\left(\frac{\beta\hbar\Omega}{2}\right). \tag{3.120}$$

In Fig. 3.7, we verify that scaling the classical or CMD first overtone band of the one-dimensional q-TIP4P/F oscillator by this quantity brings its intensity into far better agreement with exact quantum mechanics. In Chapter 4, we will validate this post-processing correction approach more strongly, by applying it to accurate models of gas-phase water and ammonia.
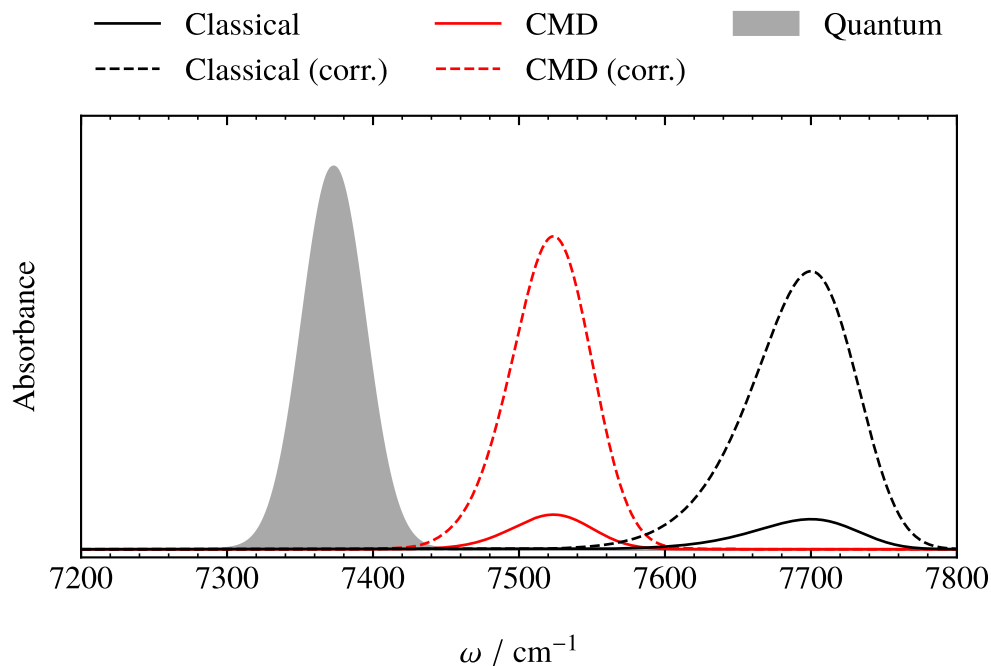
Figure 3.7: First overtone regions of IR absorption spectra calculated for the one-dimensional q-TIP4P/F oscillator at 300 K, corrected by applying the post-processing scaling factors of Eq. (3.120), taking Ω in each case to be the first moment of the corresponding fundamental band. The predictions of classical MD and CMD are compared against the exact quantum spectrum. Note that the uncorrected results are identical to the $M = 1$ results from Figs. 3.2 (classical) and 3.4 (CMD)

.

3.4.4 A word on lineshape broadening

Figs. 3.2 and 3.4 illustrate an interesting and apparently paradoxical effect. As the number of modes M increases, the lineshapes of the Matsubara spectra are erroneously broadened relative to the quantum lineshapes (which, of course, would be infinitely narrow had we not applied Gaussian damping to mimic decoherence). This contrasts with the positions and intensities of the peaks, which, as discussed above, come into closer agreement with the quantum result. Making the reasonable assumption that this trend continues as $M \to \infty$, it would seem as though converged Matsubara dynamics misses some quantum coherence that is captured by CMD, RPMD, and even classical dynamics.

Mechanically, we can understand this as a side effect of Matsubara heating. In the 'bead picture', the broadening mechanism is analogous to that which occurs when the temperature is raised; namely, the beads access regions of configuration space with stronger anharmonicity, and thus sample a wider range of frequencies (recalling that the frequency of oscillation along any given trajectory depends on the action). In the 'mode picture', the fluctuation modes vibrate with fundamental frequencies close to that of the centroid, so energy is easily
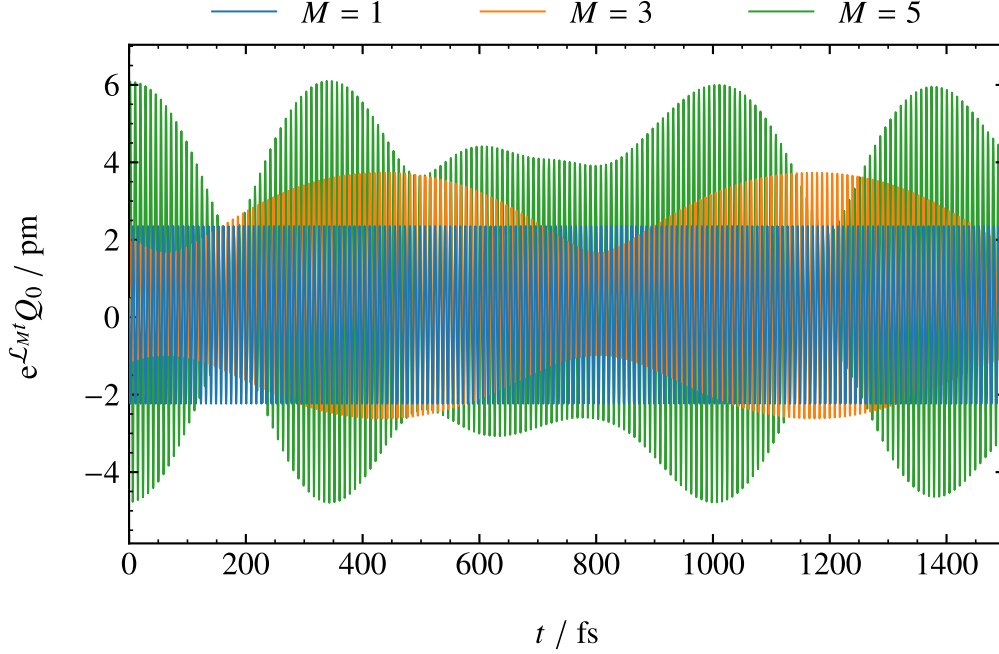
Figure 3.8: Typical centroid trajectories from truncated Matsubara dynamics simulations of the q-TIP4P/F oscillator described in Section 3.4.1, illustrating the characteristic beating pattern that occurs for $M > 1$ as a result of centroid–fluctuation coupling. Similar behaviour is observed in mean-field Matsubara dynamics.

transferred among them in the presence of an anharmonic perturbation. This causes the centroid to undergo a pronounced beating pattern, as illustrated in Fig. 3.8, such that more than one oscillation frequency contributes to each trajectory. In CMD, however, one can regard the frequencies of the fluctuation modes as being raised so as to achieve adiabatic separation from the centroid motion. Any energy flow is substantially reduced, and occurs on a timescale that is instantaneous relative to the period of oscillation of the centroid. The beating pattern therefore vanishes, giving rise to a much sharper spectrum.

Still, this behaviour is somewhat surprising, given that CMD may be derived as an approximation to Matsubara dynamics. For further insight, we turn to the theoretical analysis of Ramírez *et al.* [142]. They showed that, for one-dimensional systems in the low-temperature limit, the second derivative of the centroid PMF at equilibrium gives an approximation to the first excitation energy of the quantum Hamiltonian:

$$\lim_{\beta \to \infty} \hbar \sqrt{\mathcal{F}''(Q_{\min})} \simeq E_1 - E_0, \tag{3.121}$$

where $\mathcal{F}'(Q_{\min}) = 0$. This holds even for raw potentials, $V(q)$, that are highly anharmonic, such as quartic potentials that themselves have vanishing second derivatives at equilibrium, and double well potentials for which $E_1 - E_0$ corresponds to a tunnelling splitting [142]. At

sufficiently low temperatures ($k_B T \ll E_1 - E_0$), each centroid trajectory of a CMD simulation must therefore contain a harmonic component, the frequency of which is close to the quantum fundamental frequency, $(E_1 - E_0)/\hbar$. This implies that CMD can capture some of the effects of quantum coherence in this regime. In the $T \to 0$ limit, it may be formally viewed as mapping the coherent oscillations between the two lowest-energy eigenstates onto the classical dynamics of a harmonic oscillator with potential $\mathcal{F}(Q_0)$.

The q-TIP4P/F oscillator considered in this chapter carries relatively mild anharmonicity, so one does not require knowledge of 'Ramírez oscillations' to justify the reasonable prediction that CMD gives for the fundamental band frequency. The sharpness of the lineshape, however, can probably be attributed (at least in part) to the ability of CMD to probe the corresponding energy quantisation. Insofar as lineshape is concerned, RPMD and classical MD may then be regarded as approximations to CMD—RPMD, because the fluctuation frequencies are shifted only part of the way towards adiabatic separation, and classical MD, because $V(q)$ and $\mathcal{F}(Q_0)$ happen to be equivalent up to $O(\varepsilon)$ (see Appendix B.3.2). While CMD can, at sufficiently high temperatures, give excellent predictions of fundamental bands for condensed-phase systems [29, 96–98], Ramírez oscillations are an artefact of restricting the dynamics to a very small number of degrees of freedom. In condensed-phase systems, most degrees of freedom possess characteristic frequencies that are small relative to $k_B T$, resulting in many closely-spaced energy levels. CMD clearly does not behave as a two-state mapping model in this regime.

Chapter 4

Simulations of infrared absorption spectra

In Chapter 3, we showed that the underestimation by centroid-following path-integral methods of first overtone and binary combination band intensities, and the corresponding overestimation of binary difference band intensities, results from neglecting the 'Matsubara heating' of the relevant centroid vibrations. Using the notation of Section 3.1, such absorption bands are collectively labelled as $\|\Delta\mathbf{n}\|_1 = 2$. We proposed a simple class of scaling factors that one can apply to the $\|\Delta\mathbf{n}\|_1 = 2$ bands given by centroid-following methods, or even by classical MD, to bring their intensities into closer agreement with quantum mechanics. However, so far we have only tested this post-processing approach on a one-dimensional model of a single O–H bond, which is far from being representative of real molecular systems.

The main goal of the present chapter is to test the applicability of the scaling factors to more challenging systems. In generating the IR spectra for these systems, we also take the opportunity to overview the capabilities of classical and path-integral methods over the whole range of frequencies up to and including the near-IR region. Section 4.1 focuses on gas-phase water, Section 4.2 on gas-phase ammonia, and Sections 4.3–4.4 on condensed-phase water. We find that the scaling factors work very well for gas-phase systems, especially considering the simplicity of the model used to derive them. In the condensed phase, where features are less well resolved and might be affected by highly anharmonic couplings that are difficult to treat perturbatively, the approach is found not to be as successful. However, we propose that it could still serve a purpose as a first step towards improving the outcomes of path-integral simulations. In the case of water, we also assess the performance of LSC-IVR, which we expect to give reasonable anharmonic absorption intensities, but lineshapes potentially distorted by the degradation of the quantum Boltzmann distribution.

4.1 Gas-phase water

Here we examine the IR spectra of gas-phase water predicted by various approximate methods, namely classical MD, QCMD, TRPMD, and LSC-IVR. We omit the results of CMD and unthermostatted RPMD, which suffer well-known defects at low temperatures that have been studied in depth elsewhere [76, 99–101] (see Section 2.4 for a summary). We also assess the effectiveness of the scaling factors proposed in Section 3.4.3 as a means of post-processing intensity correction for $\|\Delta\mathbf{n}\|_1 = 2$ bands.

4.1.1 Computational details

The raw data from QCMD simulations were provided by G. Trenins. Details of these simulations can be found in ref. 107, where they were also used to generate IR spectra (but only the mid- to far-IR regions were reported). To enable fair comparisons with the QCMD results, our classical, TRPMD, LSC-IVR, and quantum calculations employed the same PES [153] and DMS [154] originally due to Partridge and Schwenke. The quantum results were obtained using the DVR3D package of Tennyson *et al.* [15].

In the classical simulations, the dipole moments of several independent water molecules were recorded along microcanonical production runs, each of length 2 ps, to yield a total of 10^5 single-molecule Newtonian trajectories. Prior to each production run, the molecules were subject to a 0.125 ps equilibration run under the influence of a local Langevin thermostat [155, 156] with friction coefficient 10 ps^{-1} (OBABO propagator splitting in the notation of ref. 157). A time step of 0.125 fs was used throughout. The dipole-derivative ACF was calculated for $0 \leqslant t < 1$ ps by time averaging over the production runs.

The TRPMD simulations were carried out in a similar fashion, but with each atom now represented by $N = 32$ ring-polymer beads at 300 K, and $N = 64$ at 150 K (the same numbers required to converge QCMD [107]). The ring polymers were subject to a path-integral Langevin equation (PILE) thermostat, as described in ref. 132. For the production runs, only the fluctuation modes were thermostatted, with friction coefficients set to the corresponding natural frequencies $2\sin(\beta_N\hbar|\omega_k|/2)/\beta_N\hbar$, whereas for equilibration, the centroid was subject to the same thermostatting employed in the classical simulations. Under the conventions laid out in ref. 132, this combination of PILE with local Langevin thermostatting of the centroid is denoted PILE-L. As per Eq. (2.106b), the dipole moment averaged over the ring-polymer beads was used to evaluate the TRPMD approximation to the Kubo-transformed dipole-derivative ACF.

For the LSC-IVR simulations, we employed the local Gaussian approximation (LGA) of Liu and Miller [60] to sample from the Wigner quasi-probability distribution, so the method is more accurately described as LSC-IVR+LGA. The LGA is an extension of the local harmonic

approximation (LHA) due to Shi and Geva [57], and is described in more detail in Appendix A.3. As for classical MD, the LSC-IVR+LGA production runs constituted Newtonian trajectories of several independent molecules, along which their dipole moments were evaluated. However, the procedure for sampling initial conditions was more involved. In order to sample from the marginal position probability density of the Wigner distribution, a set of ring polymers with the same specifications as for TRPMD were propagated under PILE-L for 2.5 ns, with one system replica (i.e., set of beads with the same index) being randomly selected at intervals of 0.125 ps. The configuration of that replica was then used to initialise a production run. The mass-weighted Hessian of the PES was evaluated at the same configuration by finite difference, so that its eigenvectors and eigenvalues could be used to sample initial momenta from the LGA conditional momentum distribution of Eq. (A.28). However, to mitigate artefacts that would arise from treating the free rotations as locally harmonic, the eigenvalues corresponding to free rotation were set to zero, such that the momentum distribution became Maxwellian for those degrees of freedom. Five sets of initial momenta were sampled independently for each initial configuration, yielding a total of 5×10^5 single-molecule trajectories. The LSC-IVR+LGA approximation to the symmetrised dipole-derivative ACF (equivalent to the real part of the standard ACF) was evaluated as per Eq. (2.81), with Eq. (A.32). Because Newtonian trajectories do not conserve the Wigner distribution, time averaging could not be performed, hence the ACF was obtained by averaging over the initial conditions only.

The IR spectra were obtained as per Eq. (2.51c) (quantum, QCMD, TRPMD), Eq. (2.51b) (LSC-IVR+LGA), or Eq. (2.52b) (classical). They were each convolved with the Hann filter

$$\tilde{f}_{\mathrm{H}}(\omega) = \frac{\pi \sin(w\omega)}{2\omega(\pi^2 - w^2\omega^2)}, \tag{4.1}$$

where $w = 0.75$ ps, which is equivalent to damping the Kubo-transformed dipole-derivative ACFs using the Hann window[a] [158]

$$f_{\mathrm{H}}(t) = \begin{cases} \cos^2(\pi t/2w) & |t| \leqslant w \\ 0 & |t| > w. \end{cases} \tag{4.2}$$

In the exact quantum case, this serves to mimic quantum decoherence, washing out some of the rotational fine structure usually observed in the gas phase (so that each band is represented by a smooth peak, rather than a series of lines). For the approximate methods, it serves to damp the long-time tails of the ACFs (which are difficult to converge numerically), reducing ringing artefacts in the corresponding spectra.

---

[a]In practice the raw LSC-IVR+LGA result, which approximates the symmetrised ACF, was first converted to the Kubo-transformed version using Eq. (2.37) and (2.43) to make the desired convolution easier to achieve.

4.1.2 Comparison of methods

In Fig. 4.1, we plot the classical, QCMD, and quantum IR spectra for gas-phase water at 300 K and 150 K. The quantum spectra are replotted with the TRPMD and LSC-IVR+LGA spectra in Fig. 4.2. The peaks are assigned up to $\|\Delta\mathbf{n}\|_1 = 2$ following ref. 153, using $\nu_1, \ldots, \nu_3$ to denote the frequencies of the symmetric stretch, bend, and antisymmetric stretch respectively.

Focusing first on the fundamental bands, which dominate the mid- to far-IR regions (0–4250 cm^{-1}) of the spectra, we find that classical MD gives generally good agreement with exact quantum mechanics, except that the stretch fundamental (ν_1/ν_3) band system has the wrong internal structure and is blueshifted by ~150 cm^{-1} (slightly more at the lower temperature). The bend fundamental (ν_2) band is also blueshifted, but by a much smaller amount. These blueshifts are easily explained as the result of classical MD missing the quantum zero-point energy, whereas the incorrect internal structure is probably caused by the neglect of real-time coherence effects on the rovibrational coupling.

QCMD produces spectra with similar lineshapes to classical MD, but the position of the ν_1/ν_3 band system is improved significantly, with its blueshift reduced to ~60 cm^{-1}. The cause of this residual, temperature-independent blueshift is not well-understood—it could be related to the inaccurate treatment of centroid–fluctuation coupling, or perhaps the neglect real-time coherence. Yu and Bowman suggested the latter explanation for the much larger blueshifts that they observed in TRPMD simulations of a highly anharmonic, protonated water cluster [105]. Nonetheless, QCMD gives overall excellent agreement with the exact quantum spectrum in the mid- to far-IR region. The reader is referred to refs. 77, 107 for more detailed discussions of this method.

TRPMD gives similar predictions to QCMD for the peak positions, but the lineshapes are unphysically broadened and under-structured, owing to the effect of the thermostat coupling weakly to the centroid vibrations. This is especially apparent in the lower temperature spectrum. Essentially, TRPMD gives damped versions of the QCMD spectra, but at much lower computational cost, since one is not required to achieve near-adiabatic separation between the (quasi-)centroid and the fluctuations around it. The unphysical broadening problem could be somewhat mitigated by using appropriately tuned, coloured-noise thermostats, in place of the conventional white-noise thermostats attached to the fluctuation modes [104, 106].

The LSC-IVR+LGA method predicts a ν_1/ν_3 band system that is visually very similar to that of TRPMD, but the cause of unphysical broadening is now the degradation of the initial quantum distribution, rather than any sort of thermostatting. While zero-point energy 'leakage' into intramolecular degrees of freedom is clearly impossible in a simulation of non-interacting molecules, the damping can be regarded partly as a consequence of the jagged (non-Matsubara) fluctuation modes participating in the dynamics [73].

The contrast between the methods is more pronounced when we turn to overtone and
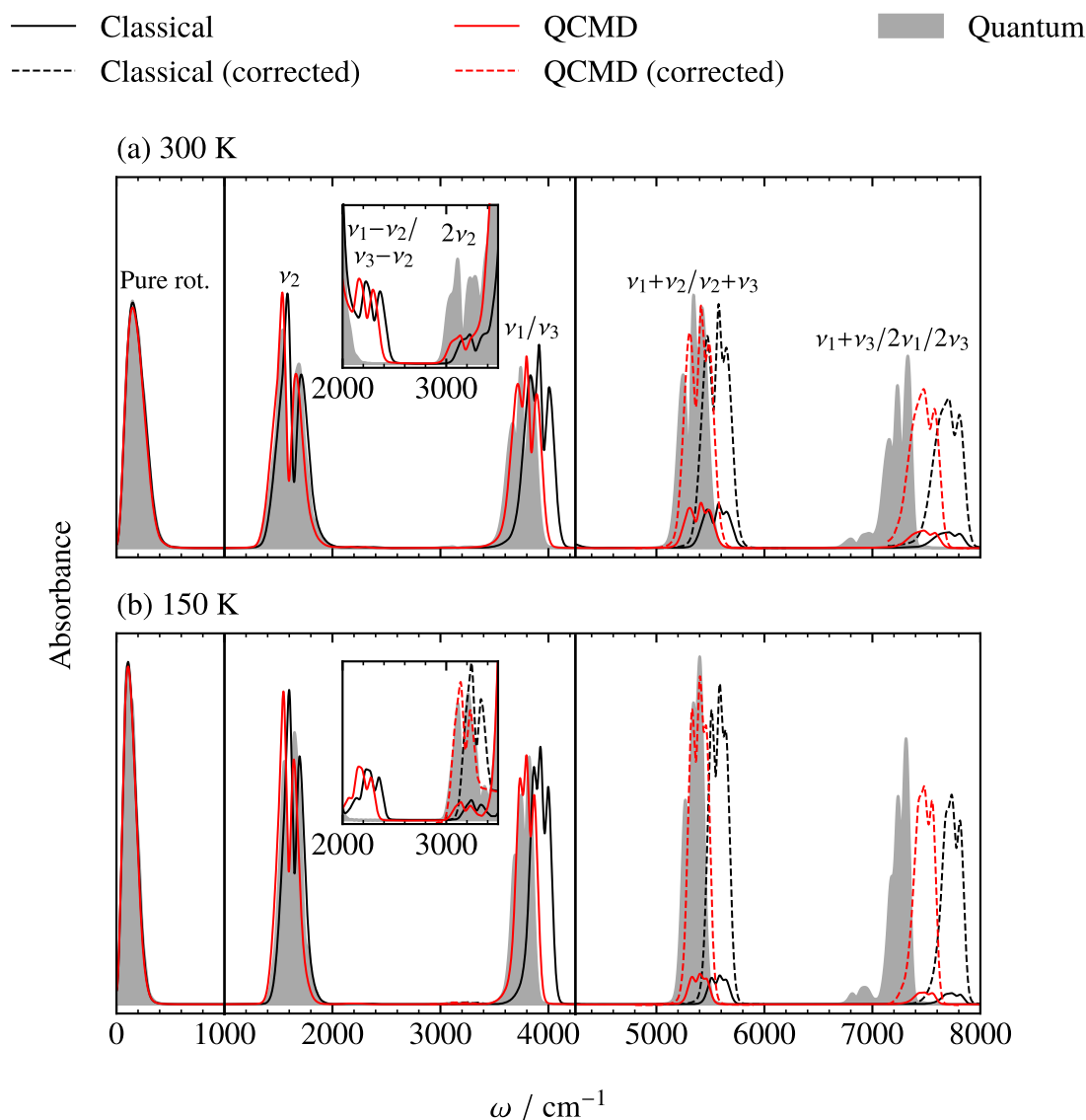
Figure 4.1: Classical, QCMD, and quantum IR absorption spectra calculated for gas-phase water using the Partridge–Schwenke PES [153] and DMS [154]. The QCMD results have been adapted from ref. 107. We also show (as dashed lines) the effects of correcting the classical and QCMD $\|\Delta\mathbf{n}\|_1 = 2$ band intensities as a post-processing step, where possible, using the scaling factors of Eq. (3.119). The absorbances in the three panels of each graph are scaled as $1 : 5 : 70$ (left-to-right), while the absorbances in the insets are each scaled by a factor of 70 relative to the panels in which they appear.

combination bands, which dominate the near-IR regions (4700–8000 cm^{-1}) of the spectra. In the quantum spectra, the $\nu_1 + \nu_2/\nu_2 + \nu_3$ combination band system at ~5300 cm^{-1} obtains most of its intensity from $\nu_2 + \nu_3$, whereas the $\nu_1 + \nu_3/2\nu_1/2\nu_3$ system at ~7300 cm^{-1} may be referred to colloquially as the 'stretch overtone', but is actually dominated by $\nu_1 + \nu_3$ [153]. We also observe the $2\nu_2$ band at ~3200 cm^{-1}. As expected from the analysis of Chapter 3, the centroid-
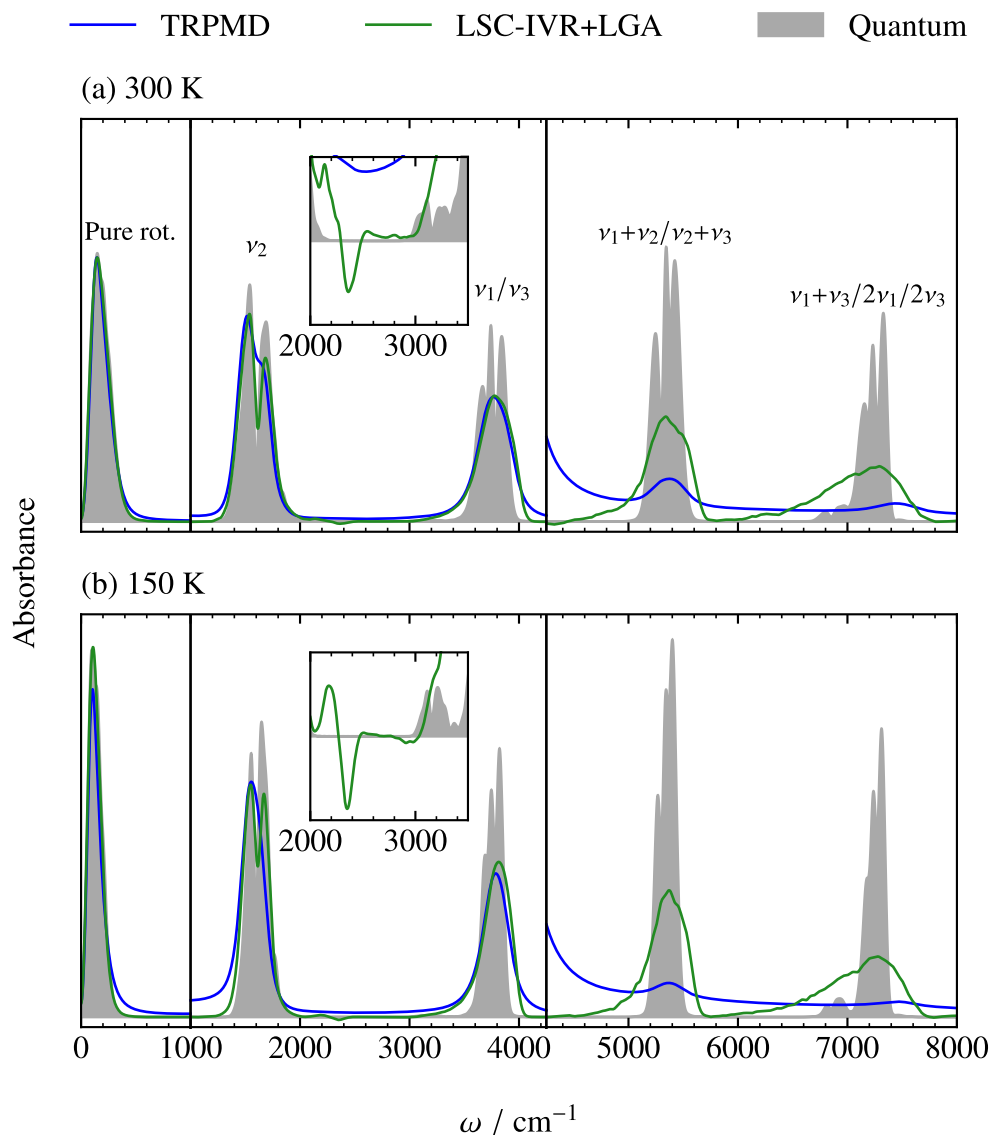
Figure 4.2: TRPMD, LSC-IVR+LGA, and quantum IR absorption spectra calculated for gas-phase water using the Partridge–Schwenke surfaces. The absorbances in the three panels of each graph are scaled as 1 : 5 : 70 (left-to-right), while the absorbances in the insets are each scaled by a factor of 25 relative to the panels in which they appear. The assignments of the features visible in the insets are omitted here for clarity, but are given in Fig. 4.1.

following methods (QCMD and TRPMD) capture only small fractions of the true intensities of these bands, performing no better than classical MD in this respect. In fact, the damping effect of the thermostat in TRPMD results in the high-frequency tails of one or more fundamental bands extending into the near-IR region, overlapping with the combination bands so that they appear almost washed out, whereas the $2\nu_2$ band (which almost coincides with ν_1/ν_3) is washed out entirely. Classical MD and QCMD additionally predict absorption at $\sim$2200 cm^{-1}, which

corresponds to the $v_1 - v_2/v_3 - v_2$ difference band system and is too weak to be visible in either of the quantum spectra. This is consistent with the counterintuitive diminishing of difference band intensity caused by Matsubara heating, as discussed in Section 3.3.3. Finally, it is notable that the residual blueshift of the centroid-following methods, mentioned above for the v_1/v_3 system, is enhanced by a factor of ~ 3 for $v_1 + v_3/2v_1/2v_3$.

On the other hand, LSC-IVR+LGA reproduces $\sim 80\%$ of the integrated intensity of $v_1 + v_2/v_2 + v_3$, and more than 90% of that of $v_1 + v_3/2v_1/2v_3$ (taking the boundary between the two band systems to be at 5800 cm^{-1}). While ostensibly promising, the near-quantitative accuracy of the latter intensity is almost certainly due, in part, to fortuitous cancellation of errors; Plé *et al.* showed that the neglect by the LGA of non-local correlations between momentum and position can lead overtone and combination band intensities to be *over*estimated, assuming the DMS is linear [65]. Our simulations employed the nonlinear Partridge-Schwenke DMS, however, and utilised a crude approximation to the static dipole-derivative estimator that effectively neglects its dependence on the non-Matsubara modes (see Appendix A.3). Even so, it is clear that LSC-IVR is the only one of the approximate methods capable of providing a reasonable description of this part of the spectrum without modification. The anharmonic features in the mid-IR region are described less well, with $2v_2$ washed out by the artificial broadening of v_1/v_3, and $v_1 - v_2/v_3 - v_2$ corrupted by a region of non-negligible negative absorbance. This negative absorbance is a clear manifestation of the violation of detailed balance. However, LSC-IVR is expected to perform better when combined with a more accurate (but expensive) method to sample from the Wigner conditional momentum distribution that accounts properly for quantum correlations, such as the Edgeworth conditional momentum approximation (ECMA) [65].

For completeness, in Appendix C.1, we plot the spectra obtained using the simpler q-TIP4P/F PES and DMS [33]. For LSC-IVR+LGA and exact quantum mechanics we also include the 300 K 'mixed' spectra, obtained using the Partridge–Schwenke PES combined with the q-TIP4P/F DMS and vice versa, in an effort to disentangle the effects that changing each surface has on the absorption bands. Most notably, we find that changing the DMS from nonlinear (Partridge–Schwenke) to linear (q-TIP4P/F) brings the LSC-IVR+LGA combination band intensities into apparently *worse* agreement with exact quantum mechanics, but better agreement with the PT results of Plé *et al.* [65].

4.1.3   Post-processing correction

We would ideally like to combine the quality of the lineshapes predicted by QCMD with intensities as least as accurate as those of LSC-IVR+LGA. In principle, we believe that Matsubara dynamics would achieve this goal, but it is too expensive to converge for even a system as small as a single water molecule. A more practical option is to apply the scaling

factors of Eq. (3.119) to the overtone and combination bands, taking Ω_i and Ω_j in each case to be the first moments of the corresponding fundamental bands or band systems. Fig. 4.1 shows the resulting QCMD spectra at 300 K and 150 K. The QCMD $\nu_1 + \nu_2/\nu_2 + \nu_3$ and $\nu_1 + \nu_3/2\nu_1/2\nu_3$ intensities are each raised to ~110% of the corresponding quantum intensities, which is remarkably close given the simplicity of the model used to derive Eq. (3.119). The $2\nu_2$ band is raised to ~105% of the quantum intensity at 150 K, but we do not attempt to correct it in the 300 K spectrum, where it overlaps more significantly with the ν_1/ν_3 band. We also opt not to show the result of applying Eq. (3.119) to the difference band system at either temperature, which would essentially amount to removing the feature entirely. Since classical MD gives intensities in close agreement with QCMD, we include the results of applying the overtone and combination scaling factors to the classical spectra as well, illustrating that the usefulness of this post-processing approach is not necessarily limited to systems for which the results of expensive path-integral simulations are available (provided that one is not too concerned with the accuracies of the peak positions).

4.2   Gas-phase ammonia

To provide a more challenging test for our post-processing correction approach, we calculated the classical spectra of ammonia at 300 K and 150 K. We employed the PES-2 surface and AQZfc DMS described by Yurchenko *et al.* in ref. 159. The peaks are assigned up to $\|\Delta \mathbf{n}\|_1 = 2$ following ref. 159, using $\nu_1, \ldots, \nu_4$ for the symmetric stretch, symmetric bend, asymmetric stretch, and asymmetric bend respectively (notation originally due to Herzberg [160]).

4.2.1   Computational details

The quantum spectra were obtained directly using the line list data supplied as Supporting Information to ref. 159.

In the classical simulations, the dipole moments of several independent ammonia molecules were recorded along microcanonical production runs, each of length 1 ps, to yield a total of 10^5 single-molecule Newtonian trajectories. Prior to each production run, the molecules were subject to an equilibration run of average length 0.1 ps, under the influence of a local Langevin thermostat [155, 156] with friction coefficient 10 ps^{-1} (OBABO propagator splitting [157]). A time step of 0.125 fs was used throughout. The dipole-derivative ACF was calculated for $0 \leqslant t < 1$ ps by time averaging over the production runs.

As for gas-phase water, the classical ammonia ACFs were damped prior to Fourier transformation using a Hann window of width $w = 0.75$ ps. For the quantum spectra, the same effect was achieved in the frequency domain, simply representing each spectral line by the (appropriately shifted and scaled) Hann filter $\tilde{f}_H(\omega)$ of Eq. (4.1).

4.2.2   Results and post-processing correction

The classical and quantum gas-phase ammonia spectra are plotted in Fig. 4.3. Compared to water, ammonia has a more crowded series of non-fundamental bands, including the $v_1 - v_2$ difference band which coincides with $v_2 + v_4$ around $2600\,\mathrm{cm}^{-1}$ (and, unlike the $v_1 - v_2/v_3 - v_2$ system of water, is intense enough to be resolved in the quantum absorbance). The peaks at $6000\,\mathrm{cm}^{-1}$ and $7800\,\mathrm{cm}^{-1}$ comprise $\|\Delta\mathbf{n}\|_1 > 2$ bands, which are beyond the scope of the present discussion, as is the $3v_2$ band that coincides (with comparable intensity) with the $v_1 - v_2/v_2 + v_4$ system. We have also neglected to label any non-fundamental bands that are dwarfed by close-by fundamental bands, such as $2v_4$, which overlaps with v_1/v_3.[b]

Similar to water, the lineshapes of the fundamental bands are fairly well captured by classical MD, but the neglect of zero-point energy causes a considerable blueshift to the v_1/v_3 band system. The combination bands and overtone that involve stretching vibrations are more severely blueshifted and, as expected, their intensities underestimated. In contrast, the classical $v_1 - v_2/v_2 + v_4$ system is an order of magnitude too intense; based on the analysis of Chapter 3, we would expect the main contribution to this peak to come from $v_1 - v_2$, with the $v_2 + v_4$ contribution *under*estimated by a comparably large factor.

We also include in Fig. 4.3 the 'corrected' classical spectra that result from applying the scaling factors of Eq. (3.119) to the $\|\Delta\mathbf{n}\|_1 = 2$ band systems. The classical intensities of the overtone and combination band systems are brought into much closer agreement with quantum results. Treating the difference band requires some more care, however, as it overlaps with two combination bands ($v_2 + v_4$ and $3v_2$). While it seems safe to assume that any contributions from the combination bands to the classical peak are small enough to ignore, this certainly does not hold true for the quantum spectra. To allow for a fair comparison, we include insets in which the assignments of ref. 159 have been used to isolate the $v_1 - v_2$ contributions to the quantum spectra. We find that the appropriate scaling factor reduces the classical intensity to ∼80% of the quantum intensity at 300 K, and ∼50% at 150 K.

4.3   Condensed-phase q-TIP4P/F water

The accuracies of path integral–based and other approximations to the vibrational spectra of condensed-phase water have already been studied extensively in the literature [28–30, 33, 34, 56, 67–69, 96, 97, 107, 116, 146, 147, 164]. However, the focus has almost entirely been on fundamental bands. The present section may be considered an extension of several previous studies in which TRPMD [29], QCMD [107], and LSC-IVR+LGA [28] were assessed for

---

[b]In fact, the $2v_4$ band is in Fermi resonance with the v_1 band, an effect more pronounced in the polarised Raman spectrum of the liquid [161–163]. Fermi resonances will be explored further in Chapter 5.
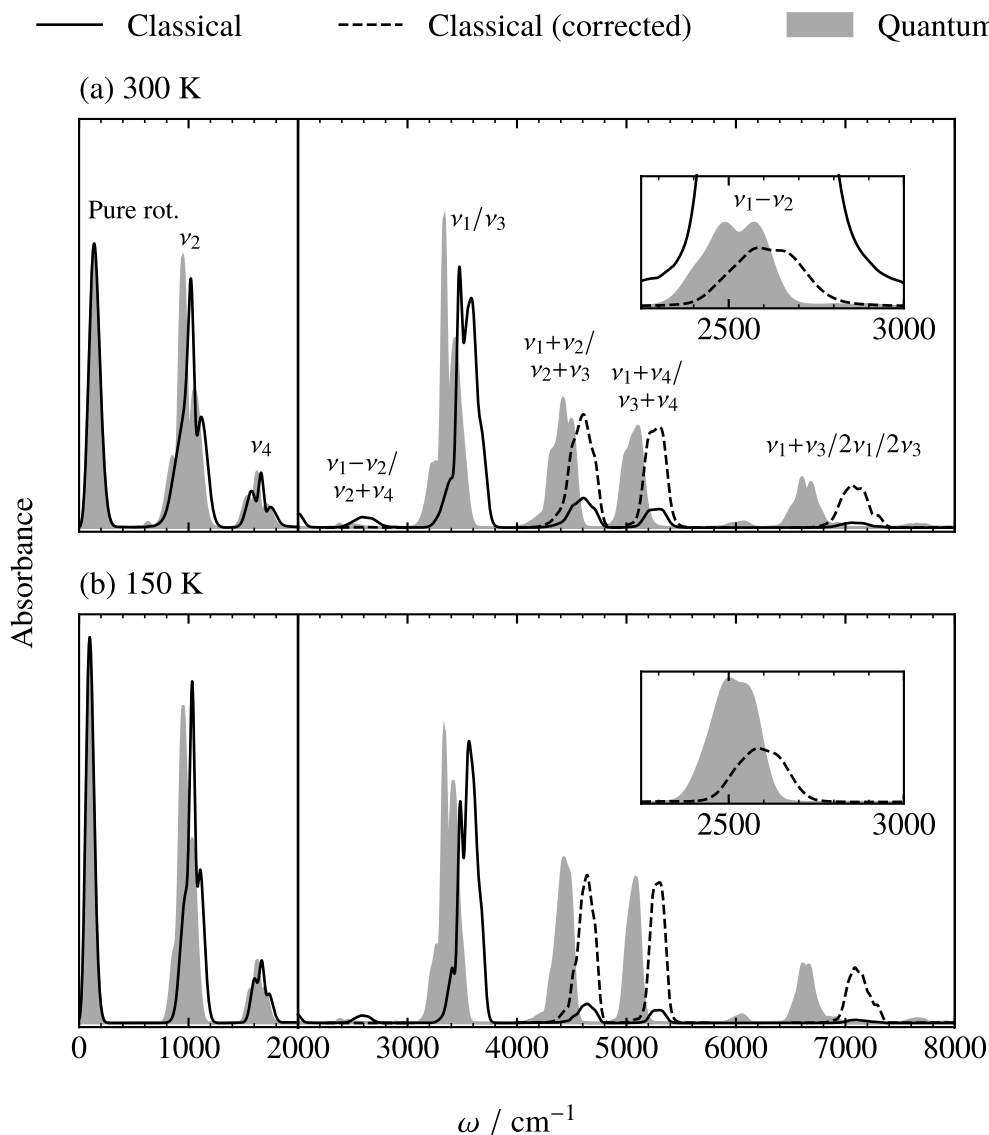
Figure 4.3: Classical and quantum IR absorption spectra calculated for gas-phase ammonia using the PES-2 surface and AQZfc DMS of Yurchenko *et al.* [159]. The quantum spectra were obtained directly using the line list data supplied as Supporting Information to ref. 159. We also show (as dashed lines) the effects of correcting the classical $\|\Delta\mathbf{n}\|_1 = 2$ band intensities as a post-processing step using the scaling factors of Eq. (3.119). Note that the scaling factor for the $v_1 - v_2$ difference band *reduces* its intensity (see inset—the 'uncorrected' difference band is too intense at 150 K to be visible in the inset of (b)). The absorbances in the two panels of each graph are scaled as 1 : 15 (left-to-right), while the absorbances in the insets are scaled by factors of (a) 1.6×10^3 (b) 1.6×10^5 relative to the panels in which they appear.

their performances in calculating the IR spectra of liquid water at 300 K and ice I_h at 150 K. To be consistent with all these studies, we have employed the q-TIP4P/F PES and associated point-charge (linear) DMS due to Habershon *et al.* [33]. These have the advantage of being

cheap, but are not accurate enough to allow for meaningful comparisons with experimental spectra. Furthermore, exact quantum calculations are unfeasible for systems of this size. Nevertheless, we will be able to make some cautious conclusions about the capabilities of the various methods, by drawing upon analogies with the gas-phase spectra of Section 4.1 and Appendix C.1.

4.3.1   Computational details

The raw data from classical MD, TRPMD, and QCMD simulations were provided by G. Trenins. Details of the TRPMD and QCMD simulations are given in ref. 107, where they were also used to generate IR spectra. The classical simulations were performed in an algorithmically identical fashion to TRPMD, but with the number of beads reduced to one. To be consistent with the other methods, the number of beads used for the PIMD component of our LSC-IVR+LGA simulations was $N = 32$ for 300 K liquid water and $N = 64$ for 150 K ice I_h. These are also consistent with our gas-phase simulations at the same temperatures. The liquid simulations employed periodic boundary conditions applied to cubic cells of side length 15.6404 Å, each containing 128 molecules. For ice, we used orthorhombic cells with dimensions $13.5552 \times 15.6522 \times 14.7570$ Å^3, each containing 96 molecules. A time step of 0.125 fs was used throughout.

For both the liquid and ice phases, the LSC-IVR+LGA simulations began with eight independently equilibrated ring-polymer simulation cells, which were taken from the TRPMD simulations of ref. 107. These were propagated for approximately 5 ns under the influence of a PILE-G thermostat, which combines PILE for the fluctuations with global Langevin thermostatting of the centroid [132]. The friction coefficients for the fluctuation modes were set to the corresponding natural frequencies $2\sin(\beta_N \hbar |\omega_k|/2)/\beta_N \hbar$, and that of the centroid to 10 ps^{-1}. The configuration of one replica was recorded at time intervals of 1 ps, yielding about 4×10^4 independent initial configurations, implicitly sampled from the marginal position probability density of the Wigner distribution.

The mass-weighted Hessian of the PES was evaluated at each of these configurations by finite difference, so that its eigenvectors and eigenvalues could be used to sample initial momenta from the LGA conditional momentum distribution of Eq. (A.28). Note that, in order to reduce the storage requirements for the Hessian matrices, they were sparsified prior to diagonalisation by setting to zero any off-diagonal elements corresponding to atoms separated by more than 2.6459 Å (5 a.u.). One set of initial momenta was sampled for each initial configuration, yielding a total of $\sim 4 \times 10^4$ phase-space points, from each of which a Newtonian trajectory of length 1 ps was propagated. The Newtonian trajectories were then used to estimate the symmetrised dipole-derivative ACF, as per Eq. (2.81) with Eq. (A.32).

The $\sim$40 ns thermostatted master trajectories were propagated using an in-house code

provided by G. Trenins, while the subsequent LGA sampling and Newtonian propagation were carried out using a modified version of the i-PI package due to Ceriotti and co-workers, with the included q-TIP4P/F driver [165].

As mentioned in Section 2.1.3, the energy absorption spectrum, $S_{q/c}(\beta; \omega)$, does not precisely correspond to the IR absorption spectrum. Rather, assuming three spatial dimensions, it is related to the Beer–Lambert absorption coefficient, $\alpha(\omega)$, (which is proportional to the absorbance) and frequency-dependent refractive index, $n(\omega)$, via

$$n(\omega)\alpha(\omega) = \frac{S_{q/c}(\beta; \omega)}{6c\mathcal{V}\varepsilon_0|\mathcal{E}|^2}, \tag{4.3}$$

where $\mathcal{V}$ is the volume of the sample, c is the speed of light in a vacuum, and ε_0 is the vacuum permittivity [101]. To achieve the closest possible connection with the quantities that would be measured experimentally for hypothetical quantum or classical q-TIP4P/F water, we choose to represent IR spectra by $n(\omega)\alpha(\omega)$, calculated using Eq. (4.3) with Eq. (2.51c) (QCMD, TRPMD), Eq. (2.51b) (LSC-IVR+LGA), or Eq. (2.52b) (classical), and taking $\mathcal{V}$ to be the volume of the simulation cell. The liquid-phase ACFs were damped prior to Fourier transformation using a Hann window of width $w = 0.6$ ps, whereas for ice, a broader window of width $w = 0.8$ ps was required to fully resolve the classical and QCMD spectra (on account of the splitting of the stretch band into symmetric and antisymmetric components—see Fig. 4.4— which is an artefact of the q-TIP4P/F potential).

4.3.2   Comparison of methods

In Fig. 4.4, we plot the IR spectra for liquid water at 300 K and ice I_h at 150 K, as given by classical MD, QCMD, TRPMD, and LSC-IVR+LGA.[c] The most prominent peaks have been assigned by analogy with the gas-phase spectra, but since intermolecular coupling causes the wave functions of individual molecules to be ill-defined, we label bands just by the nature of the vibrations involved (stretch, bend, or libration), rather than the specific normal modes being excited.

---

[c]Note that the LSC-IVR+LGA results for the liquid were calculated using very similar parameters to those employed in ref. 28, but there are small discrepancies between the resulting spectra, because ours was obtained from the symmetrised ACF and the spectrum in ref. 28 from the Kubo-transformed ACF. We found that using symmetrised ACFs resulted in less noisy spectra, especially in the near-IR regions, but that the low-frequency (librational) regions ended up in slightly worse agreement with classical MD (which is expected to be accurate there). We plot the spectra obtained from the Kubo-transformed ACFs in Appendix C.2.
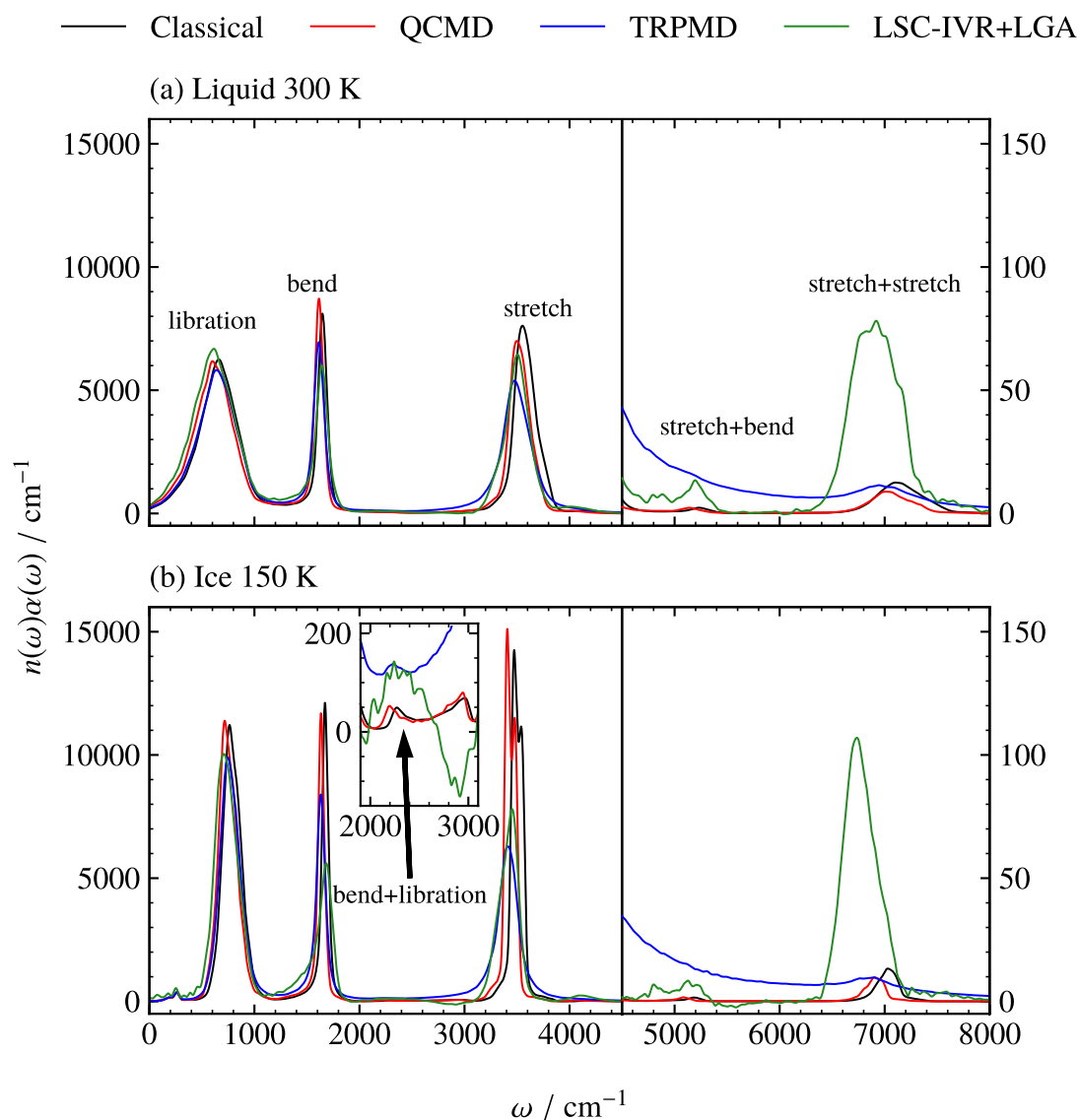
Figure 4.4: Classical, QCMD, TRPMD, and LSC-IVR+LGA IR absorption spectra calculated for liquid water and ice I_h using the q-TIP4P/F PES and DMS [33]. The QCMD and TRPMD results have been adapted from ref. 107, and the classical results (calculated in a similar fashion) were provided by G. Trenins. The inset of (b) magnifies the region of the bend–libration combination band, as well as the suspected stretch–libration difference band (not labelled), which carries erroneously negative absorbance in the LSC-IVR+LGA spectrum.

Fundamental bands and zero-point energy leakage

In the mid- to far-IR region, classical MD, QCMD, and TRPMD behave similarly as they do in the gas phase. Namely, TRPMD gives broadened versions of the QCMD spectra, which we suspect gives fundamental bands close to what would be obtained from exact quantum calculations. Classical MD, on the other hand, gives lineshapes in very good agreement

with QCMD, but the neglect of zero-point energy causes the stretch band to be considerably blueshifted (especially in the ice spectrum).

The LSC-IVR+LGA results are in reasonable agreement with QCMD overall, but the broadening of the bend and stretch bands is more severe than in the gas phase. The bend suffers a blueshift that grows upon decreasing the temperature, while the libration suffers an increasing redshift. While deficiencies of the LGA (especially applied to the very anharmonic librational degrees of freedom) may have some part to play, these artefacts are thought to be due predominantly to the violation of detailed balance, which in the condensed phase causes zero-point energy to 'leak' into the intermolecular degrees of freedom. Habershon and Manolopoulos investigated this phenomenon in their LSC-IVR+LGA simulations of the 300 K liquid. They found that the instantaneous centre-of-mass temperature, defined as

$$T_{\text{cm}}(t) = \frac{2}{3k_{\text{B}}} \frac{1}{(2\pi\hbar)^F Z_{\text{q}}(\beta)} \int \mathrm{d}^F\mathbf{p} \int \mathrm{d}^F\mathbf{q} \left[\hat{U}(-\mathrm{i}\beta\hbar) \right]_{\text{W}}(\mathbf{p}, \mathbf{q}) \, \mathrm{e}^{\mathcal{L}t} \frac{1}{F/9} \sum_{r=1}^{F/9} \mathcal{T}_r(\mathbf{p}), \qquad (4.4)$$

increases by almost 400 K over the course of the 1 ps simulation [28], where $\mathcal{T}_r(\mathbf{p})$ is the classical centre-of-mass kinetic energy of water molecule r and the Wigner distribution is here understood to be approximated by the LGA. The leakage thus raises the effective temperature of the libration (which is intermolecular), while lowering that of the bend (which is intramolecular). We can rationalise the blueshift of the bend and redshift of the libration by observing that both the corresponding bands in the classical spectrum are blueshifted as the temperature is lowered. The stretch is not as severely affected, probably because it does not couple as strongly to the librational modes (the bending motion being closer in frequency to the libration).

Relative to the initial distribution, our simulations of 150 K ice suffer an even larger zero-point energy leakage, with $T_{\text{cm}}(t)$ rising by ~300 K as shown in Fig. 4.5. This was calculated by averaging over ~5000 LSC-IVR+LGA trajectories. Superimposed on the graph are visualisations of the ice simulation cell at several points along a typical one of these trajectories, which reveal that the observed rise in $T_{\text{cm}}(t)$ is sufficient to melt the contents of the cell within 1 ps. While the deterioration of the (approximate) quantum Boltzmann distribution appears rather dramatic based on Fig. 4.5, it is important to remember that it occurs on a similar timescale to the decorrelation of the dipole-derivative ACF. This is why it does not lead to a similarly dramatic deterioration of the IR spectrum.

**Overtone and combination bands**

The lack of free rotation in the condensed phase gives rise to certain peaks not present in the gas-phase spectra, most notably the bend–libration combination band around 2300 cm^{-1} in the ice spectrum (in the liquid spectrum, this becomes difficult to separate from the bend fundamental
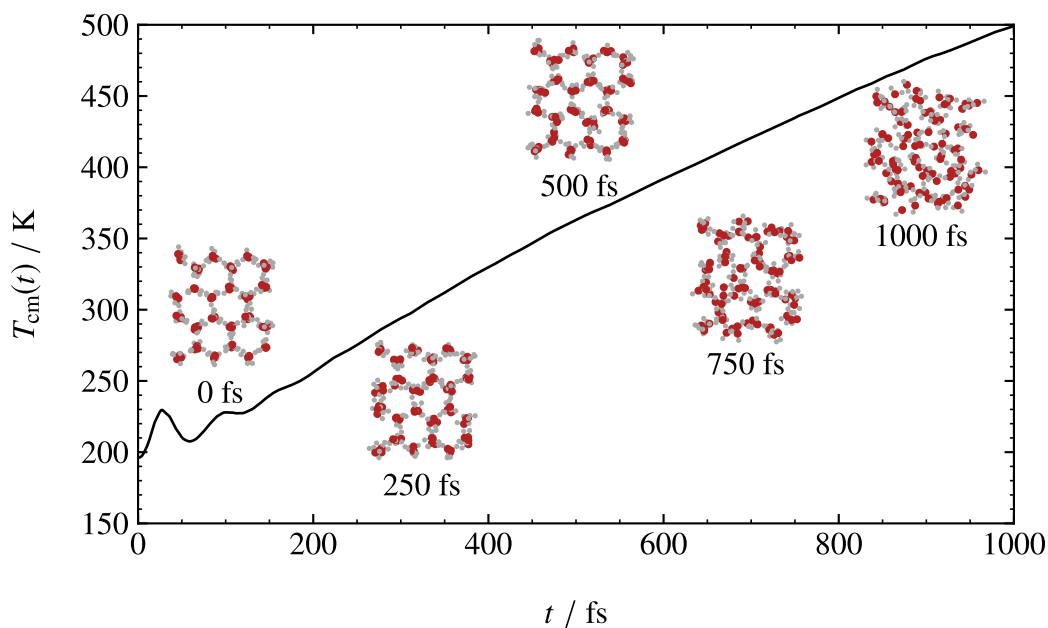
Figure 4.5: Plot of instantaneous centre-of-mass temperature, as defined in Eq. (4.4), against time for ice I_h. Superimposed on the graph are visualisations of the ice simulation cell at 250 fs intervals along a typical LSC-IVR+LGA trajectory. The crystalline order has visibly deteriorated by 1 ps, as a result of intramolecular zero-point energy 'leaking' into the intermolecular degrees of freedom.

band). This assignment was confirmed in ref. 29 using the local monomer (LMon) method, whereby the time-independent Schrödinger equation is solved numerically for a small number of individual molecules selected from snapshots of the PIMD simulation cell, while freezing most of the intermolecular degrees of freedom [166, 167]. In Fig. 4.6 we replot the QCMD and LSC-IVR+LGA results alongside those of LMon-4, for which a single intermolecular mode was un-frozen (in addition to the three intramolecular modes). The raw LMon-4 line spectra, which were provided by the authors of ref. 29, have been convolved with the appropriate Hann filter (see Eq. (4.1)) and scaled such that the intensity integrated over 3000–4250 cm^{-1} matches that of QCMD.

Since LMon-4 neglects most of the intermolecular dynamics, it gives fairly poor predictions of the libration bands, but good agreement with QCMD for the bend and stretch bands. On the other hand, QCMD captures only a small fraction of the bend–libration combination intensity that is predicted by LMon-4. This was also noted in ref. 107, where it was speculated that this feature depends on an accurate description of Matsubara fluctuations; the perturbative analysis of Chapter 3 confirms this interpretation. Classical MD and QCMD each give an artefact at ~2900 cm^{-1}, which we suspect could be a stretch–libration difference band that has been erroneously intensified by the neglect of Matsubara heating, whereas LMon-4 gives a bend
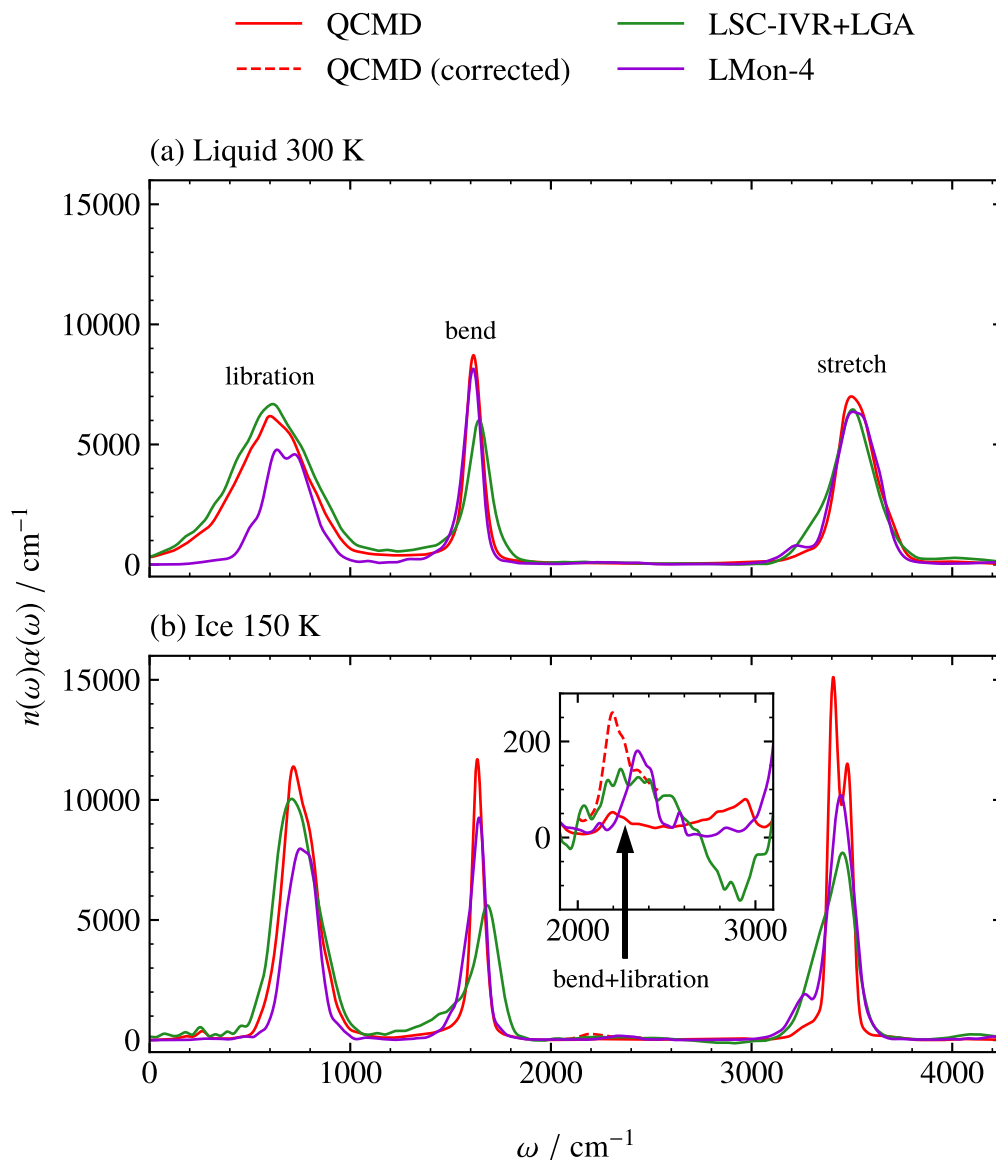
Figure 4.6: The same QCMD and LSC-IVR+LGA results as in Fig. 4.4, compared against the LMon-4 results from ref. 29. 'Correcting' the QCMD bend–libration combination band (dashed line) using the appropriate scaling factor (Eq. (3.119)) brings its intensity closer to that predicted by LMon-4, but the theoretical justification of this post-processing procedure is somewhat questionable in the condensed phase.

overtone at ~3200 cm^{-1}. It is likely that this overtone borrows some intensity from the stretch fundamental band as a result of Fermi resonance (see Chapter 5). LSC-IVR+LGA seems to give a reasonable prediction of the combination band, and a broadened version of the overtone that has the effect of skewing the stretch fundamental band. However, the spectrum is contaminated by a significant region of negative absorbance where the difference band would be; this is clearly an artefact brought about by the violation of detailed balance, and is consistent with Plé

et al.'s perturbative analysis of LSC-IVR+LGA difference bands at low temperatures [65].

One would expect our post-processing correction approach, which interprets Eq. (3.119) as a class of scaling factors for $\|\Delta\mathbf{n}\|_1 = 2$ bands, to be much less reliable for the condensed phase than for the gas phase. For condensed-phase water in particular, the intensities are affected by anharmonic coupling through hydrogen bonds, and such effects are clearly missing from the simple perturbative model considered in Chapter 3. Furthermore, the peaks in condensed-phase spectra tend to be less well separated and more difficult to assign. Nevertheless, in the inset of Fig. 4.6, we include the 'corrected' QCMD bend–libration combination band as a proof of principle. Indeed, it is intensified such that it somewhat more resembles the corresponding LMon-4 peak, but the validity of the rescaling is especially dubious here, given the significant extent to which the combination band overlaps with other peaks, as well as the somewhat arbitrary way in which the LMon-4 data was scaled in the first place.

Turning to the near-IR region, LSC-IVR+LGA predicts much stronger intensities than classical MD, QCMD, and TRPMD, just as in the gas-phase spectra. Unfortunately, converged LMon-4 data is not available for this region of the spectrum, so we have no benchmark against which to assess the accuracies of the trajectory-based methods. However, based on our gas-phase results, it seems likely that LSC-IVR+LGA captures intensities reasonably close to what would have been obtained from an exact quantum calculation, but with the lineshapes erroneously broadened because of the violation of detailed balance. The broadening problem is probably worse in the condensed phase than in the gas phase, given the large zero-point energy leakage phenomenon described above.

The relative intensities of the LSC-IVR+LGA $\|\Delta\mathbf{n}\|_1 = 2$ bands in the condensed phase are different from those of their gas-phase counterparts in Fig. 4.2: the stretch overtone at $\sim$7000 cm^{-1} is much stronger than the stretch–bend combination band at $\sim$5200 cm^{-1}. However, this is almost certainly a result of the different choice of (monomer) DMS, given that a similar change in intensity is found when the gas-phase calculations are repeated using the q-TIP4P/F DMS. These results are reported in Appendix C.1. Another difference from the gas-phase is the feature at $\sim$4000 cm^{-1} (visible in Fig. 4.4 but not magnified), which appears as a shoulder on the stretch fundamental band for the liquid, but for ice separates into a well-defined peak. Based on its frequency, we suggest that this feature is a stretch–libration combination band.

4.4 A more accurate model of liquid water: MB-pol/MB-μ

There is little to be achieved by applying our post-processing correction approach to the near-IR regions of the q-TIP4P/F condensed-phase spectra, since we lack a reliably accurate benchmark against which to assess the results. More sophisticated water surfaces have been developed,

however, that allow path-integral simulations (or wave function–based approaches such as LMon) to reproduce experimental properties with far greater accuracy. In particular, the WHBB PES due to Bowman and co-workers [56, 164, 166, 168, 169] and the MB-pol PES due to Paesani and co-workers [30, 97, 118–120, 146, 147, 170] both employ the spectroscopically accurate Partridge–Schwenke PES for the intramolecular contributions, and a many-body expansion fitted to *ab initio* electronic structure data for the intermolecular contributions [171].

Here we report the classical spectrum of liquid water at 298.15 K, calculated by G. Trenins using the MB-pol PES [118–120] and associated MB-μ DMS [97]. Unlike q-TIP4P/F, the MB-μ DMS includes induced dipole effects, which allows it to yield far better agreement with experimental spectral intensities. The q-TIP4P/F bend fundamental band, for instance, is comparable in intensity to the stretch band, whereas experimentally it is much weaker. For water, the choice of DMS is somewhat more important than the choice of PES for capturing the relative intensities of vibrational absorption bands, as demonstrated in refs. 164, 170, and also evident from our 'mixed' gas-phase spectroscopy results in Appendix C.1. This is because the IR activity of a given vibration is largely controlled by the derivative of the dipole moment along the corresponding normal mode coordinate, whereas the underlying potential mostly controls the positions and widths of the peaks.

The classical simulation involved eight independent, cubic cells of side length 18.6428 Å, each containing 216 water molecules and subject to periodic boundary conditions. They were equilibrated by propagating for 250 ps under a global Langevin thermostat [155, 156] (BAOAB propagator splitting [157]) with friction coefficient 10 ps^{-1}, using a time step of 0.2 fs. The dipole-derivative ACF was then calculated for $0 \leqslant t \leqslant 0.6$ ps by time averaging over a 100 ps production run, in which each cell was propagated under the same conditions as for equilibration. The spectrum $n(\omega)\alpha(\omega)$ was calculated using Eq. (4.3) with Eq. (2.51c), damping the ACF prior to Fourier transformation with a Hann window of width $w = 0.6$ ps.

In Fig. 4.7, we plot the classical IR spectrum alongside the experimental spectrum of Bertie and Lan [172]. The high quality of the PES and DMS suggest that the main differences arise from the approximate treatment of the quantum statistics and dynamics inherent to classical MD. The fundamental band intensities are mostly in reasonable agreement with experiment, with the ~40% underestimate of the integrated stretch intensity probably due mostly to the neglect of quantum statistical sampling of the nonlinear dipole moment. The poor treatment of the bend overtone component by classical MD could also be partly responsible. Note that the MB-pol/MB-μ CMD spectrum of ref. 97 also underestimates the integrated intensity of the stretch fundamental band, but only by ~20%.

As expected, classical MD strongly underestimates the intensities of the stretch overtone, as well as the bend–libration and stretch–bend combination bands. While the theoretical justification for applying the scaling factors of Eq (3.119) to condensed-phase spectra may
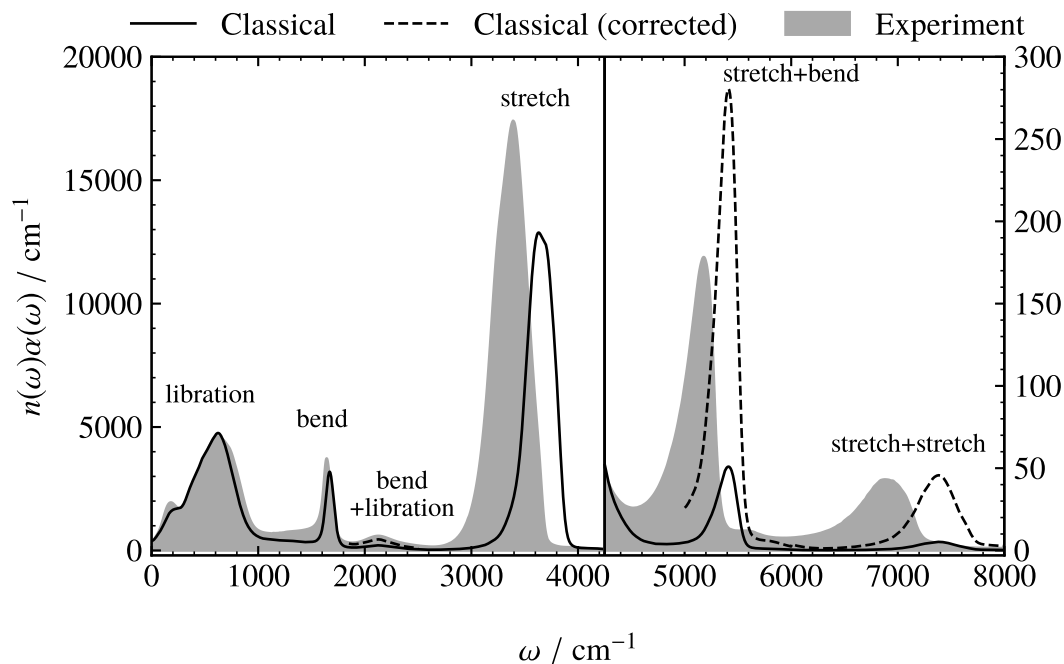
Figure 4.7: Classical IR spectrum of liquid water at 298.15 K, computed using the MB-pol PES [118–120] and MB-μ DMS [97], compared with the experimental spectrum of ref. 172. To enable direct comparison with MD results, the experimental spectrum is represented by $n(\omega)\alpha(\omega)$, calculated from the raw experimental data downloaded from ref. 173. 'Correcting' the classical non-fundamental intensities using the appropriate scaling factors (Eq. (3.119)) brings their intensities somewhat closer to those predicted by experiment.

be questionable, in this case we find that it brings each of the $\|\Delta\mathbf{n}\|_1 = 2$ bands qualitatively somewhat closer to experimental results. It is least successful for the stretch–bend combination band, which ends up considerably more intense than its experimental counterpart.

4.5   Discussion

Each of the simulation methods discussed in this chapter has its advantages within the context of condensed-phase vibrational spectroscopy. For condensed-phase water, QCMD provides highly accurate descriptions of the fundamental bands, although further work is required to generalise this method to other systems. TRPMD provides damped versions of the QCMD spectra at much lower computational cost, and for now has the significant advantage of being formulated generally, so it is applicable to other molecular systems. In fact, aside from classical MD, TRPMD is probably the closest to a 'black-box' method of all those considered. LSC-IVR+LGA gives comparable accuracy to TRPMD for the fundamental bands, but has the advantage over centroid-following methods of giving a *qualitatively reasonable* description of anharmonic (non-fundamental) absorption intensities, in particular those of $\|\Delta\mathbf{n}\|_1 = 2$ bands

(but excluding binary difference bands, for which one requires a more accurate approximation to the Wigner distribution that accounts for the $t = 0$ momentum–position correlations [65]). LMon provides a crude description of intermolecular dynamics, but unlike trajectory-based approaches, involves explicitly solving the time-independent Schrödinger equation and is thus able to treat fundamental and non-fundamental bands on an equal footing. Even classical MD, the cheapest method, is not necessarily useless for systems with highly quantum nuclei, provided both the mechanical and electrical anharmonicities are reasonably small as is the case for q-TIP4P/F water.

LSC-IVR+LGA is unreliable at low temperatures, where zero-point energy leakage causes q-TIP4P/F ice I_h to melt on a sub-picosecond timescale (an effect that would presumably be replicated by LSC-IVR proper if it could be simulated for such a large system—the leakage is not thought to be strongly related to our choice of the LGA to sample the momenta). In this regime, a preferable approach to predicting $\|\Delta\mathbf{n}\|_1 = 2$ intensities might be to apply the scaling factors of Eq. (3.119) as post-processing corrections to the QCMD spectrum, however this is limited to systems for which the $\|\Delta\mathbf{n}\|_1 = 2$ bands are well separated and can be assigned. Alternatively, provided with a highly accurate PES and DMS, the scaling factors could be employed to help confirm whether a proposed assignment is reasonable (by comparing the 'corrected' [Q]CMD or classical intensities with experimental results). There is also no reason Eq. (3.119) could not be generalised to $\|\Delta\mathbf{n}\|_1 > 2$ bands, although it is unclear whether its physical origin would still be interpretable as Matsubara heating.

Chapter 5

Fermi resonances

The results of Chapters 3 and 4 demonstrate that the effects responsible for making quantum overtone and combination bands more intense (and difference bands less intense) than their classical counterparts can be mostly captured by first-order perturbation theories applied to a harmonic reference system. The intensity differences were shown to result from the Matsubara fluctuation modes coupling to the centroid, and 'Matsubara heating' the $\|\Delta\mathbf{n}\|_1 = 2$ vibrations to those of a classical system held at frequency-dependent, quantum effective temperatures.

These perturbative arguments, however, have assumed a system free of degeneracy or near-degeneracy, and have therefore ignored the possibility of two or more vibrations coming into resonance with one another. Most generally, degeneracy in the reference system occurs when the harmonic frequencies are rationally related, meaning that $\mathbf{j} \cdot \mathbf{\Omega} = 0$ for some set of integers $\mathbf{j} = (j_1, \ldots, j_F)^\mathrm{T} \neq \mathbf{0}$. Near-degeneracy refers to the scenario where $|\mathbf{j} \cdot \mathbf{\Omega}|$ is small relative to the frequency shifts induced by the perturbation. The specific case of $\|\mathbf{j}\|_1 = 3$ is of greatest relevance to us, because there will then be some cubic perturbation that is capable, if present, of lifting the (near-)degeneracy and causing resonant behaviour. In the context of vibrational spectroscopy, this means that a $\|\Delta\mathbf{n}\|_1 = 1$ band and a $\|\Delta\mathbf{n}\|_1 = 2$ band, which would otherwise be almost coincident, instead mix and 'repel' one another. The $\|\Delta\mathbf{n}\|_1 = 2$ band is said to 'borrow' intensity from the $\|\Delta\mathbf{n}\|_1 = 1$ band, such that their intensities become comparable. This effect, known as Fermi resonance, gives the appearance of a bifurcated $\|\Delta\mathbf{n}\|_1 = 1$ (fundamental) band or 'Fermi dyad', with the distance between the two peaks referred to as the 'Fermi splitting'. Unlike non-resonant overtone intensities, which scale as $O(\varepsilon^2)$, Fermi splittings scale as $O(\varepsilon)$ [122].

Liu and Liu showed, by comparison with experiment, that LSC-IVR+LGA gives a reasonable description of the Fermi resonance between the stretch fundamental and the first bend overtone in the isotropic Raman spectrum of liquid water (using the POLI2VS potential) [69]. More recently, Plé *et al.* showed that LSC-IVR (with or without the LGA) yields near-quantitative agreement with exact quantum Fermi splittings for a simplified model of

CO_2 [65, 117]. Similar to water, the resonance in CO_2 occurs between the symmetric stretch fundamental and the first overtone of the (here doubly degenerate) bend mode [122]. In contrast to LSC-IVR, the centroid-following path-integral methods CMD and TRPMD were shown to yield only the classical Fermi splitting, which is considerably smaller than the quantum splitting [117]. This is somewhat unsurprising, given the failure of these methods to capture the correct quantum overtone intensity in the non-resonant case of Chapter 3. The difficulty faced by CMD and TRPMD in describing the CO_2 Fermi resonance supports earlier findings due to Rossi *et al.* for the Zundel cation $H_5O_2^+$ [102], although it should be noted that the resonance in that system is of the higher-order type $\|\mathbf{j}\|_1 = 5$ (involving a $\|\Delta\mathbf{n}\|_1 = 1$ band and a $\|\Delta\mathbf{n}\|_1 = 4$ band) [174].

It is already clear that quantum coherence is not necessarily required for an accurate description of Fermi splittings, otherwise LSC-IVR would fail in this regard. In this chapter, we show that the enhancement of the quantum splitting over the classical one is attributable to Matsubara heating. Section 5.1 examines the three-dimensional model of the CO_2 resonance studied in refs. 65, 117, 121, 122. Exploiting the weak anharmonicity of this system, we introduce a 'harmonic decorrelation' (HD) approximation to Matsubara dynamics, which allows us to run simulations with up to 45 Matsubara modes (albeit at the expense of detailed balance). We find that this is almost enough to achieve agreement with the quantum Fermi splitting, and demonstrate the relevance of Matsubara heating via purely classical simulations with the oscillators prepared at their Matsubara effective temperatures.

For completeness and for the benefit of other researchers investigating the quasi-classical behaviour of Fermi resonances, in Section 5.2, we discuss some anomalous behaviour observed for the simplest case of two coupled oscillators. In particular, we observe a splitting in the classical power spectrum of the low-frequency oscillator that is of comparable magnitude to the normal Fermi splitting (which occurs in the spectrum of the high-frequency oscillator). Introducing centroid–fluctuation coupling enhances both splittings, even though only the Fermi splitting is observed quantum mechanically. Based on the semiclassical analysis of Noid *et al.* [175], and comparisons with an analogous three-dimensional model in which the secondary splitting is absent, we argue that this splitting is an artefact of neglecting quantum coherence.

5.1 Numerical studies of a simplified model of CO_2

Intended to capture the relevant dynamics of the symmetric stretch and bend modes of CO_2, the quantum Hamiltonian studied in refs. 65, 117, 121, 122 is given by

$$\hat{H}_{CO_2} = \hat{H}_{CO_2}^{(0)} + \varepsilon \hat{V}_{CO_2}^{(1)}, \tag{5.1}$$

Table 5.1: Parameters used in the CO_2 model Fermi resonance Hamiltonian, taken from ref. 65.

Parameter	Value
Ω_1	1261 cm^{-1}
Ω_2	634 cm^{-1}
$\varepsilon\eta$	1.479×10^{-7} a.u.

with

$$\hat{H}_{CO_2}^{(0)} = \frac{1}{2}\left(\hat{p}_x^2 + \hat{p}_y^2 + \hat{p}_z^2 + \Omega_1^2\hat{x}^2 + \Omega_2^2\hat{y}^2 + \Omega_2^2\hat{z}^2\right) \tag{5.2a}$$

$$\hat{V}_{CO_2}^{(1)} = \frac{1}{2}\eta\hat{x}\left(\hat{y}^2 + \hat{z}^2\right), \tag{5.2b}$$

where x represents the symmetric stretch coordinate and (y, z) are the degenerate bend co-ordinates. This is, of course, a special case of the system of coupled oscillators defined in Section 3.2.1. Basire *et al.* calculated the first-order quantum and classical Fermi splittings for this model by using a mode-localisation procedure to obtain maximally decorrelated spectra, finding that the classical splitting exhibits (approximately) an erroneous $T^{1/2}$ dependence [121]. While it might be possible to generalise this approach to Matsubara dynamics, or indeed to follow a canonical PT analysis along the lines of Section 3.2, this would be long and involved[a] and is unlikely to offer significant physical insight beyond what can be obtained from numerical studies. We therefore adopt the latter strategy.

We parametrise the CO_2 model following ref. 65 with the values given in Table 5.1, which satisfy $\Omega_1 \approx 2\Omega_2$ as required. Only the dynamics of the IR-inactive stretch vibration, which exhibits Fermi resonance, are presently of interest. As a simplified proxy for the Raman spectrum, we consider the product of inverse temperature with the Fourier transform of the Kubo-transformed stretch velocity ACF (or *velocity autocorrelation spectrum* for short),

$$R(\omega) \sim \beta\widetilde{G}_{\dot{x}\dot{x}}(\omega). \tag{5.3}$$

Eq. (5.3), and its classical analogue $R(\omega) \sim \beta g_{\dot{x}\dot{x}}(\omega)$, are based on the assumption that the polarisability is linear in x. In Fig. 5.1(a), we plot the quantum, classical, and $M = 3$ Matsubara spectra calculated at 150 K. All the spectra have been convolved with the Gaussian filter of Eq. (3.114), taking $w = 0.5$ ps. Further computational details are provided in Appendix D.2.1.

Following Basire *et al.*, we define the Fermi splitting as the distance between the first moments of the two components of the dyad. We find that the classical ($M = 1$) splitting is only 54% of the quantum splitting, whereas $M = 3$ gives 76%.

---

[a]Canonical PT is made considerably more complicated by the presence of near-degeneracy, owing to the problem of small denominators; for a discussion see e.g. ref. 176.
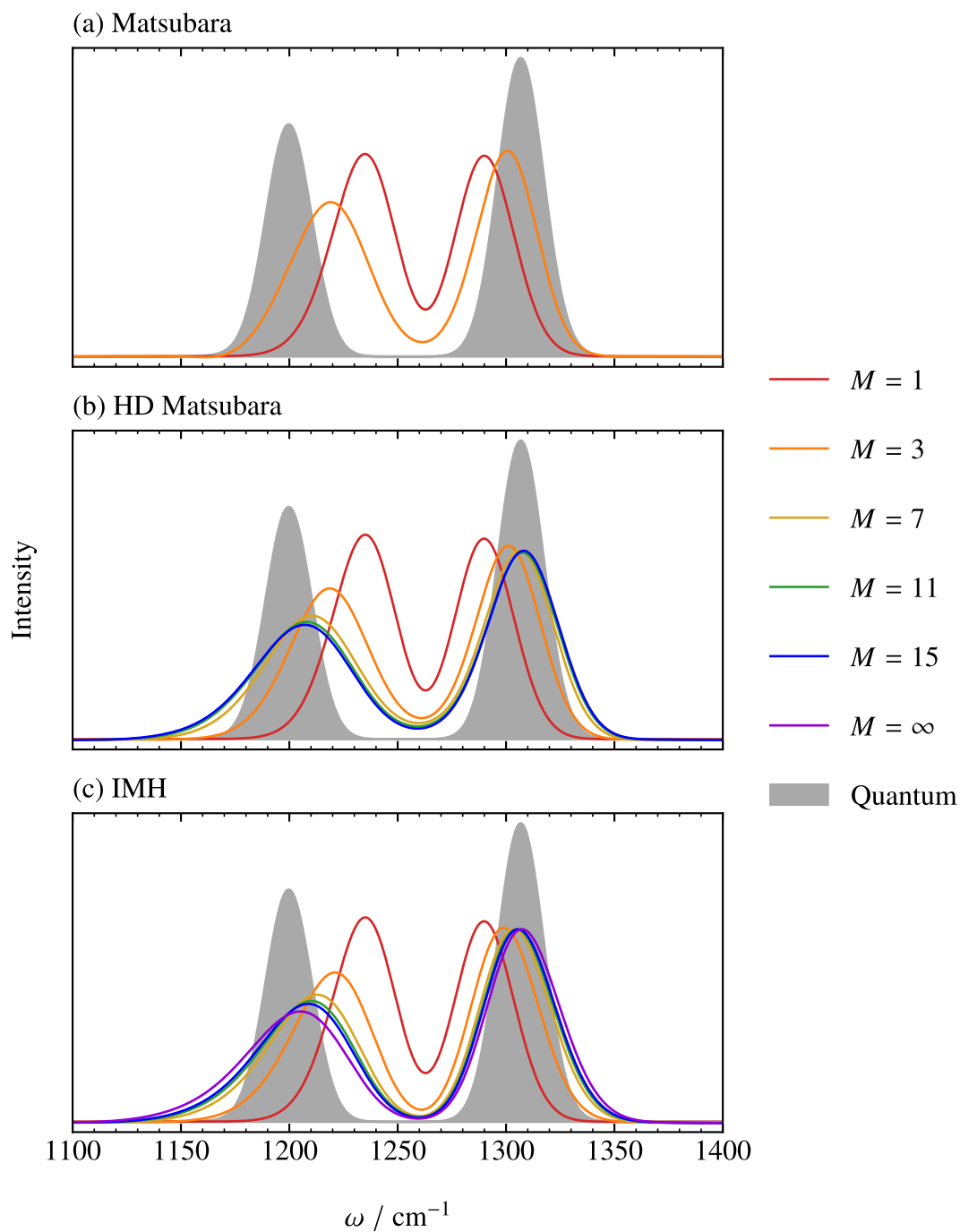
Figure 5.1: Matsubara, HD Matsubara, IMH, and quantum velocity autocorrelation spectra, scaled by inverse (effective) temperature, at 150 K for the simplified CO_2 model of Eqs. (5.1–5.2) as parametrised in ref. 65 (see also Table 5.1). The Fermi splitting predicted by Matsubara dynamics approaches the quantum result as the number of modes per degree of freedom, M, is increased.

5.1.1 Harmonic decorrelated Matsubara dynamics

It is computationally unfeasible to converge brute-force Matsubara dynamics simulations of the CO_2 model, except with a very small number of modes ($M \leqslant 3$ at 150 K), because the phase $\widetilde{\theta}_M(\mathbf{P}, \mathbf{Q})$ becomes too oscillatory to integrate over numerically. However, we can investigate the effect of including more modes by introducing a phase-free 'harmonic decorrelation' (HD) approximation, which is a globally harmonic analogue of the locally harmonic approximation introduced by Karsten *et al.* in ref. 177. It is based on the observation that, in a harmonic system, the terms

$$\exp\left(-\frac{\beta}{2}\left(P_{i,k}^2 + \Omega_i^2 Q_{i,-k}^2 - 2i\omega_k P_{i,k} Q_{i,-k}\right)\right) \tag{5.4}$$

in the Matsubara distribution can be replaced by the product of the marginal distributions in $P_{i,k}$ and $Q_{i,-k}$, proportional to

$$\exp\left(-\frac{\beta(\Omega_k^2 + \omega_k^2)}{2\Omega_i^2}\left(P_{i,k}^2 + \Omega_i^2 Q_{i,-k}^2\right)\right), \tag{5.5}$$

provided the function to be integrated over does not contain mixed products of $P_{i,k}$ and $Q_{i,-k}$. In the HD approximation, we sample $(\mathbf{P}, \mathbf{Q})$ from the harmonic part of the Matsubara distribution approximated thus, but propagate the (truncated) Matsubara dynamics exactly. Within the context of studying the Fermi resonance of the CO_2 model, we expect this to be a very good approximation, because the perturbative dependence of the centroid on the fluctuation modes is likely to be dominated by quadratic terms. Mixed products involving $P_{i,k}$ and $Q_{i,-k}$ (where $\mathbf{Q}_k \equiv (X_k, Y_k, Z_k)^\mathrm{T}$ and similarly for $\mathbf{P}$) can appear only at quartic or higher powers,[b] which are $O(\varepsilon^2)$ and therefore small enough to ignore. A key drawback of the HD approximation is that it breaks detailed balance, but this is of limited relevance over the timescales required to measure the Fermi splitting.

Fig. 5.1(b) shows that the HD approximation yields an $M = 3$ spectrum almost indistinguishable from that calculated with brute-force sampling. The inclusion of additional fluctuation modes pushes the HD Matsubara Fermi splitting closer to the quantum result, reaching 96% at $M = 15$.

5.1.2 Imitated Matsubara heating

In Section 3.3, we showed that the coupling of the Matsubara fluctuation modes to the centroid increases the overtone and combination intensities to what would be obtained from a classical calculation with the oscillators prepared at the effective temperatures $T_i^{[M]} = 1/(k_\mathrm{B}\beta_i^{[M]})$,

---

[b]This is easily proved by noting that functions that are odd powers of $P_{i,k}$ or $Q_{i,-k}$, with $k > 0$, are antisymmetric with respect to imaginary-time inversion.
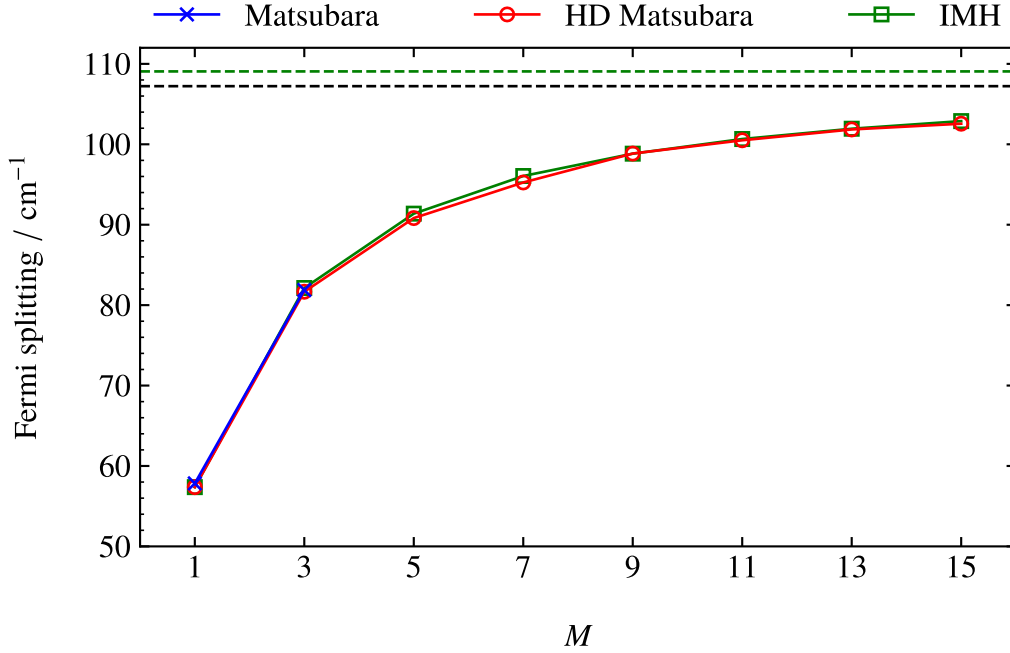
Figure 5.2: Matsubara, HD Matsubara, and IMH Fermi splittings plotted as a function of M, including the results for intermediate values of M not included in Fig. 5.1. The Fermi splitting is defined as the distance between the first moments of the two components of the Fermi dyad. The dashed lines represent the exact quantum splitting (black) and the $M \rightarrow \infty$ limit of the IMH splitting (green), which are in agreement to within $2\,\mathrm{cm}^{-1}$.

where $\beta_i^{[M]}$ was defined in Eq. (3.92). To show that the increase in the low-temperature Fermi splitting for the CO_2 model behaves analogously, we plot in Fig. 5.1(c) the spectra $\beta_x^{[M]} g_{\dot{x}\dot{x}}(\beta^{[M]}; \omega)$ obtained from purely classical calculations with 'imitated Matsubara heating' (IMH). In this approach, (p_i, q_i) were sampled from the classical harmonic oscillator Boltzmann distribution with frequency Ω_i and temperature $T_i^{[M]}$, then propagated under the full classical equations of motion (where $\mathbf{q} = (x, y, z)^{\mathrm{T}}$ and similarly for $\mathbf{p}$). The ACFs were thus obtained as effective thermal averages over the distribution involving the classical reference Hamiltonian, $H_{CO_2}^{(0)}(\mathbf{p}, \mathbf{q})$, while the dynamics were generated by the perturbed Hamiltonian $H_{CO_2}(\mathbf{q})$. In this scenario, (p_i, q_i) represent approximations to the dynamical variables of a single Matsubara 'bead', $(\tilde{p}_{i,l}, \tilde{q}_{i,l})$, as defined in Section 3.3.2.

For $M = 1$, IMH is equivalent to HD Matsubara dynamics. For $M > 1$, the IMH spectra are still very close to the corresponding HD Matsubara spectra, and the two sets of splittings are almost indistinguishable up to $M = 15$ as plotted in Fig. 5.2. It is also evident from the slope of the curve in Fig. 5.2 that the convergence with respect to $M > 15$ is slow, which is to be expected given the long Matsubara convergence 'tails' found in calculations of some static properties [135]. However, the Fermi splitting in the $M \rightarrow \infty$ limit seems to be tending to within a few cm^{-1} of the exact quantum result, notwithstanding small discrepancies in the

lineshape of the Fermi dyad. To consolidate this, we repeated the IMH calculations with the oscillators prepared at the quantum effective temperatures $T_i^{[\infty]} = \hbar\Omega_i \coth(\beta\hbar\Omega_i/2)/(2k_{\mathrm{B}})$, obtaining a Fermi splitting accurate to within 2 cm^{-1} (see Figs. 5.1 and 5.2).

5.2 Anomalous classical behaviour of a two-dimensional model

The simplest model system with a $2 : 1$ Fermi resonance, which we will call FR2, has a quantum Hamiltonian given by

$$\hat{H}_{\mathrm{FR2}} = \hat{H}_{\mathrm{FR2}}^{(0)} + \varepsilon\hat{V}_{\mathrm{FR2}}^{(1)}, \tag{5.6}$$

with

$$\hat{H}_{\mathrm{FR2}}^{(0)} = \frac{1}{2}\left(\hat{p}_x^2 + \hat{p}_y^2 + 4\Omega^2\hat{x}^2 + \Omega^2\hat{y}^2\right) \tag{5.7a}$$

$$\hat{V}_{\mathrm{FR2}}^{(1)} = \frac{1}{2}\eta\hat{x}\hat{y}^2. \tag{5.7b}$$

This is a special case of the system considered by Noid *et al.* in ref. 175. The eigenstates of the reference Hamiltonian $\hat{H}_{\mathrm{FR2}}^{(0)}$ can be fully characterised by the Cartesian quantum numbers $n_x, n_y \in \{0, \dots, \infty\}$ as $|n_x, n_y\rangle$. The corresponding energy eigenvalues are

$$E_{n_x,n_y}^{(0)} = \left(2n_x + n_y + \frac{3}{2}\right)\hbar\Omega. \tag{5.8}$$

It is more instructive, however, to define a principal quantum number $n \in \{0, \dots, \infty\}$ that determines the energy via $E_n^{(0)} = (n + 3/2)\hbar\Omega$, and a second quantum number

$$\ell \in \begin{cases} \{0, \pm1, \dots, \pm n/4\} & n \text{ divisible by } 4 \\ \{0, \pm1, \dots, \pm(n-1)/4\} & n-1 \text{ disivible by } 4 \\ \{\pm1, \dots, \pm(n+2)/4\} & n \text{ even, not divisible by } 4 \\ \{\pm1 \dots, \pm(n+1)4\} & n-1 \text{ even, not divisible by } 4, \end{cases} \tag{5.9}$$

such that eigenstates are characterised as $|n, \ell\rangle$ (each of which is, in general, a linear combination of several degenerate $|n_x, n_y\rangle$ states). From Eq. (5.9), the degeneracy is $(n/2) + 1$ if n is even or $(n+1)/2$ if n is odd [175]. Semiclassically, Noid *et al.* showed that states with $\ell < 0$ and $\ell > 0$ correspond to trajectories localised either side of a separatrix defined by the surface $K = 0$, where

$$K = 2\Omega^2xy^2 - 2p_y^2x + 2p_xp_y = \sqrt{2\Omega J_x^{(0)}}J_y^{(0)}\sin\left(2\phi_y^{(0)} - \phi_x^{(0)}\right), \tag{5.10}$$

and $(J_x^{(0)}, \phi_x^{(0)})$ and $(J_y^{(0)}, \phi_y^{(0)})$ are action-angle variables defined in the usual way (see Section 3.1.2). Accordingly, the smaller number of states with $\ell = 0$ correspond to trajectories that are localised *on* the separatrix [175].

Consider, as a simplified proxy for the IR or Raman spectrum, the full velocity autocorrelation spectrum scaled by inverse temperature,

$$\beta \widetilde{G}_{vv}(\beta; \omega) = \beta \widetilde{G}_{\dot{x}\dot{x}}(\beta; \omega) + \beta \widetilde{G}_{\dot{y}\dot{y}}(\beta; \omega). \tag{5.11}$$

Let us examine the contributions to Eq. (5.11) that arise from only the four lowest-energy eigenstates of $\hat{H}_{\mathrm{FR2}}^{(0)}$,

$$|n = 0, \ell = 0\rangle = |n_x = 0, n_y = 0\rangle \tag{5.12a}$$

$$|n = 1, \ell = 0\rangle = |n_x = 0, n_y = 1\rangle \tag{5.12b}$$

$$|n = 2, \ell = +1\rangle = \frac{1}{\sqrt{2}}\left(|n_x = 1, n_y = 0\rangle + |n_x = 0, n_y = 2\rangle\right) \tag{5.12c}$$

$$|n = 2, \ell = -1\rangle = \frac{1}{\sqrt{2}}\left(|n_x = 1, n_y = 0\rangle - |n_x = 0, n_y = 2\rangle\right). \tag{5.12d}$$

To $O(\varepsilon)$, the perturbation of Eq. (5.7b) lifts the degeneracy of $|n = 2, \ell = +1\rangle$ and $|n = 2, \ell = -1\rangle$ without mixing them. Therefore, $\beta \widetilde{G}_{\dot{x}\dot{x}}(\beta; \omega)$ is expected to exhibit a Fermi dyad centred at $\omega \simeq 2\Omega$, corresponding to the transitions between each of these two states and the ground state. In contrast, the strongest contribution to $\beta \widetilde{G}_{\dot{y}\dot{y}}(\beta; \omega)$ is a singlet at $\omega \simeq \Omega$, corresponding to the transition $|n = 0, \ell = 0\rangle \rightarrow |n = 1, \ell = 0\rangle$. To illustrate this, the quantum spectra $\beta \widetilde{G}_{\dot{x}\dot{x}}(\beta; \omega)$ and $\beta \widetilde{G}_{\dot{y}\dot{y}}(\beta; \omega)$ are plotted for two different temperatures in Fig. 5.3, with the parameters of the potential set to $\Omega = 0.5$ a.u. and $\varepsilon\eta = -0.08$ a.u. Since both the temperatures considered satisfy $\beta\hbar\Omega \gg 1$ (i.e., $k_{\mathrm{B}}T$ is small relative to the first excitation energy), the Fermi splitting is roughly independent of temperature. This is consistent with the perturbative analysis carried out by Basire *et al.* on the CO_2 model of Section 5.1. Note that all the spectra reported in this section have been convolved with the Gaussian filter of Eq. (3.114), taking $w = 250$ a.u; further computational details are provided in Appendix D.2.2.

Also in Fig. 5.3, we plot the classical (power) spectra $\beta g_{\dot{x}\dot{x}}(\beta; \omega)$ and $\beta g_{\dot{y}\dot{y}}(\beta; \omega)$ for the same system. Similar to the quantum case, $\beta g_{\dot{x}\dot{x}}(\beta; \omega)$ exhibits a Fermi dyad centred at $\omega \simeq 2\Omega$, but the Fermi splitting is considerably smaller than its quantum counterpart, scaling approximately as $T^{1/2}$. This is, again, consistent with the results of ref. 121, and reflects the fact that classical mechanics misses the zero-point energy that ensures a non-zero quantum Fermi splitting in the limit $T \rightarrow 0$. As alluded to earlier, the two components of the classical Fermi dyad correspond to perturbed trajectories initiated either side of the $K = 0$ separatrix (although the separatrix is no longer strictly defined for $\varepsilon \neq 0$, since K is no longer a conserved quantity). Fig. 5.3 shows that the splitting is enhanced when the lowest two Matsubara fluctuation modes
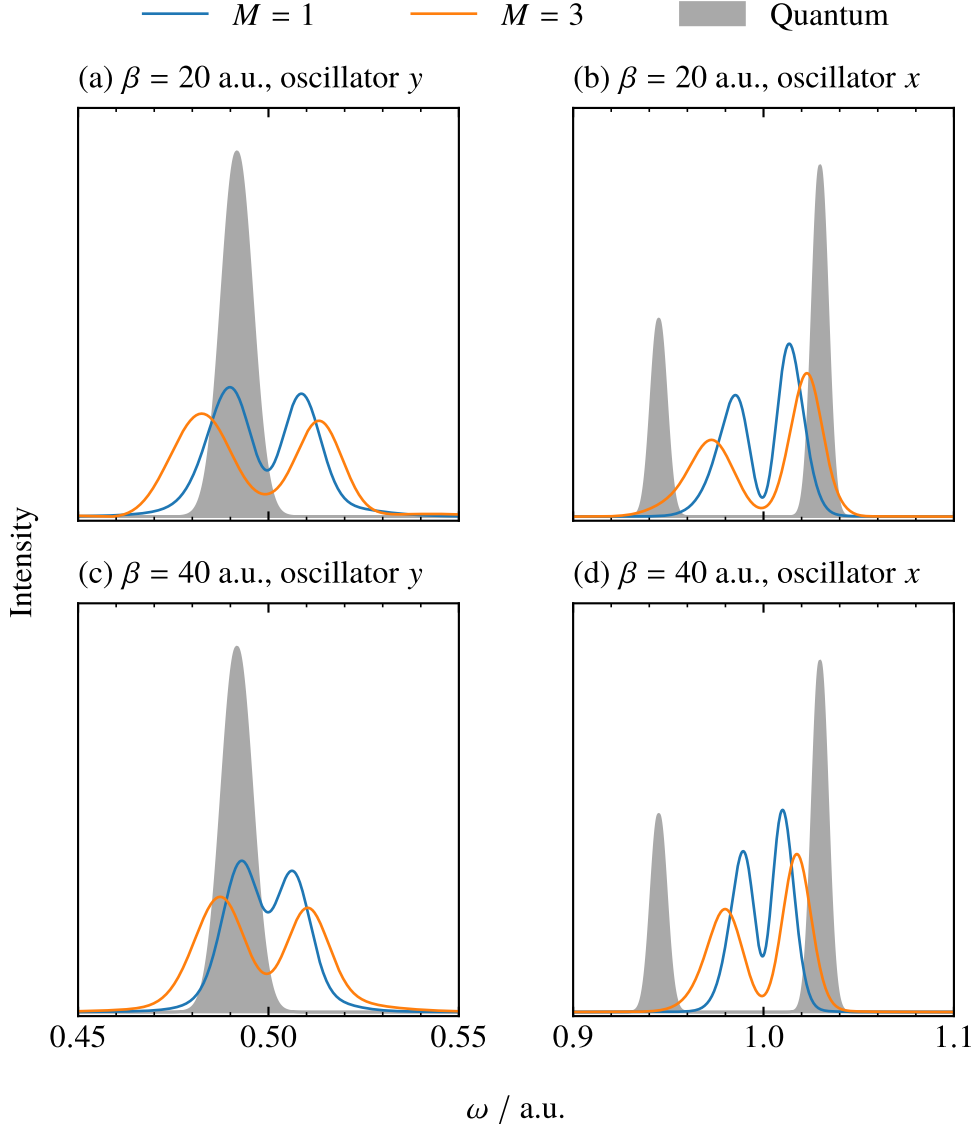
Figure 5.3: Matsubara and quantum Kubo-transformed velocity autocorrelation spectra, scaled by inverse temperature, for the FR2 system with $\Omega = 0.5$ a.u. and $\varepsilon\eta = -0.08$ a.u. Note $M = 1$ Matsubara dynamics is equivalent to classical dynamics. In addition to the expected Fermi splittings in the spectra of oscillator x, classical dynamics gives pronounced splittings in the spectra of oscillator y that grow in magnitude upon including the lowest four fluctuation modes. This is believed to be an artefact caused by the neglect of quantum coherence, specific to this two-dimensional model. The intensities in (b) and (d) are scaled by 1.5 relative to those in (a) and (c).

for each oscillator are allowed to interact with the centroid (i.e., $M = 3$ truncated Matsubara dynamics, involving a total of six Matsubara modes).

The most striking feature of Fig. 5.3, which has not to our knowledge been previously discussed, is the doublet centred at $\omega \simeq \Omega$ observed in $\beta g_{\dot{y}\dot{y}}(\beta; \omega)$. This is drastically different

from the singlet observed in its quantum analogue, $\beta \widetilde{G}_{\dot{y}\dot{y}}(\beta; \omega)$. From a classical mechanics perspective, however, the additional bifurcation is unsurprising: the average perturbed oscillation frequency of $e^{\mathcal{L}t}\dot{y}$ is expected to differ for the two ensembles of trajectories either side of the separatrix, just as for $e^{\mathcal{L}t}\dot{x}$. Similar to the classical Fermi splitting, we find numerically that the size of this secondary splitting scales approximately as $T^{1/2}$. Fig. 5.3(a) also reveals that including the lowest four Matsubara fluctuation modes enhances the secondary splitting, just as we found for the Fermi splitting. To contrast with this behaviour, in Fig. 5.4 we plot $\beta = 20$ spectra calculated in the same way but for the three-dimensional 'FR3' Hamiltonian

$$\hat{H}_{\text{FR3}} = \frac{1}{2}\left(\hat{p}_x^2 + \hat{p}_y^2 + \hat{p}_z^2 + 4\Omega^2\hat{x}^2 + \Omega^2\hat{y}^2 + \Omega^2\hat{z}^2\right) + \frac{1}{2}\varepsilon\eta\hat{x}\left(\hat{y}^2 + \hat{z}^2\right), \tag{5.13}$$

in which we have introduced a new *physical* oscillator z that is degenerate to y. This is clearly very closely related to the CO_2 model of Section 5.1, with the main difference being that the resonance condition $\Omega_1 = 2\Omega_2$ is met exactly for FR3 (for which $\Omega_1 = 2\Omega_2 = 2\Omega$) but only approximately for CO_2. We find that the presence of oscillator z eliminates the splitting in the classical and Matsubara power spectra of oscillator y, so that they appear in qualitatively better agreement with quantum mechanics.

Given the enhancement of the secondary splitting upon including fluctuation modes in two physical dimensions, and its absence altogether in three physical dimensions, we propose that it is an artefact of neglecting quantum coherence. To understand this, consider that the splitting does not occur in the quantum spectra because the $n = 1$ eigenstate is non-degenerate; this non-degeneracy can be attributed to the Einstein–Brillouin–Keller quantisation of $K \neq 0$ trajectories yielding only states with $n \geqslant 2$ [175]. In contrast, the $K = 0$ trajectories that quantise to give $\ell = 0$ states occupy (in the $\varepsilon \to 0$ limit) an infinitesimal volume of the classical phase space, so the classical spectrum is dominated by contributions from $K \neq 0$.

Further work will be required to substantiate, or otherwise, this interpretation of the secondary splitting. The important thing for now is that it appears to be an artefact of restricting the dynamics to two physical dimensions, which is clearly not a realistic scenario for any condensed-phase system.

5.3 Discussion

The numerical results of this chapter support the view that Matsubara heating is responsible for the quantum mechanical enhancement of Fermi splittings in the vibrational (Raman) spectra of CO_2 and similar systems. Our investigations were limited to simple models comprising two or three harmonic oscillators coupled by cubic contributions to the PES, so we cannot make any definitive conclusions about the Fermi resonances of systems that lie outside of this scope,
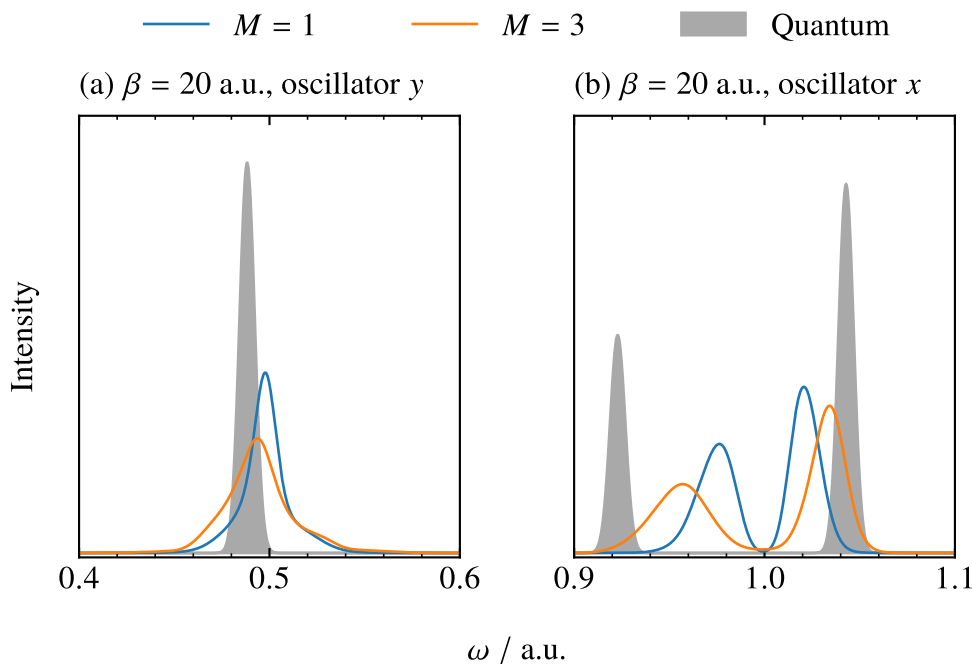
Figure 5.4: Matsubara and quantum Kubo-transformed velocity autocorrelation spectra for the FR3 system with $\Omega = 0.5$ a.u. and $\varepsilon\eta = -0.08$ a.u. Unlike its two-dimensional analogue, FR2 (see Fig. 5.3), this model does not display a splitting in the Matsubara y mode spectra. The $M = y$ mode spectrum does have a noticeable shoulder to the right of the fundamental band, which can probably be assigned to the binary difference band. The intensity in (b) is scaled by 1.5 relative to that in (a).

such as the Zundel cation [174]. However, as noted by Basire *et al.* [121], models of the kind considered here are known to be effective for a range of other molecules [161–163, 178–180]. These include ammonia, for which the $\nu_1/2\nu_2$ resonance is particularly pronounced in the liquid phase [161–163].

At their core, the models studied in this chapter differ from those of Chapter 3 only in the relative values of their frequencies—our perturbative analysis of anharmonic absorption intensities in Chapter 3 was simplified by the assumption of non-resonance. While we have not attempted to carry out a similar analysis of Fermi resonances, given the similarity of the models it is unsurprising that the same fundamental physical phenomenon (i.e., Matsubara heating) seems to be relevant in both scenarios.

Chapter 6

Conclusions

The primary aim of this work was to better understand the descriptions of vibrational spectra given by path-integral approaches to combining quantum statistics with classical dynamics. We paid particular attention to identifying the underlying physics responsible for the poor treatment by many such methods of anharmonic spectral features such as overtones, combination bands, and Fermi resonances [29, 65, 107]. By applying first-order perturbation theory (PT) to a simple model of coupled harmonic oscillators, we derived analytic expressions for the quantum, classical, and Matsubara dynamics [73] integrated infrared (IR) absorption intensities of first overtones, and binary combination and difference bands (collectively $\|\Delta\mathbf{n}\|_1 = 2$ bands using the notation introduced in Section 3.1). We found the reassuring result that Matsubara dynamics properly accounts for the quantum intensification of overtone and combination bands—and de-intensification of difference bands—in the limit that the number of modes, M, per degree of freedom tends to infinity. This was argued to be the case for both the original, 'truncated' formulation of the theory and for the mean-field formulation due to Trenins and Althorpe [76]. The recent work of Plé *et al.* supports our conclusions—they used an alternative, but equivalent, formulation of PT to derive the same results for Matsubara $\|\Delta\mathbf{n}\|_1 = 2$ band intensities independently [65, 117].

The mechanism responsible for the (de-)intensification of $\|\Delta\mathbf{n}\|_1 = 2$ bands was shown to be 'Matsubara heating', whereby the centroid–fluctuation coupling increases the amplitudes of the relevant centroid vibrations to those expected of classical oscillators prepared at their quantum (frequency-dependent) effective temperatures. The improper treatment of the Matsubara fluctuation dynamics by centroid-following methods, such as [quasi-]centroid molecular dynamics ([Q]CMD) [78–81, 107] and [thermostatted] ring-polymer molecular dynamics ([T]RPMD) [82, 83, 102], was shown to be responsible for their failure to treat anharmonic absorption intensities any more accurately than classical MD. Even the planetary model, which follows the approximate time-evolution of one fluctuation coordinate [75, 115, 116], is only able to capture the contributions from electrical anharmonicity.

As an attempt to rectify this, we proposed a very simple form of scaling factor that one can apply to $\|\Delta\mathbf{n}\|_1 = 2$ intensities in classical or path-integral spectra (we suggest QCMD) as a means of post-processing correction, derived from the ratio of integrated intensities given by quantum and classical perturbation theories. This was found to work well for a simple one-dimensional model of an O–H bond and, more surprisingly, for accurate models of gas-phase water and ammonia based on fits to *ab initio* potential energies and dipole moments. The 'corrected' QCMD spectra of gas-phase water in particular show excellent agreement with exact quantum results across the whole range of frequencies considered. We anticipate that QCMD will yield similarly impressive results for gas-phase ammonia and similar systems once appropriate definitions of the quasi-centroid coordinates have been devised.

Our gas-phase water simulation results also support the theoretical analysis of Plé *et al.* [65], which shows the linearised semiclassical initial value representation (LSC-IVR) [20, 54–56] to reproduce the quantum intensities of most $\|\Delta\mathbf{n}\|_1 = 2$ bands with reasonable accuracy. To our knowledge, it is the only established quantum statistics–classical dynamics method (or, more strictly, class of methods) that is capable of doing so. However, it suffers the potentially serious drawback of violating detailed balance, resulting in spectral lineshapes that are too broad. While our simulations employed the local Gaussian approximation (LGA) of Liu and Miller [60] to sample from the Wigner distribution, other choices are available [58, 59, 61, 62, 64, 65], and indeed Plé *et al.* demonstrated that more accurate approaches such as the Edgeworth conditional momentum approximation (ECMA) yield better results for anharmonic absorption intensities. This is because, unlike the LGA, the ECMA accounts for non-local quantum correlations between momentum and position [65].

Turning to condensed-phase water, we extended the results of refs. 28, 29, 107 to assess the performances of classical MD, TRPMD, QCMD, and LSC-IVR+LGA across a wider range of frequencies than had previously been considered. The overall picture is broadly as for the gas phase—QCMD provides the best description of fundamental bands, TRPMD gives damped versions of the QCMD spectra, and LSC-IVR+LGA is the only one of these methods suitable for obtaining a qualitatively reasonable description of anharmonic spectral features. However, the violation of detailed balance by LSC-IVR+LGA results in considerable zero-point energy leakage from the high-frequency intramolecular degrees of freedom to the low-frequency intermolecular degrees of freedom, as first analysed by Habershon and Manolopoulos [28]. This becomes particularly severe for ice I_h, which to our knowledge had not previously been simulated using LSC-IVR—apparently for good reason, given that the $\sim 2k_\mathrm{B}T$ leakage is sufficient to melt the contents of the simulation cell on a sub-picosecond timescale.

Unsurprisingly, our post-processing correction procedure did not yield results as impressive for the condensed phase as it did for the gas phase. This is partly on account of the difficulty of applying the appropriate scaling to bands that are not well separated, but the validity of

the approach is likely also compromised by other effects that lie beyond the scope of our perturbative analysis, such as highly anharmonic coupling through the hydrogen bond network. For example, when tested on a classical spectrum of liquid water computed using the highly accurate MB-pol and MB-μ surfaces [97, 118–120], it was found to improve the descriptions of overtone and combination band intensities, but only crudely. In particular, the stretch–bend combination band became considerably overstated. It is also significant that even the intensity of the stretch fundamental band is badly underestimated by classical MD, which we attributed mainly to the poor treatment of electrical anharmonicity; the classical time-correlation function (TCF) is only a reasonable proxy for the quantum Kubo-transformed TCF when the observables concerned are approximately linear.

Our numerical studies on the prototypical model of Fermi resonance in CO_2 [65, 121, 122] suggested that one can invoke Matsubara heating to account for quantum mechanics predicting a larger Fermi splitting than classical mechanics. This builds on the discovery of ref. 65 that LSC-IVR also gives good agreement with the quantum splitting, proving beyond reasonable doubt that real-time quantum coherence plays, at most, a minor role in governing its magnitude. Basire *et al.* developed a scheme for post-processing correction that is based on fitting the parameters of the Hamiltonian using the analytic results of classical perturbation theory (PT) [121]. This could complement our own post-processing correction approach for non-resonant $\|\Delta\mathbf{n}\|_1 = 2$ band intensities. An even simpler option than explicitly fitting the parameters would be simply to interpret the ratio of PT results for quantum and classical Fermi splittings as a temperature-dependent scaling factor, analogous to the intensity scaling factors derived in this work.

One obvious task for future work is to test the intensity scaling factors on the vibrational spectra of more complex systems, and to generalise them to $\|\Delta\mathbf{n}\|_1 > 2$ bands by extending the perturbative analysis to different types of anharmonicity, (near-)degenerate systems, and possibly higher orders of perturbation. Until the QCMD method has been generalised, the preferable candidate for post-processing correction is CMD at temperatures for which the curvature problem is not too severe, or classical MD at lower temperatures. Coloured-noise (generalised Langevin equation) TRPMD [104, 106] may also be a viable option if the artificial broadening can be mitigated enough to prevent the non-fundamental bands from being too washed out. It is important to note that one does not necessarily need to use very expensive potential energy surfaces to obtain absorption intensities of acceptable accuracy; the results of refs. 164, 170 demonstrate that the choice of the dipole moment surface (or presumably polarisability surface for Raman spectra) is somewhat more important.

While post-processing correction of intensities might have its place, its scope it very much limited by the requirement for bands to be unambiguously assigned, which is rarely a trivial task. They also need to be reasonably well separated. It may find use as a quick and efficient method

to help confirm proposed assignments, by comparing the 'corrected' classical or path-integral intensities with those given by experiment. Ultimately, though, we hope to discover a more general and reliable simulation method to account for Matsubara fluctuations in vibrational spectroscopy, ideally without requiring a priori knowledge of the expected spectral features. Given the high accuracy of LSC-IVR at short times (i.e., before the quantum distribution has significantly deteriorated), it is tempting to propose using the mean-field Matsubara dynamics of a single point on the imaginary-time path as a detailed balance–observing refinement of this method. However, the symmetry arguments of Trenins reveal that the corresponding phase-space distribution would not be phase-free, because the coordinate of a single point on the path is neither invariant with respect to translation nor to reversal in imaginary time [77].

It may be possible to devise a scheme similar to the planetary model, in which the dynamics of the fluctuations would be represented (perhaps at a first-order PT level) by a single fluctuation coordinate, but without ignoring the coupling to the centroid mode that is required for Matsubara heating. It is currently unknown, however, whether one could achieve this in a way that eliminates enough of the Matsubara sign problem while also respecting detailed balance. An efficient and promising alternative to path-integral methods is given by the adaptive quantum thermal bath (adQTB). Proposed by Mangaud *et al.*, this is a heuristic method that accounts for quantum statistical effects using a coloured-noise thermostat, and mitigates zero-point energy leakage by updating the parameters of the thermostat on the fly so as to enforce the quantum fluctuation dissipation theorem [181]. Plé *et al.* showed that, like Matsubara dynamics and LSC-IVR, adQTB gives correct $\|\Delta \mathbf{n}\|_1 = 2$ integrated intensities up to second order in the perturbation parameter. For condensed-phase water, it gives IR spectra of broadly similar accuracy LSC-IVR+LGA, but without suffering severe zero-point energy leakage, so that ice retains its structural integrity over the full length of a simulated trajectory [65, 117, 182].

Taking a pragmatic view, the best way to obtain reliable theoretical predictions of condensed-phase vibrational spectra may not be to rely on a single 'black-box' method, but to use different methods for different ranges of frequencies. For example, one might decide to trust classical MD if they are only interested in the low-frequency (far-IR) region of a spectrum, which is typically dominated by librations and restricted translations. For the mid-IR region containing bend and stretch fundamental bands, QCMD would give a better account of the peak positions. If one is specifically interested in anharmonic spectral features, which typically dominate the near-IR region but are often found also at lower frequencies (especially difference bands), the most reliable option currently available is probably to turn to an approximate wave function–based scheme like the local monomer (LMon) method [166, 167]. It might also be possible to use LMon or a similar method to refine our procedure for post-processing intensity correction—one could envisage running an wave function calculation to obtain acceptably accurate estimates of the integrated intensities, then scaling the peaks in a QCMD spectrum

accordingly. This would be likely to result in more accurate overall lineshapes than can be obtained from LMon calculations alone.

We finish with a reminder of a point noted in Chapters 1 and 3, that much of the interest among the spectroscopy community in describing anharmonic spectral features arises from their special relevance in nonlinear spectroscopy. For instance, two-dimensional IR experiments and computations can be used to obtain much more detailed information about anharmonic coupling strengths than is easily accessible via one-dimensional IR. Furthermore, the two-dimensional spectroscopic signature of a Fermi resonance is less ambiguous than the simple doublet observed in one-dimensional spectra, which sometimes has more than one plausible physical origin [114]. An interesting, but likely challenging, direction for future work would be to extend our perturbative analysis to the multi-time formulation of Matsubara dynamics developed by Jung *et al.* [138, 139], in order to determine whether an accurate account of the nuclear quantum statistics is sufficient to capture the two-dimensional representations of overtone, combination, and difference bands.

Appendix A

Further background theory

A.1   Multidimensional Matsubara dynamics

In the Matsubara dynamics of a system with F physical degrees of freedom, the particles are represented in the phase space of smooth, imaginary-time paths $(\tilde{\mathbf{p}}(\tau), \tilde{\mathbf{q}}(\tau))$, where

$$\tilde{\mathbf{q}}(\tau) \equiv \big(\tilde{q}_1(\tau), \ldots, \tilde{q}_F(\tau)\big) = \mathbf{Q}_0 + \sqrt{2} \sum_{k=1}^{\overline{M}} \big[\sin(\omega_k \tau)\mathbf{Q}_k + \cos(\omega_k \tau)\mathbf{Q}_{-k}\big]. \tag{A.1}$$

Here the $\mathbf{Q}_k \equiv (Q_{1,k}, \ldots, Q_{F,k})^{\mathrm{T}}$ are vectors of Matsubara mode coordinates, which can be gathered for convenience into the vector of vectors $\mathbf{Q} \equiv (\mathbf{Q}_{-\overline{N}}^{\mathrm{T}}, \ldots, \mathbf{Q}_{\overline{N}}^{\mathrm{T}})^{\mathrm{T}}$. Analogous definitions hold for $\mathbf{p}(\tau)$, $\mathbf{P}_k$, and $\mathbf{P}$. The multidimensional Matsubara Hamiltonian is

$$\widetilde{H}_M(\mathbf{P}, \mathbf{Q}) = \frac{1}{\beta\hbar} \int_0^{\beta\hbar} \mathrm{d}\tau \, H\big(\tilde{\mathbf{p}}(\tau), \tilde{\mathbf{q}}(\tau)\big) = \frac{1}{2} \sum_{k=-\overline{M}}^{\overline{M}} \mathbf{P}_k \cdot \mathbf{M}^{-1}\mathbf{P}_k + \widetilde{U}_M(\mathbf{Q}), \tag{A.2}$$

with potential

$$\widetilde{U}_M(\mathbf{Q}) = \frac{1}{\beta\hbar} \int_0^{\beta\hbar} \mathrm{d}\tau \, V\big(\tilde{\mathbf{q}}(\tau)\big). \tag{A.3}$$

The Matsubara Liouvillian is given correspondingly by

$$\widetilde{\mathcal{L}}_M = -\{\widetilde{H}_M, \, \cdot \, \} = \sum_{k=-\overline{M}}^{\overline{M}} \big[\mathbf{M}^{-1}\mathbf{P}_k \nabla_{\mathbf{Q}_k} - \nabla_{\mathbf{Q}_k}\widetilde{U}_M(\mathbf{Q})\nabla_{\mathbf{P}_k}\big], \tag{A.4}$$

and the phase is

$$\widetilde{\theta}_M(\mathbf{P}, \mathbf{Q}) = -\frac{1}{\beta\hbar} \int_0^{\beta\hbar} \mathrm{d}\tau \, \tilde{\mathbf{p}}(\tau) \cdot \frac{\partial \tilde{\mathbf{q}}(\tau)}{\partial \tau} = \sum_{k=-\overline{M}}^{\overline{M}} \omega_k \mathbf{P}_k \cdot \mathbf{Q}_{-k}. \tag{A.5}$$

The estimator for a observable $A \equiv A(\mathbf{q})$ is defined analogously to $\widetilde{U}_M(\mathbf{Q})$ i.e.,

$$\widetilde{A}_M(\mathbf{Q}) = \frac{1}{\beta\hbar} \int_0^{\beta\hbar} \mathrm{d}\tau \, A\big(\tilde{\mathbf{q}}(\tau)\big). \tag{A.6}$$

Kubo-transformed TCFs are then approximated by

$$\widetilde{C}_{AB}^{[M]}(\beta;t) = \frac{\alpha_M^F}{(2\pi\hbar)^F \widetilde{Z}_M(\beta)} \int \mathrm{d}^{FM}\mathbf{P} \int \mathrm{d}^{FM}\mathbf{Q} \, \mathrm{e}^{-\beta[\widetilde{H}_M(\mathbf{P},\mathbf{Q})+\mathrm{i}\widetilde{\theta}_M(\mathbf{P},\mathbf{Q})]} \widetilde{A}_M(\mathbf{Q}) \mathrm{e}^{\widetilde{\mathcal{L}}_M t}\widetilde{B}_M(\mathbf{Q}), \tag{A.7}$$

where

$$\widetilde{Z}_M(\beta) = \frac{\alpha_M^F}{(2\pi\hbar)^F} \int \mathrm{d}^{FM}\mathbf{P} \int \mathrm{d}^{FM}\mathbf{Q} \, \mathrm{e}^{-\beta[\widetilde{H}_M(\mathbf{P},\mathbf{Q})+\mathrm{i}\widetilde{\theta}_M(\mathbf{P},\mathbf{Q})]} \tag{A.8}$$

converges to the exact quantum partition function in the limit $M \to \infty$.

A.2   Classical canonical perturbation theory

Detailed derivations and applications of classical CPT may be found in many standard texts on analytical mechanics, such as ref. 124. One first rewrites the Hamiltonian in terms of the action-angle variables $(\mathbf{J}^{(0)}, \boldsymbol{\phi}^{(0)})$ for the unperturbed system, giving

$$\overline{H}\big(\mathbf{J}^{(0)}, \boldsymbol{\phi}^{(0)}\big) = H(\mathbf{p}, \mathbf{q}) = E^{(0)}\big(\mathbf{J}^{(0)}\big) + \varepsilon\overline{V}^{(1)}\big(\mathbf{J}^{(0)}, \boldsymbol{\phi}^{(0)}\big), \tag{A.9}$$

where

$$\overline{V}^{(1)}\big(\mathbf{J}^{(0)}, \boldsymbol{\phi}^{(0)}\big) = V^{(1)}(\mathbf{p}, \mathbf{q}). \tag{A.10}$$

Since p_i and q_i are periodic in $\phi_i^{(0)}$, the perturbation $\overline{V}^{(1)}$ must have a Fourier-series representation,

$$\overline{V}^{(1)}\big(\mathbf{J}^{(0)}, \boldsymbol{\phi}^{(0)}\big) = \sum_{\mathbf{n}} \overline{V}_{\mathbf{n}}^{(1)}\big(\mathbf{J}^{(0)}\big)\mathrm{e}^{\mathrm{i}\mathbf{n}\cdot\boldsymbol{\phi}^{(0)}}, \tag{A.11}$$

where $\overline{V}_{\mathbf{n}}^{(1)} = (\overline{V}_{-\mathbf{n}}^{(1)})^*$. We then assume that the transformed Hamiltonian can be expressed as a power series in ε,

$$E(\mathbf{J}) = \sum_{\alpha=0}^{\infty} \varepsilon^\alpha E^{(\alpha)}(\mathbf{J}). \tag{A.12}$$

The aim of CPT is to find a series of canonical transformations, starting from $(\mathbf{J}^{(0)}, \boldsymbol{\phi}^{(0)})$, that remove the angle-dependence of the Hamiltonian to progressively higher orders of ε. However, only the first-order corrections are required for our purposes. Introducing the type-II generating function

$$Y\big(\mathbf{J}, \boldsymbol{\phi}^{(0)}\big) = \sum_{\alpha=0}^{\infty} \varepsilon^\alpha Y^{(\alpha)}\big(\mathbf{J}, \boldsymbol{\phi}^{(0)}\big), \tag{A.13}$$

where

$$Y^{(0)}\left(\mathbf{J}, \boldsymbol{\phi}^{(0)}\right) = \mathbf{J} \cdot \boldsymbol{\phi}^{(0)}, \tag{A.14}$$

the perturbed ('new') and unperturbed ('old') variables are related by

$$\mathbf{J}^{(0)} = \frac{\partial Y\left(\mathbf{J}, \boldsymbol{\phi}^{(0)}\right)}{\partial \boldsymbol{\phi}^{(0)}} = \mathbf{J} + \sum_{\alpha=1}^{\infty} \varepsilon^{\alpha} \frac{\partial Y^{(\alpha)}\left(\mathbf{J}, \boldsymbol{\phi}^{(0)}\right)}{\partial \boldsymbol{\phi}^{(0)}} \tag{A.15a}$$

$$\boldsymbol{\phi} = \frac{\partial Y\left(\mathbf{J}, \boldsymbol{\phi}^{(0)}\right)}{\partial \mathbf{J}} = \boldsymbol{\phi}^{(0)} + \sum_{\alpha=1}^{\infty} \varepsilon^{\alpha} \frac{\partial Y^{(\alpha)}\left(\mathbf{J}, \boldsymbol{\phi}^{(0)}\right)}{\partial \mathbf{J}}. \tag{A.15b}$$

Assuming that each term in the perturbation expansion of $Y(\mathbf{J}, \boldsymbol{\phi}^{(0)})$ has a Fourier-series representation

$$Y^{(\alpha)}\left(\mathbf{J}, \boldsymbol{\phi}^{(0)}\right) = \sum_{\mathbf{n}} Y_{\mathbf{n}}^{(\alpha)}(\mathbf{J}) e^{i\mathbf{n} \cdot \boldsymbol{\phi}^{(0)}}, \tag{A.16}$$

one can show [124] that the coefficients in the first-order term are given by

$$Y_{\mathbf{n}}^{(1)}(\mathbf{J}) = \frac{i\overline{V}_{\mathbf{n}}^{(1)}(\mathbf{J})}{\mathbf{n} \cdot \boldsymbol{\Omega}} \tag{A.17}$$

for $\mathbf{n} \neq \mathbf{0}$, and that the first-order energy correction is

$$E^{(1)}(\mathbf{J}) = \overline{V}_{\mathbf{0}}^{(1)}(\mathbf{J}), \tag{A.18}$$

which is the average of the perturbation over one period of oscillation. The zero-frequency component of the generating function, $Y_{\mathbf{0}}^{(1)}(\mathbf{J})$, gives only a constant phase shift, thus we can choose to set $Y_{\mathbf{0}}^{(1)}(\mathbf{J}) = 0$ without loss of generality. Using Eq. (A.15), the old variables expressed in terms of the new ones are

$$\mathbf{J}^{(0)} = \mathbf{J} - \varepsilon \sum_{\mathbf{n} \neq \mathbf{0}} \mathbf{n} \overline{V}_{\mathbf{n}}^{(1)}(\mathbf{J}) \frac{e^{i\mathbf{n} \cdot \boldsymbol{\phi}}}{\mathbf{n} \cdot \boldsymbol{\Omega}} + O(\varepsilon^2) \tag{A.19a}$$

$$\boldsymbol{\phi}^{(0)} = \boldsymbol{\phi} - i\varepsilon \sum_{\mathbf{n} \neq \mathbf{0}} \frac{\partial \overline{V}_{\mathbf{n}}^{(1)}(\mathbf{J})}{\partial \mathbf{J}} \frac{e^{i\mathbf{n} \cdot \boldsymbol{\phi}}}{\mathbf{n} \cdot \boldsymbol{\Omega}} + O(\varepsilon^2). \tag{A.19b}$$

Finally, these expression can be substituted into Eq. (3.22) to obtain the original dynamical variables, $(\mathbf{p}, \mathbf{q})$, in terms of the new action-angle variables, $(\mathbf{J}, \boldsymbol{\phi})$.

A.3   Local Gaussian approximation

Let us write the LSC-IVR approximation to the symmetrised TCF as

$$
\begin{aligned}
C_{AB}^{[\mathrm{R}]}(\beta; t) \approx \frac{1}{(2\pi\hbar)^F Z_{\mathrm{q}}(\beta)} \int \mathrm{d}^F\mathbf{p} \int \mathrm{d}^F\mathbf{q} \, \big[\hat{U}(-\mathrm{i}\beta\hbar)\big]_{\mathrm{W}}(\mathbf{p}, \mathbf{q}) \\
\times f_A^{[\mathrm{sym}]}(\mathbf{p}, \mathbf{q}) \, \mathrm{e}^{\mathcal{L}t}\big[\hat{B}\big]_{\mathrm{W}}(\mathbf{p}, \mathbf{q}),
\end{aligned}
\tag{A.20}
$$

where we have factorised the static component of the integrand into the unnormalised Wigner quasi-probability distribution

$$
\big[\hat{U}(-\mathrm{i}\beta\hbar)\big]_{\mathrm{W}}(\mathbf{p}, \mathbf{q}) = \int \mathrm{d}^F\mathbf{\Delta} \, \mathrm{e}^{\mathrm{i}\mathbf{p}\cdot\mathbf{\Delta}/\hbar} \big\langle \mathbf{q} + \mathbf{\Delta}/2 \big| \hat{U}(-\mathrm{i}\beta\hbar) \big| \mathbf{q} - \mathbf{\Delta}/2 \big\rangle,
\tag{A.21}
$$

and the estimator

$$
f_A^{[\mathrm{sym}]}(\mathbf{p}, \mathbf{q}) = \frac{\mathrm{Re}\big[\hat{U}(-\mathrm{i}\beta\hbar)\hat{A}\big]_{\mathrm{W}}(\mathbf{p}, \mathbf{q})}{\big[\hat{U}(-\mathrm{i}\beta\hbar)\big]_{\mathrm{W}}(\mathbf{p}, \mathbf{q})}.
\tag{A.22}
$$

The LGA of Liu and Miller [60] is an extension of the local harmonic approximation (LHA), proposed earlier by Shi and Geva [57]. To derive the LHA, the PES is approximated by its second-order Taylor expansion about configuration $\mathbf{q}$, giving

$$
V(\mathbf{q} + \delta\mathbf{q}) \simeq V(\mathbf{q}) + \delta\mathbf{q} \cdot \nabla_{\mathbf{q}} V(\mathbf{q}) + \frac{1}{2}\delta\mathbf{q} \cdot \mathbf{M}^{1/2}\mathbf{K}(\mathbf{q})\mathbf{M}^{1/2}\delta\mathbf{q},
\tag{A.23}
$$

where $\mathbf{K}(\mathbf{q})$ is the mass-weighted Hessian matrix,

$$
\mathbf{M}^{1/2}\mathbf{K}(\mathbf{q})\mathbf{M}^{1/2} = \big(\nabla_{\mathbf{q}} \otimes \nabla_{\mathbf{q}}\big)V(\mathbf{q}).
\tag{A.24}
$$

It can be shown [57, 60] that the corresponding approximation to the imaginary-time propagator is

$$
\big\langle \mathbf{q} + \mathbf{\Delta}/2 \big| \hat{U}(-\mathrm{i}\beta\hbar) \big| \mathbf{q} - \mathbf{\Delta}/2 \big\rangle \simeq \big\langle \mathbf{q} \big| \hat{U}(-\mathrm{i}\beta\hbar) \big| \mathbf{q} \big\rangle \exp\left(-\frac{\mathbf{\Delta} \cdot \mathbf{M}^{1/2}\mathbf{\Phi}(\mathbf{q})\mathbf{M}^{1/2}\mathbf{\Delta}}{2\beta\hbar^2}\right),
\tag{A.25}
$$

where the 'quantum correction factor' (QCF) $\mathbf{\Phi}(\mathbf{q})$ is defined as

$$
\mathbf{\Phi}(\mathbf{q}) = g\big(\mathbf{K}^{1/2}(\mathbf{q})\big),
\tag{A.26}
$$

with

$$
g(\omega) = \frac{\beta\hbar\omega}{2}\coth\left(\frac{\beta\hbar\omega}{2}\right).
\tag{A.27}
$$

Substituting Eq. (A.25) into Eq. (A.21), and evaluating the multidimensional Fourier integral, gives

$$\frac{\left[\hat{U}(-i\beta\hbar)\right]_W(\mathbf{p}, \mathbf{q})}{\langle\mathbf{q}|\hat{U}(-i\beta\hbar)|\mathbf{q}\rangle} \simeq \frac{\exp\left(-\frac{\beta}{2}\mathbf{p}\cdot\mathbf{M}^{-1/2}\mathbf{\Phi}^{-1}(\mathbf{q})\mathbf{M}^{-1/2}\mathbf{p}\right)}{\sqrt{\beta^{-1}\det(2\pi\mathbf{M}^{1/2}\mathbf{\Phi}(\mathbf{q})\mathbf{M}^{1/2})}} \tag{A.28}$$

for the conditional momentum distribution. This is the LHA. To obtain the LGA, one simply replaces $f(\gamma_i(\mathbf{q}))$ by $1/f(|\gamma_i(\mathbf{q})|)$ for each eigenvalue $\gamma_i^2(\mathbf{q})$ of $\mathbf{K}(\mathbf{q})$ that is negative and for which $\beta\hbar|\gamma_i(\mathbf{q})| > \pi$. This *ad hoc* modification ensures that the momentum distribution remains normalisable at barriers [60].

In a typical LSC-IVR+LGA simulation, the marginal position distribution $\langle\mathbf{q}|\hat{U}(-i\beta\hbar)|\mathbf{q}\rangle$ (appropriately normalised) is sampled using PIMD (or PIMC). The momenta are then sampled from the right-hand size of (A.28) in the basis of instantaneous normal modes (i.e., the eigenbasis of $\mathbf{K}(\mathbf{q})$) [60]. To be able to calculate symmetrised TCFs, one also requires an efficient way to evaluate the estimators $f_A^{[\text{sym}]}(\mathbf{p}, \mathbf{q})$ and $[\hat{B}]_W(\mathbf{p}, \mathbf{q})$; this can be formulated on a case-by-case basis. In the case that $\hat{A}$ and $\hat{B}$ are both the dipole moment operator $\hat{\mu} \equiv \mu(\hat{\mathbf{q}})$, which we assume to to be a three-dimensional column vector, their Wigner transforms are trivially

$$\left[\hat{\mu}\right]_W(\mathbf{p}, \mathbf{q}) = \mu(\mathbf{p}, \mathbf{q}). \tag{A.29}$$

To obtain a tractable expression for $f_\mu^{[\text{sym}]}(\mathbf{p}, \mathbf{q})$, one expands the matrix elements of $\hat{U}(-i\beta\hbar)\hat{\mu}$ to $O(\Delta)$ to obtain

$$f_\mu^{[\text{sym}]}(\mathbf{p}, \mathbf{q}) \simeq \mu(\mathbf{q}), \tag{A.30}$$

which is exact in the case that the DMS is linear. If the DMS is nonlinear, the leading error in Eq. (A.30) is $O(\hbar^2)$, and may be viewed in the phase space of imaginary-time Feynman paths as a consequence of neglecting the dependence of the dipole moment on the non-Matsubara modes [73]. If, instead, $\hat{A}$ and $\hat{B}$ are both the dipole-derivative operator $\hat{\dot{\mu}} = (i/\hbar)[\hat{H}, \mu(\hat{\mathbf{q}})]$, then it is straightforward to show (by applying the quantum phase-space Liouvillian to Eqs. (A.29–A.30)) that [68]

$$\left[\hat{\dot{\mu}}\right]_W(\mathbf{p}, \mathbf{q}) = \dot{\mu}(\mathbf{p}, \mathbf{q}) = \mathbf{\Xi}(\mathbf{q})\mathbf{M}^{-1}\mathbf{p}, \tag{A.31}$$

and

$$f_{\dot{\mu}}^{[\text{sym}]}(\mathbf{p}, \mathbf{q}) \simeq \dot{\mu}(\mathbf{p}, \mathbf{q}), \tag{A.32}$$

where we have defined the $3 \times F$ effective charge matrix

$$\mathbf{\Xi}(\mathbf{q}) = \frac{\partial\mu(\mathbf{q})}{\partial\mathbf{q}^T}. \tag{A.33}$$

To calculate LSC-IVR+LGA approximations to Kubo-transformed TCFs, the procedure

is the same, except that the static estimator $f_A^{[\text{sym}]}(\mathbf{p}, \mathbf{q})$ is replaced by its Kubo-transformed version,

$$f_A^{[\text{Kubo}]}(\mathbf{p}, \mathbf{q}) = \frac{1}{\beta\hbar} \frac{\int_0^{\beta\hbar} \mathrm{d}\tau \left[\hat{U}(-\mathrm{i}(\beta\hbar - \tau))\hat{A}\hat{U}(-\mathrm{i}\tau)\right]_{\mathrm{W}}(\mathbf{p}, \mathbf{q})}{\left[\hat{U}(-\mathrm{i}\beta\hbar)\right]_{\mathrm{W}}(\mathbf{p}, \mathbf{q})}. \tag{A.34}$$

For the dipole derivative, one can exploit the identities

$$\frac{1}{\beta\hbar} \int_0^{\beta\hbar} \mathrm{d}\tau \left[\hat{U}(-\mathrm{i}(\beta\hbar - \tau))\hat{A}\hat{U}(-\mathrm{i}\tau)\right]_{\mathrm{W}}(\mathbf{p}, \mathbf{q}) = \frac{2}{\beta\hbar} \operatorname{Im}\left[\hat{U}(-\mathrm{i}\beta\hbar)\hat{A}\right]_{\mathrm{W}}(\mathbf{p}, \mathbf{q}) \tag{A.35}$$

and

$$\operatorname{Im}\left[\hat{U}(-\mathrm{i}\beta\hbar)\hat{\mathbf{q}}\right]_{\mathrm{W}}(\mathbf{p}, \mathbf{q}) = \frac{\hbar}{2}\nabla_{\mathbf{p}}\left[\hat{U}(-\mathrm{i}\beta\hbar)\right]_{\mathrm{W}}(\mathbf{p}, \mathbf{q}) \tag{A.36}$$

to show that the lowest-order approximation to this estimator is [68]

$$f_{\boldsymbol{\mu}}^{[\text{Kubo}]}(\mathbf{p}, \mathbf{q}) \simeq \boldsymbol{\Xi}(\mathbf{q})\mathbf{M}^{-1/2}\boldsymbol{\Phi}^{-1}(\mathbf{q})\mathbf{M}^{-1/2}\mathbf{p}. \tag{A.37}$$

Appendix B

Additional derivations

B.1 Quantum $\|\Delta\mathbf{n}\|_1 = 2$ intensities to second order

Our goal here is to evaluate the quantum integrated $\|\Delta\mathbf{n}\|_1 = 2$ intensities, up to second order in ε, for the system of coupled harmonic oscillators defined in Section 3.2.1. Let us start by considering the simplified perturbations,

$$V^{(1)}(\mathbf{q}) = \eta_{ijk} q_i q_j q_k + \eta_{ijl} q_i q_j q_l \tag{B.1}$$

and

$$\mu^{(1)}(\mathbf{q}) = \kappa_{ij} q_i q_j, \tag{B.2}$$

with $i \neq j$ and $k, l \notin \{i, j\}$. Later on, we will generalise to account for all the summands of Eqs. (3.47–3.48). By re-expressing $\hat{V}^{(1)}$ in terms of creation and annihilation operators, $\hat{a}^\dagger$ and $\hat{a}$ respectively, where

$$\hat{a}_i = \frac{1}{\sqrt{2\hbar\Omega_i}} (\Omega_i \hat{q}_i + i\hat{p}_i), \tag{B.3}$$

and noting that their effects on the unperturbed eigenkets are

$$\hat{a}_i^\dagger |\ldots, n_i, \ldots\rangle = \sqrt{n_i + 1} |\ldots, n_i + 1, \ldots\rangle \tag{B.4a}$$

$$\hat{a}_i |\ldots, n_i, \ldots\rangle = \sqrt{n_i} |\ldots, n_i - 1, \ldots\rangle, \tag{B.4b}$$

we find that Eq. (3.50) and (3.51) reduce straightforwardly to

$$E_{\mathbf{n}}^{(1)} = 0 \tag{B.5}$$

and

$$
\left|\psi_{\mathbf{n}}^{(1)}\right\rangle = \sum_{k'\in\{k,l\}} \frac{\eta_{ijk'}}{4} \sqrt{\frac{2\hbar}{\Omega_i\Omega_j\Omega_{k'}}}
$$

$$
\times\Bigg[-(\Omega_i+\Omega_j+\Omega_{k'})^{-1}\left|\ldots,n_i+1,\ldots,n_j+1,\ldots,n_{k'}+1,\ldots\right\rangle\sqrt{(n_i+1)(n_j+1)(n_{k'}+1)}
$$

$$
+(\Omega_i-\Omega_j-\Omega_{k'})^{-1}\left|\ldots,n_i-1,\ldots,n_j+1,\ldots,n_{k'}+1,\ldots\right\rangle\sqrt{n_i(n_j+1)(n_{k'}+1)}
$$

$$
-(\Omega_i-\Omega_j+\Omega_{k'})^{-1}\left|\ldots,n_i+1,\ldots,n_j-1,\ldots,n_{k'}+1,\ldots\right\rangle\sqrt{(n_i+1)n_j(n_{k'}+1)}
$$

$$
-(\Omega_i+\Omega_j-\Omega_{k'})^{-1}\left|\ldots,n_i+1,\ldots,n_j+1,\ldots,n_{k'}-1,\ldots\right\rangle\sqrt{(n_i+1)(n_j+1)n_{k'}}
$$

$$
-(\Omega_i-\Omega_j-\Omega_{k'})^{-1}\left|\ldots,n_i+1,\ldots,n_j-1,\ldots,n_{k'}-1,\ldots\right\rangle\sqrt{(n_i+1)n_jn_{k'}}
$$

$$
+(\Omega_i-\Omega_j+\Omega_{k'})^{-1}\left|\ldots,n_i-1,\ldots,n_j+1,\ldots,n_{k'}-1,\ldots\right\rangle\sqrt{n_i(n_j+1)n_{k'}}
$$

$$
+(\Omega_i+\Omega_j-\Omega_{k'})^{-1}\left|\ldots,n_i-1,\ldots,n_j-1,\ldots,n_{k'}+1,\ldots\right\rangle\sqrt{n_in_j(n_{k'}+1)}
$$

$$
+(\Omega_i+\Omega_j+\Omega_{k'})^{-1}\left|\ldots,n_i-1,\ldots,n_j-1,\ldots,n_{k'}-1,\ldots\right\rangle\sqrt{n_in_jn_{k'}}\Bigg].
$$

(B.6)

For the $\nu_i \pm \nu_j$ combination/difference band, Eq. (3.9) for the integrated intensity reduces to

$$
\mathcal{I}_{\nu_i\pm\nu_j}^{[\mathrm{q}]} = \varepsilon^2 I_{\nu_i\pm\nu_j}^{[\mathrm{q}]} + O(\varepsilon^3),
\tag{B.7}
$$

where

$$
I_{\nu_i\pm\nu_j}^{[\mathrm{q}]}(\beta) = \frac{2\pi}{\hbar}|\mathcal{E}|^2(\Omega_i\pm\Omega_j)\big(1-\mathrm{e}^{-\beta\hbar(\Omega_i\pm\Omega_j)}\big)
$$

$$
\times\big(1-\mathrm{e}^{-\beta\hbar\Omega_i}\big)\big(1-\mathrm{e}^{-\beta\hbar\Omega_j}\big)\big(1-\mathrm{e}^{-\beta\hbar\Omega_k}\big)\big(1-\mathrm{e}^{-\beta\hbar\Omega_l}\big)
$$

$$
\times\sum_{n_i=0}^{\infty}\sum_{n_j=(1\mp1)/2}^{\infty}\sum_{n_k=0}^{\infty}\sum_{n_l=0}^{\infty}\mathrm{e}^{-\beta\hbar(n_i\Omega_i+n_j\Omega_j+n_k\Omega_k+n_l\Omega_l)}
$$

$$
\times\Bigg\{\xi_k^2\left|\langle\mathbf{n}|\hat{q}_k|\psi_{\mathbf{n}+\Delta\mathbf{n}}^{(1)}\rangle + \langle\psi_{\mathbf{n}}^{(1)}|\hat{q}_k|\mathbf{n}+\Delta\mathbf{n}\rangle\right|^2 + \xi_l^2\left|\langle\mathbf{n}|\hat{q}_l|\psi_{\mathbf{n}+\Delta\mathbf{n}}^{(1)}\rangle + \langle\psi_{\mathbf{n}}^{(1)}|\hat{q}_l|\mathbf{n}+\Delta\mathbf{n}\rangle\right|^2
$$

$$
+ \kappa_{ij}^2\left|\langle\mathbf{n}|\hat{q}_i\hat{q}_j|\mathbf{n}+\Delta\mathbf{n}\rangle\right|^2
$$

$$
+ 2\xi_k\xi_l\,\mathrm{Re}\Big[\big(\langle\mathbf{n}|\hat{q}_k|\psi_{\mathbf{n}+\Delta\mathbf{n}}^{(1)}\rangle + \langle\psi_{\mathbf{n}}^{(1)}|\hat{q}_k|\mathbf{n}+\Delta\mathbf{n}\rangle\big)\big(\langle\mathbf{n}+\Delta\mathbf{n}|\hat{q}_l|\psi_{\mathbf{n}}^{(1)}\rangle + \langle\psi_{\mathbf{n}+\Delta\mathbf{n}}^{(1)}|\hat{q}_l|\mathbf{n}\rangle\big)\Big]
$$

$$
+ 2\xi_k\kappa_{ij}\,\mathrm{Re}\Big[\big(\langle\mathbf{n}|\hat{q}_k|\psi_{\mathbf{n}+\Delta\mathbf{n}}^{(1)}\rangle + \langle\psi_{\mathbf{n}}^{(1)}|\hat{q}_k|\mathbf{n}+\Delta\mathbf{n}\rangle\big)\langle\mathbf{n}+\Delta\mathbf{n}|\hat{q}_i\hat{q}_j|\mathbf{n}\rangle\Big]
$$

$$
+ 2\xi_l\kappa_{ij}\,\mathrm{Re}\Big[\big(\langle\mathbf{n}|\hat{q}_l|\psi_{\mathbf{n}+\Delta\mathbf{n}}^{(1)}\rangle + \langle\psi_{\mathbf{n}}^{(1)}|\hat{q}_l|\mathbf{n}+\Delta\mathbf{n}\rangle\big)\langle\mathbf{n}+\Delta\mathbf{n}|\hat{q}_i\hat{q}_j|\mathbf{n}\rangle\Big]\Bigg\},
$$

(B.8)

in which $\Delta n_{k'} = \delta_{ik'} \pm \delta_{jk'}$. Substituting Eq. (B.6) into Eq. (B.8) yields, after some algebra,

$$
\begin{aligned}
I^{[\mathrm{q}]}_{\nu_i \pm \nu_j}(\beta) = {}& \pi |\mathcal{E}|^2 \mathrm{e}^{-\beta\hbar(\Omega_j \mp \Omega_j)/2}\left(1 - \mathrm{e}^{-\beta\hbar(\Omega_i \pm \Omega_j)}\right)\left(1 - \mathrm{e}^{-\beta\hbar\Omega_i}\right)\left(1 - \mathrm{e}^{-\beta\hbar\Omega_j}\right) \\
& \times \frac{\hbar(\Omega_i \pm \Omega_j)}{2\Omega_i\Omega_j}\left[\kappa_{ij} + \sum_{k' \in \{k,l\}} \frac{\eta_{ijk'}\xi_{k'}}{(\Omega_i \pm \Omega_j)^2 - \Omega_{k'}^2}\right]^2 \\
& \times \sum_{n_i=0}^{\infty}\sum_{n_j=0}^{\infty} \mathrm{e}^{-\beta\hbar(n_i\Omega_i + n_j\Omega_j)}(n_i + 1)(n_j + 1).
\end{aligned}
\tag{B.9}
$$

The infinite sums are readily evaluated by applying standard formulae for geometric series and their derivatives, leading to

$$
I^{[\mathrm{q}]}_{\nu_i \pm \nu_j}(\beta) = \frac{1}{2}\left[\kappa_{ij} + \sum_{k' \in \{k,l\}} \frac{\eta_{ijk'}\xi_{k'}}{(\Omega_i \pm \Omega_j)^2 - \Omega_{k'}^2}\right]^2 \tilde{I}^{[\mathrm{q}]}(\beta; \Omega_i, \pm\Omega_j),
\tag{B.10}
$$

where

$$
\tilde{I}^{[\mathrm{q}]}(\beta; \Omega_i, \Omega_j) = \frac{\pi |\mathcal{E}|^2 \hbar(\Omega_i + \Omega_j)}{2\Omega_i\Omega_j}\left[\coth\left(\frac{\beta\hbar\Omega_i}{2}\right) + \coth\left(\frac{\beta\hbar\Omega_j}{2}\right)\right].
\tag{B.11}
$$

One can refine Eq. (B.10) by repeating the preceding derivation with $i = j$ and finding that, for the overtone band $2\nu_i$, a factor of $1/2$ emerges. Furthermore, if $k \in \{i, j\}$ or $l \in \{i, j\}$, one obtains an additional factor of $1/2$ if $i \neq j$, or $1/3$ if $i = j$. If $\hat{V}^{(1)}$ is now chosen to be defined as in Eq. (3.47), and $\hat{\mu}$ as in Eq. (3.46), one must in turn alter Eq. (B.10) to sum over all $k, l \in \{1, \ldots, F\}$. Accounting carefully for the numbers of unique permutations of indices, as well as the emerging factors of $1/2$ and $1/3$ noted above, the final result is

$$
I^{[\mathrm{q}]}_{\nu_i \pm \nu_j}(\beta) = C_{ij}(\boldsymbol{\eta}, \boldsymbol{\xi}, \boldsymbol{\kappa}, \boldsymbol{\Omega})\tilde{I}^{[\mathrm{q}]}(\beta; \Omega_i, \pm\Omega_j),
\tag{B.12}
$$

where

$$
C_{ij}(\boldsymbol{\eta}, \boldsymbol{\xi}, \boldsymbol{\kappa}, \boldsymbol{\Omega}) = \frac{2 - \delta_{ij}}{4}\left[\kappa_{ij} + \sum_{k=1}^{F} \frac{\eta_{ijk}\xi_k}{(\Omega_i \pm \Omega_j)^2 - \Omega_k^2}\right]^2,
\tag{B.13}
$$

as quoted in Eqs. (3.53–3.55).

B.2 Classical perturbation theory of coupled harmonic oscillators

Here we apply classical CPT, as outlined in Appendix 3.2.3, to the system of coupled harmonic oscillators defined in Section 3.2.1. The cubic perturbation of Eq. (3.47) may be written in terms of the old action-angle variables as

$$\overline{V}^{(1)}\big(\mathbf{J}^{(0)}, \boldsymbol{\phi}^{(0)}\big) = \frac{\sqrt{2}}{3} \sum_{i=1}^{F} \sum_{j=1}^{F} \sum_{k=1}^{F} \eta_{ijk} \sqrt{\frac{J_i^{(0)} J_j^{(0)} J_k^{(0)}}{\Omega_i \Omega_j \Omega_k}} \sin\big(\phi_i^{(0)}\big) \sin\big(\phi_j^{(0)}\big) \sin\big(\phi_k^{(0)}\big). \quad \text{(B.14)}$$

From Eqs. (A.18) and (A.19) we then obtain

$$E^{(1)} = 0 \qquad \text{(B.15)}$$

and

$$
\begin{aligned}
J_i^{(0)} &= J_i + \frac{\varepsilon}{\sqrt{8}} \sum_{j=1}^{F} \sum_{k=1}^{F} \eta_{ijk} \sqrt{\frac{J_i J_j J_k}{\Omega_i \Omega_j \Omega_k}} \\
&\times \left[\frac{\sin(\phi_i + \phi_j + \phi_k)}{\Omega_i + \Omega_j + \Omega_k} + \frac{\sin(\phi_i - \phi_j - \phi_k)}{\Omega_i - \Omega_j - \Omega_k} \right. \\
&\left. - \frac{\sin(\phi_i + \phi_j - \phi_k)}{\Omega_i + \Omega_j - \Omega_k} - \frac{\sin(\phi_i - \phi_j + \phi_k)}{\Omega_i - \Omega_j + \Omega_k} \right] + O(\varepsilon^2)
\end{aligned}
\qquad \text{(B.16a)}
$$

$$
\begin{aligned}
\phi_i^{(0)} &= \phi_i + \frac{\varepsilon}{\sqrt{32}} \sum_{j=1}^{F} \sum_{k=1}^{F} \eta_{ijk} \sqrt{\frac{J_j J_k}{\Omega_i \Omega_j \Omega_k J_i}} \\
&\times \left[\frac{\cos(\phi_i + \phi_j + \phi_k)}{\Omega_i + \Omega_j + \Omega_k} + \frac{\cos(\phi_i - \phi_j - \phi_k)}{\Omega_i - \Omega_j - \Omega_k} \right. \\
&\left. - \frac{\cos(\phi_i + \phi_j - \phi_k)}{\Omega_i + \Omega_j - \Omega_k} - \frac{\cos(\phi_i - \phi_j + \phi_k)}{\Omega_i - \Omega_j + \Omega_k} \right] + O(\varepsilon^2).
\end{aligned}
\qquad \text{(B.16b)}
$$

Substituting Eq. (B.16) into

$$q_i = \sqrt{\frac{2 J_i^{(0)}}{\Omega_i}} \sin\big(\phi_i^{(0)}\big) \qquad \text{(B.17)}$$

gives the position coordinate for oscillator i as

$$
\begin{aligned}
q_i &= \sqrt{\frac{2 J_i}{\Omega_i}} \sin(\phi_i) \\
&- \frac{\varepsilon}{2} \sum_{j=1}^{F} \sum_{k=1}^{F} \eta_{ijk} \sqrt{\frac{J_j J_k}{\Omega_j \Omega_k}} \left[\frac{\cos(\phi_j + \phi_k)}{(\Omega_j + \Omega_k)^2 - \Omega_i^2} - \frac{\cos(\phi_j - \phi_k)}{(\Omega_j - \Omega_k)^2 - \Omega_i^2} \right] + O(\varepsilon^2),
\end{aligned}
\qquad \text{(B.18)}
$$

which was quoted in Eq. (3.64)

B.3 Matsubara perturbation theory

B.3.1 Vanishing first-order perturbation to the Matsubara phase

To show that the Matsubara phase is unperturbed to first order in ε, consider that the phase is itself a constant of the motion. Thus, we expect there to exist a canonical transformation from $(\mathbf{P}, \mathbf{Q})$ to a set of action-angle variables $(L, \ldots, \phi_L, \ldots)$, where

$$L = -\frac{\beta\hbar}{2\pi}\widetilde{\Theta}_M(\mathcal{J}, \boldsymbol{\varphi}) = \sum_{k=-\overline{M}}^{\overline{M}} k P_{-k} Q_k \tag{B.19}$$

is one of the action coordinates and ϕ_L is its conjugate angle, such that

$$\frac{\partial}{\partial\phi_L} = \{\cdot, L\} = \sum_{k=-\overline{M}}^{\overline{M}} k\left[P_k\frac{\partial}{\partial P_{-k}} + Q_k\frac{\partial}{\partial Q_{-k}}\right]. \tag{B.20}$$

The dynamical variables of the Matsubara modes depend implicitly on the imaginary-time origin, τ_0, through

$$p(\tau + \tau_0) = P_0(\tau_0) + \sqrt{2}\sum_{k=1}^{\overline{M}}\left[P_k(\tau_0)\sin(\omega_k\tau) + P_{-k}(\tau_0)\cos(\omega_k\tau)\right] \tag{B.21a}$$

$$q(\tau + \tau_0) = Q_0(\tau_0) + \sqrt{2}\sum_{k=1}^{\overline{M}}\left[Q_k(\tau_0)\sin(\omega_k\tau) + Q_{-k}(\tau_0)\cos(\omega_k\tau)\right]. \tag{B.21b}$$

It follows that

$$P_k(\tau_0) = P_k(0)\cos(\omega_k\tau_0) - P_{-k}(0)\sin(\omega_k\tau_0) \tag{B.22a}$$

$$Q_k(\tau_0) = Q_k(0)\cos(\omega_k\tau_0) - Q_{-k}(0)\sin(\omega_k\tau_0), \tag{B.22b}$$

and therefore

$$\frac{\partial P_k}{\partial\tau_0} = -\omega_k P_{-k} \tag{B.23a}$$

$$\frac{\partial Q_k}{\partial\tau_0} = -\omega_k Q_{-k}. \tag{B.23b}$$

By applying the chain rule, we can construct an 'imaginary-time Liouvillian'.

$$\frac{\partial}{\partial \tau_0} = \sum_{k=-\overline{M}}^{\overline{M}} \omega_k \left[P_k \frac{\partial}{\partial P_{-k}} + Q_k \frac{\partial}{\partial Q_{-k}} \right], \tag{B.24}$$

Comparing Eq. (B.24) to Eq. (B.20), we see that

$$\phi_L = \frac{2\pi\tau_0}{\beta\hbar} + \delta_L, \tag{B.25}$$

where δ_L is an arbitrary, constant phase shift. Since the Matsubara potential is imaginary-time translation invariant, and thus independent of ϕ_L, it follows from Eq. (A.19a) that

$$\widetilde{\Theta}_M(\boldsymbol{\mathcal{J}}, \boldsymbol{\varphi}) = \widetilde{\Theta}_M^{(0)}(\boldsymbol{\mathcal{J}}, \boldsymbol{\varphi}) + O(\varepsilon^2), \tag{B.26}$$

which was quoted in Eq. (3.75) and is what we set out to show.

B.3.2 Equivalence of perturbations in truncated and mean-field Matsubara dynamics

Here we show that, for a one-dimensional oscillator with only cubic anharmonicity, the mean-field and truncated Matsubara potentials are equivalent to first order in the perturbation parameter, up to a constant shift in the position of equilibrium. The quantum Hamiltonian is

$$\hat{H} = \hat{H}^{(0)} + \varepsilon \hat{V}^{(1)}, \tag{B.27}$$

where

$$\hat{H}^{(0)} = \frac{1}{2}(\hat{p}^2 + \Omega^2 \hat{q}^2) \tag{B.28}$$

and

$$\hat{V}^{(1)} = \frac{\eta}{6}\hat{q}^3. \tag{B.29}$$

The truncated Matsubara potential is thus

$$\widetilde{U}_M(\mathbf{Q}) = \frac{\Omega^2}{2} \sum_{|k| \leqslant \overline{M}} Q_k^2 + \varepsilon \widetilde{U}_M^{(1)}(\mathbf{Q}), \tag{B.30}$$

where

$$\widetilde{U}_M^{(1)}(\mathbf{Q}) = \frac{\eta}{6}Q_0^3 + \frac{\eta}{2}Q_0 \sum_{0 < |k| \leqslant \overline{M}} Q_k^2 + \Upsilon_M(\mathbf{Q}), \tag{B.31}$$

and Υ_M contains only terms that are independent of the centroid,

$$\Upsilon_M(\mathbf{Q}) = \frac{\sqrt{2}\eta}{4} \sum_{j=1}^{\overline{M}-1} \sum_{k=j+1}^{\overline{M}} \left[Q_{j-k}(Q_j Q_k + Q_{-j}Q_{-k}) - Q_{k-j}(Q_j Q_{-k} - Q_{-j}Q_k) \right]. \tag{B.32}$$

The total force acting on the centroid in truncated Matsubara dynamics is therefore

$$-\frac{\partial \widetilde{U}_M(\mathbf{Q})}{\partial Q_0} = -\Omega^2 Q_0 - \frac{\varepsilon\eta}{2} \sum_{|k| \leqslant \overline{M}} Q_k^2. \tag{B.33}$$

In the mean-field formulation, the force on the centroid is instead given by

$$-\frac{\partial \widetilde{\mathcal{F}}_M^{(1)}(\mathbf{Q})}{\partial Q_0} = -\lim_{M' \to \infty} \frac{\int \mathrm{d}^{M'-M}\mathbf{Q}_{|k|>\overline{M}} \ \exp\left(-\beta\left[\frac{1}{2}\sum_{\overline{M}<|k|\leqslant\overline{M}'}\omega_k^2 Q_k^2 + \widetilde{U}_{M'}(\mathbf{Q})\right]\right)\frac{\partial \widetilde{U}_{M'}^{(1)}(\mathbf{Q})}{\partial Q_0}}{\int \mathrm{d}^{M'-M}\mathbf{Q}_{|k|>\overline{M}} \ \exp\left(-\beta\left[\frac{1}{2}\sum_{\overline{M}<|k|\leqslant\overline{M}'}\omega_k^2 Q_k^2 + \widetilde{U}_{M'}(\mathbf{Q})\right]\right)}. \tag{B.34}$$

Expanding the integrands in powers of ε gives

$$\exp\left(-\beta\left[\frac{1}{2}\sum_{\overline{M}<|k|\leqslant\overline{M}'}\omega_k^2 Q_k^2 + \widetilde{U}_{M'}(\mathbf{Q})\right]\right)$$

$$= \exp\left(-\frac{\beta}{2}\sum_{|k|\leqslant\overline{M}}\Omega^2 Q_k^2\right)\exp\left(-\frac{\beta}{2}\sum_{\overline{M}<|k|\leqslant\overline{M}'}\left[\Omega^2 + \omega_k^2\right]Q_k^2\right)\left[1 + \varepsilon\beta\widetilde{U}_{M'}^{(1)}(\mathbf{Q})\right] + O(\varepsilon^2) \tag{B.35}$$

and

$$\exp\left(-\beta\left[\frac{1}{2}\sum_{\overline{M}<|k|\leqslant\overline{M}'}\omega_k^2 Q_k^2 + \widetilde{U}_{M'}(\mathbf{Q})\right]\right)\frac{\partial \widetilde{U}_{M'}^{(1)}(\mathbf{Q})}{\partial Q_0}$$

$$= \exp\left(-\frac{\beta}{2}\sum_{|k|\leqslant\overline{M}}\Omega^2 Q_k^2\right)\exp\left(-\frac{\beta}{2}\sum_{\overline{M}<|k|\leqslant\overline{M}'}\left[\Omega^2 + \omega_k^2\right]Q_k^2\right) \tag{B.36}$$

$$\times \left[\Omega^2 Q_0 + \frac{\varepsilon\eta}{2}\sum_{|k|\leqslant\overline{M}}Q_k^2 + \frac{\varepsilon\eta}{2}\sum_{\overline{M}<|k|\leqslant\overline{M}'}Q_k^2 - \varepsilon\beta\Omega^2 Q_0^2\widetilde{U}_{M'}^{(1)}(\mathbf{Q})\right] + O(\varepsilon^2).$$

Performing the integration over $\mathbf{Q}_{|k|>\overline{M}}$, and using the definition of Matsubara effective inverse temperature from Eq. (3.92), yields

$$-\frac{\partial \widetilde{\mathcal{F}}_M^{(1)}(\mathbf{Q})}{\partial Q_0} = -\Omega^2 Q_0 - \frac{\varepsilon\eta}{2} \sum_{|k| \leqslant \overline{M}} Q_k^2 - \frac{\varepsilon\eta}{2\Omega^2}\left(\frac{1}{\beta^{[\infty]}} - \frac{1}{\beta^{[M]}}\right) + O(\varepsilon^2). \tag{B.37}$$

Finally, redefining the centroid position

$$Q_0 \leftarrow Q_0 + \frac{\varepsilon\eta}{2\Omega^4}\left(\frac{1}{\beta^{[\infty]}} - \frac{1}{\beta^{[M]}}\right) \tag{B.38}$$

gives

$$-\frac{\partial\widetilde{\mathcal{F}}_M^{(1)}(\mathbf{Q})}{\partial Q_0} = -\Omega^2 Q_0 - \frac{\varepsilon\eta}{2}\sum_{|k|\leqslant\overline{M}} Q_k^2 + O(\varepsilon^2), \tag{B.39}$$

which, to first order, is equivalent to the truncated force with a constant shift in the position of equilibrium. It follows that the expressions for spectral intensities given in Chapter 3, which were derived by applying first-order canonical perturbation theory to truncated Matsubara dynamics, apply with equal validity to the mean-field formulation.

B.3.3 Multidimensional Matsubara $\|\Delta\mathbf{n}\|_1 = 2$ intensities to second order

Here we outline the multidimensional analogue of the Matsubara CPT described in Section 3.2.4, with the PES and DMS as specified in Section 3.2.1. The action-angle variables, $\mathcal{J}_k \equiv (\mathcal{J}_{1,k}, \ldots, \mathcal{J}_{F,k})^{\mathrm{T}}$ and $\boldsymbol{\varphi}_k \equiv (\varphi_{1,k}, \ldots, \varphi_{F,k})^{\mathrm{T}}$, are defined analogously to their one-dimensional counterparts, and similarly for the 'old' variables $(\mathcal{J}_k^{(0)}, \boldsymbol{\varphi}_k^{(0)})$. The perturbation to the Matsubara potential written in terms of the old variables is

$$\overline{\widetilde{U}}_M^{(1)}(\mathcal{J}^{(0)}, \boldsymbol{\varphi}^{(0)}) = \sum_{i=1}^{F}\sum_{j=1}^{F}\sum_{j'=1}^{F}\eta_{ijl}\sqrt{\frac{2\mathcal{J}_{i,0}^{(0)}\mathcal{J}_{j,0}^{(0)}\mathcal{J}_{j',0}^{(0)}}{9\Omega_i\Omega_j\Omega_{j'}}}\sin(\varphi_{i,0}^{(0)})\sin(\varphi_{j,0}^{(0)})\sin(\varphi_{j',0}^{(0)})$$

$$+ \sum_{i=1}^{F}\sum_{j=1}^{F}\sum_{j'=1}^{F}\eta_{ijl}\sqrt{\frac{2\mathcal{J}_{i,0}^{(0)}}{\Omega_i\Omega_j\Omega_{j'}}}\sum_{0<|k|<\overline{M}}^{\overline{M}}\sqrt{\mathcal{J}_{j,k}^{(0)}\mathcal{J}_{j',k}^{(0)}}\sin(\varphi_{j,k}^{(0)})\sin(\varphi_{j',k}^{(0)}) + \ldots \tag{B.40}$$

Following the standard CPT procedure then gives the centroid variable of oscillator i in terms of the new action-angle variables as

$$Q_{i,0} = \sqrt{\frac{2\mathcal{J}_{i,0}}{\Omega_i}}\sin(\varphi_{i,0})$$

$$-\frac{\varepsilon}{2}\sum_{j=1}^{F}\sum_{j'=1}^{F}\sum_{k=-\overline{M}}^{\overline{M}}\eta_{ijj'}\sqrt{\frac{\mathcal{J}_{j,k}\mathcal{J}_{j',k}}{\Omega_j\Omega_{j'}}}\left[\frac{\cos(\varphi_{j,k}+\varphi_{j',k})}{(\Omega_j+\Omega_{j'})^2-\Omega_i^2} - \frac{\cos(\varphi_{j,k}-\varphi_{j',k})}{(\Omega_j-\Omega_{j'})^2-\Omega_i^2}\right] \tag{B.41}$$

$$+ O(\varepsilon^2).$$

The dipole moment estimator is given by

$$\tilde{\mu}_M(\mathbf{Q}) = \mu_0 + \boldsymbol{\xi} \cdot \mathbf{Q}_0 + \frac{1}{2} \sum_{i=1}^{F} \sum_{j=1}^{F} \kappa_{ij} \sum_{k=-\overline{M}}^{\overline{M}} Q_{i,k} Q_{j,k}, \tag{B.42}$$

and the Matsubara integrated intensity of band $\nu_i \pm \nu_j$ is given by

$$\mathcal{I}_{\Delta\mathbf{n}}^{[M]}(\beta) = \varepsilon^2 I_{\Delta\mathbf{n}}^{[M]}(\beta) + O(\varepsilon^3), \tag{B.43}$$

where

$$I_{\nu_i \pm \nu_j}^{[M]}(\beta) = \frac{\pi \alpha_M^F |\mathcal{E}|^2 \beta (\Omega_i \pm \Omega_j)^2}{2(2\pi\hbar)^F \Omega_i^2 \Omega_j^2 \widetilde{Z}_M^{(0)}(\beta)} \frac{2 - \delta_{ij}}{4} C_{ij}(\boldsymbol{\eta}, \boldsymbol{\xi}, \boldsymbol{\kappa}, \boldsymbol{\Omega})$$

$$\times \sum_{k=-\overline{M}}^{\overline{M}} \sum_{k'=-\overline{M}}^{\overline{M}} \int \mathrm{d}^{FM}\mathbf{\Pi} \int \mathrm{d}^{FM}\mathbf{X} \, e^{-\beta[H_M^{(0)}(\mathbf{\Pi},\mathbf{X}) + \mathrm{i}\theta_M(\mathbf{\Pi},\mathbf{X})]} \tag{B.44}$$

$$\times \left(\Pi_{i,k} - \mathrm{i}\Omega_i X_{i,k}\right)\left(\Pi_{j,k} \mp \mathrm{i}\Omega_j X_{j,k}\right)\left(\Pi_{i,k'} + \mathrm{i}\Omega_i X_{i,k'}\right)\left(\Pi_{j,k'} \pm \mathrm{i}\Omega_j X_{j,k'}\right)$$

and

$$\widetilde{Z}_M^{(0)}(\beta) = \prod_{i=1}^{F} \frac{\alpha_M}{\beta\hbar\Omega_i} \prod_{k=1}^{\overline{M}} \frac{4\pi^2}{\beta^2(\Omega_i^2 + \omega_k^2)}. \tag{B.45}$$

The variables $(\mathbf{\Pi}_k, \mathbf{X}_k) = (\mathbf{P}_k, \mathbf{Q}_k) + O(\varepsilon)$ are defined analogously to their one-dimensional counterparts. Eq. (B.44) may be evaluated by analytically continuing $\overline{\mathbf{\Pi}} = \mathbf{\Pi} + \mathrm{i}\omega_k \mathbf{X}_{-k}$ onto the real axis, leading to

$$I_{\nu_i \pm \nu_j}^{[M]}(\beta) = C_{ij}(\boldsymbol{\eta}, \boldsymbol{\xi}, \boldsymbol{\kappa}, \boldsymbol{\Omega}) \tilde{I}^{[M]}(\beta; \Omega_i, \pm\Omega_j), \tag{B.46}$$

where

$$\tilde{I}^{[M]}(\beta; \Omega_i, \Omega_j) = \tilde{I}^{[c]}\left(\mathbf{B}^{[M]}; \Omega_i, \Omega_j\right). \tag{B.47}$$

Hence

$$I_{\nu_i \pm \nu_j}^{[M]}(\beta) = I_{\nu_i \pm \nu_j}^{[c]}\left(\mathbf{B}^{[M]}\right), \tag{B.48}$$

as quoted in Eq. (3.91).

Appendix C

Supplementary numerical results

C.1 Gas-phase q-TIP4P/F water

In Figs. C.1 and C.2, we plot IR spectra for gas-phase water that have been calculated using the intramolecular part of the q-TIP4P/F PES with its associated point-charge DMS [33]. The computational details are otherwise as described in Section 4.1.1, with the QCMD results provided by G. Trenins calculated analogously to those of ref. 107.

The overall behaviour of each method is broadly the same as we observed for the more sophisticated Partridge–Schwenke surfaces (Figs. 4.1 and 4.2), with LSC-IVR+LGA the only quantum statistics–classical dynamics method able to give a reasonable description of the $\|\Delta \mathbf{n}\|_1 = 2$ band intensities. In fact, the lineshapes of the LSC-IVR+LGA $\|\Delta \mathbf{n}\|_1 = 2$ bands are considerably improved for the q-TIP4P/F model, with hardly any unphysical broadening relative to the corresponding quantum results. Upon closer inspection, however, we find that the integrated intensities of some of these bands are quite considerably overestimated, with ~190% (~230%) of the quantum $v_1 + v_2/v_2 + v_3$ intensity and ~130% (~120%) of the quantum $v_1 + v_3/2v_1/2v_3$ predicted at 300 K (150 K). This is consistent with the perturbative analysis of Plé *et al.*, which showed that erroneously high intensity can be a consequence of the LGA neglecting non-local correlations between momentum and position. Interestingly, the $2v_2$ band—which LSC-IVR+LGA was unable to resolve for the Partridge–Schwenke model— appears to be described the most accurately of all the $\|\Delta \mathbf{n}\|_1 = 2$ bands for the q-TIP4P/F model.

In Fig. C.1, we also apply the post-processing scaling factors of Eq. (3.119) to the classical and QCMD results. Like earlier, we have taken Ω_i and Ω_j in each case to be the first moments of the corresponding fundamental bands or band systems. Similar to the Partridge–Schwenke model, we find that the post-processing correction brings the $\|\Delta \mathbf{n}\|_1 = 2$ band regions of the QCMD spectrum especially into good agreement with exact quantum mechanics.

To help disentangle the effects that changing each surface has on the IR absorption bands, in
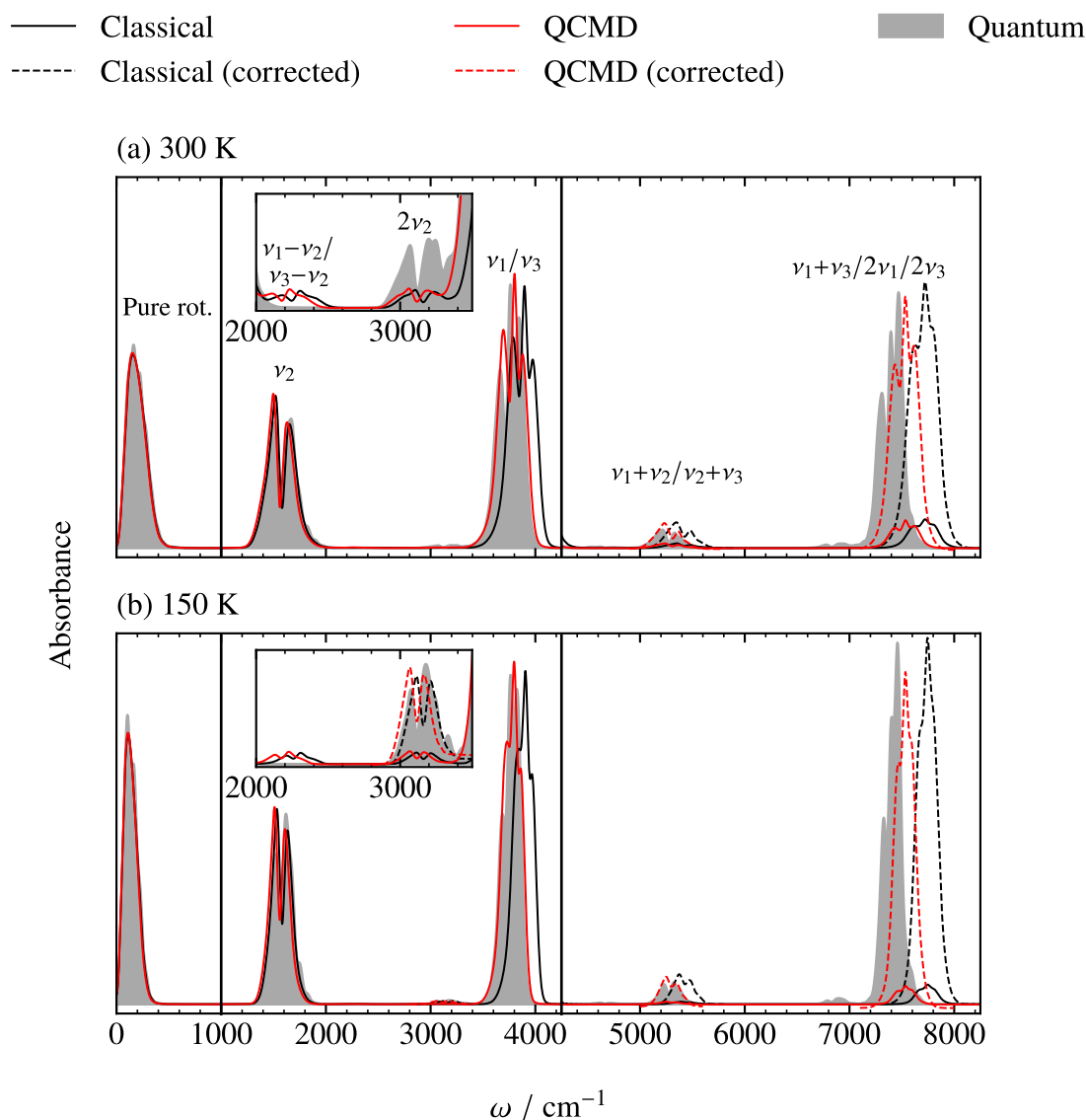
Figure C.1: As in Fig. 4.1, but using the q-TIP4P/F surfaces of ref. 33. The absorbances in the three panels of each graph are scaled as 1 : 2 : 100 (left-to-right), while the absorbances in the insets are each scaled by a factor of 25 relative to the panels in which they appear.

Fig. C.3, we plot the quantum and LSC-IVR+LGA spectra obtained at 300 K by mixing (a) the Partridge–Schwenke PES with the q-TIP4P/F DMS, and (b) vice versa. We see by comparing with Figs. 4.2(a) and C.2(a) that, as expected, the choice of DMS has a much greater effect on the absorption intensities than the choice of PES. The latter mostly controls the positions and lineshapes, and we note in particular that LSC-IVR+LGA gives better descriptions of the $\|\Delta\mathbf{n}\|_1 = 2$ lineshapes for the q-TIP4P/F PES than for the Partridge–Schwenke PES (regardless of the DMS), which is probably attributable to the milder anharmonicity of q-TIP4P/F. On the other hand, the $\nu_1 + \nu_2/\nu_2 + \nu_3$ and $\nu_1 + \nu_2/\nu_2 + \nu_3$ intensities are considerably overestimated
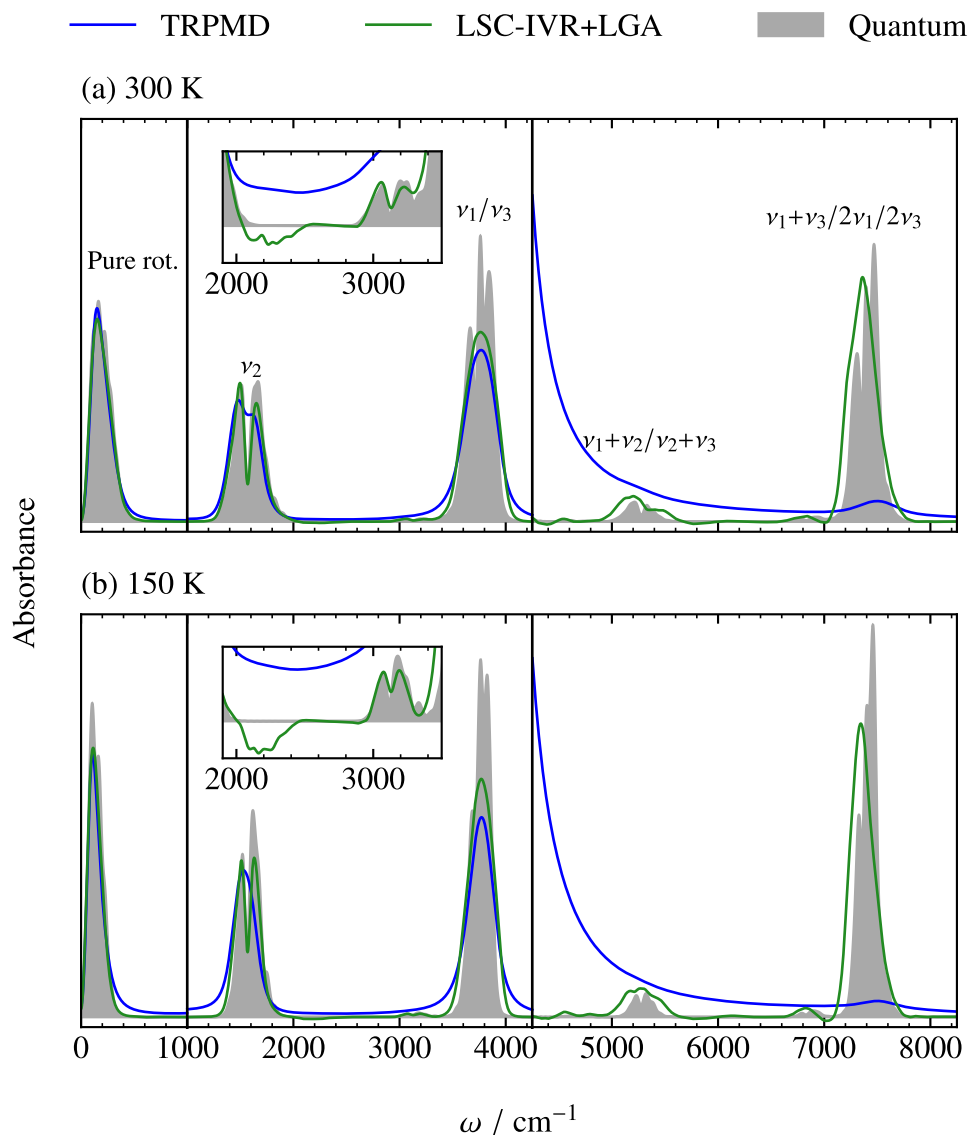
Figure C.2: As in Fig. 4.2, but using the q-TIP4P/F surfaces of ref. 33. The absorbances in the three panels of each graph are scaled as 1 : 2 : 100 (left-to-right), while the absorbances in the insets are each scaled by a factor of 15 relative to the panels in which they appear.

by LSC-IVR+LGA whenever the DMS is linear (q-TIP4P/F), whereas they are (on average) slightly underestimated when the DMS is nonlinear (Partridge–Schwenke). This is consistent with the perturbative analysis of Plé *et al.*, which assumed a linear DMS [65]. As noted in Section 4.1.2, the net underestimation of $\|\Delta \mathbf{n}\|_1 = 2$ intensities for a nonlinear DMS is almost certainly a result, at least in part, of neglecting $O(\hbar^2)$ and higher terms in Eq. (A.32) for the static dipole-derivative estimator.
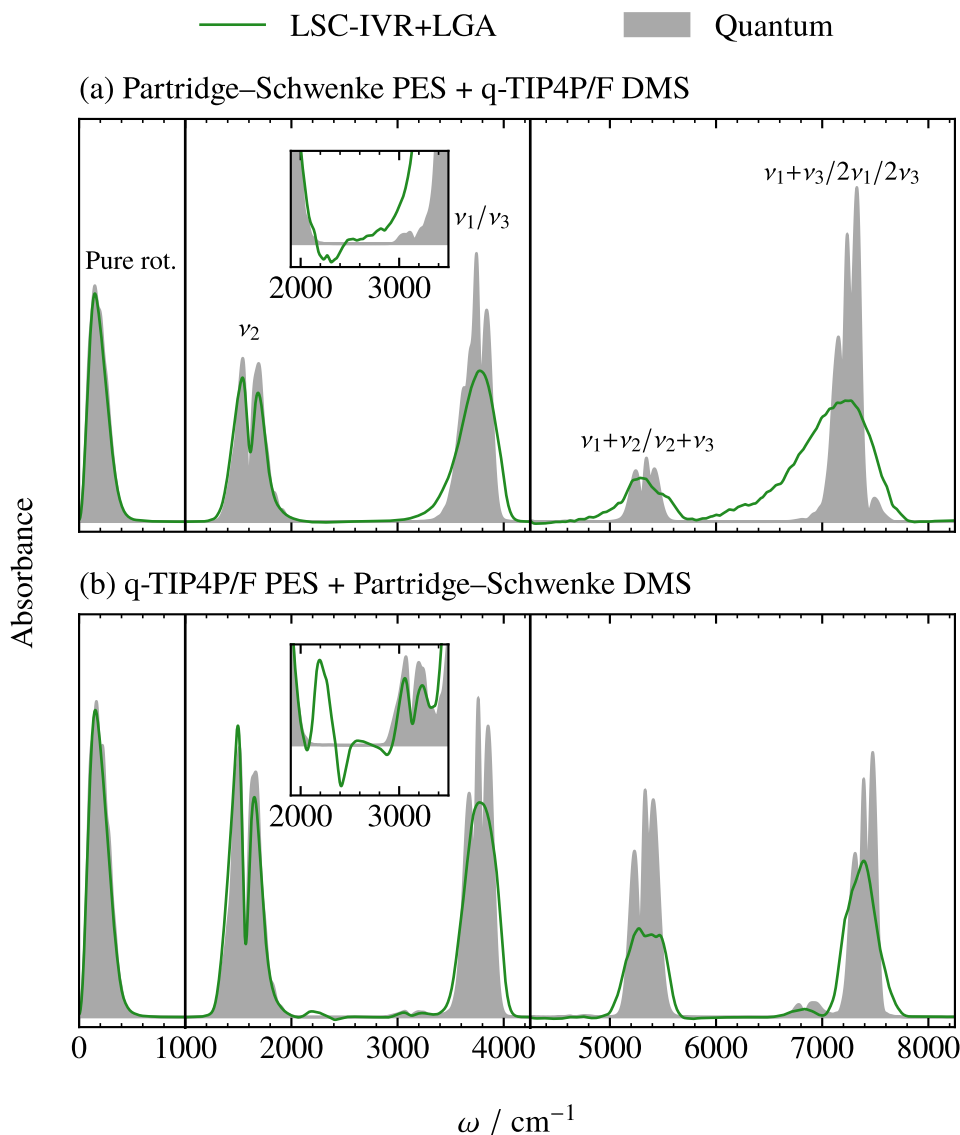
Figure C.3: LSC-IVR+LGA and quantum spectra of gas-phase water at 300 K, computed by combining the Partridge–Schwenke PES with the q-TIP4P/F DMS and vice versa. The absorbances in the three panels of each graph are scaled as (a) 1 : 2 : 100 (b) 1 : 5 : 70 (left-to-right), while the absorbances in the insets are scaled by factors of (a) 25 (b) 15 relative to the panels in which they appear.

C.2   Variants of LSC-IVR+LGA for condensed-phase water

Fig. C.4 shows how the IR spectra given by LSC-IVR+LGA, for condensed-phased q-TIP4P/F water, vary depending on whether one uses the simulation output to approximate the symmetrised or Kubo-transformed dipole-derivative ACFs. In what follows, we refer to these just as 'symmetrised spectra' and 'Kubo spectra', respectively. The symmetrised spectra in Fig. C.4
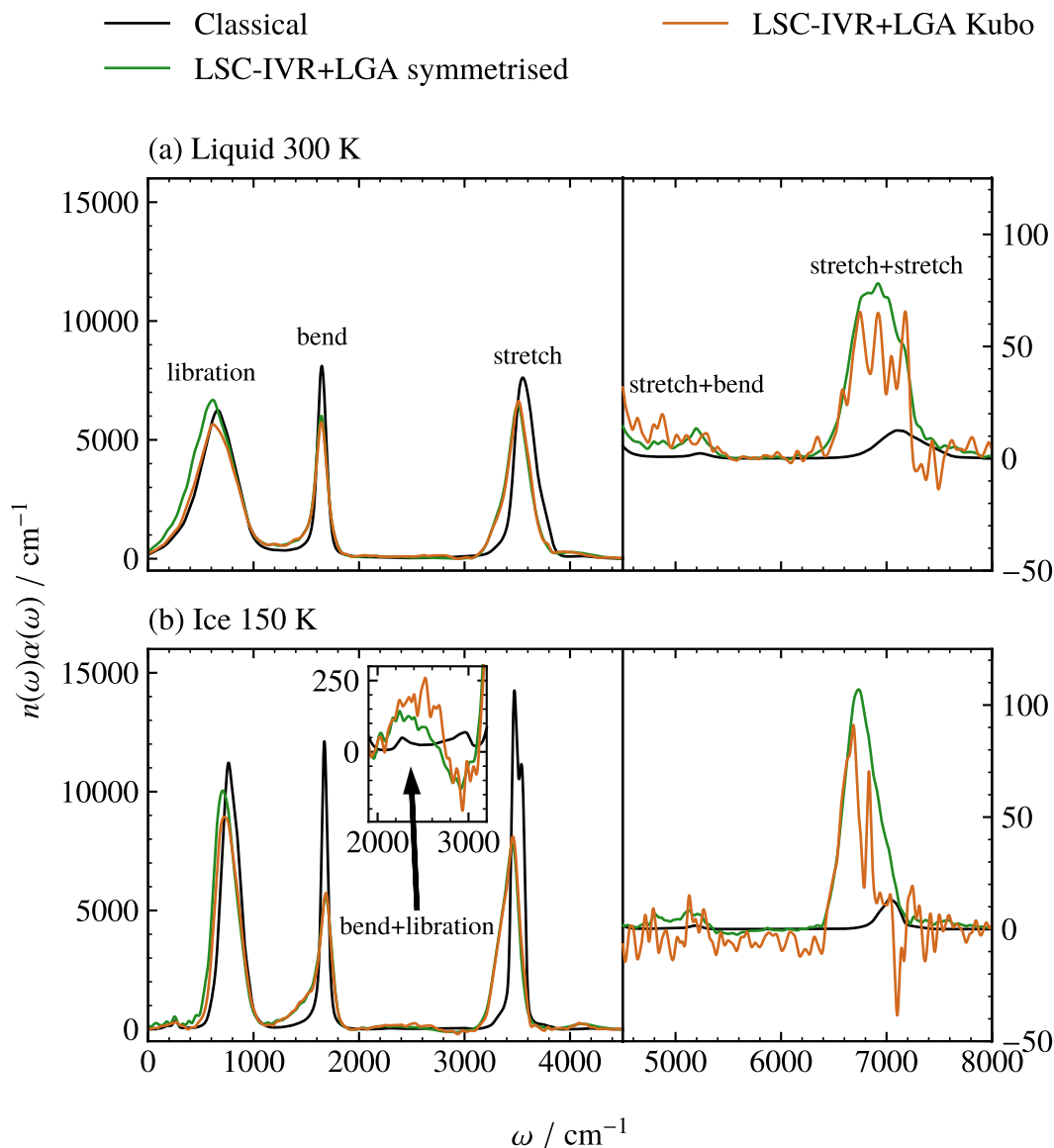
Figure C.4: Comparison of IR absorption spectra calculated with LSC-IVR+LGA for condensed-phase q-TIP4P/F water, as obtained from the symmetrised and Kubo-transformed dipole-derivative ACFs. The symmetrised spectra were plotted earlier in Figs. 4.4 and 4.6, and we also include the classical spectra from Fig. 4.4 for reference. Note that the Kubo spectra are probably under-converged in the near-IR region.

are the same as those plotted in Figs. 4.4 and 4.6. The Kubo spectra were obtained in the same way (as described in Section 4.3.1), but using Eq. (A.37) instead of Eq. (A.32) for the static dipole-derivative estimator, and Eq. (2.51c) instead of Eq. (2.51b) to process the ACFs. The classical spectra of Fig. 4.4 are also replotted in Fig. C.4, for reference.

Below 4500 cm^{-1}, the Kubo spectrum for the 300 K liquid is in good agreement with that reported by Habershon and Manolopoulos in ref. 28. Both the Kubo spectra are generally

close in this region to the corresponding symmetrised spectra, aside from the libration bands, which show slightly better agreement with classical MD (which we expect to be accurate at such low frequencies). Specifically, the libration bands in the symmetrised spectra exhibit larger erroneous redshifts than they do in the Kubo spectra. We attributed these redshifts in Section 4.3.2 to the effects of zero-point energy leakage. It is possible that the superior accuracy of the Kubo libration bands arises from fortuitous cancellation of errors; the estimator of Eq. (A.37) used in calculating the Kubo-transformed ACF is approximate even when DMS is linear, having been derived under the LGA. In contrast, Eq. (A.32) used in calculating the symmetrised ACF is exact when the DMS is linear, even without assuming the LGA.

More pronounced differences are apparent above $4500\,\mathrm{cm}^{-1}$, where the Kubo spectra exhibit high levels of noise. For ice I_h at 150 K, the noise is sufficient to overshadow the stretch–bend combination band completely. Some of this noise could probably be reduced by increasing the number of production runs used to calculate the ACFs, but symmetrised ACFs are clearly the preferable choice if one requires a qualitatively reasonable description of the near-IR region.

C.3   Artefacts in RPMD spectra of liquid SPC/F water

In ref. 101, Habershon *et al.* reported the RPMD spectrum of liquid water at 300 K, calculated using the simple SPC/F PES and DMS of ref. 150. Similar to q-TIP4P/F, SPC/F is a point-charge model in which the dipole is linear. The objective of the Habershon *et al.* study was to illustrate the contamination of the stretch fundamental band by spurious resonance, even in the absence of electrical anharmonicity. However, upon close inspection of the spectrum, one also notices a small peak at $\sim 2750\,\mathrm{cm}^{-1}$ that is absent in the classical and partially adiabatic CMD spectra [101], and somewhat resembles the bend–libration combination band that is observed experimentally (albeit at a lower frequency—see Fig. 4.7). This would be a surprising result given that, as discussed in Chapter 3, RPMD is incapable of properly describing the Matsubara heating of $\|\Delta \mathbf{n}\|_1 = 2$ band intensities.

To investigate this further, we reproduced the SPC/F RPMD spectrum of ref. 101, mostly following the simulation strategy described therein. However, instead of using an Andersen thermostat, we equilibrated the system using the PILE-G thermostat of Section 4.3.1. We found that the spectrum reached an acceptable level of convergence using just two microcanonical production of runs of length 25 ps, for 12 independently equilibrated simulation cells. The simulation was performed using the i-PI package due to Ceriotti and co-workers [165].

The resulting spectrum is plotted in Fig. C.5, and shows good agreement with that of ref. 101. We have magnified the region of the 'combination band' in the inset. Repeating the calculation at the slightly higher temperature of 350 K, however, provides evidence that this peak is nothing but a manifestation of the unphysical internal oscillations of the ring-
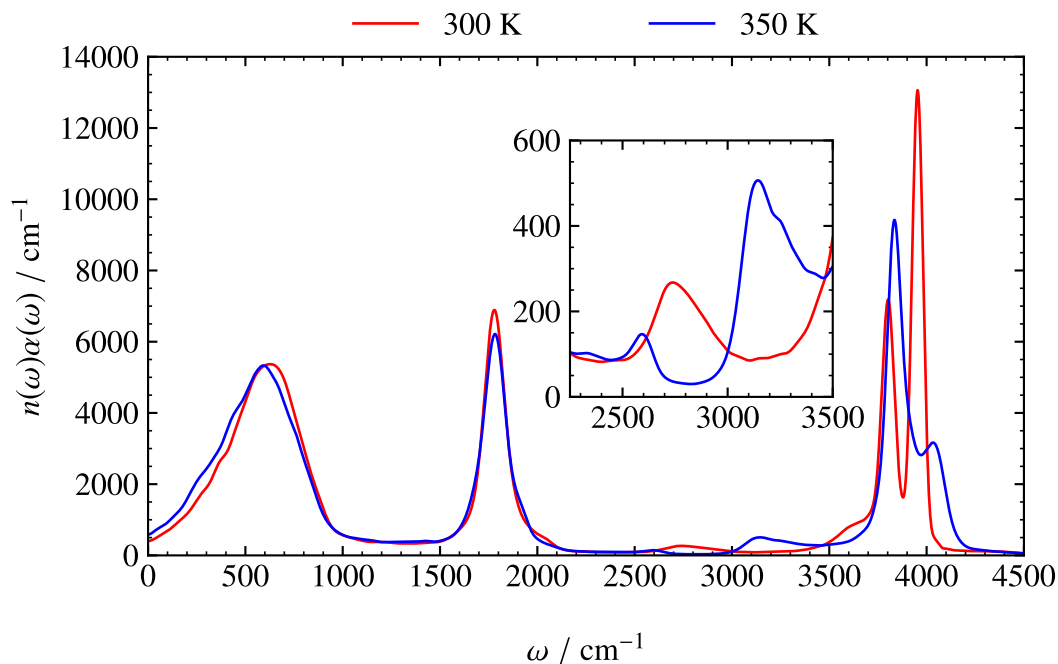
Figure C.5: IR absorption spectra of liquid water, calculated with RPMD using the SPC/F PES and DMS of ref. 150. Varying the temperature reveals that the feature resembling a bend–libration combination band at 300 K is in fact an artefact of the internal ring-polymer vibrations.

polymer. If it were a true combination band, once would expect it to persist at roughly the same frequency of ~2750 cm^{-1} as the temperature is increased. Instead, we find that is replaced by one peak of lower intensity at ~2600 cm^{-1} and one of higher intensity at ~3200 cm^{-1}. This strong temperature dependence is characteristic of spurious peaks and resonances in RPMD, consistent with the temperature dependence of the harmonic spring terms in the ring-polymer potential [99].

Appendix D

Additional computational details

D.1 One-dimensional q-TIP4P/F O–H calculations

Quantum calculations

The Hamiltonian was diagonalised in the DVR of Colbert and Miller [14], on a grid of 200 points evenly spaced over the interval -5 a.u. $\leqslant q < 5$ a.u. Matrix elements were evaluated from the wave functions interpolated using cubic splines on a finer grid of $2^9 + 1 = 513$ points. Kubo-transformed ACFs were then evaluated from the energies and matrix elements of the 50 lowest eigenstates.

Truncated Matsubara calculations

Prior to the truncated Matsubara simulations, closed-form expressions for the required Matsubara potentials and forces were computed as a function of the Matsubara mode coordinates $Q_{-\overline{M}}, \cdots, Q_{\overline{M}}$, using Eq. (2.93) with Eq. (2.88). As noted in ref. 73, this is possible provided that the raw potential $V(q)$ can be written as a polynomial in q, and avoids the need to discretise the imaginary-time path.

To evaluate the Matsubara approximations to the Kubo-transformed velocity ACF, for each value of M, 100 instances of the system were propagated along 10^4 microcanonical production runs of length 1 ps. These were each preceded by an equilibration run of length 0.125 ps, during which a local Langevin thermostat [155, 156] (OBABO propagator splitting [157]) with friction coefficient 1.03353 fs^{-1} was attached to each mode. A time step of 0.125 fs was used throughout. This thermostatting enabled sampling of the strictly positive, classical Boltzmann–like part of the Matsubara distribution, which in its unnormalised form is given by

$\mathrm{e}^{-\beta \widetilde{H}_M(\mathbf{P},\mathbf{Q})}$. The phase factor, however, had to be accounted for explicitly, using

$$\widetilde{C}_{\dot{q}\dot{q}}^{[M]}(\beta;t) = \frac{\left\langle \mathrm{e}^{-\mathrm{i}\beta\widetilde{\theta}_M(\mathbf{P},\mathbf{Q})} \dot{Q}_0 \mathrm{e}^{\mathcal{L}_M t} \dot{Q}_0 \right\rangle_{M,\mathrm{p.d.}}}{\left\langle \exp\left(-\frac{\beta}{2}\sum_{k=-\overline{M}}^{\overline{M}} m\omega_k^2 Q_k^2\right) \right\rangle_{M,\mathrm{p.d.}}}, \tag{D.1}$$

where

$$\langle \ldots \rangle_{M,\mathrm{p.d.}} = \frac{\int \mathrm{d}^M\mathbf{P} \int \mathrm{d}^M\mathbf{Q}\ \mathrm{e}^{-\beta\widetilde{H}_M(\mathbf{P},\mathbf{Q})} \ldots}{\int \mathrm{d}^M\mathbf{P} \int \mathrm{d}^M\mathbf{Q}\ \mathrm{e}^{-\beta\widetilde{H}_M(\mathbf{P},\mathbf{Q})}}, \tag{D.2}$$

and the averaging was performed over time as well as initial conditions. The $M = 3$ power spectra (see Fig. 3.3) were calculated analogously.

Mean-field Matsubara calculations

Mean-field Matsubara forces cannot generally be written in closed form, even when the raw potential is polynomial in position. Instead, they were computed on the fly following the adiabatic algorithm of ref. 76, using $N = 64$ ring-polymer beads and an adiabaticity parameter of $\Gamma = 64$, meaning that the masses of the $N - M$ modes subject to mean-field averaging were scaled so as to make their natural frequencies equal $\Gamma/(\beta_N\hbar)$. A local Langevin thermostat [155, 156] (OBABO propagator splitting [157]) with friction coefficient $2\Gamma/(\beta_N\hbar)$ was attached to each of these modes during production as well as equilibration. In contrast, the M Matsubara modes were only thermostatted during equilibration, with friction coefficients 1.03353 fs^{-1}. A small time step of $0.125/\Gamma = 0.001953125$ fs was required, owing to the high oscillation frequencies of the mean-field averaged modes.

To evaluate the mean-field Matsubara approximations to the Kubo-transformed velocity ACF, for each value of M, two instances of the system were propagated along 10^4 production runs of length 1 ps, each preceded by an equilibration run of length 0.125 ps. Averaging over the Matsubara phase space was accomplished in the same way as it was for the truncated Matsubara calculations. The $M = 3$ power spectra (see Fig. 3.3) were calculated analogously.

[T]RPMD calculations

The [T]RPMD simulations employed $N = 64$ beads for each of 20 ring polymers, which were propagated along 1000 production runs of length 1 ps. The RPMD production runs were unthermostatted (microcanonical), whereas for TRPMD, the fluctuation modes were subject to the PILE thermostat of ref. 132, with friction coefficients set to either $2\sin(\beta_N\hbar|\omega_k|/2)/\beta_N\hbar$ or $4\sin(\beta_N\hbar|\omega_k|/2)/\beta_N\hbar$ as specified in Section 3.4.2. For both methods, each production run was preceded by a PILE-L equilibration run of length 0.125 ps, with the friction coefficients of the fluctuation modes set to $2\sin(\beta_N\hbar|\omega_k|/2)/\beta_N\hbar$ and those of the centroids to 1.03353 fs^{-1}.

A time step of 0.125 fs was used throughout. The Kubo-transformed velocity ACFs were approximated by time averaging over production runs.

Planetary model calculations

The time step and number of ring-polymer beads employed for the planetary model simulations were the same as for the [T]RPMD simulations described above. The PILE(-L) thermostatting [132] employed friction coefficients of $2\sin(\beta_N\hbar|\omega_k|/2)/\beta_N\hbar$ for the fluctuation modes, and 1.03353 fs^{-1} for the centroid mode where appropriate.

First, the path-integral frequency $\Omega(Q_0)$ of Eq. (2.125) was evaluated at 2000 evenly spaced points spanning -5 a.u. $\leqslant Q_0 < 5$ a.u. This was achieved by time averaging over 10 independent, centroid-constrained PIMD trajectories at each grid point, each of length 6250 fs and subject to PILE thermostatting. Following this, the centroid position and momentum were recorded along 10^4 TRPMD production runs of length 2 ps for each of 10 independent ring polymers. Each production run was preceded by a PILE-L equilibration run of length 0.125 ps.

For each centroid trajectory, 64 independent planets were initialised by sampling $(\tilde{p}_\delta, \tilde{q}_\delta)$ from their (locally) Gaussian distributions of Eq. (2.120). Rather than integrating their equations of motion directly, which would require time derivatives of $\Omega^2(Q_0)$ and $a^2(Q_0)$, we carried out real-time propagation in the dimensionless basis $(\tilde{p}_\delta/a(Q_0), \tilde{q}_\delta/[m\Omega(Q_0)a(Q_0)])$ as described in ref. 75. The symmetrised velocity ACF was approximated for $0 \leqslant t < 1$ ps by time averaging over all 6.4×10^6 planetary trajectories.

LSC-IVR calculations

The LSC-IVR approximation to the symmetrised velocity ACF is given by the real part of Eq. (2.81), with $\hat{A} = \hat{B} = \hat{q} = \hat{p}/m$. A discretisation of the accessible phase space was constructed from the Cartesian product of a 513-point position grid spanning -5 a.u. $\leqslant q < 5$ a.u with a 1539-point momentum grid spanning -80.373 a.u. $\leqslant p \leqslant 80.373$ a.u (both evenly spaced). The static part of the integrand,

$$\frac{1}{2\pi\hbar Z_q(\beta)}\frac{1}{m}\left[\hat{U}(-\mathrm{i}\beta\hbar)\hat{p}\right]_W(p,q), \tag{D.3}$$

was computed in the energy basis from the output of the DVR calculations described above. The time-dependent part,

$$\mathrm{e}^{\mathcal{L}t}\frac{1}{m}\left[\hat{p}\right]_W(p,q) = \mathrm{e}^{\mathcal{L}t}\frac{p}{m}, \tag{D.4}$$

was then computed by propagating the entire set of phase-space points for 1 ps, using the standard velocity Verlet algorithm with time step 0.0125 fs.

D.2 Fermi resonance calculations

D.2.1 CO$_2$ model

Quantum calculations

The Hamiltonian $\hat{H}_{CO_2}$ of Eq. (5.1) was diagonalised in the in the eigenbasis of the harmonic oscillator Hamiltonian $\hat{H}_{CO_2}^{(0)}$ of Eq. (5.2a), truncated so as to include only states for which the three vibrational quantum numbers $n_x, n_y, n_z \in \{0, \ldots, 10\}$. Kubo-transformed ACFs were then evaluated from the energies and matrix elements of the 50 lowest eigenstates of $\hat{H}_{CO_2}$.

Truncated Matsubara calculations

The Matsubara forces were computed analytically, analogously to the one-dimensional case described in Section D.1 (although with multiple physical degrees of freedom, the relevant equations are Eqs. (A.1) and A.3)). For each value of M, 64 instances of the system were propagated along 2000 microcanonical production runs of length 10 ps. These were each preceded by an equilibration run of length 0.5 ps, during which a local Langevin thermostat [155, 156] (OBABO propagator splitting [157]) with friction coefficient 0.25 fs^{-1} was attached to each mode. A time step of 0.1 fs was used throughout. The Matsubara approximations to the Kubo-transformed velocity ACFs were obtained by time averaging over production runs using the straightforward generalisation of Eq. (D.1) to multiple degrees of freedom.

HD Matsubara calculations

The HD Matsubara simulations were carried out in a similar fashion to the truncated Matsubara simulations. However, in place of Langevin-thermostatted equilibration runs, the initial phase-space points were sampled directly from the (much simpler) HD Matsubara distribution defined in Section 5.1.1. Because the effects of the Matsubara phase are accounted for implicitly (albeit approximately) within this distribution, the phase did *not* need to be sampled over in the explicit way that was required in truncated Matsubara simulations. Furthermore, since Matsubara trajectories do not rigorously conserve the HD Matsubara distribution, time averaging could not be performed, hence the ACFs were approximated by averaging over the initial conditions only.

IMH calculations

The IMH simulations were algorithmically equivalent to the $M = 1$ HD Matsubara simulations, except that the sampling of phase-space points was performed at the appropriate Matsubara

effective temperatures, $T_i^{[M]} = 1/(k_B \beta_i^{[M]})$, as defined in Eq. (3.92) (rather than the actual temperature, $T = 1/(k_B \beta)$).

D.2.2 FR2 and FR3 models

Quantum calculations

These were performed analogously to the quantum calculations for the CO_2 model as described in Section D.2.2.

Truncated Matsubara calculations

The Matsubara forces were computed analytically as for the CO_2 model. In this case, for each value of M, just one instance of the system was propagated along 2000 microcanonical production runs of length 2000 a.u. These were each preceded by an equilibration run of length 200 a.u., during which a local Langevin thermostat [155, 156] (OBABO propagator splitting [157]) with friction coefficient 1 a.u. was attached to each mode. A time step of 0.05 a.u. was used throughout. The Matsubara approximations to the Kubo-transformed velocity ACFs were obtained by time averaging over production runs using the straightforward generalisation of Eq. (D.1) to multiple degrees of freedom.

References

1. P. Atkins and R. Friedman, *Molecular Quantum Mechanics*, Oxford University Press, New York, 5th edn, 2011.

2. A. Nitzan, *Chemical Dynamics in Condensed Phases: Relaxation, Transfer and Reactions in Condensed Molecular Systems*, Oxford University Press, New York, 2006.

3. D. J. Wales, *Energy Landscapes: Applications to Clusters, Biomolecules and Glasses*, Cambridge University Press, Cambridge, 2004.

4. A. Szabo and N. S. Ostlund, *Modern Quantum Chemistry: Introduction to Advanced Electronic Structure Theory*, Dover Publications, Mineola, 1996.

5. W. Koch and M. C. Holthausen, *A Chemist's Guide to Density Functional Theory*, Wiley-VCH, Weinheim, 2nd edn, 2001.

6. M. E. Tuckerman, *Statistical Mechanics: Theory and Molecular Simulation*, Oxford University Press, Oxford, 2010.

7. T. Carrington, *J. Chem. Phys.*, 2017, **146**, 120902.

8. P. S. Thomas, T. Carrington, J. Agarwal and H. F. Schaefer, *J. Chem. Phys.*, 2018, **149**, 064108.

9. A. Martín Santa Daría, G. Avila and E. Mátyus, *Phys. Chem. Chem. Phys.*, 2021, **23**, 6526.

10. S. Manzhos, T. Carrington Jr and K. Yamashita, *J. Phys. Chem. Lett.*, 2011, **2**, 2193.

11. U. Kuenzer, J.-A. Sorarù and T. S. Hofer, *Phys. Chem. Chem. Phys.*, 2016, **18**, 31521.

12. M. J. Schuler, T. S. Hofer, Y. Morisawa, Y. Futami, C. W. Huck and Y. Ozaki, *Phys. Chem. Chem. Phys.*, 2020, **22**, 13017.

13. J. C. Light, I. P. Hamilton and J. V. Lill, *J. Chem. Phys.*, 1985, **82**, 1400.

14. D. T. Colbert and W. H. Miller, *J. Chem. Phys.*, 1992, **96**, 1982.

15. J. Tennyson, M. A. Kostin, P. Barletta, G. J. Harris, O. L. Polyansky, J. Ramanlal and N. F. Zobov, *Comput. Phys. Commun.*, 2004, **163**, 85.

16. D. Frenkel and B. Smit, *Understanding Molecular Simulation: From Algorithms to Applications*, Academic Press, London, 2nd edn, 2002.

17. E. Sanz, C. Vega, J. L. Abascal and L. G. MacDowell, *Phys. Rev. Lett.*, 2004, **92**, 255701.

18. H. A. Scheraga, M. Khalili and A. Liwo, *Annu. Rev. Phys. Chem.*, 2007, **58**, 57.

19. J. M. Delaye, S. Peuget, G. Bureau and G. Calas, *J. Non. Cryst. Solids*, 2011, **357**, 2763.

20. W. H. Miller, *J. Phys. Chem. A*, 2001, **105**, 2942.

21. W. H. Miller, *J. Chem. Phys.*, 2006, **125**, 132305.

22. W. H. Miller, *J. Chem. Phys.*, 2012, **136**, 210901.

23. F. Paesani, W. Zhang, D. A. Case, T. E. Cheatham III and G. A. Voth, *J. Chem. Phys.*, 2006, **125**, 184507.

24. L. Pereyaslavets, I. Kurnikov, G. Kamath, O. Butin, A. Illarionov, I. Leontyev, M. Olevanov, M. Levitt, R. D. Kornberg and B. Fain, *Proc. Natl. Acad. Sci. U. S. A.*, 2018, **115**, 8878.

25. T. E. Markland and M. Ceriotti, *Nat. Rev. Chem.*, 2018, **2**, 109.

26. M. Rossi, *J. Chem. Phys.*, 2021, **154**, 170902.

27. W. Fang, J. Chen, M. Rossi, Y. Feng, X. Z. Li and A. Michaelides, *J. Phys. Chem. Lett.*, 2016, **7**, 2125.

28. S. Habershon and D. E. Manolopoulos, *J. Chem. Phys.*, 2009, **131**, 244518.

29. M. Rossi, H. Liu, F. Paesani, J. Bowman and M. Ceriotti, *J. Chem. Phys.*, 2014, **141**, 181101.

30. S. K. Reddy, D. R. Moberg, S. C. Straight and F. Paesani, *J. Chem. Phys.*, 2017, **147**, 244504.

31. T. E. Markland and D. E. Manolopoulos, *J. Chem. Phys.*, 2008, **129**, 024105.

32. J. E. Lawrence and D. E. Manolopoulos, *Faraday Discuss.*, 2019, **221**, 9.

33. S. Habershon, T. E. Markland and D. E. Manolopoulos, *J. Chem. Phys.*, 2009, **131**, 024501.

34. F. Paesani and G. A. Voth, *J. Phys. Chem. B*, 2009, **113**, 5702.

35. M. Ceriotti, W. Fang, P. G. Kusalik, R. H. McKenzie, A. Michaelides, M. A. Morales and T. E. Markland, *Chem. Rev.*, 2016, **116**, 7529.

36. L. E. Ballentine, *Quantum Mechanics: A Modern Development*, World Scientific Publishing, Singapore, 1998.

37. R. P. Feynman, A. R. Hibbs and D. F. Styer, *Quantum Mechanics and Path Integrals: Emended Edition*, Dover Publications, 2010.

38. R. Shankar, *Principles of Quantum Mechanics*, Plenum Press, New York, 2nd edn, 2011.

39. D. Chandler and P. G. Wolynes, *J. Chem. Phys.*, 1981, **74**, 4078.

40. M. F. Herman, E. J. Bruskin and B. J. Berne, *J. Chem. Phys.*, 1981, **76**, 5150.

41. M. Parrinello and A. Rahman, *J. Chem. Phys.*, 1984, **80**, 860.

42. M. Ceriotti, D. E. Manolopoulos and M. Parrinello, *J. Chem. Phys.*, 2011, **134**, 084104.

43. F. Brieuc, H. Dammak and M. Hayoun, *J. Chem. Theory Comput.*, 2016, **12**, 1351.

44. V. Kapil, J. Behler and M. Ceriotti, *J. Chem. Phys.*, 2016, **145**, 234103.

45. O. Marsalek and T. E. Markland, *J. Chem. Phys.*, 2016, **144**, 054112.

46. C. John, T. Spura, S. Habershon and T. D. Kühne, *Phys. Rev. E*, 2016, **93**, 043305.

47. M. Rossi, W. Fang and A. Michaelides, *J. Phys. Chem. Lett.*, 2015, **6**, 4233.

48. K. Fidanyan, I. Hamada and M. Rossi, *Adv. Theory Simulations*, 2021, **4**, 2000241.

49. B. Hirshberg, V. Rizzi and M. Parrinello, *Proc. Natl. Acad. Sci. U. S. A.*, 2019, **116**, 21445.

50. B. Hirshberg, M. Invernizzi and M. Parrinello, *J. Chem. Phys.*, 2020, **152**, 171102.

51. N. Makri, *J. Math. Phys.*, 1995, **36**, 2430.

52. D. B. Fairlie, *Chaos, Solitons and Fractals*, 1999, **10**, 365.

53. J. Liu and W. H. Miller, *J. Chem. Phys.*, 2007, **126**, 234110.

54. H. Wang, X. Sun and W. H. Miller, *J. Chem. Phys.*, 1998, **108**, 9726.

55. X. Sun, H. Wang and W. H. Miller, *J. Chem. Phys.*, 1998, **109**, 7064.

56. H. Liu, Y. Wang and J. M. Bowman, *J. Chem. Phys.*, 2015, **142**, 194502.

57. Q. Shi and E. Geva, *J. Phys. Chem. A*, 2003, **107**, 9059.

58. J. A. Poulsen, G. Nyman and P. J. Rossky, *J. Chem. Phys.*, 2003, **119**, 12179.

59. J. Liu and W. H. Miller, *J. Chem. Phys.*, 2006, **125**, 224104.

60. J. Liu and W. H. Miller, *J. Chem. Phys.*, 2009, **131**, 074113.

61. M. Basire, D. Borgis and R. Vuilleumier, *Phys. Chem. Chem. Phys.*, 2013, **15**, 12591.

62. J. Beutier, D. Borgis, R. Vuilleumier and S. Bonella, *J. Chem. Phys.*, 2014, **141**, 084102.

63. J. Liu, *Int. J. Quantum Chem.*, 2015, **115**, 657.

64. T. Plé, S. Huppert, F. Finocchi, P. Depondt and S. Bonella, *J. Chem. Phys.*, 2019, **151**, 114114.

65. T. Plé, S. Huppert, F. Finocchi, P. Depondt and S. Bonella, *J. Chem. Phys.*, 2021, **155**, 104108.

66. S. Popat, *An Analysis of Three Path-Integral Based Approximations to Quantum Dynamics*, PhD thesis, University of Cambridge, 2021.

67. J. Liu, W. H. Miller, F. Paesani, W. Zhang and D. A. Case, *J. Chem. Phys.*, 2009, **131**, 164509.

68. J. Liu, W. H. Miller, G. S. Fanourgakis, S. S. Xantheas, S. Imoto and S. Saito, *J. Chem. Phys.*, 2011, **135**, 244503.

69. X. Liu and J. Liu, *Mol. Phys.*, 2018, **116**, 755.

70. B. J. Ka, Q. Shi and E. Geva, *J. Phys. Chem. A*, 2005, **109**, 5527.

71. B. J. Ka and E. Geva, *J. Phys. Chem. A*, 2006, **110**, 9555.

72. J. Liu, A. Nakayama and N. Makri, *Mol. Phys.*, 2006, **104**, 1267.

73. T. J. H. Hele, M. J. Willatt, A. Muolo and S. C. Althorpe, *J. Chem. Phys.*, 2015, **142**, 134103.

74. T. J. H. Hele, *Mol. Phys.*, 2017, **115**, 1435.

75. M. J. Willatt, *Matsubara Dynamics and its Practical Implementation*, PhD thesis, University of Cambridge, 2017.

76. G. Trenins and S. C. Althorpe, *J. Chem. Phys.*, 2018, **149**, 014102.

77. G. Trenins, *Quasicentroid Molecular Dynamics*, PhD thesis, University of Cambridge, 2020.

78. J. Cao and G. A. Voth, *J. Chem. Phys.*, 1994, **100**, 5106.

79. J. Cao and G. A. Voth, *J. Chem. Phys.*, 1994, **101**, 6157.

80. J. Cao and G. A. Voth, *J. Chem. Phys.*, 1994, **101**, 6168.

81. G. A. Voth, *Adv. Chem. Phys.*, 1996, **93**, 135.

82. I. R. Craig and D. E. Manolopoulos, *J. Chem. Phys.*, 2004, **121**, 3368.

83. S. Habershon, D. E. Manolopoulos, T. E. Markland and T. F. Miller III, *Ann. Rev. Phys. Chem.*, 2013, **64**, 387.

84. T. J. H. Hele, M. J. Willatt, A. Muolo and S. C. Althorpe, *J. Chem. Phys.*, 2015, **142**, 191101.

85. T. J. H. Hele, *Mol. Phys.*, 2016, **114**, 1461.

86. S. Miura, S. Okazaki and K. Kinugawa, *J. Chem. Phys.*, 1999, **110**, 4523.

87. Y. Yonetani and K. Kinugawa, *J. Chem. Phys.*, 2004, **120**, 10624.

88. T. D. Hone and G. A. Voth, *J. Chem. Phys.*, 2004, **121**, 6412.

89. T. F. Miller III and D. E. Manolopoulos, *J. Chem. Phys.*, 2005, **122**, 184503.

90. T. F. Miller and D. E. Manolopoulos, *J. Chem. Phys.*, 2005, **123**, 154504.

91. Y. V. Suleimanov, *J. Phys. Chem. C*, 2012, **116**, 11141.

92. Y. Minamino and K. Kinugawa, *Chem. Phys. Lett.*, 2016, **664**, 114.

93. B. Cheng, A. T. Paxton and M. Ceriotti, *Phys. Rev. Lett.*, 2018, **120**, 225901.

94. N. Boekelheide, R. Salomón-Ferrer and T. F. Miller, *Proc. Natl. Acad. Sci. U. S. A.*, 2011, **108**, 16159.

95. J. S. Kretchmer and T. F. Miller, *Inorg. Chem.*, 2016, **55**, 1022.

96. F. Paesani, S. S. Xantheas and G. A. Voth, *J. Phys. Chem. B*, 2009, **113**, 13118.

97. G. R. Medders and F. Paesani, *J. Chem. Theory Comput.*, 2015, **11**, 1145.

98. O. Marsalek and T. E. Markland, *J. Phys. Chem. Lett.*, 2017, **8**, 1545.

99. A. Witt, S. D. Ivanov, M. Shiga, H. Forbert and D. Marx, *J. Chem. Phys.*, 2009, **130**, 194510.

100. S. D. Ivanov, A. Witt, M. Shiga and D. Marx, *J. Chem. Phys.*, 2010, **132**, 031101.

101. S. Habershon, G. S. Fanourgakis and D. E. Manolopoulos, *J. Chem. Phys.*, 2008, **129**, 074501.

102. M. Rossi, M. Ceriotti and D. E. Manolopoulos, *J. Chem. Phys.*, 2014, **140**, 234116.

103. F. Calvo, P. Parneix and N. T. Van-Oanh, *J. Chem. Phys.*, 2010, **132**, 124308.

104. Y. Litman, J. Behler and M. Rossi, *Faraday Discuss.*, 2020, **221**, 526.

105. Q. Yu and J. M. Bowman, *J. Phys. Chem. A*, 2019, **123**, 1399.

106. M. Rossi, V. Kapil and M. Ceriotti, *J. Chem. Phys.*, 2018, **148**, 102301.

107. G. Trenins, M. J. Willatt and S. C. Althorpe, *J. Chem. Phys.*, 2019, **151**, 054109.

108. A. Horikoshi and K. Kinugawa, *J. Chem. Phys.*, 2005, **122**, 174104.

109. J. C. Breeze, C. C. Ferriso, C. B. Ludwig and W. Malkmus, *J. Chem. Phys.*, 1965, **42**, 402.

110. M. A. Czarnecki, Y. Morisawa, Y. Futami and Y. Ozaki, *Chem. Rev.*, 2015, **115**, 9707.

111. V. H. Segtnan, Š. Šašić, T. Isaksson and Y. Ozaki, *Anal. Chem.*, 2001, **73**, 3153.

112. G. R. Choppin and M. R. Violante, *J. Chem. Phys.*, 1972, **56**, 5890.

113. Y. Jin and S. Ikawa, *J. Chem. Phys.*, 2003, **119**, 12432.

114. P. Hamm and M. Zanni, *Concepts and Methods of 2D Infrared Spectroscopy*, Cambridge University Press, New York, 2011.

115. K. K. G. Smith, J. A. Poulsen, G. Nyman and P. J. Rossky, *J. Chem. Phys.*, 2015, **142**, 244112.

116. M. J. Willatt, M. Ceriotti and S. C. Althorpe, *J. Chem. Phys.*, 2018, **148**, 102336.

117. T. Plé, *Nuclear Quantum Dynamics: exploration and comparison of trajectory-based methods*, PhD thesis, Sorbonne Université, 2020.

118. V. Babin, C. Leforestier and F. Paesani, *J. Chem. Theory Comput.*, 2013, **9**, 5395.

119. V. Babin, G. R. Medders and F. Paesani, *J. Chem. Theory Comput.*, 2014, **10**, 1599.

120. G. R. Medders, V. Babin and F. Paesani, *J. Chem. Theory Comput.*, 2014, **10**, 2906.

121. M. Basire, F. Mouhat, G. Fraux, A. Bordage, J. L. Hazemann, M. Louvel, R. Spezia, S. Bonella and R. Vuilleumier, *J. Chem. Phys.*, 2017, **146**, 134102.

122. E. Fermi, *Zeitschrift für Phys.*, 1931, **71**, 250.

123. J. J. Sakurai and J. Napolitano, *Modern Quantum Mechanics*, Cambridge University Press, Cambridge, 2nd edn, 2017.

124. H. Goldstein, C. Poole and J. Safko, *Classical Mechanics*, Addison–Wesley, New York, 3rd edn, 2002.

125. R. Kubo, *Rep. Prog. Phys.*, 1966, **29**, 255.

126. S. A. Egorov, K. F. Everitt and J. L. Skinner, *J. Phys. Chem. A*, 1999, **103**, 9494.

127. T. Mikami, M. Shiga and S. Okazaki, *J. Chem. Phys.*, 2001, **115**, 9797.

128. M. Diem, *Modern Vibrational Spectroscopy and Micro-Spectroscopy : Theory, Instrumentation and Biomedical Applications*, John Wiley & Sons, Chichester, 2015.

129. P. L. Silvestrelli, M. Bernasconi and M. Parrinello, *Chem. Phys. Lett.*, 1997, **277**, 478.

130. M. P. Gaigeot and M. Sprik, *J. Phys. Chem. B*, 2003, **107**, 10344.

131. T. Tassaing, J. C. Soetens, I. Vyalov, M. Kiselev and A. Idrissi, *J. Chem. Phys.*, 2010, **133**, 214505.

132. M. Ceriotti, M. Parrinello, T. E. Markland and D. E. Manolopoulos, *J. Chem. Phys.*, 2010, **133**, 124104.

133. M. Ceriotti, J. More and D. E. Manolopoulos, *Comput. Phys. Commun.*, 2014, **185**, 1019.

134. M. Hillery, R. F. O'Connell, M. O. Scully and E. P. Wigner, *Phys. Rep.*, 1984, **106**, 121.

135. D. M. Ceperley, *Rev. Mod. Phys.*, 1995, **67**, 279.

136. C. Chakravarty, M. C. Gordillo and D. M. Ceperley, *J. Chem. Phys.*, 1998, **109**, 2123.

137. K. A. Jung, P. E. Videla and V. S. Batista, *J. Chem. Phys.*, 2018, **148**, 244105.

138. K. A. Jung, P. E. Videla and V. S. Batista, *J. Chem. Phys.*, 2019, **151**, 034108.

139. K. A. Jung, P. E. Videla and V. S. Batista, *J. Chem. Phys.*, 2020, **153**, 124112.

140. S. C. Althorpe and T. J. H. Hele, *J. Chem. Phys.*, 2013, **139**, 084115.

141. T. D. Hone, P. J. Rossky and G. A. Voth, *J. Chem. Phys.*, 2006, **124**, 154103.

142. R. Ramírez, T. López-Ciudad and J. C. Noya, *Phys. Rev. Lett.*, 1998, **81**, 3303.

143. R. Ramírez and T. López-Ciudad, *J. Chem. Phys.*, 1999, **111**, 3339.

144. R. Ramírez and T. López-Ciudad, *Phys. Rev. Lett.*, 1999, **83**, 4456.

145. R. P. Feynman and H. Kleinert, *Phys. Rev. A*, 1986, **34**, 5080.

146. F. Paesani, *Acc. Chem. Res.*, 2016, **49**, 1844.

147. K. M. Hunter, F. A. Shakib and F. Paesani, *J. Phys. Chem. B*, 2018, **122**, 10754.

148. D. A. Thomas, E. Mucha, M. Lettow, G. Meijer, M. Rossi and G. Von Helden, *J. Am. Chem. Soc.*, 2019, **141**, 5815.

149. S. J. Yao and J. Overend, *Spectrochim. Acta Part A Mol. Spectrosc.*, 1976, **32**, 1059.

150. K. Toukan and A. Rahman, *Phys. Rev. B*, 1985, **31**, 2643.

151. J. L. Skinner and K. Park, *J. Phys. Chem. B*, 2001, **105**, 6716.

152. R. Ramírez, T. López-Ciudad, P. Kumar P and D. Marx, *J. Chem. Phys.*, 2004, **121**, 3973.

153. H. Partridge and D. W. Schwenke, *J. Chem. Phys.*, 1997, **106**, 4618.

154. D. W. Schwenke and H. Partridge, *J. Chem. Phys.*, 2000, **113**, 6592.

155. G. Bussi and M. Parrinello, *Phys. Rev. E*, 2007, **75**, 056707.

156. G. Bussi and M. Parrinello, *Comput. Phys. Commun.*, 2008, **179**, 26.

157. B. Leimkuhler and C. Matthews, *Appl. Math. Res. eXpress*, 2013, **2013**, 34.

158. W. H. Press, S. A. Teukolsky, W. T. Vetterling and B. P. Flannery, *Numerical Recipes in Fortran 77: The Art of Scientific Computing*, Cambridge University Press, 2nd edn, 1992.

159. S. N. Yurchenko, R. J. Barber, A. Yachmenev, W. Thiel, P. Jensen and J. Tennyson, *J. Phys. Chem. A*, 2009, **113**, 11845.

160. G. Herzberg, *Infrared and Raman Spectra of Polyatomic Molecules*, D. Van Nostrand, New York, 1945.

161. M. Schwartz and C. H. Wang, *J. Chem. Phys.*, 1973, **59**, 5258.

162. J. W. Lundeen and W. H. Koehler, *J. Phys. Chem.*, 1975, **79**, 2957.

163. W. H. Koehler, J. W. Lundeen, A. Moradi-Araghi, B. de Bettignies, L. D. Schultz and M. Schwartz, *J. Phys. Chem.*, 1979, **83**, 3264.

164. H. Liu, Y. Wang and J. M. Bowman, *J. Phys. Chem. B*, 2016, **120**, 1735.

165. V. Kapil, M. Rossi, O. Marsalek, R. Petraglia, Y. Litman, T. Spura, B. Cheng, A. Cuzzocrea, R. H. Meißner, D. M. Wilkins, B. A. Helfrecht, P. Juda, S. P. Bienvenue, W. Fang, J. Kessler, I. Poltavsky, S. Vandenbrande, J. Wieme, C. Corminboeuf, T. D. Kühne, D. E. Manolopoulos, T. E. Markland, J. O. Richardson, A. Tkatchenko, G. A. Tribello, V. Van Speybroeck and M. Ceriotti, *Comput. Phys. Commun.*, 2019, **236**, 214.

166. Y. Wang and J. M. Bowman, *J. Chem. Phys.*, 2011, **134**, 154510.

167. Y. Wang and J. M. Bowman, *J. Chem. Phys.*, 2012, **136**, 144113.

168. Y. Wang, X. Huang, B. C. Shepler, B. J. Braams and J. M. Bowman, *J. Chem. Phys.*, 2011, **134**, 094509.

169. H. Liu, Y. Wang and J. M. Bowman, *J. Phys. Chem. B*, 2013, **117**, 10046.

170. G. R. Medders and F. Paesani, *J. Chem. Phys.*, 2015, **142**, 212411.

171. J. M. Bowman, Y. Wang, H. Liu and J. S. Mancini, *J. Phys. Chem. Lett.*, 2015, **6**, 366.

172. J. E. Bertie and Z. Lan, *Appl. Spectrosc.*, 1996, **50**, 1047.

173. John Bertie's Download Site, `https://sites.ualberta.ca/~jbertie/JBDownload.HTM` (last accessed June 2021).

174. G. Niedner-Schatteburg, *Angew. Chem. Int. Ed.*, 2008, **47**, 1008.

175. D. W. Noid, M. L. Koszykowski and R. A. Marcus, *J. Chem. Phys.*, 1979, **71**, 2864.

176. E. J. Heller, *The Semiclassical Way to Dynamics and Spectroscopy*, Princeton University Press, Oxford, 2018.

177. S. Karsten, S. D. Ivanov, S. I. Bokarev and O. Kühn, *J. Chem. Phys.*, 2018, **149**, 194103.

178. S. S. Bala, P. K. Panja and P. N. Ghosh, *J. Mol. Struct. THEOCHEM*, 1987, **151**, 113.

179. E. Kish, M. M. Mendes Pinto, D. Bovi, M. Basire, L. Guidoni, R. Vuilleumier, B. Robert, R. Spezia and A. Mezzetti, *J. Phys. Chem. B*, 2014, **118**, 5873.

180. R. Costard, C. Greve, H. Fidder and E. T. Nibbering, *J. Phys. Chem. B*, 2015, **119**, 2711.

181. E. Mangaud, S. Huppert, T. Plé, P. Depondt, S. Bonella and F. Finocchi, *J. Chem. Theory Comput.*, 2019, **15**, 2863.

182. N. Mauger, T. Plé, L. Lagardère, S. Bonella, É. Mangaud, J.-P. Piquemal and S. Huppert, *J. Phys. Chem. Lett.*, 2021, **12**, 8285.